TILTROTOR MULTIDISCIPLINARY OPTIMIZATION

A Thesis

Presented to

The Academic Faculty

by

Martin Stettner

In Partial Fulfillment

of the Requirements for the Degree

Doctor of Philosophy in Aerospace Engineering

Georgia Institute of Technology

August 1995

TILTROTOR MULTIDISCIPLINARY OPTIMIZATION

Approved:

Daniel P. Schrage, Chairman

Dewey H. Hodges

J.V.R. Prasad

Date approved by Chairman: 8/11/95

ACKNOWLEDGMENTS

I would like to thank my advisor, Dr. Daniel P. Schrage, for his support through this research, and the freedom he allowed me in pursuing my own ideas. I am very grateful to the members of my advisory committee, Dr. Dewey H. Hodges and Dr. J.V.R. Prasad, for their patience and valuable discussions. I am indebted to Dr. David A. Peters, whose guidance as my advisor through the Master's research prepared me for this task, and whose exceptional spirit as a scholar will always be a great example to me. He also served on my reading committee with Dr. Aldo A. Ferri, to whom I extend my thanks. I would also like to express my appreciation for Dr. G. Alvin Pierce's service on the advisory committee until June 1995; he provided me with important feedback from the "analyst's point of view".

Financial support was initially provided by the Sikorsky Aircraft Division of the United Technologies Corporation. My thanks to David Matuska, the technical monitor of the project.

This research would not have been possible without the opportunities created by the Aerospace System Design Laboratory at Georgia Tech's CAE/CAD Laboratory. The efforts by Dr. Dimitri N. Mavris and Ms. Sandra H. Pierotti in creating and maintaining this environment are highly appreciated. I would like to express my special gratitude to Mr. Vincent B. Fox for excellent computer support. The feedback of members of "the lab" and the department were instrumental in generation of new ideas and solution of problems. Discussions with Mr. Mark A. Hale provided important inspirations in the design methodology sector, and he helped overcome many computational obstacles. I am very grateful to Dr. Carlos Cesnik, whose analytical knowledge and "engineering common sense" rescued me at several occasions. Besides providing immediate help, they join the

long list of friends who gave me what was maybe even more important: Friendship, support, and motivation throughout my time in Atlanta. Dr. Harald Buschek, William J. Marx, Hannah E. Mitchell, and Dr. Peter J. Röhl are only a few of the persons I could always count on - and can always count on.

Last, but not least: I would not be where I am now without the love and support of my family.

I thank y'all!

TABLE OF CONTENTS

LIST OF TABLES

LIST OF ILLUSTRATIONS

SUMMARY

A short-haul transportation system using civil tiltrotor aircraft has recently been considered as a means for airport congestion alleviation. Several separate sub-problems have been addressed, but not the global impact of new technologies on the economic feasibility of the system. Multidisciplinary Design Optimization (MDO) techniques facilitate such a task, but published applications did not employ a structured approach to problem decomposition down to the single data item level, and existing integration frameworks do not provide the flexibility required to respond quickly to changes in design requirements.

In this dissertation, an integration method is developed which incorporates a four step decomposition - recomposition procedure. The method aids in conversion of a given design problem in general terms into a specific infrastructure of available resources which allows the solution of such a problem. Intellectual tasks in form of human decisions regarding allocation of existing resources are separated from integration tasks which can be automated. Consideration of disciplinary needs and knowledge is an integral part of decomposition. Flexibility in the recomposition is provided by the representation of the information flow in matrix form, the enhanced Data Coupling Matrix, DCM^{+}. The matrix allows restructuring of the design process and identification of unnecessary resource executions in the sensitivity analysis. A computational infrastructure which employs this integration method, the Design and Optimization Coupling Code, DOCC, was developed and its proper operation verified on a small sample problem.

This method was applied to a civil tiltrotor optimization problem with an emphasis on airframe aeroelastic modeling, involving separate analyses for performance and sizing,

airframe structural dynamics, wing unsteady aerodynamics, rotor dynamics and subsystem coupling, and flutter suppression control system design. The objective function was the Productivity Index, PI, which served a simplified indicator for the aircraft's productivity to cost ratio. Computational resources were carefully selected and modified to match modeling requirements. Contributions in this sector include incorporation of transverse shear flexibility in an equivalent plate structural analysis, and implementation of a finite-state wake model for wing unsteady aerodynamics. Correlation studies with a Doublet-Lattice Method were performed and showed that the finite-state wake model is comparable in accuracy to traditional methods.

Optimization studies demonstrated the feasibility of the approach taken to large scale design and optimization problems. The impact of using a variable diameter rotor design (Variable Diameter Tiltrotor, VDTR), airframe aeroelastic tailoring, and active flutter suppression on designed configurations was explored using a non-hierarchic decomposition approach. Based on limited available rotor performance data and large blade retraction mechanism weight increment, VDTR designs were not competitive with conventional configurations with respect to PI. Tailoring of the wing structure to both static and aeroelastic criteria for free-free, symmetric modes was successfully demonstrated. Concerns regarding the applicability of the tiltrotor wing weight estimation in the VTOL Aircraft Sizing and Performance Computer Code, VASCOMP, to design for aeroelastic stability of a free-free aircraft configuration were raised. The impact of aeroelastic and aeroservoelastic tailoring on the objective function was generally outshadowed by the trade-off between rotor/airframe clearance and center of gravity location constraints, which is believed to be caused by the non-hierarchic decomposition/single objective function approach. A multilevel optimization scheme, or multi-objective optimization is suggested for future investigations.

CHAPTER I

INTRODUCTION

1.1. Motivation

In the last two decades, airport congestion has become a serious problem for the national air transportation system of the United States. An analysis of traffic at airports in the northeastern corridor indicated that at a disproportionally large number of runway slots is taken by small aircraft with fewer than 50 seats /Boeing CTR 87/. The number of US airports to experience significant delays is projected to increase from 23 to 33 in this decade (baseline: 1991, projection: 2002 /Lacy and Wilkerson 95/). Alleviation of congestion problems could be achieved by transferring this traffic from the runways to a new transportation system based on vertical take-off and landing (VTOL) aircraft. Landing pads can be located close to airport terminals and in city centers, which reduces taxi times and eventually the total travel times. Studies have shown that such a system bears the potential for taking a significant market share in the short haul sector due to the combination of VTOL capability with turboprop-like cruise efficiency, comfort, and speed /Hoyle et al.

87/. Techno-economic aspects of the tiltrotor configuration were investigated in a study funded by NASA, FAA, and DOD in 1986/87. Possible configurations were identified in this study conducted under the direction of Boeing Commercial Airplanes Company /Boeing CTR 87/, but the importance of further technological advancements was emphasized as a prerequisite for the development of cost-effective concepts /Wilkerson and Taylor 88/. NASA Ames Research Center engaged four contractors in 1990 to identify these technology needs for high-speed rotorcraft. Structural weight reduction, drag reduction, and engine specific fuel consumption reduction were considered primary drivers for all configurations (/Conway 91/, /Scott 91/, /Wilkerson and Schneider 91/). Tiltrotor aircraft specifically were shown to be very susceptible to weight growth with design cruise speed (/Conway 91/), which can be attributed to wing design for proprotor whirl stability and resulting high thickness-to-chord ratios and structural weight. Reduction of wing thickness and stiffness (/Conway 91/), tailoring fully coupled bending-torsion mode shapes, and applying active flutter suppression (/Wilkerson and Schneider 91/) were considered as enabling technologies. Scott also emphasized the importance of coupled wing-proprotor unsteady aerodynamics and dynamics modeling for Variable Diameter Tiltrotor (VDTR) designs. Wilkerson and Schneider concluded: "A more detailed design and analysis of the wing and rotor, backed by model scale tests, would be necessary to identify the specific combination of design parameters." This statement is a motivation for reviewing previous analysis techniques in the area of whirl flutter alleviation and results obtained, and marks the general direction of the research presented in this thesis.

1.2. Literature Review

Proprotor whirl flutter is a coupled rotor / support structure aeroelastic instability resulting from aerodynamic perturbation forces as the rotor axis performs a precessional motion in high speed flight. This flutter mode was first identified by /Taylor and Browne 38/ for propeller-engine systems and more closely investigated by /Scanlan and Truman 50/. The source was seen in inplane aerodynamic forces and moments which excite shaft precession. Research activity in the area increased significantly when in 1960 the loss of two Lockheed Electra aircraft was attributed to this phenomenon. After first experiments (/Abbot et al. 60/), analytical investigations described causes and approaches to whirl flutter alleviation (/Reed and Bland 61/, /Houbolt and Reed 62/). /Sewall 62/ and /Bennet and Bland 64/ showed the significant influence of wing mode shapes on the instability. Most of this work used aerodynamic stability derivatives for propellers derived by /Ribner 45/.

In 1962, an early tiltrotor design, the Bell XV-3, experienced a low frequency, high amplitude rotor-pylon precession during full-scale tests in the NASA Ames 40×80 ft wind tunnel. /Hall 66/ emphasized the importance of the XV-3 rotor's flapping degree of freedom in the phenomenon encountered, since articulated rotor systems transmit moments from the rotor into the hub only through hinge offset. Instead, the relative motion of swashplate to rotor disk of a flexibly mounted rotor-pylon system creates cyclic blade pitch changes, which may result in destabilizing forces on the hub for a particular phase relation. Subsequently, Hall suggested introduction of swashplate retardation (control phasing) to counter critical phasing and swashplate-pylon coupling to reduce cyclic pitch induced by shaft precession (the swashplate is coupled to the pylon such that it remains nearly parallel to the rotor disk on pylon deflection). /Young and Lytwyn 67/ showed that rotor damping in this mode can be maximized by introducing a flapping restraint, and calculated an

optimum natural frequency in flapping of 1.1/rev to 1.2/rev. /Wernicke and Gaffey 67/ commented that this approach might lead to excessive maneuver blade loads and that, in fact, the trade-off between whirl stability and acceptable rotor blade loads might create incompatible lower and upper constraints on blade flapping restraint. Instead, they proposed a "focused rotor" design for elimination of relative rotor disk-swashplate motion in which rotor and swashplate would be mounted to a gimbal hinge upstream of the rotor disk. Extensive trend studies were performed by /Kvaternik 73/ for a rigid-blade rotor system with flapping degrees only, coupled to an elastic support. Results indicated that pitch-flap coupling, suggested by Wernicke and Gaffey to reduce transient flapping, decreases rotor damping at low frequencies. Further results indicated the stabilizing influence of swashplate-pylon coupling and control phasing. Kvaternik also pointed out that use of quasi-steady wing aerodynamics overpredicts damping, and suggested approximate inclusion of unsteadiness by using the Theodorsen lift deficiency function /Theodorsen 35/ with a reduced frequency equivalent to the lowest flutter mode frequency.

The models developed by Kvaternik, enhanced by including rotor lead-lag, form the core of NASA Langley's Proprotor Aeroelastic Stability Analysis, PASTA. A more comprehensive model allowing inclusion of elastic blade modes was developed by /Johnson 74/, which formed the basis for the Comprehensive Analytical Model for Rotorcraft Aerodynamics and Dynamics, CAMRAD /Johnson 80b/. DYN4, a program very similar to PASTA, and CAMRAD were used by /Popelka et al. 85/ in comparisons between analytical models and wind tunnel model test data. Their results indicated that a rigid-blade model is sufficient to capture the essentials of the whirl flutter phenomenon. Furthermore, using a soft rotor blade-yoke attachment for a gimbaled rotor, a so-called "coning hinge," was shown to have a positive effect on whirl stability. /Nixon 92/ considered inplane and flapping modes for a rotor system coupled to a wing with beamwise

and chordwise bending, and torsional degrees of freedom, and concluded that lag frequency tuning is a practical method for increasing the flutter speed. He refined Kvaternik's findings on pitch-flap coupling by showing that stability of a stiff-inplane rotor system is less sensitive to negative than to positive δ_3. Trend studies indicated that for increasing forward sweep (decreasing sweep angle) of a homogeneous wing the flutter speed is decreased. For sweep angles of less than -30°, a powered rotor condition is conservative. This observation qualified the conclusion drawn by /Johnson 75/ from unswept wing / rotor investigations, which stated that the autorotation case is conservative.

The work covered in the previous paragraphs addressed passive means for whirl flutter suppression. Johnson's predecessor to CAMRAD (/Johnson 74/) was used in gust alleviation controller design studies based on Linear Quadratic Regulator Theory by /Frick and Johnson 74/. For a coupled rotor-wing system, it was shown that using a wing flap control in addition to rotor controls added a powerful means to stabilize the system by damping wing beamwise bending modes. /Ham and Whitaker 78/ concluded from experimental results that a vane, located at the wing half chord, however, is not very effective. /Nasu 86/ succeeded in stabilizing a proprotor/wing by introducing wing tip motion feedback into rotor cyclic control, where the feedback gains were determined by a harmonic balancing technique. /van Aken 91/ achieved flutter speed increases of approximately 10% for an XV-15 model by applying wing tip acceleration to longitudinal cyclic feedback only and varying the feedback gain manually. /Parham and Chao 89/ described the practical application of control system design to the V-22 Osprey. The focus of this work was not primarily on flutter speed increase, but on guaranteeing required stability margins of the flight control system in the directional loop, which was achieved by adding a structural filter. /Miller and Ham 88/ proved that application of active controls is

also a powerful means for solving the blade load / whirl stability trade-off dilemma described by /Wernicke and Gaffey 67/.

Propulsive efficiency is another important factor regarding economic feasibility. Proprotors operate in two very different modes: In hover, disk loading is high and inflow is low; in cruise, the situation is reversed. The necessity for trade-off between the opposing design requirements has been extensively discussed in the literature (for example /McVeigh et al. 83/ and /Farrell 89/). Two main approaches to solving this problem can be found in previous research: First, modification of the rotor geometry between a "cruise" and a "hover" configuration; and second, compromising in the layout. In hover, a relatively small twist of the blade is required, whereas high advance ratios in cruise dictate large twist angles for good propulsive efficiency. Since proprotors commonly operate at reduced rotational frequency (rpm) in cruise in order to reduce tip Mach numbers, the rpm change may be used in conjunction with extension-twist coupling of advanced composite blades to change twist between the two conditions /Kosmatka et al. 95/. Rotor diameter reduction from hover to cruise condition is effective in reducing induced power in hover, parasite power in cruise, and the effect of geometric constraints like rotor-fuselage clearance in cruise. /Fradenburgh 88/ discussed these benefits as a function of disk loading. /Fradenburgh and Matuska 92/ identified additional potential merits of the Variable Diameter Tiltrotor (VDTR) design with respect to acoustic footprint, internal noise levels, cruise gust response, and conversion profile. The concept's feasibility, including diameter change during conversion, was demonstrated and performance claims were supported in wind tunnel tests (/Studebaker and Matuska 93/). These two approaches are examples for expanding design freedom by introducing complexity. If the rotor design is to remain simple, numerical optimization techniques can facilitate the trade-off process. Multiobjective optimization techniques were applied to proprotor design with respect to

hover and cruise performance (/McCarthy et al. 94/), combined performance, aeroelastic, and structural limit considerations (/Chattopadhyay et al. 93a/), and in order to investigate the propagation of proprotor design into the weight breakdown of a tiltrotor aircraft (/Chattopadhyay et al. 93b/).

These last three examples reflect a trend towards numerical optimization of rotors including several classical disciplines (aerodynamics, structures, performance, aeroelasticity,...) and objectives (hover performance, cruise performance, drive system, weight reduction,...) simultaneously. Recent approaches follow this tendency by adding structural design of the wing to this list, from concepts (/Mais-Rohani and Baker 94/), via preliminary design including structural and aeroelastic constraints (/Friehmelt et al. 94/), to integrated wing/rotor aeroelastic tailoring (/Popelka et al. 95/, /McCarthy et al. 95/). In contrast to research reviewed so far, the structural model is subject to modification during optimization, simultaneously with the rotor layout. Along the lines of the quote by Wilkerson and Schneider's used as a transition into this section, the analysis tools for a "... more detailed design and analysis of the wing and rotor..." are available; the key is to combine these tools in order to "... identify the specific combination of design parameters". The most recent studies in aeroelastic tailoring of airframe and/or rotor perform exactly this task, and are applications of techniques from a new class of methods, which can be summarized under the term Multidisciplinary Design and Optimization (MDO). The following paragraphs present a review of decomposition-based techniques. The existence of a large class of new approaches to design space exploration and optimization is acknowledged at this point, but not made subject to further consideration.

The "Blueprint for Development" (/Sobieski 82/) is generally viewed as the pioneering work in the field of MDO. Sobieski reasoned that decomposing a system into its parts and devising a scheme by which the partial problem solutions are coordinated

should improve both efficiency and accuracy as compared to the traditional, sequential design process. The hierarchic suggested decomposition procedure calls for partitioning of the problem into a hierarchy of subsystems - disciplines, or any data converters - which allow only dependencies between upper level "parent" and lower level "child", but not between children. Design variables are allocated to a particular subsystem, and the subsystems, or design subspaces, are optimized independently. In this multilevel optimization, the system level is optimized with respect to the objective function, whereas the "child" processes use a different objective function and return a cumulative metric of constraint violation. The coordination between the upper and lower level problems is achieved by using the optimum sensitivities of the lower level objective functions and cumulative constraints, as linear approximations in the upper level optimization. Hierarchic decomposition and multilevel optimization was successfully applied to a practical aerospace engineering problem, the design of a transport wing, by /Wrenn and Dovi 88/. Some engineering problems, however, cannot be decomposed into a strict hierarchy because of interrelations between all sub-problems. /Sobieski 88a/ suggested a different approach for this case. In order to provide answers to "what if" questions (/Sobieski 88a/) regarding response and sensitivities of the complete, coupled system, local questions are answered, and the answers subsequently combined. In more mathematical terms, it means that sensitivities obtained from local sensitivity analyses about the contributing analyses, or CAs, of a coupled system are used to calculate the global, or system-related, sensitivities in application of the Implicit Function Theorem. The global sensitivities, dY_a/dX, of the output vector from CA "a", Y_a, with respect the design variables, X, are obtained by solving the Global Sensitivity Equations, GSE,

$$\begin{bmatrix} I & -\frac{\partial Y_a}{\partial Y_b} \\ -\frac{\partial Y_b}{\partial Y_a} & I \end{bmatrix} \begin{Bmatrix} \frac{dY_a}{dX} \\ \frac{dY_b}{dX} \end{Bmatrix} = \begin{Bmatrix} \frac{\partial Y_a}{\partial X} \\ \frac{\partial Y_b}{\partial X} \end{Bmatrix} \tag{1.1}$$

here only shown for an example with two Contributing Analyses, a and b. As Sobieski pointed out, the derivatives of the GSE's solution with respect to the elements of the left hand side matrix provide information about the coupling strength between different CAs, which can be used to find weak couplings which might be temporarily or permanently dropped from the model (/Sobieski 88a/). The solution of the GSE provides a linear approximation of the design space, which may be used for gradient-based optimization techniques (here referred to as global design space, or GDS, approach since the entire design space is subject to exploration in one system global optimization step). Large-scale systems optimized using this approach included controlled space structures and supersonic transport aircraft (/Padula et al. 91/, /Barthelemy et al. 91/). /Wujek and Renaud 94/ used second-order derivatives based on the GSE in a sequential quadratic GDS scheme. Compared to a first order approach, they encountered reduced robustness to the chosen step size in local sensitivity analyses.

Local sensitivity analyses may be performed in parallel; hierarchic decomposition schemes, however, include the distinctive advantage of allowing parallel subspace optimizations. /Sobieski 88b/ expanded the concept of subspace optimizations (SSOs) to non-hierarchic systems by partitioning the design variable vector into disjoint subspace design variable vectors, and introducing an extra set of coefficients per subspace. In similarity to multi-level optimization, these coefficients are set constant in the concurrent subspace optimizations (CSSOs), in which they determine either the "responsibility" for reducing a violated subspace cumulative constraint (one per subspace), or allow a "trade-off" between temporary subspace constraint violation and objective function improvement. The coordination procedure then uses linear approximations of the cumulative constraints and objective function to minimize the objective function with respect to the coefficients, not the original design variables. The result is used in the next subspace optimizations.

The algorithm was applied and verified by /Bloebaum et al. 90/, but showed oscillating convergence histories if no move limits for the "trade-off" coefficients were chosen. /Renaud and Gabriele 93/ proposed a different coordination procedure in which a second-order approximation of the system, based on data acquired during the subspace optimizations, is used. Linear approximations from solution of the GSE account for non-local influences in the subspace optimizations. A very similar algorithm was presented by /Renaud et al. 94/ for mixed discrete/continuous systems. In this case, the GSE was removed, and the quadratic approximation technique replaced by a neural network, trained with results from the SSOs.

Overlap between the original multilevel and non-hierarchic schemes is indicated by devising design subspaces in both CSSO and multilevel schemes. Another link is marked by early attempts to weaken the separation of design variable sets assigned to a particular level in multilevel approaches by formulating the separation requirement as constraints in the "child" optimizations (/Haftka 84/, /Renaud and Gabriele 90/), or use of a global sensitivity matrix as an aid in multilevel optimization (/Padula and Polignone 90/). A more precise nomenclature was introduced by /Balling and Sobieski 94/, which takes the operational modes of "contributing analyses" in account. The new classification consists of three main descriptors: One to distinguish between single and multiple optimizers used (on system and / or discipline level; "Single" and "Multi"), and the remaining to separate disciplinary evaluators ("SAND" for simultaneous analysis and design) and analyzers ("NAND" for nested analysis and design) on the system and disciplinary levels, respectively. Disciplinary evaluators refer to tools which create a set of states which are required to converge in an iteration loop around the tool only, or including others; disciplinary analyzers include such a loop and do not require coordination. In terms of their formulation, the CSSO, for example, has a Multi-NAND-NAND structure; a single

objective optimization task with all iteration loops interrupted and reformulated into constraints would be a Single-SAND-SAND. A short hand notation was presented for describing derivatives of the six basic options.

CSSO and GDS approaches are primarily concerned with improvement of the sensitivity-based optimization efficiency. All methods use design space approximations, however, which need to be compared to the actual values at some point by a "system analyzer" call, in the terms of /Balling and Sobieski 94/. The efficient and intelligent scheduling of this process, on the other hand, is a field previously associated primarily with operation research. /Steward 81/ ordered tasks along the periphery of the design structure matrix, DSM, and denoted couplings between two tasks by marking the matrix element in the associated row and column. This visual aid allowed identification of sequential, parallel, and coupled tasks, and rescheduling of the task sequence by reordering the matrix. A computational implementation of this procedure, the Design Manager's Aide for Intelligent Decomposition, DeMAID, was developed by /Rogers 89/.

DeMAID uses heuristics like the number of feedbacks, crossovers, or parallel executions in the N^2 Diagram, Fig. 1.1, to reorganize processes. Feedbacks which can not be eliminated are combined into "Circuits," which may then be executed in sequence. This is in contrast to the Axiomatic Approach to Design, AAD /Suh 90/, which calls for elimination of all such couplings by redesign. As an extension to DeMAID's original capabilities, rules incorporating coupling strength information determined from the system's GSE have been formulated and used by /Bloebaum 92/. DeMAID is an example for a tool which is less related to the development of new optimization algorithms, but with the implementation and execution of decomposed analysis problems in a timely and efficient manner. An example for inclusion of such considerations into an aircraft analysis

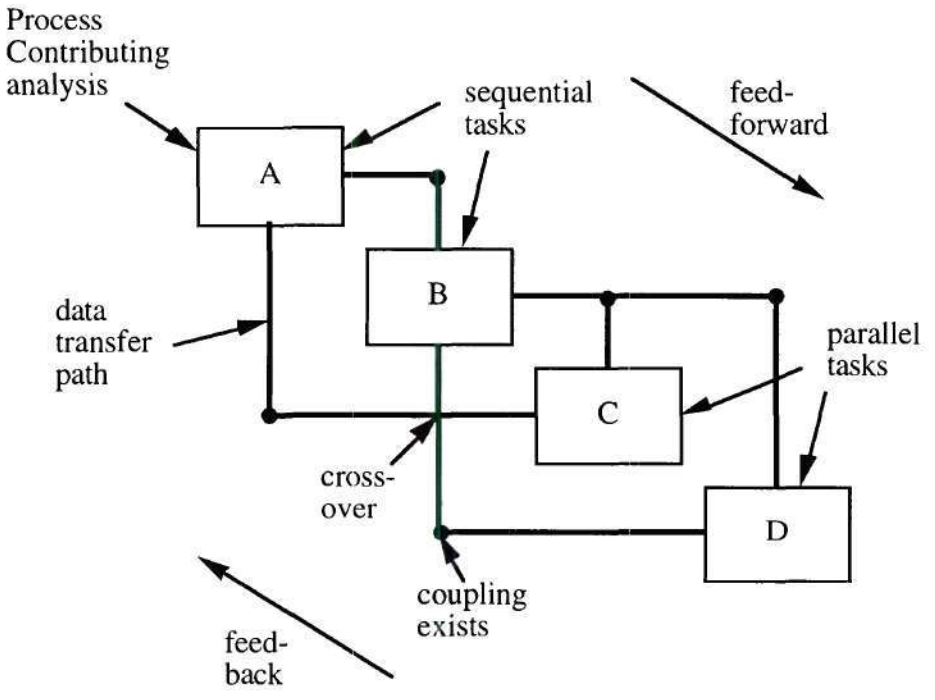

Fig. 1.1: Elements of the N^2 Diagram

and synthesis code is the Program for Aircraft Synthesis Studies, PASS (/Kroo and Takai 88/). PASS incorporates a quasi-procedural approach, in which subroutine modules and their order of execution are selected by a computational path generator, depending on "valid" inputs in a central data base and desired outputs. /Gage and Kroo 92/ indicated significant computational time savings opportunities in two situations: First, finite-differencing operations about the entire analysis; and second, iteration loops. The path generator picks only the modules necessary for execution; by properly ordering tasks the number total module executions can be significantly reduced (/Gage and Kroo 92/). In the first case, this can be accomplished by organization of design variables such that results

from previous steps can be reused. In the second case, variables subject to iteration are replaced by a an equality constraint-design variable pair. The effort associate with introduction of a new design variable, however, is minimized through the quasi-procedural approach as described above. Hence, computational time savings are maximized.

MDO is meant to facilitate execution of large problems, so a branch of this new discipline is dedicated to development of computational infrastructures for tool integration and optimization task execution. /Hollowell and Bitten 92/ distinguished between "external linkage" approaches in which disciplines are represented on-line by values and sensitivities calculated off-line by a disciplinary expert, and "internal linkage" methods which include high fidelity programs on-line. The trend appears to go towards the internal linkage approach: Implementations of multilevel optimization (/Wrenn and Dovi 88/) and GDS techniques (/Dovi et al. 92/) included large, stand-alone programs. In both cases, executive software was written in UNIX shell. The HiSAIR/Pathfinder system by /Dovi et al. 92/ included separate stand-alone programs for performance and sizing (FLOPS /McCullers 93/), aerodynamics (WINGDES /Carlson and Walkley 84/), and structures (ELAPS /Giles 89/). Executive and program tools communicated with a central data base, a common factor for the frameworks reviewed. "Task Control Procedures" were programmed for executing functional analyses like trim, static aeroelastic analysis, or deformed wing shape calculation, controlled by a central executive block. With this feature, the order of events to take place was hardcoded in the framework. Transparency of data dependencies was limited. A different approach was taken by /Jones at al. 92/ with the HiSAIR Data Management (HDM) system. Data tracking and accountability was identified as an important issue and utilities for browsing and modification of data in distributed files and data bases through a Graphical User Interface, GUI, were provided. Initial disciplinary data requirements were determined via query forms, and the resulting information was

input to DeMAID to determine an execution order. The Framework for Interdisciplinary Design Optimization, FIDO (/Townsend et al. 93/) combines features from Pathfinder and HDM in a heterogeneous computing environment. Like Pathfinder, discipline drivers may combine several programs in order to perform a certain task. Similar to HDM, a "SPY" segment allows the user to view (or modify) data and execution progress through a GUI. The primary difference, however, lies in the way data are transferred. Via an interface, the driver routines communicate through a central communication library, which allows them to obtain data either from a central data base, or directly from other drivers. In the latter case, tracking of data might present a problem, since traditional tool input and output files were eliminated. The notion of data "accountability" - the "what, why, when and how" context added to information (/Hale and Craig 94/) - was first introduced by /Stevens 93/ in the Laboratory Environment for the Generation, Evaluation and Navigation of Design, LEGEND, framework. Instrumental to LEGEND and IMAGE, the Intelligent Multidisciplinary Aircraft Generation Environment (/Hale and Craig 94/), is to provide first: fast interaction, data transfer, and control capability in the spirit of FIDO; and second, options for identification and avoidance of automation-related problems through information accountability. LEGEND and IMAGE, currently in development, expand the scope of design environments from pure data handling, process control, and data visualization, via planning and scheduling (as in DeMAID or PASS), to the more fundamental considerations of Meta-Design and Decision-Based Design (/Bras and Mistree 91/).

1.3. Summary and Scope of Work

Proprotor whirl flutter has been identified as a primary design driver early in the development of tiltrotor aircraft. The problem has been investigated with respect to influences of one contributor at a time. Early works analyzed the impact of flapping restraint, or pitch-flap coupling only; in the 1970's and 1980's, detailed rotor configurations were mounted to airframe models to predict the coupled system stability; and several approaches have been made in the last 20 years to flutter suppression controller design. At a time when the introduction of a tiltrotor transportation system into a highly competitive market is being seriously discussed, an evaluation of whirl flutter as a design driver, and approaches to its alleviation in terms of their respective impact on the economic viability of this system seems necessary. Such an approach must include a comprehensive model of the aircraft's dynamics which allows simultaneous trade-offs between previously separately addressed contributions. Until very recently, the impact of aeroelastic tailoring of the wing structure which supports the rotor has not been addressed in published research. Hence, the model should provide flexibility for inclusion of more detailed rotor system and control system design, but focus on airframe aeroelastic tailoring. Issues of both structural modeling and unsteady aerodynamics are to be addressed in this context. In order to allow exploitation of possible weight or drag reductions, re-sizing and performance analysis must be closely coupled to the dynamic model. The primary question to be addressed is:

> *What is the global impact of rotor design (conventional / VDTR), aeroelastic modeling accuracy and fidelity (tailoring), and active flutter suppression on an economics-related metric of a civil tiltrotor aircraft configuration?*

The preceding literature review revealed that no single analysis or method matches this description, but that some parts of it are available. Existing integration frameworks do not match the flexibility and transparency required for coupling of these programs: First, new programs and modified existing tools require calibration and frequent user intervention, which implies the necessitiy of access to the entire information generated. Hence, they cannot be used as "black boxes" as required by the recently developed design environments, in particular since these frameworks are in a development stage themselves. Second, the hardcoded "task control" elements of Pathfinder or "drivers" of FIDO do not allow a simple implementation and task rescheduling of a design problem as different from supersonic transport aircraft design as the tiltrotor problem outlined above. Third, given that this task has been accomplished, none of the framework architectures reviewed seems to allow a quick reconfiguration, for example in order to include a new discipline which might become important during the design process, or, more related to the tiltrotor case, to replace a simple disciplinary tool by a higher fidelity one in order to study the impact on the total system performance. PASS provides for execution rescheduling through the quasi-procedural approach, but requires modules to be implemented in subroutine form which practically rules out inclusion of existing stand-alone tools. Finally, no examples were found in which the development of a design task formulation into a structured model (disciplines, data flow, connectivities, etc.) for its execution was described in detail. In conclusion, the following secondary questions need to be answered:

How can the structure of a design problem be determined in an organized manner?

How can the structure of a design problem be implemented such that it can be easily changed?

It is believed that the selection and / or development of appropriate tools for the "Tiltrotor Design Simulation Model" is as integral to addressing the questions mentioned above as the integration of these codes in an efficient, flexible manner, and that these two issues are inseparable. The primary thrust in this work is therefore not on attempting to answer all questions related to the impact of whirl flutter and whirl alleviation on tiltrotor economic viability, but on providing a structured, generic approach that permits such exhaustive investigations. As a result, a method that merges both disciplinary analysis and integration issues has been developed and is presented in Chapter 2. The implementation of this method, that is, development of analytical tools for the tiltrotor design simulation model and of an integration framework, is covered in Chapter 3; details like calibration studies have been included in the Appendices. Application of the framework and Design Simulation Model to selected optimization cases is shown in Chapter 4. Conclusions and recommendations are summarized in Chapter 5.

CHAPTER II

APPROACH:

A FOUR-STEP DESIGN INTEGRATION METHOD

2.1 Basic Considerations

Sobieski rationalized that early approaches to optimization of complex systems were unsuccessful because they "... tended to exclude the human intellect from the process ..." and "... disregarded the engineers' thoroughly practical desire to form specialty groups, each group assuming responsibility for part of the design problem in exchange for a professional independence in the choice of means to do the job." (/Sobieski 89/). Despite this intended incorporation of the disciplinary analyst in the process, however, the impression gained from seeing their discipline degraded to a black box, either "wrapped" (/Stevens 93/, /Hale and Craig 94/) or their codes degraded to "subroutine form" (/Weston et al. 94/), could lead to the conclusion that the disciplines are to be "pocketed" by MDO. By definition, the MDO expert cannot accumulate the disciplinary knowledge which a disciplinary analyst has. On the other hand, the analyst might not be in a position to gain

the overview over the total design process which the MDO specialist has. A certain tension arising from these different positions is not beneficial to the goal of integration and harmonization of the design process. Implementation of MDO techniques therefore requires a balance between the managerial character of MDO and the independence of the disciplines, and the resource "human intellect" must be part of both elements. The experiences gained during this research effort from attempting to include both disciplinary and MDO considerations into an integrated approach are formalized in the method described in the following section.

2.2 Four-Step Integration Method

It is assumed that through brainstorming, market analysis, a Request for Proposal (RFP), or contract wording, a "Problem Definition" has been obtained which may be summarized in a form similar to that depicted in Fig. 2.1. This form is just a suggestion with no claim on completeness. Similarities with the "baseline model for a design problem" used by /Mistree et al. 93/ to outline the Compromise Decision Support Problem (DSP) technique and its differences to mathematical and goal programming (/Mistree et al. 94/) are not coincidental ("Given...," "Find...," "Satisfy...," "Minimize..."). The structure was adapted since it allows a very dense representation of a design problem and is independent of the optimization strategy chosen. The primary difference is the addition of the Focus Statement, which emphasizes disciplinary analysis aspects, and the Analysis Statement, which outlines the tasks to perform once the conditions in the Search Statement are satisfied, and how to evaluate the results.

Given this starting point, four steps are taken towards a complete definition of the data transfer structure and execution schedule. Much of the terminology has been adapted

Given:	The "Basis Statement" background, a certain configuration factors to be held fixed (constants) factor that may be varied
Find:	The "Search Statement" points or domains in the design space described above which satisfy a search criterion, which can be formulated in terms of minimization or maximization
Satisfy:	The "Constraint Statement" constraints that have to be satisfied goals which should be met bounds on variables
Emphasize:	The "Focus Statement" areas of particular interest which require special attention
Evaluate:	The "Analysis Statement" investigations to be made at the point(s) or in the domains found, like robustness issues, comparative studies, etc. if not covered in the Search Statement

Fig. 2.1: Problem Definition

from /Pahl and Beitz 92/ and the work of /Stevens 93/ in LEGEND, and /Hale and Craig 95/ in IMAGE in order to show parallels. Since the terms are used frequently, their origin is not indicated individually. Instead, they are capitalized throughout this thesis and summarized in Appendix G. Two major phases can be identified: Decomposition and Recomposition, sketched in Fig. 2.2 and Fig. 2.3, respectively. Each phase is divided in two steps, which are described in the following paragraphs.

2.2.1. Decomposition (Fig. 2.2)

The basic philosophy is the following: Given a concentrated description of the problem as in the Problem Definition, a Process can be identified which generates the information required to make decisions which eventually result in solution of the problem. It is assumed that the Design Simulation Model is composed of a set of known Processes. The information required and generated by these Processes can be completely described for a certain level of fidelity by a set of single data items, called Attributes. The goal of decomposition is to identify these Attributes, and the Resources (computer codes, experimental data bases, heuristics, teams of engineers,...) which generate information which can be converted into these Attributes. The approach suggested is to reduce the level of abstraction in two steps. The first step provides an initial, preliminary structure, and is based on a thought process which includes both intuition and physical elements. The second step eliminates the intellectual element and partitions information into clearly separable and disjoint sets.

2.2.1.1. Step 1: Level I Decomposition

The Problem Definition is analyzed for Disciplines involved. The Design Simulation Model is then broken down into several Processes in a joint effort by disciplinary and integration experts, in form of a brainstorming or an informal query procedure. Processes will generally be associated with one Discipline only, but it is not required. The information required to execute these Processes, and the information generated by them is described in very general terms and based on intuition; completeness is the only requirement at this point. Terms are chosen to name this input / output information. The contents of these "Intuitive Data Sets" is discussed to avoid misunderstandings and provide homogenization. The result is a first-sketch decomposition in terms of vaguely defined Attribute Set Descriptors.

2.2.1.2. Step 2: Level II Decomposition

Based on the general information definitions obtained, and on consideration of the maximum level of fidelity anticipated within the scope of the Problem Definition (in particular the Focus Statement), Resources are chosen for each Process by the disciplinary experts involved. It is important to note that at this stage no decision is made as to which level of accuracy will be used, but how high the accuracy requirement might be. A Process may require more than one Resource (Fig. 2.2); for example, an "aerodynamic" Process with Function "generate lift" and Form "wing" could include a wind tunnel test for generating airfoil data in table form (Resource R_a1) which are then used in a computer program (Resource R_a2) to generate 3D lift information. Identification of the Resources allows a more detailed description of information input and output. In the example given, the input for Resource R_a1 could be summarized in the terms "cross section, airfoil" and "flow conditions," the output of Resource R_a2 could include "pressure distribution."

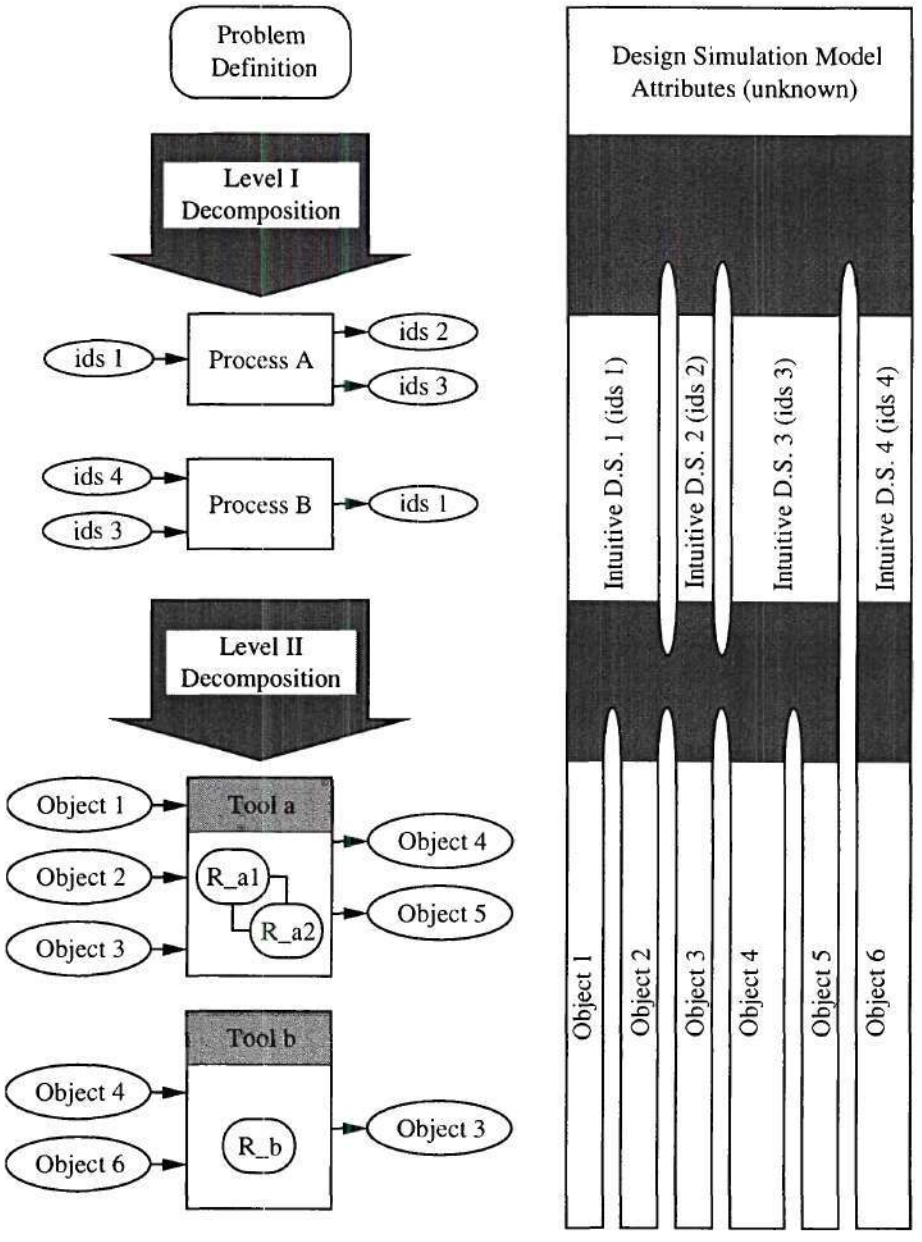

Fig. 2.2: Decomposition

These information descriptors, called "Objects," may contain Form information, as in the first case, or Function information, as in the second example. In contrast to the Intuitive Data Sets which the Objects are derived from, no overlap is allowed between Objects. In other words, the Attribute sets formed by Objects are disjoint.

At this step, the Object definitions are homogenized between the Disciplines in preparation for recomposition, and a standard format for information exchange is agreed upon. A Resource or group of Resources executing a particular Process and communicating Objects using this standard protocol is denoted a "Tool." The result of Level II Decomposition is therefore a set of Tools and Objects. Accuracy has been considered, but not implemented.

2.2.2. Recomposition (Fig. 2.3)

Considerations regarding connectivity between Processes or Tools have been avoided so far, except for conventions made in definitions of Intuitive Data Sets and Objects. The intention behind this approach is to eliminate any preconceived hierarchies or structures by first detailing the parts. Knowledge of the Tool information requirements then enables the integration expert to compose the Design Simulation Model by strictly connecting information source and information receiver(s) for each Attribute separately (Level II Recomposition). The information flow structure obtained defines certain bounds on the order in which Contributing Analyses are to be executed, but still allows certain freedom. The process leading from the "hard" structure resulting from the first recomposition step to the "soft," user-defined execution order is the subject of the Level I Recomposition.

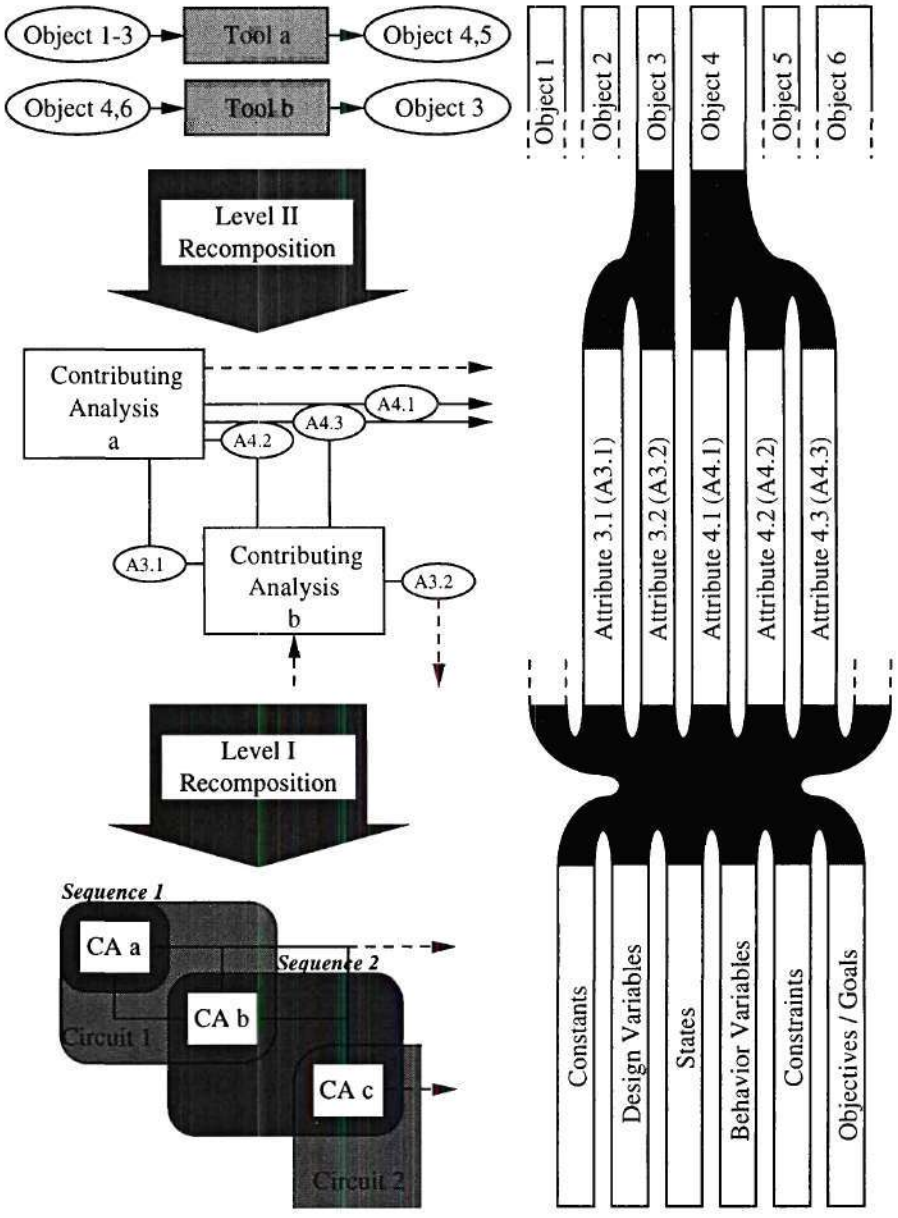

Fig. 2.3: Recomposition

2.2.2.1. Step 3: Level II Recomposition

This step is by far the most cumbersome and tedious task. First, the Objects are defined in terms of single Attributes (Fig. 2.3). This process should be aimed at reducing the number of Attributes to a minimum, and depends strongly on fidelity and connectivity considerations. For example, the Object "wing dynamic properties in vacuum" is described by the eigenvalues, eigenvectors, and generalized masses of the structural modes. An initial approach might be to use deflections in 20% chord steps at five spanwise locations in order to describe the mode shapes. If the structural model employs only five assumed shape functions in bending, two in torsion, and one for cross-sectional deformations, then all mode shapes are described by eight coefficients. These mode shapes could subsequently be used in a Tool performing an "unsteady aerodynamic" Process with a Resource that implements the Model "thin airfoil theory, flat plate." In this case, the cross-sectional deflection information is superfluous, and seven Attributes per mode are sufficient. Additional reductions might be possible by incorporating frequency limits imposed by the validity of the aerodynamic Model used. The resulting accuracy- and connectivity-dependent set of Attributes describing a particular Object is called a Schema, and the connected Tool is termed Contributing Analysis.

Second, the paths of each Attribute are traced from its origin (the generating Tool) to all of its destinations (the receiving Tools). This book-keeping task is facilitated by a tabular representation of the input and output characteristics of each Attribute, termed the Data Coupling Matrix, DCM (Fig. 2.4). Attributes are arranged here by Schema in the rows; the columns are associated with the Contributing Analyses. The numbers in the matrix denote whether a particular Attribute is not used (0), is required as input (1), or generated (2) by the Contributing Analysis (CAs) associated with the column it is placed in.

A fourth option is possible for these "Input / Output Indicators," symbolized by a value of 3: In some cases, an Attribute generated by a CA is updated on every execution of the CA. For example, if a CA includes a Resource which requires iteration, it is possible to speed up convergence by using the result of the previous CA run as a starting point. This particular Attribute is therefore both input and output. Fig. 2.4 depicts such a situation for the Attribute "A1.1" in the CA "CA c."

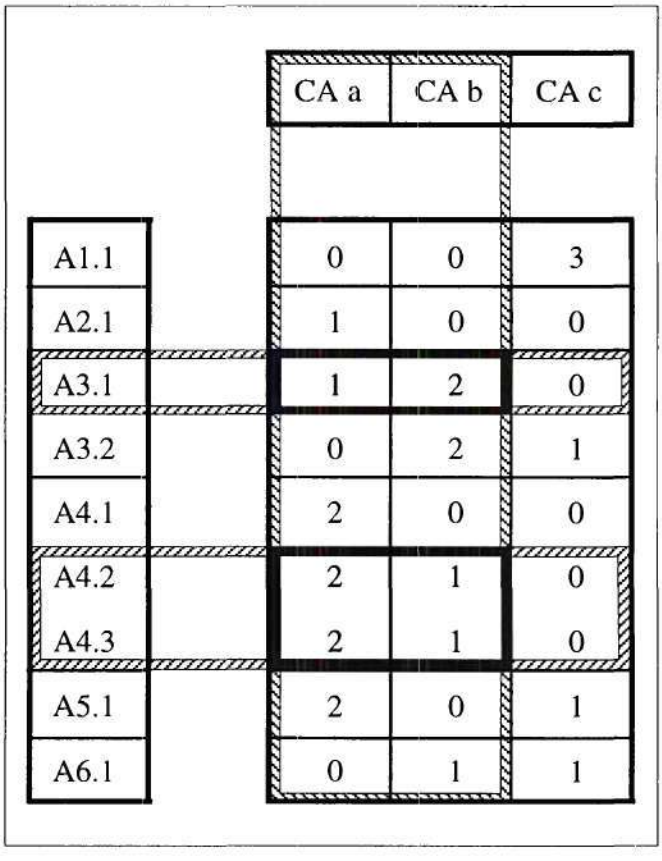

Fig. 2.4: Data Coupling Matrix, DCM

The DCM is an aid for ensuring that no inconsistencies between CA Attribute generation and Attribute requirement exist (Level I Compatibility). A first check is aimed at pinpointing information generation conflict - each row must contain only one column with a "2" element in it. The next step is to distinguish between Connective, Input and Output Attributes: Rows with "2" and "1" elements indicate Connective Attributes. Consider the rows "A3.1," "A4.2," and "A4.3" in Fig. 2.4; the former is generated in "CA b" and needed in "CA a," the latter two are generated by "CA a" and used in "CA b." Generally speaking, this loop would be solved by iterating on the Attributes A3.1, A4.2 and A4.3 until a specified convergence is achieved. Another option is to open one of the connections, for example by A3.1, introduce a new input, for example $A3.1^*$, and impose an equality constraint on these two values. It is assumed for the further discussions that the iteration solution has been chosen. The Attribute "A2.1" row in Fig. 2.4 does not show any "2," indicating that it is not generated by any CA in the Design Simulation Model. As an Input Attribute to the Design Simulation Model it must be either mentioned in the Basis Statement, indicating that it is constant, or in the Search Statement, meaning that it will be varied during the design space search. If none of these applies, then an inconsistency exists. To restore Level I Compatibility, either one of the existing CAs must generate this Attribute, or another CA must be added in order to perform this task. Finally, Attribute "A4.1" is an Output Attribute since it is generated by "CAa," but not required as input to any CA.

Fig. 2.3 depicts the situation described above in a graphical representation similar to the commonly used N^2 Diagram. Note that only data flow between Contributing Analyses is shown, so that no Input Attributes appear. The iteration loop is represented by the feed-forward branch with A4.2, and the feedback branch with A3.1.

2.2.2.2. Step 4: Level I Recomposition

Given the information connections identified in the previous paragraph, a certain order of execution is inherently implied. /Balling and Sobieski 94/ used a short hand notation for classification of decomposition approaches which is useful for describing this order:

[ ]	nested execution; coupled tasks
$\Rightarrow$	sequential execution
$\|\|$	parallel execution
SA[ ]	System Analyzer
SO[ ]	System Optimizer
E_i	Evaluator, Discipline i (no iteration or coordination performed; this task is transferred to an Optimizer)
A_i	Analyzer, Discipline i (includes coordination / iteration tasks)
O_i	Optimizer, Discipline i

(2.1)

/Rogers 89/ discussed scheduling of CA executions and introduced the term "Circuit" for a nested group of CAs. In reference to this work, the following "Circuit Analyzer" operator, C[ ], is defined for execution of iterative processes. This definition is in slight deviation from the terminology of /Balling and Sobieski 94/, where a "Disciplinary Analyzer" with a similar task is used. The Circuit Analyzer operator is similar in function, but may include several disciplinary Contributing Analyses.

Identification of coupled Contributing Analyses (CAs) has been discussed above. Sequential execution of two CAs is indicated information flow on one direction only, for example through generation of Attribute "A3.2" in "CA b" and reception in "Ca c" in Fig. 2.4. CAs can be executed in parallel, or independently from each other if no such Attribute input / output pair can be found. It is assumed for demonstration purposes that no additional CAs exist. Analysis of the Design Simulation Model, in the following sections denoted the ANALYSIS task, can then be expressed in a quasi-code form, here referred to as the Problem Execution Code:

$$SA[\ C[\ CA\ a \parallel CA\ b\ ] \Rightarrow C[\ CA\ c\ ]\ ] \qquad (2.2)$$

The central element of this expression is the Circuit. Feedbacks between the Contributing Analyses which form the Circuit are hidden within it. It is furthermore required that information flows between Circuits in one direction only, so that a feedback loop including Circuits is not allowed (/Rogers 89/). Instead, the Circuits would be extended to include this feedback. As a result, the following syntax element for the Problem Execution Code can be formulated:

Rule 1: Circuits are executed sequentially.

With this in mind, definition of Circuits becomes an important issue if available resources such as CPU time, total user time, or available computer platforms are considered. A complex, coupled Design Simulation Model can always be viewed as a single iteration loop, that is one Circuit. This "all at once" approach might be advantageous, for example, if a computationally intensive iteration loop is followed by a long series of less intensive CAs, a large sufficient number of host computers or processors is available, and total user time is more important than CPU time. If no parallel processing capability exists and CPU time is the main cost driver, then one would attempt

to eliminate as many feedback loops as possible to reduce redundant executions. For visualization purposes, it is useful to organize the Contributing Analyses on the main diagonal of an N^2 Diagram (Fig. 1.1) and to connect them if information flow is indicated by the DCM. If the Model is very complex, identification of Circuits depending on parallel, minimum feedback, or coupling strength considerations (as in /Bloebaum 92/) is facilitated by using the information in the N^2 Diagram in DeMAID /Roger 89/. The chosen Circuits are then entered into the DCM as a new row, Fig. 2.5, where the execution order follows the size of the Circuit number, beginning with 1.

	Type	CA a	CA b	CA c
Circuit Seq.		1 1	1 2	2 2
A1.1	2	0	0	3
A2.1	0	1	0	0
A3.1	3	1	2	0
A3.2	2	0	2	1
A4.1	4	2	0	0
A4.2	5	2	1	0
A4.3	3	2	1	0
A5.1	4	2	0	1
A6.1	1	0	1	1

Fig. 2.5: Enhanced Data Coupling Matrix, DCM +

The observations made so far referred to generation of zeroth order design space information, called here the ANALYSIS task of the Design Simulation Model. A large class of optimization algorithms require additionally first order information, or sensitivities. The traditional approach to obtaining this information, referred to as the SENSITIVITY task, was performed by nesting the ANALYSIS task in a finite-differencing loop in which Design Variables were subsequently perturbed. A radically different philosophy was made possible by Sobieski's Global Sensitivity Equations (GSE /Sobieski 88a/). Instead of obtaining sensitivities about the entire Design Simulation Model, local sensitivity analyses are performed about each Contributing Analysis independently of each other, and the global sensitivities are obtained by arranging these local derivatives in the GSE and solving it. Due to the modularity of the method, particular advantages in accuracy arise compared to the traditional approach, since analytical sensitivity expressions have been obtained for many applications, replacing the step-width dependent finite-differencing approximation by an exact solution (for example unsteady aerodynamics, fixed /Yates 87/ and rotary wing /He and Peters 92/; controls/structures integration problems, /Sobieski et al 88/, /Gilbert 88/). Improvements in accuracy have also been reported in applications of automatic differentiation tools for computer programs in source code form (for example ADIFOR). Users of ADIFOR (/Bischof et al. 91/), however, warned that the computational cost involved increases with the number of independent variables just as in finite-differencing, and suggested development of pre- and post processors for reduction in the number of variables (/Barthelemy and Hall 93/). In the same sense, the user may decide not to run a local sensitivity analysis about every single Contributing Analysis if the number of independent variables (non-constant Input Attributes) is large, but include a number of CAs, if the total number of sensitivity analyses can be reduced significantly.

It was concluded that the approach followed for the ANALYSIS task should be paralleled by a similar method in the SENSITIVITY task, where groups of Contributing Analyses termed Sequences take a role similar to that of the Circuits. Unlike the ANALYSIS case, grouping of Contributing Analyses is not dictated by the information flow structure. The definition of Sequences depends on practical considerations related to the dimension of the information flow between Contributing Analyses. Consider the situation depicted in Fig. 2.3. If there would be a large number of Attributes like "A3.2" generated by "CA b" and required by "CA c," then a local sensitivity analysis about "CA c" alone is very expensive. Assuming that the number of non-constant input Attributes of " CA b" is much smaller, then it is more efficient to combine these two Contributing Analyses into a Sequence. If operators for the Sequence sensitivity analysis, S [ ], and the Global Sensitivity Equations, GSE, are defined, then the SENSITIVITY task, SD[ ], for this example can be expressed in the following form:

$$SD\,[\,(\,S\,[\,CA\ a\,]\,\|\,S\,[\,CA\ b \Rightarrow CA\ c\,]\,) \Rightarrow GSE\,] \qquad (2.3)$$

The sequential execution of "CA b" and "CA c" represents the most likely case in which a Sequence is chosen to enclose a large volume, one-way information flow (hence the name); in a more general case, Circuit Analyzers may be required inside a Sequence. Local sensitivity analyses are independent of each other, forming a second element of the Problem Execution Code syntax:

Rule 2: Sequences can be executed in parallel.

The chosen Sequences are entered in the second row of the DCM like the Circuits before. In this configuration, the DCM is termed the enhanced Data Coupling Matrix, or DCM^{+} (Fig. 2.5).

2.2.3. Problem Execution

The first two rows of the DCM+ provide information about Contributing Analysis grouping in the ANALYSIS and SENSITIVITY tasks. Given the two syntax rules developed above, this grouping defines the Contributing Analysis execution order within each task. In the global design space approach (GDS, refer to Section 1.2), information is then fed directly into the System Optimizer, SO, which searches for sets of "Design Variable" Attributes, d, which satisfy the conditions in the Search and Constraint Statements of the Problem Definition (Fig. 2.1). For the example used before, the complete Problem Execution Code has the following form:

$$
\begin{aligned}
d \;=\; & SO\,[\,SA, SD\,] \\
=\; & SO\,[\\
& \quad SA[\; C\,[\; CA\,a \;\|\; CA\,b\;]\Rightarrow C\,[\,CA\,c\,]\;], \qquad (2.4)\\
& \quad SD\,[\,(\,S\,[\,CA\,a\,]\,\|\,S\,[\,CA\,b\Rightarrow CA\,c\,]\,)\;\Rightarrow GSE\,] \\
&]
\end{aligned}
$$

The form of (2.4) is specific to the GDS approach, but the approach per se is general and applicable to other techniques. In the case of Concurrent Subspace Optimization, CSSO, for example, subspace optimizers and a coordination procedure with their own specific syntax would be added similarly to the system analyzer (SA) and system sensitivity analyzer (SD).

If all functional elements in (2.4) exist - for example in form of computer programs using a standard protocol, or subroutines - then d can be determined if the elements' input Attributes can be identified and accessed. Additionally, independent and dependent variables must be identified for Sequence Sensitivity Analyzers, S. Finally, System

Optimizer, SO, inputs (Constraints, Objectives) and outputs (Design Variables) must be defined.

This information is also contained in the DCM+. Contributing Analysis input and output Attributes are denoted by a "1" or "2," respectively, in the according column (Section 2.2.2.1.). The Sequence (non-constant) input and output Attributes are identical to Sequence sensitivity analysis independent and dependent variables, respectively; hence, they can be identified by the according Input / Output Indicator in the respective Sequence column partition of the DCM+. Since these Attributes are relevant in calculation of inputs for the GSE, they are called "Behavior Variables"*. An exception from this rule are the "States"**, that is Attributes which are only transferred between Contributing Analyses in the same Sequence. All Behavior Variables qualify as Constraints and Objectives, and Design Simulation Model Input Attributes (see Section 2.2.2.1.) could be either Constants or Design Variables. The particular selection depends on the statements of the Problem Definition. The associated Attribute Type indicators (see below) are entered in the second column of the DCM+. In the previously used example (Fig. 2.5), Attributes A2.1 and A6.1 can be clearly identified as Input Attributes; in the situation depicted, A2.1 is a Constant (type 0) and A6.1 is a Design Variable (type 1). Attribute A3.2 is only transferred between Contributing Analyses in Sequence 2 (hatched column partition), and qualifies as a State (type 2). Similarly, A1.1 is input to and output from CAc only, and is therefore also classified as a State. All other Attributes are Behavior Variables in terms of input/output connectivity (type 3). Note that from these, A4.1 and A5.1 are Constraints (type 4) and A4.2 is an Objective (type 5).

---

* in accordance with /Sobieski 88b/

** in similarity to /Balling and Sobieski 94/

Since the DCM$^+$ contains complete information about the information flow between Contributing Analyses, it can be used for tasks beyond determination of input and output data. The possibility for finding Circuits was described in Section 2.2.2.2. Another option is the identification of superfluous Contributing Analysis executions during the SENSITIVITY task. Consider Fig. 2.5: Attribute "A5.1" is an independent variable of Sequence 2, but it is not an input to CAb. If A5.1 is perturbed in a local finite differencing loop, the output of CAb will not change, so that this Contributing Analysis need not be executed. The associated parsing operation uses both Circuit and Sequence grouping. Recall that Circuits are executed sequentially, which is also true within a Sequence. Beginning with the first Circuit in a Sequence, it is checked whether a particular independent variable is a Circuit input. If this is the case, then this and all other "downstream" Circuits must be executed; otherwise, the particular Circuit execution can be omitted. In Fig. 2.5, Circuit 1 (CAb) is the first Circuit in Sequence 2, and A5.1 is not an input to this Circuit. Circuit 2 (CAc), however, requires A5.1 as input, and must be executed.

This procedure is similar to the identification of "computational paths" in quasi-procedural programming (/Kroo and Takai 88/). Computational path generation is based on subroutine (or CA) input and output requirements, whereas the present approach combines an Attribute flow representation (the DCM$^+$) with rules stemming from CA grouping. The method described here is therefore information flow based, as supposed to operator-based quasi-procedural programming.

In summary: The intellectual tasks in this integration method are, first, problem decomposition, selection of Resources and determination of a common set of Attributes communicated between the Contributing Analyses (the optimization engine is also a

Contributing Analysis in this context). Second, Contributing Analyses are grouped according to the particular requirements of the environment in which the design process is to be performed. Based on these decisions, the information flow structure, Attribute Types, and execution order are coded in the DCM$^+$ - a task which can be partially automated. The DCM$^+$, however, can be parsed through standard data base operations, and so the information contained in it recovered without human interaction. This information, combined with the presented syntax of the Problem Execution Code, allows automated execution of a design problem. Hence, a separation of human decisions and their "mechanical" implementation has been performed.

2.3 Discussion - New Elements

The presented approach represents a combination and extension of existing techniques, supplemented by a new representation of subsystem coupling from an information flow point of view (the DCM$^+$), which provides a template for very large system structured decomposition from an initial task statement to the single data level, and subsequent recomposition and execution. Literature on this issue is scarce. In most presented problems, the task is to prove the validity of a new technique, not to execute a previously stated problem. Hence, the system parts were known, and the information flow structure was intuitive, for example the five-bar truss (/Renaud et al. 94/), ten-bar truss (/Haftka and Zürdal 92/, /Bloebaum et al. 90/) sample cases in structural optimization. An exception to some extend is the approach taken during the HiSAIR / Pathfinder program. /Jones et al. 92/ reported that survey forms were sent out to contributing disciplines by a Data Management Team in the beginning of the project. The information requested pertained to analysis programs in use in each discipline, and the required input and output

data. The task of the Data Management Team task was to analyze the forms, establish the information structure, and devise an execution scheme. Two more cycles of this process were necessary until information flow compatibility was established. The execution order was then determined using DeMAID. Decomposition and recomposition were separated as in the present approach. In contrast to the method suggested in Section 2.2 however, the disciplines were less involved in the decomposition process: The Design Simulation Model had already been decomposed by the integration experts beforehand, and the only task of the disciplinary representatives was to state their input and output data. It is conceivable that revisions could have been avoided, had the decomposition procedure followed a gradual progression from an abstract to the physical level and involved disciplinary input at each level for harmonization.

The most important difference between the method presented and previous approaches lies in the recomposition technique. A distinction is made between design problem-independent functional operators and problem-specific information. Generic operators like Circuit solvers can be supplied in form of a tool box, and form - together with the Contributing Analyses - the functional building blocks of the design problem solver. These operators process groups of Contributing Analyses and execute CAs in a certain order. The link between operators and CAs in this hierarchy are therefore CA groups. Given that Attribute input/output compatibility is ensured, the CAs are supplied with the required input data, and process exception is defined. The latter two blocks of connectivity information are problem-dependent and stored in the DCM^{+}. Hence, this generic framework can be programmed through the information contained in this matrix. It is therefore possible to include changes in the problem structure - from inclusion of new information flow channels or neglect of connections - during the design process. The latter case is particularly interesting since solution of the GSE is an inherent part of the present

approach, so that information for restructuring of the ANALYSIS based on coupling strength (/Bloebaum 92/) is readily available and could be applied at each iteration. Addition of Contributing Analyses is similarly possible by adding a column, possibly Attribute rows, and updating Circuit and sequence numbers in the DCM+ (given that the associated Resources have been combined in a Tool as defined in Section 2.2.1.2.). This feature could be referred to as a "soft model" as supposed to the "hard models" of HiSAIR/Pathfinder (/Dovi et al. 91/, /Jones 92/) and FIDO (/Townsend et al. 93/).

The previous section showed furthermore that the Attribute flow based information in the DCM+ may also be used for reduction of computational effort. The idea of identification of only those Contributing Analyses which are necessary to generate a particular Attribute input / output pair, for example from an independent to a dependent variable in a sensitivity calculation was pioneered in quasi-procedural programming by /Kroo and Takai 88/. The current approach follows a very different strategy based on design process scheduling considerations by /Steward 81/ and /Rogers 89/, but generates comparable results.

CHAPTER III

IMPLEMENTATION:

DEVELOPMENT OF A TILTROTOR DESIGN SIMULATION MODEL AND A GENERIC INTEGRATION FRAMEWORK

3.1. Level I Decomposition:

Problem Definition and Disciplinary Structuring

The "Problem Definition" as defined in Section 2.2. for the tiltrotor case was based on the conclusions drawn from Chapter 1. The process described in Chapter 1 is part of Step 1 of the methodology described in Chapter 2, since the conclusions drawn from the literature review feed into the Problem Definition. It is, in fact, only a subset of the Problem Definition derived for this research in Section 1.3. - since development of the integration methodology is not part of the tiltrotor case per se. Hence, Fig. 3.1 is only a compressed version of Section 1.3, using the structure proposed in Section 2.2.

Fig 3.2 shows a sketch of the design mission profile, adapted from /Boeing CTR 87/. This mission was chosen for its economic significance (/Boeing CTR 87/) and utilization in previous research (/Schleicher 93/). The Productivity Index, PI, provides a simple representation for the ratio of aircraft productivity to acquisition and operating cost (represented by empty weight and fuel weight, respectively). PI has been previously used by /Conway 91/ in CTR performance studies.

The following Disciplines were identified from Fig. 3.1: Performance from the Basis, Search, and Constraint Statements (item 2); sizing from the search and Constraint Statements (items 1 and 2); airframe dynamic structural analysis from all but the Basis Statement; airframe static structural analysis from the Constraint Statement; airframe aerodynamics from the Constraint, Focus, and Analysis Statements; rotor aeroelasticity from the Search and Constraint statements; and control system design from the Analysis Statement. Additionally, dynamic system coupling, not really a separate Discipline, was emphasized in the Constraint Statement. The Discipline "optimization" is directly induced by the Search Statement. These Disciplines were then checked for combination into composite Processes, and analyzed for required Intuitive Data Set inputs and outputs. Three-letter strings refer to set names listed in Table 3.1. Items specified by "rotor" apply to the rotor, "airframe" to the airframe only, and "aircraft" refers to the complete configuration including both subsystems.

Fig. 3.3 shows the associated Processes, as developed in the next paragraph. Performance and sizing is denoted by "PaS," structures by "Str," unsteady aerodynamics by "Uae," dynamic plant model by "Acp," control system by "Csd," the analysis-optimizer conversion by "Obj," and optimization by "Opt."

Given: (Basis Statement)

40 passenger / 600 nm civil tiltrotor mission

Find: (Search Statement)

local optima of a civil tiltrotor aircraft configuration with respect to the Productivity Index, PI,

$$PI = \frac{\text{Payload Weight} \times \text{Block Speed}}{\text{Operating Empty Weight} + \text{Mission Fuel Weight}}$$

in the design space spanned by geometric layout (wing, fuselage, rotor), wing internal structure, rotor geometry and dynamics, and design cruise speed.

Satisfy: (Constraint Statement)

the constraints:

- geometric compatibility of aircraft components
- fuel weight ratio
- wing structural integrity in the 2g-jump take-off condition
- sufficient velocity margin from aeroelastic stability boundary of the coupled rotor / airframe dynamic system in cruise, free flight aircraft configuration (free-free, symmetric)
- static stability in aircraft and helicopter mode

Emphasize: (Focus Statement)

modeling of airframe contribution to system aeroelasticity

Evaluate: (Analysis Statement)

the change in location and objective function value as a function of:

- rotor system (conventional vs. variable diameter design)
- airframe aeroelastic modeling fidelity
- aeroelastic stability augmentation (passive vs. active)

Fig. 3.1: Problem Definition - Tiltrotor Case

Performance and sizing are usually treated as one Process, since sizing is the iteration loop around subsequent weight / size estimate and mission performance Processes; hence the two Disciplines were combined into one Process. Required is a set of data describing the general layout of the aircraft (geo), rotor layout specific data (rgo), a description of the mission to be flown (mis), and possibly externally computed or given component weights (wgt). Output consists of the remaining geometric, dimensional information, as determined by the sizing process (siz), component weights for the sized aircraft (wgt), estimated aerodynamic coefficients (sae), the aircraft's mission performance (mis), and data which may be used for subsequent economic analyses, or economic data directly supplied by the discipline (eco), if applicable.

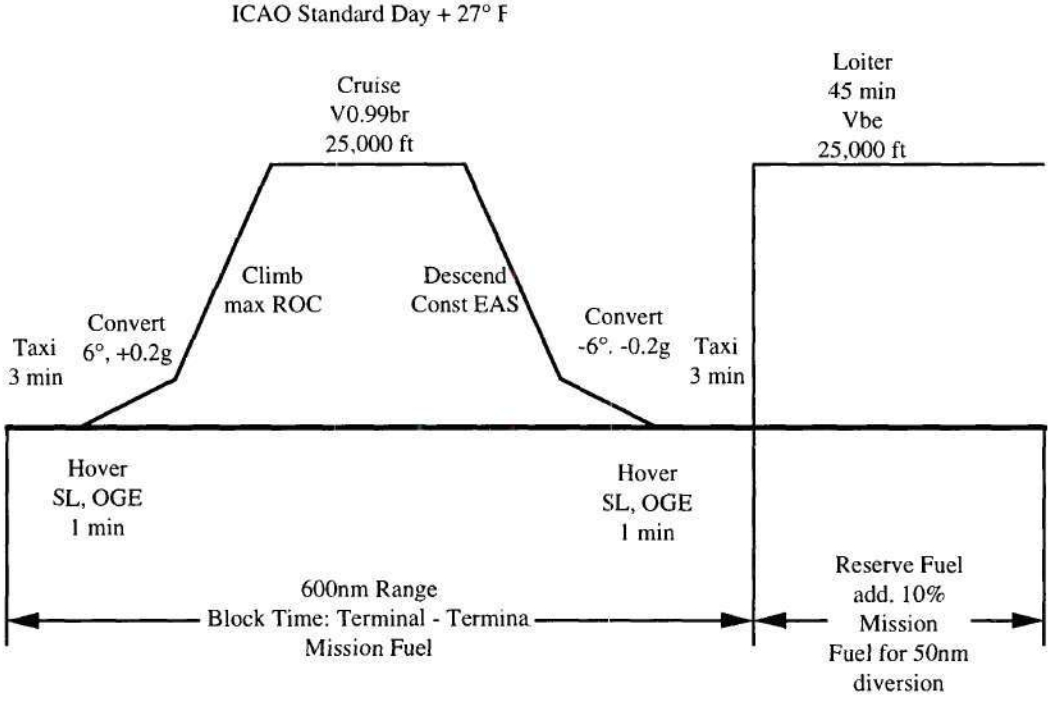

Fig. 3.2: Design Mission Profile

Static and dynamic structural analysis are also commonly performed in conjunction. In order to execute this Process for a particular component or group of components, its dimensions (geo, siz), inner layout (str), material strength, stiffness, and density (str), and weights of attached components must be known. The results include the structural weight of the component (wgt), margins of safety for the specified static load cases (str), and eigenvalues , generalized masses, and mode shapes from the dynamic analysis (dyn).

Based on the Focus Statement, low priority was assigned to steady aerodynamics, which was therefore not expanded past the scope by which it had already been included in performance and sizing. Unsteady airframe aerodynamics, however, were strongly emphasized, and therefore represented by a separate Process. This Process was defined as conversion of the in-vacuum dynamic system of a structure into an aeroelastic system. In other words, for a given body (geo, siz) with certain dynamic properties (dyn) at a specified steady-state flow condition (mis, sae), unsteady aerodynamic forces as a result of the body's motion are added to its dynamic characteristics to form its aeroelastic properties (aeo).

Similar considerations, based on the literature review of previous approaches to tiltrotor aeroelasticity presented in Section 1.2, resulted in combination of rotor aeroelasticity and dynamic system coupling into one Process. Rotor aeroelasticity was assumed to be defined by its geometry and dynamics (geo, rgo, siz, rdy) and rotor steady-state flow conditions (sae, mis). Airframe aeroelastic properties (aeo), are coupled with this system, where the masses of the components play an important role (wgt). The output was to include a comprehensive description of the coupled system dynamics, for example by its representation in matrix form (acp).

Control system design requires information about the plant to be controlled (acp). Additionally, the second item in the Constraint Statement requires that the controller's activity and its impact on the dynamic system be checked to comply with physical limitations (csd) in a particular condition (mis). The result of this check (csd) must indicate that no limits are violated.

The necessity for existence of a sixth operator was deducted from the multitude of Processes contributing to both objective (PI) and constraint generation. An interface Process was defined in order to translate disciplinary constraint information (csd, geo, siz, sae, str) into a form suitable for optimization, and compose the objective function from disciplinary information (eco, wgt). No specific name was assigned to the output data set; constraints remained associated with the respective input set. The optimization Process then generates an updated set of decision variables (geo, mis, str, rdy, rgo, csd) from this information.

In this step, Processes have been derived from the Problem Definition, and in consideration of available disciplinary Resources. Input and output relations in terms of Intuitive Data Sets have been obtained from a preliminary analysis of the data conversion process associated with each Process. In terms of the method presented in Chapter II, the Design Simulation Model has been Level I-decomposed.

Table 3.1: Intuitive Data Set Names

Data Set Name	Data included	Component
apd	dynamic plant model	aircraft
aeo	aeroelastic	airframe
csd	control system limit / performance	aircraft
dyn	dynamic (vacuum)	airframe
eco	economics	aircraft
geo	configurational	aircraft
mis	mission profile related	aircraft
rdy	dynamic	rotor
rgo	configurational	rotor (spec.)
sae	steady aerodynamic	aircraft
siz	dimensional (size)	aircraft
str	structural (dimensions, loads, ...)	airframe
wgt	inertias and weights	aircraft

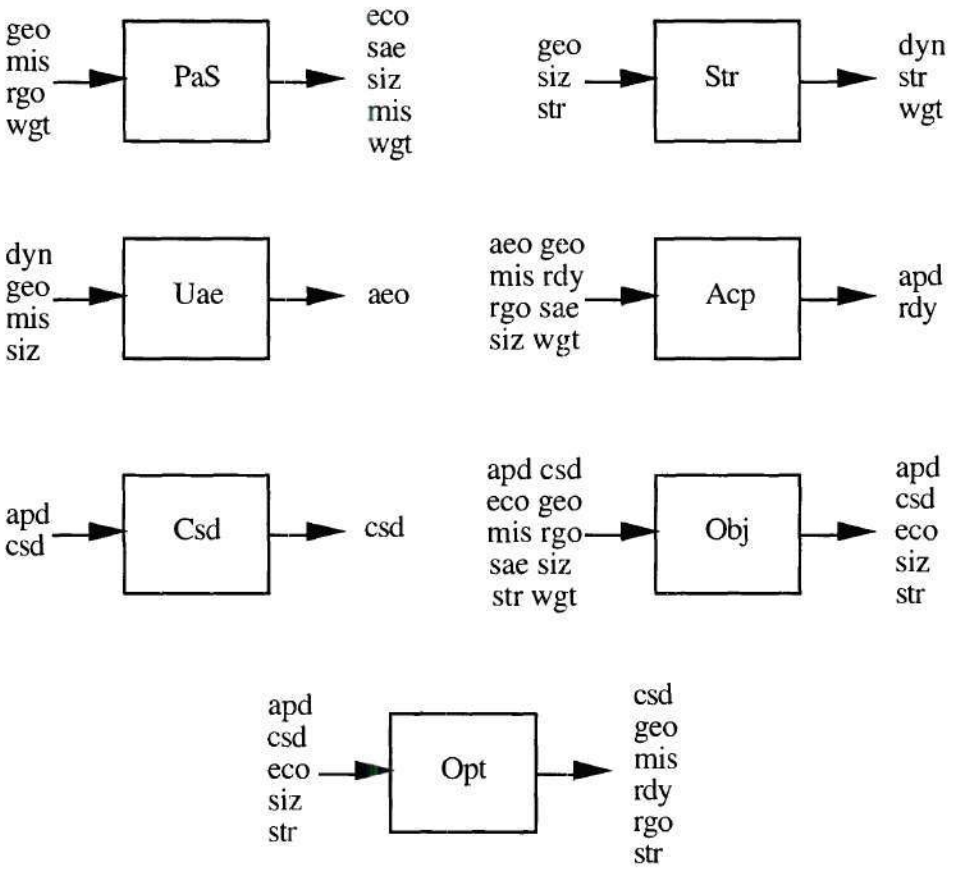

Fig. 3.3: Process Intuitive Data Set Input and Output

3.2. Level II Decomposition: Disciplinary Methodology Selection and / or Tool Development

After the preliminary definition in the Level I Decomposition, the Processes are analyzed in detail in this section, Resources selected, and Tools formed. Based on the knowledge of input data requirements associated with the particular Resource(s), the Intuitive Data Sets are decomposed into Objects.

The importance of this step shall be re-emphasized at this point. Processes, the result or the Level I Decomposition, are largely independent of Resources and problem focus. Tool input, operation, and output, on the other hand, are determined by the Resource(s) included, which are chosen based on availability, fidelity, and accuracy as indicated in the problem definition. Conversion of Processes into Tools therefore requires detailed understanding of the Disciplines involved, in order to arrive at a feasible and satisfactory Design Simulation Model. Hence, reviews of methods and Resources associated with Disciplines feeding into each Process, and choice of method and implementation are described in the next seven subsections. Strings in quotes in the subsection titles indicate the name assigned to the associated Tool. Each part concludes with a more detailed list of Objects either required as input or generated, grouped by the Intuitive Data Sets defined in Table 3.1.

3.2.1. Performance and Sizing ("vascomp")

The V/STOL Aircraft Sizing and Performance Program, VASCOMP (/Schoen et al. 80/), is a multidisciplinary design synthesis code including geometry generation, aerodynamics, propulsion, and component weight models as well as a mission performance analysis. It proved to be a very useful Resource in previous performance-related studies (/Schleicher 93/), and was used as the core program for general vehicle layout. The program covers all detail analyses not expressly included in this approach by offering either low-fidelity or approximate methods or offering input of externally generated data, in particular the propulsion system with engine fuel flow and propeller efficiency tables. Section 3.2.1.1 presents an outline of the code's operation. The combination of comprehensiveness and moderate program size, results either in simple disciplinary representations, the necessity to prepare VASCOMP input data off-line using specialized disciplinary Resources, or in restricting simplifications. Examples for these three cases, encountered when reviewing the program's disciplinary Models, are described in Section 3.2.1.2. A more detailed treatment of these issues can be found in Appendix A.

3.2.1.1. Overview of VASCOMP

The sizing cycle commences with a set of parameters describing the vehicle's geometric configuration, a complete description of the mission to be flown, and an initial gross weight guess The configurational description is not complete; the remaining parameters are derived from the existing ones using the aircraft's gross weight. Based on this complete geometric description, component weights are estimated from statistically determined equations. Engine sizing is an iterative process, since nacelle drag is updated based on the engine size. The available fuel weight is calculated as the difference of the gross weight guess and the sum of component weights and payload weight. The required

fuel weight is then determined from a mission analysis. Based on the difference of available and required fuel weight, the gross weight is adjusted, and the sizing cycle continues until the two fuel weight representations converge. This process is known as fuel weight ratio iteration, or R_f Method.

The mission analysis utilizes disciplinary routines for airframe aerodynamics and propulsion (engine fuel flow and power available, propeller / rotor efficiency, and transmission). Parasite drag is based on component drag buildup, using Reynolds number corrected skin friction, profile drag, and lifting surface compressibility drag rise. Interference between lifting surfaces and fuselage or nacelle is included, as well as induced drag derived from lift coefficient, wing aspect ratio, and Oswald efficiency factor. The turboshaft engine cycle is modeled by tables representing referred power, referred fuel flow, referred gas generator speed, and referred power turbine speed as a function of Mach number and turbine inlet temperature. Table look-up options are also offered for rotor hover Figure of Merit (as a function of tip Mach number and thrust coefficient to solidity ratio) and propeller power coefficient (as a function of thrust coefficient and advance ratio).

3.2.1.2. Disciplinary Model Modifications, Additions, and Data Preparation

Fidelity of the dynamic model was a pivotal part of this research, as outlined in Chapter 1. VASCOMP's disciplinary models were therefore reviewed with special emphasis on the impact on this aspect. The most important feature in this context is rotor and airframe dynamic tuning. VASCOMP's wing weight estimation, adapted from /Schmidt and Dyess 90/, is based on a simple structural layout of the load carrying wing structure, with added weights for fittings and flaps: Given the span, chord of the structural part of the wing, and wing thickness, wall thicknesses and spar cap areas are calculated in order to match or exceed given beamwise bending, chordwise bending, and torsional

frequencies (including rotor and nacelle mass representations). If necessary, weight is then added in order to achieve acceptable stress levels at the wing root in a 2g jump take-off condition. The main point of concern is the lack of connectivity between wing and rotor tuning, the latter not being included at all; wing frequency placement is based on results reported by /Johnson et al. 86/, and does not include structural tailoring options. As a result, an override of the internal wing weight calculations was installed. In the modified program, wing structural weight is an input, flap weight is based on a method described by Torenbeek /Torenbeek 82/, and fitting weight is calculated as before.

Tailplane sizing was another area of closer investigation. Since free-free aircraft boundary conditions were chosen for the dynamic analysis, proper center of gravity placement was mandatory. Unless horizontal stabilizer area and moment arm are specified, VASCOMP uses an undocumented formula for the required tail volume coefficient, assumes a fixed moment arm of 48% of the fuselage length, and sizes the stabilizer accordingly. In Appendix A.1 it is shown that this formula was probably derived in order to guarantee center of gravity (cg) travel of 50% of the mean aerodynamic chord (mac) without violating control capacity (front) and static stability (aft) limits for a configuration similar to a 40 PAX tiltrotor. Hence, the formula was not changed. However, an override for the moment arm fuselage percentage was installed in order to allow a trade-off between tail plane size, fuselage length, and the relative locations of wing and tail. In order to ensure 50% mac cg travel, a post processing capability was added. This utility calculates parameters necessary for determining violations of front and aft cg limits in aircraft configuration, as well as front cg location in helicopter configuration (static stability at 45 kts forward flight). The derivation of an approximate expression for the rotor contribution to pitching moment is outlined in Appendix A.2.

Under certain circumstances, transmission and engine may be sized for the conversion condition. If this is the case, then the power profile during conversion can have a significant effect on aircraft weight. /Schleicher 93/ discussed the sensitivity of power required to climb angle during conversion. His results show that for high climb gradients, maximum power requirements occur at the end of outbound conversion (conversion angle reduced from 90° - helicopter configuration - to 0° - aircraft configuration), which is equivalent to the conversion sizing condition in VASCOMP. For low rates of climb however, the power peak is found at conversion angles larger then zero. It is instructive to study this effect for a VDTR design, where the rotor diameter change from a large to a small value during outbound conversion. In VASCOMP II (Version 1.09, August 1993), the rotor maintains its hover diameter throughout conversion. The program was modified to include diameter scheduling with the conversion angle in order to investigate the influence of the schedule on power requirements in conversion. In an attempt to match the curves suggested in /Studebaker and Matuska 93/ with simple means, it was assumed that the rotor diameter is the hover value above 60° conversion angle, and is then linearly reduced to the cruise value at 0°. Fig. 3.4 shows that the influence on power required is fairly small. Fig. 3.5. though indicates clearly that it occurs at the peak of the power curve and increases with rising speed. This means that for larger climb gradients the effect will be more dominant. In the light of possible future requirements for steep climb gradients, proper consideration of diameter scheduling on engine sizing in VASCOMP is strongly suggested.

The component weights determined by the program were used to calculate fuselage, nacelle, wing, and rotor/tilt mechanism inertial properties for the dynamic analysis. Point masses were lumped into groups and/or distributed along the fuselage axis or the engine nacelle volume. Corrections were used to match V-22 nacelle inertias reported by

/Sprangers and Stevenson 86/. A description of this addition to VASCOMP can be found in Appendix A.3.

A critical issue with respect to vehicle performance are the engine cycle and propeller / rotor performance tables required by VASCOMP. The tables for a General Electric GLC38-T1M1 turboshaft engine and hover performance maps for a V-22 type rotor (from wind tunnel test results) used by Schleicher /Schleicher 93/ were adopted without change. Results from wind tunnel model test results reported by Studebaker and Matuska /Studebaker and Matuska 93/ were used to generate VDTR tables. For a given cruise solidity, the hover value was adjusted to match data of the configuration tested /Matuska 93/, and an estimate for other extension ratios (cruise diameter divided by hover diameter) was provided. The preparation of VDTR test data is presented in Appendix A.4. The fixed diameter rotor previously used exhibits significantly better hover performance. Test runs with VASCOMP indicated that also propulsive efficiencies were roughly 10% higher than those of the variable diameter design. It is fair to assume that this effect had a significant influence on the vehicle size.

Table 3.2. presents a more detailed list of Objects contained in the data sets required and generated by the Tool "vascomp." Note that in the actual Tool implementation, cruise speed was linearly linked to equivalent airspeed in descent and all component design speeds.

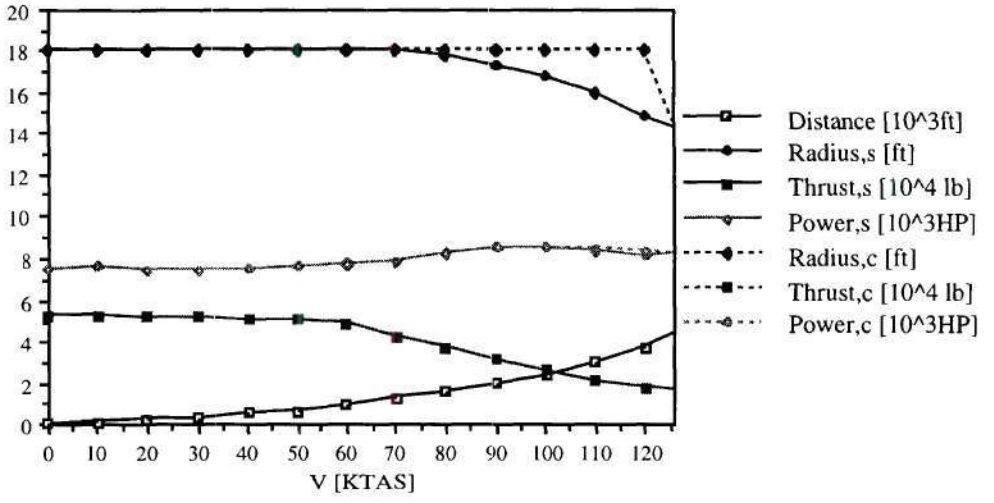

Fig. 3.4: Effect of Diameter Scheduling during Outbound Conversion

(c - constant diameter; s - linear diameter scheduling)

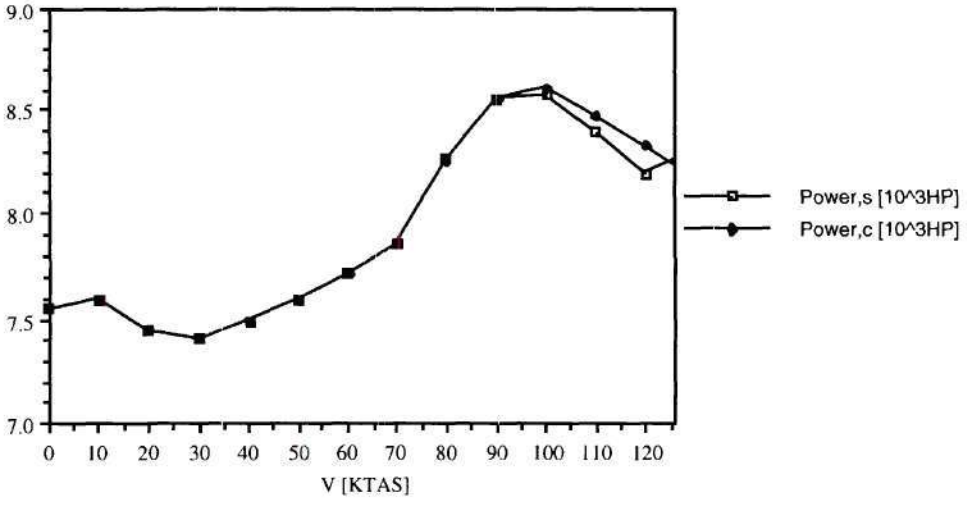

Fig. 3.5: VDTR Power Requirement during Outbound Conversion

(c - constant diameter; s - linear diameter scheduling)

Table 3.2: Tool Input / Output Relations - "vascomp"

Tool:		vascomp	
Given / Assumptions:		mission profile, engine maps, rotor performance tables	
Input		Output	
geo	wing, rotor, fuselage layout ; component locations	eco	economics (block speed)
		sae	stability derivatives, cg limits
mis	mission (cruise speed)	siz	wing, rotor, fuselage dimensions; clearances
rgo	tip speed, extension ratio, cruise solidity	mis	mission (limit speed)
wgt	component weights (wing structural)	wgt	component masses and inertias, empty weight, fuel weight

3.2.2. Airframe Structure ("elaps")

Finite Element (FEM) Analyses are generally credited with the highest accuracy and flexibility for modeling structures, checking their integrity in static load cases, and obtaining information about dynamic characteristics. This flexibility, however, results in a large number of modeling options, which might be confusing in the early stages of the aircraft design process, when little information about the structure is available. Recently, efforts have been under way to facilitate generation of FEM input files by providing interactive interfaces. Simplifying assumptions regarding geometry are made in order to obtain a full model description based on a small number of input data /Stevens et al. 94/. A different approach is to use a simpler yet acceptably accurate methodology, so that less

information is required to begin with. One example of these methods is described in the next subsection.

3.2.2.1. Equivalent Plate Analyses

In recent research on fighter design and the High Speed Civil Transport, HSCT, equivalent plate analyses have become a popular Resource for modeling low aspect ratio wing structures in aeroelastic analyses (/Barthelemy et al. 91/, /Jones at al. 92/, /Townsend et al 93/, /Livne et al. 92/). If transverse shear effects are not dominant, these methods perform well in comparison to FEM while reducing computational effort /Giles 89/. In rigorous numerical comparisons including shear flexibility, however, these approaches failed to perform satisfactorily /Livne et al. 93/. One successful approach to improve equivalent plate models was to relax the Kirchhoff kinematic assumptions inherent to Classical Plate Theory, CPT, and introduce First-order Shear Deformation Plate Theory, FSDPT /Livne 93/. At the time of Resource selection for this research, this new program was not yet available, and the CPT-based Equivalent Laminated Plate Solution, ELAPS /Giles 89/ was obtained. Proper modeling of torsional degrees of freedom, however, is mandatory for tiltrotor wing design under whirl flutter constraints. As a result, a minimum-change approach to upgrading this program for inclusion of transverse shear flexibility was performed.

In the Ritz solution technique used in ELAPS, the chordwise, spanwise, and vertical deflections of the structure, modeled by a number of trapezoidal elements, are expanded using a set of comparison functions, $a_j(x,y)$, which are power series terms of the form $x^k y^l$ in the chordwise and spanwise coordinate, x and y, respectively:

$$u_0(x,y,t) = \{a_u(x,y)\}^T \{q_u(t)\}, \tag{3.1a}$$

$$v_0(x,y,t) = \{a_v(x,y)\}^T \{q_v(t)\}, \tag{3.1b}$$

$$w_0(x,y,t) = \{a_w(x,y)\}^T \{q_w(t)\}. \tag{3.1c}$$

The $q_i(t)$ are sets of time-dependent, generalized coordinates. The functions in (3.1) describe the deflection in the x,y-plane. The Kirchhoff assumption in CPT states that material lines normal to the reference plane as described in (3.1) remain straight and normal to it in the deflected structure, so that the deflections off the reference plane are

$$u(x,y,z,t) = u_0(x,y,t) - z\frac{d\,w_0(x,y,t)}{d\,x} \tag{3.2a}$$

$$v(x,y,z,t) = v_0(x,y,t) - z\frac{d\,w_0(x,y,t)}{d\,y} \tag{3.2b}$$

$$w(x,y,z,t) = w_0(x,y,t) \tag{3.2c}$$

The total energy of the deflected structure is

$$E = U - T + V \tag{3.3}$$

The strain energy, U, is a quadratic function in the combined vector of generalized coordinates, q(t), and a stiffness term; the kinetic energy, T, is a quadratic function in its first time derivative and a mass term; and the potential of applied loads, V, is a linear function in q(t) and the vector of external forces, Q. If simple harmonic motion is assumed, then Rayleigh's Principle is equivalent to the condition that the total energy is stationary with respect to the generalized coordinates, or

$$\frac{d\,E}{d\,q} = -\omega^2 M q - Q + K q = 0 \tag{3.4}$$

The stiffness (K) and mass matrix (M) are produced by differentiating the potential and kinetic energy twice with respect to q. For the homogeneous part of the problem, (3.4) reduces to an eigenvalue problem in ω, the solution of which provide upper bounds on the real system's natural frequencies. Equations (3.2) provide kinematic constraints which drive these bounds to higher values; this is equivalent to the observation that structural models using CPT are too "stiff" in modes to which these constraints apply, for example those with large shear, or torsional contributions /Livne 93/. Hence, in FSDPT this constraint is relaxed by introducing a new set of degrees of freedom,

$$\Psi_x(x,y,t) = \left\{a_{\Psi_x}(x,y)\right\}^T \left\{q_{\Psi_x}(t)\right\} \tag{3.5a}$$

$$\Psi_y(x,y,t) = \left\{a_{\Psi_y}(x,y)\right\}^T \left\{q_{\Psi_y}(t)\right\} \tag{3.5b}$$

and using

$$u(x,y,z,t) = u_0(x,y,t) + z\,\Psi_x(x,y,t) \tag{3.6a}$$

$$v(x,y,z,t) = v_0(x,y,t) + z\,\Psi_y(x,y,t) \tag{3.6b}$$

instead of equations (3.2a) and (3.2b).

The new coordinates provide flexibility to the plate-beam model, allowing the upper skin to be translated in u and v with respect to the lower plate in ways other than those prescribed by (3.2). This observation spawned another approach: Instead of adding the "shear" degrees of freedom of equation (3.5), upper and lower plate deflections were described by initially independent sets of comparison functions in the form of equations (3.1). Hence, upper and lower skin have their own set of generalized coordinates. This step doubles the number of degrees of freedoms and is therefore inferior to FSDPT with regard to efficiency. On the other hand, ELAPS provides for multiple "displacement

systems" which may be connected by springs, so that no changes to the program architecture were necessary. If one is satisfied with limiting relative vertical motions of the skins by means of massless springs, then only the in-plane relative motion of the skins needs to be constrained. This can be achieved by adding strain energy and kinetic energy of shear panels attached to both skins to the total energy expressions. ELAPS performs approximate line integrations on the planform by assuming the properties to be constant in an interval and adding the results from these local kinetic or strain energy integrations. Similarly, the shear panels were divided into intervals, and each interval was represented by two triangular panel elements, Fig. 3.6. A constant shear stress distribution and constant thickness in this sub-element was assumed, so that the average shear stress was simply a linear function of the corner displacements. These displacements, in return, were described by the comparison function sets, equation (3.2). The shear strain energy was therefore calculated without integration in the panel. A similar approach was followed for the kinetic energy. Refer to Appendix B.1 for details.

Comments on choice of comparison functions and geometric representation are necessary at this point. In order to permit shear of a structure clamped at $y = 0$, the extended ELAPS (denoted ELAPS*) comparison functions must include x^0y^1. This term allows a spanwise slope of the skins at the root, as in shear deformation. In the original model, this would create a rigid body degree of freedom in roll. Furthermore, each skin requires its only geometric definition as a plate with center line and box depth (Fig. 3.7). The z-locations obtained from combining these two data sets define the "box center lines" of the new upper and lower "boxes." The "box skin thickness" reduces to half the value of the wing representation. The "box depth" may be set to zero if the skins are approximated as membranes. However, unless upper and lower skins are parallel to the x,y-plane, there will always be a residual bending influence from the w-slope term in equations (3.2). In

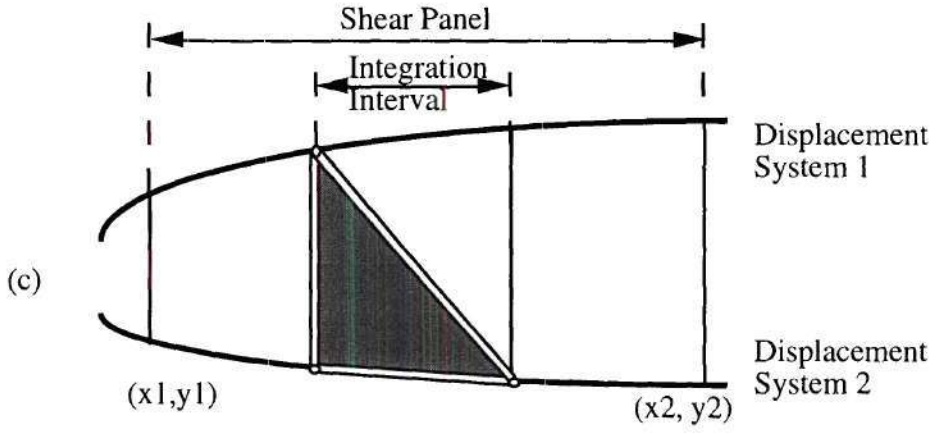

Fig. 3.6: Shear Panel Element in ELAPS

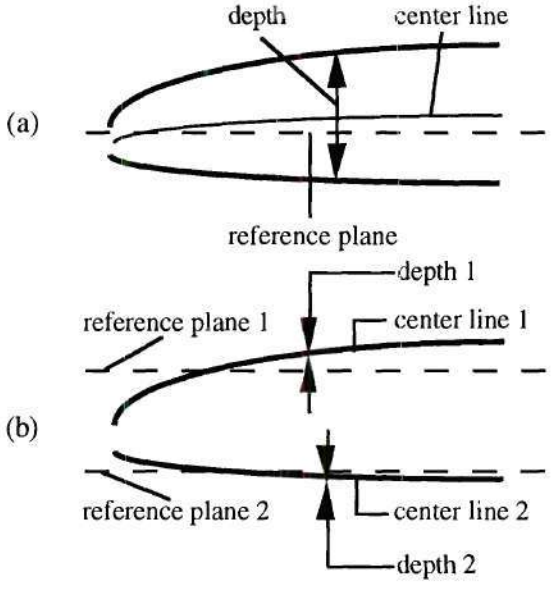

Fig. 3.7: Changes in ELAPS Wing Box Geometry Definition
(a): Original; (b): with Shear Panels

order to reduce this effect, an individual reference plane was defined for each skin. The vertical offset of this plane from z = 0 is calculated as the average of the "box center line"

Results from modal analyses of a large, high aspect ratio, swept wing with strong coupling of torsional and bending modes using an ASTROS finite element model /Venkayya et al. 94/, the original ELAPS, and ELAPS* are compared in Appendix B.2. The correlation of the torsional modes was improved, while paying a small penalty in the bending modes. Possible explanations for this effect are discussed in Appendix B.2. Considering the overall benefits, the enhanced version was used in the tiltrotor simulation model.

3.2.2.2. The Tiltrotor Airframe Structural Model in ELAPS

The choice of power series as a generating set, combined with utilities which manipulate these functions symbolically, is the primary reason for the computational efficiency of ELAPS. As a result, all geometric information may also be input in form of coefficients. In fact, discrete data points are internally converted into power series by curve-fitting. This is a useful feature in early design stages, since coefficient input keeps the number of input data low and allows the designer to make qualitative statements about the structure.

Such a qualitative approach was taken by assuming that the 2g jump take-off condition is an important design driver, and considering the expected near-linear bending moment distribution for this load case. As a result, a linear distribution in spanwise direction was chosen for most structural properties. Linearly tapering wing box structural chord (linear taper as applied to the aerodynamic planform), wing box thickness (through constant thickness-to-chord ratio of the airfoil along the span), ply thicknesses, and spar

cap areas resulted in significant weight savings compared to constant crossection designs in preliminary studies by Friehmelt /Friehmelt et al. 94/. The model used in this research featured also linearly tapered shear webs between the caps of the two spars at 5% and 55% of the aerodynamic chord, respectively. Leading and trailing edge spar cap areas and web thicknesses were sized independently. Eleven streamwise oriented ribs of the same, constant thickness were located equally spaced on the semi-span. These elements were assumed to consist of plies with +/-45° fiber orientation, and to resist only to shear loading. Thicknesses of orthotropic carbon/epoxy laminate plies with 0°, 90°, +45°, and -45° fiber orientation were constant chordwise, and identical for upper and lower skin (ply orientation is measured with respect to the spanwise coordinate, y). Minimum gauge thickness side constraints of 0.0025 ft (roughly 4 plies of 190 grade tape) and minimum crossectional area side constraints of 0.01 ft^2 were imposed on plies and spar cap areas, respectively. Fifth-order curve fits in the normalized chordwise coordinate across the structural box were obtained for camber and depth using the V-22 wing box cross section depicted in /Sprangers and Stevenson 86/. Wing box depth was scaled with the thickness-to-chord ratio, while camber remained constant. The structural planform was described by one trapezoidal segment, which was assumed to reach from the aircraft's center line to the wing tip. The set of comparison function was for both displacements in the form

$$\left\{a_u(x,y)\right\}^T = \left\{x^i y^j\right\}^T; \quad i = 0,1; j = 0\ldots4; \tag{3.7a}$$

$$\left\{a_v(x,y)\right\}^T = \left\{x^k y^l\right\}^T; \quad k = 0,1,2; l = 1\ldots5; \tag{3.7b}$$

$$\left\{a_w(x,y)\right\}^T = \left\{x^m y^n\right\}^T; \quad m = 0,1; n = 0\ldots4; \tag{3.7c}$$

so that only spanwise displacement is locked at the root, which corresponds to free-free symmetric boundary conditions for the 2-displacement system model.

As outlined in Section 3.1, two tasks were to be performed by the structural model: First, a check on exceeding structural limits in a jump take-off condition; and second, a free-free modal analysis of the complete airframe with rigid representations of the fuselage/ tail group, engine nacelle, and rotor. Both of these operations require special modeling considerations due to certain limitations of the code.

ELAPS does not provide for inclusion of gravity loads, so inertial forces in the static load case (helicopter configuration) had to be simulated. Masses attached to the flexible structure at a certain location were replaced by a force equal their weight (fuselage and engine nacelle). The rotor force was attached at the tilt axis location, with a value of half the gross weight, less the rotor and tilt mechanism weight. The wing group weight (structural, non-structural, and total fuel, limited by the wing box volume) was assumed to be evenly distributed over the structural wing planform, and included as a pressure load. The weights were then scaled by the jump take-off load factor (2.0). Refer to Appendix A.3 for a description of the structural groups used. The integrity of each ply with respect to maximum stress, maximum strain, Tsai-Hill, Hoffman, and Tsai-Wu Criteria /Tsai and Massard 87/, separately for upper and lower skin, was checked at the leading and trailing edge in 10% semi-span steps with a procedure added to ELAPS by Friehmelt /Friehmelt et al. 94/. Material data, summarized in Table 3.3, were taken from /Tsai and Massard 87/. Buckling failure modes were not considered.

The total number of structural integrity data (failure indices) per half wing generated is 1188; this large amount of information was replaced by a single cumulative measure, the Kreisselmeir-Steinhauser (KS) envelope function /Kreisselmeir and Steinhauser 80/. The KS function of a set of N constraints, $\{g\}$, is defined as

$$KS(\{g\}) = g_{max} + \frac{1}{\rho} \ln\left[\sum_{i=1}^{N} e^{\rho(g_i - g_{max})}\right] \tag{3.8}$$

where ρ is a user-defined constant which determines the smoothness of this envelope when one element of $\{g\}$ is replaced by another one as the most violated constraint, g_{max}. KS approaches g_{max} for very large values of ρ, and represents an increasingly smooth, and increasingly conservative upper bound to the set $\{g\}$ as ρ is reduced. Smoothness was an important factor in choosing the KS function, since constraints must be differentiable for gradient-based optimization (the value chosen here was $\rho = 10$). Additionally, the number of constraints is conveniently reduced.

Rigid body degrees of freedom in the dynamic analysis in pitch and plunge (vertical displacement) were limited by very soft springs. Since no rotational inertias can be input directly into ELAPS, fuselage pitch and nacelle pitch, roll, and yaw inertias were simulated by equivalent systems of two and six concentrated masses, respectively. The fuel weight was represented by a "spar" inside the wing box, with the density of fuel and negligible stiffness. The same approach was followed for wing non-structural mass, in this case the spar was located at the trailing edge to simulate flap and drive shaft inertias.

Table 3.4 summarizes the partitioning of Intuitive Data Sets input to, or generated by "elaps" into Objects after inclusion of the information gathered in this section.

Table 3.3: Graphite / Epoxy Material Data

Properties	Strength	
$E_{11} = 30 \times 10^6$ psi	$\sigma_{11,t} = 507.6 \times 10^5$ psi	$\sigma_{11,c} = -223.4 \times 10^5$ psi
$E_{22} = 16 \times 10^6$ psi	$\sigma_{22,t} = 8.1 \times 10^3$ psi	$\sigma_{22,c} = -2.17 \times 10^3$ psi
$G_{12} = 1.2 \times 10^6$ psi	$\tau_{12} = 14.2 \times 10^3$ psi	
$\nu_{12} = 0.32$		
$\rho = 5.6 \times 10^{-2}$ slugs/in^3	$\varepsilon_{11,t} = 17.24 \times 10^{-3}$	$\varepsilon_{11,c} = -7.59 \times 10^{-3}$
	$\varepsilon_{22,t} = 5.0 \times 10^{-3}$	$\varepsilon_{22,c} = -13.39 \times 10^{-3}$
	$\gamma_{12} = 11.67 \times 10^{-3}$	

Table 3.4: Tool Input / Output - "elaps"

Tool:	elaps		
Given / Assumptions:	material; comparison functions sets; spar, rib locations; V-22 type cross section linear taper of thicknesses, planform		
Input		Output	
geo	wing, fuselage, component	dyn	natural frequencies, generalized
siz	locations		masses, mode shapes
str	internal structure - [cap areas,	str	failure criteria (KS of ...)
	skin, 0°/90°/+45°/-45° (lin.), rib,	wgt	component weights [wing
	spar web thicknesses (const)]		structural]
wgt	component weights and inertias		

3.2.3. Airframe Unsteady Aerodynamics ("pwake")

3.2.3.1. Unsteady Aerodynamics for Aeroservoelastic Applications

Potential Flow Theory offers several possibilities for modeling of subsonic flow unsteadiness. Strip theory treats the three-dimensional problem of airflow about a lifting surface by solving the two-dimensional problem in a set of chordwise crossections. For simple harmonic motion, aerodynamic feedback from the shed wake (induced inflow) is modeled using Theodorsen function (/Theodorsen 35/). General airfoil motions are considered by applying Fourier integral methods or Laplace transforms to numerical approximations of the Wagner function (/Wagner 25/), the lift response due to an inflow step change. Three-dimensional approaches are commonly based on harmonic oscillations of doublets, either by a functional approaches known as Kernel Function Methods (for example /Watkins et al. 59/), or by discretization like the Doublet-Lattice Method (DLM) /Albano and Rodden 1969/. These so-called "k-type" methods predict eigenvalues of an aeroelastic system only for purely harmonic motions, which only occur when no damping exists - at the flutter boundary. Accordingly, solutions from k-type aerodynamics are only valid for points on the imaginary axis of the complex frequency plane. Classical flutter analyses add artificial structural damping to the system in order to achieve sinusoidal time-dependency, and the sign of this entity, which is commonly plotted vs. the speed (V-g plot) determines stability or instability . The magnitude of this auxiliary value, however, is not directly related to the true damping of the system /Desmarais and Bennett 74/. Approximated true damping values can be computed from k-type aerodynamics by p-k Iteration /Hassig 71/ (the notation, p, stands for a complex generalized frequency). The system information is only valid for the one point to which the iteration converges; in terms

of the complex frequency plane, the solution is only valid in single points spread over the entire plane. This prohibits using calculated damping, frequency, and generalized mass of the system from p-k iteration in time-domain representations, which is the basis for flutter suppression controller design and general disturbance response studies. One solution to this dilemma is the use of Padé-Approximants in order to span an approximate surface describing aerodynamic forces generated by the moving structure over the entire complex frequency plane. The variables of this finite-state expansion technique are introduced as additional states to the system, and the associated coefficient matrices are determined by curve-fitting data obtained from k-type analyses performed at a sufficient number of reduced frequencies, k (/Vepa 77/, /Edwards 77/). The resulting coupled aerodynamics-structures system can be expressed by linear, time-invariant coefficient matrices and time-dependent, which is a requirement for linear feedback control system design. Padé-Approximants have therefore frequently been used in aeroservoelastic studies, for example by /Newsom 79/. For repeated aeroelastic analyses which occur in aeroelastic tailoring, the method is less advantageous, since it involves multiple executions of the unsteady aerodynamics analysis before the finite-state aerodynamic expansion can be obtained. A direct calculation of "p-type" aerodynamics is more desirable.

A finite-state wake model for calculation of rotor-induced steady and dynamic inflow has been developed by /Peters and He 87/. They showed theoretically that the 2D lift-deficiency function of the theory converges to the two classical benchmark solutions, the Loewy function for non-lifting climb and the Theodorsen function at an infinite climb rate. For rotary-wing cases, the method performed satisfactorily in correlation studies with 3D free-wake and experimental rotor time-response; and 3D experimental, time-averaged and time-dependent inflow in forward flight (/Peters et al. 87/, /Peters and He 89/). A variation of the theory for completely edgewise flow (/Wang 92/) has been applied to both

rotating and fixed wing flutter calculations by /Nibbelink 92/. Results obtained for a constant chord, unswept wing with an Aspect Ratio of 6 captured the main characteristics of imaginary and real part of harmonic lift from the 3D-corrected Theodorsen theory by /Reissner and Stevens 47/.

The wake model deals with the "outer problem" of airload-induced wake feedback only, which conveniently allows the separation of the "outer problem" from the "inner problem" of lifting surface airload generation. In the simplest case, the inner problem can be approached using lifting-line theory (/Nibbelink 92/), but more recent applications aimed at exploitation of this feature by including thin airfoil theory /Peters and Karonamoorthy 94/, stall models (/Peters et al. 94/), and general airfoil deflections for higher order generalized force calculations of deformable airfoils (/Peters and Johnson 94/), all also in state-space form. Computational efficiency, elegance of approach, and demonstrated accuracy in previous, simple fixed-wing sample cases justified the extra effort of implementation and calibration of a combined induced flow / airloads model for more general wing configurations. The next section is a review of the Peters / He wake theory, and outlines the general approach taken. A detailed treatment of issues involved in the practical implementation of the method in the program PWAKE, and results from comparison with combined DLM / p-k iteration are presented in Appendix C.

A set of reference data for normalization of all entities used is introduced first. Length is divided by the reference disk radius, R; velocity by the reference velocity, U (freestream velocity, V_∞, for fixed wing; rotor tip speed, ΩR, for rotary wing); time by R/U; frequency by U/R; lift per unit length by $\rho U^2 R$ (ρ is the air density); and pressure or moment per unit length by $\rho U^2 R^2$. All data in Section 3.2.3.2. and 3.2.3.3 are normalized according to these conventions.

3.2.3.2. The Peters / He Finite-State Wake Model

The continuity and momentum equation for incompressible potential flow can be written in the following index notation

$$q_{i,i} = 0 \tag{3.9a}$$

$$q_i^* - V_\infty \, q_{i,\xi} = -\Phi_{,i} \tag{3.9b}$$

where the q_i is the perturbation velocity component in the coordinate directions, i. The terms q_i^*, $q_{i,\xi}$, and $q_{i,i}$ denote its derivatives with respect to (nondimensional) time, along freestream direction, and along coordinate direction, i, respectively. The two terms on the left hand side of equation (3.9b) suggest separation of the perturbation pressure, Φ. Let Φ^V be associated with a momentum flux contribution,

$$\Phi^V{}_{,i} = V_\infty \, q_{i,\xi} \tag{3.10a}$$

Φ^A with acceleration,

$$\Phi^A{}_{,i} = -q_i^* \tag{3.10b}$$

and

$$\Phi = \Phi^A + \Phi^V \tag{3.11}$$

By differentiating the momentum equation (3.9b) in coordinate direction, i, and subsequently applying the continuity equation (3.9a), it can be shown that both parts must satisfy Laplace's equation and are, therefore, of the form of acceleration potentials. A candidate function is Prandtl's acceleration potential for circular wings in the ellipsoidal coordinates ν (radial), η (offset from reference disk plane), and ψ (azimuth),

$$\Phi(\nu,\eta,\psi,t) = \sum_{m,n} P_n^m(\nu)\, Q_n^m(i\eta)\left[C_n^m(t)\cos(m\psi) + D_n^m(t)\sin(m\psi)\right] \tag{3.12}$$

which models a pressure discontinuity on the reference disk ($\nu = \sqrt{1-r^2}$, η =0) for n+m odd and $n \geq m$,

$$\phi(r,\psi,t) = -2\sum_{m,n} P_n^m(\nu)\, Q_n^m(i0)\left[C_n^m(t)\cos(m\psi) + D_n^m(t)\sin(m\psi)\right] \tag{3.13}$$

P_n^m and Q_n^m are associated Legendre functions of the first and second kind, respectively, and C_n^m and D_n^m are time-dependent coefficients. Equations (3.10) can be solved for the perturbation velocity perpendicular to the reference disk, q_z, in the following equations denoted by λ, and its time derivative, λ^*, by introducing the linear operators, L and C:

$$\lambda(r,\psi,t) = \frac{1}{V_\infty}\int_\infty^0 \left(\frac{\partial \Phi^V}{\partial z}\right) d\xi = L\left[\Phi^V\right] \tag{3.14a}$$

$$\lambda^*(r,\psi,t) = -\left.\frac{\partial \Phi^A}{\partial \xi}\right|_{z=0} = C\left[\Phi^A\right] \tag{3.14b}$$

Replacing the perturbation pressure components in equation (3.11) using equations (3.14) yields

$$C^{-1}[\lambda^*] + L^{-1}[\lambda] = \Phi \tag{3.15}$$

which is a first order differential equation in the unknown inflow velocity, in response to the right hand side perturbation pressure, Φ, if the operators can be inverted. This is possible if an expansion similar to (3.12) and (3.13) is chosen for λ,

$$\lambda(r,\psi,t) = \sum_{m,n} \frac{\overline{P}_n^m(\nu)}{\nu}\left[a_n^m(t)\cos(m\psi) + b_n^m(t)\sin(m\psi)\right] \tag{3.16}$$

with the cosine and sine inflow states, a_n^m and b_n^m, respectively. The bar over the Legendre functions denotes that they have been normalized by their integral over the interval $\nu = [0,1]$. After substitution of (3.16) into (3.15), pre-multiplication by $\bar{P}_n^m(\nu)\cos(m\psi)$, and integration over the reference disk, a set of first order differential equations in the a_n^m is found,

$$\left[M^c\right]\left\{a_j^r\right\}^* + \left[N^c\right]\left\{a_j^r\right\} = \tfrac{1}{2}\left\{\tau_n^{m,c}\right\} \tag{3.17}$$

and an equivalent equation for the b_n^m if multiplied by $\sin(m\psi)$ (replace superscript c by s). The wake 'mass' matrix [M] and 'damping' matrix [N] are known functions of the wake skew angle, χ. [N] is in fact the inverse of another matrix originating from the operator L. /Wang 92/ reports closed form solutions for this inverse in edgewise flow ($\chi = 90°$) for an infinite number of wake states (Appendix C). These solutions are also accurate for two special kinds of truncated systems: (a) cos-partition, maximum order of azimuthal harmonics, m, odd; and (b) sin-partition; maximum order of azimuthal harmonics even. Closed form solutions can therefore not be used if cosine- and sine partitions have the same maximum order. This is not a significant restriction though, since symmetric and anti-symmetric modes are usually also separated in structural dynamics.

The right hand side of equation (3.17) represents the wake system excitation through an imposed pressure discontinuity, P, which can be expressed in terms of the structural deflections of the wing by any airloads theory (inner problem), and thus represents the link between the two aeroelastic subsystems, structures and aerodynamics:

$$\tau_n^{m,c} = \frac{1}{\pi}\int_0^{2\pi}\int_0^1 P(r,\psi,t)\frac{\bar{P}_n^m(\nu)}{\nu}\,dr\,\cos(m\psi)\,d\psi\,. \tag{3.18}$$

An alternative formulation in Cartesian coordinates (compare with Fig. 3.8) is

$$\tau_n^{m,c} = \frac{1}{\pi}\int_{-S}^{S}\int_{x_{te}}^{x_{le}} P(x,y,t)\frac{\bar{P}_n^m(\nu)}{\nu}\cos(m\psi)\,d\psi\,dx\,dy \tag{3.19}$$

In the special case m = 0 (uniform inflow), the expressions are divided by 2. The pressure distribution, P, can be expressed in terms of the spanwise circulatory lift per unit length, $L_\tau(y,t)$, and a chordwise distribution. Before choosing such a chordwise distribution, it is important to recall that equation (3.17) models the outer problem only, which deals with the effects of feedback from vorticity shed into the wake. Therefore bound vorticity, the central element of the inner problem of lift generation, must be filtered out. This can be achieved by using pressure distributions which do not induce any velocities on the interval over which they are defined - which is, in general, the airfoil chord - the induced velocity in this interval is only that resulting from wake feedback. A distribution which has this desired property is

$$P(x,y,t) = \frac{L_\tau(y,t)}{\pi\, b(y)\sin(\theta)} \tag{3.22}$$

The forcing functions are then

$$\tau_n^{m,c}(y) = \frac{1}{\pi}\int_{-S}^{S} L_\tau(y,t)\left\{\frac{1}{\pi}\int_0^\pi \frac{P_n^m(\nu)}{\nu}\cos(m\psi)\,d\theta\right\}dy \tag{3.23}$$

where the transformation

$$\cos(\theta) = \frac{x - y\tan(\Lambda)}{b(y)} \tag{3.24}$$

has been used (Fig. 3.8). If the normalwash at the chord due to freestream velocity change, airfoil shape change, or airfoil motion, ω, and the induced velocity, λ, are expanded in a Fourier series (here only shown for λ, similarly for ω),

$$\lambda(x,y,t) = \sum_{n=0}^{\infty} \lambda_n(y,t)\cos(n\theta), \tag{3.25a}$$

$$\lambda_0(y,t) = \tfrac{1}{\pi}\int_0^{\pi} \lambda(x,y,t)\, d\theta; \quad \lambda_i(y,t) = \tfrac{2}{\pi}\int_0^{\pi} \lambda(x,y,t)\cos(i\theta)\, d\theta;\ i = 1\ldots\infty \tag{3.25b}$$

then the circulatory lift can be expressed in terms of only the first two coefficients of the series /Johnson 80a/:

$$L_\tau(y,t) = 2\pi\, b(y)\left[\left(\omega_0(y,t) + \tfrac{1}{2}\omega_1(y,t)\right) - \left(\lambda_0(y,t) + \tfrac{1}{2}\lambda_1(y,t)\right)\right] \tag{3.26}$$

Inserting the assumed induced flow distribution, equation (3.16), into (3.25b), and this expression into (3.26), yields for a symmetric problem

$$L_\tau(y,t) = 2\pi\, b(y)\left[\left(\omega_0(y,t) + \tfrac{1}{2}\omega_1(y,t)\right) - \sum_{r,j}\left(\lambda^{r;c}_{j;0}(y) + \tfrac{1}{2}\lambda^{r;c}_{j;1}(y)\right) a^r_j(t)\right] \tag{3.27}$$

where the following short-hand notations for integrals involved have been used:

$$\lambda^{r;c}_{j;0}(y) = \tfrac{1}{\pi}\int_0^{\pi} \frac{\overline{P}^r_j(\nu)}{\nu}\cos(r\psi)\, d\theta; \quad \lambda^{r;c}_{j;1}(y) = \tfrac{2}{\pi}\int_0^{\pi} \frac{\overline{P}^r_j(\nu)}{\nu}\cos(r\psi)\cos(\theta)\, d\theta \tag{3.28}$$

Note that through the choice of pressure distribution, equation (3.22), the chordwise integral in equation (3.23) has the form of the first integral in (3.28). ω_0 and ω_1 are functions of the structural states (Appendix C.1.), and (3.27) shows the expansion of the wake feedback part in the wake states; hence, the wake forcing functions are described by both structural and wake states, which is used in the wake-airframe coupling procedure (Appendix C.2.). Equation (3.27) is used to eliminate L_τ in the pressure distribution, P (3.22), which is then eliminated in the forcing function, equation (3.19):

$$\tau_n^{m,c}(t) = 2\int_{-S}^{S} b(y)\lambda_{n;0}^{m;c}(y)\left(\omega_0(y,t) + \tfrac{1}{2}\omega_1(y,t)\right) dy$$

$$-2\int_{-S}^{S} b(y)\lambda_{n;0}^{m;c}(y)\sum_{r,j}\left(\lambda_{j;0}^{r;c}(y) + \tfrac{1}{2}\lambda_{j;1}^{r;c}(y)\right)a_j^r(t)\, dy \qquad (3.29)$$

The integration technique is of particular importance to accuracy and efficiency of the procedure. A discussion of three different approaches is included in Appendix C.3. An approach to improving efficiency by model order reduction is described in Appendix C.4. Correlation of the model, as programmed in the code PWAKE (Appendix C.5), with an implementation of the Doublet-Lattice Method is shown in Appendix C.6.

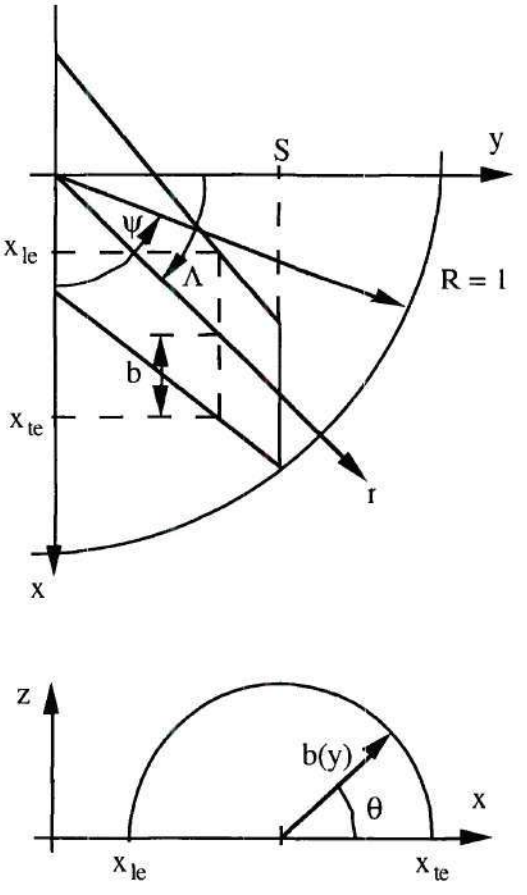

Fig. 3.8: Coordinate Systems for Wing and Airfoil

3.2.3.3. The Tiltrotor Wing Aeroelastic Model in PWAKE

PWAKE models wings as thin airfoils with trapezoidal planforms, so that the geometry is fully determined by quarter chord sweep, area, aspect ratio, and taper of the wing. A trailing edge flap was specified by the inboard end at 50% of the span, the outboard end at the wing tip, and a flap chord of 30% of the wing aerodynamic chord. This configuration is similar to that the outboard flaperon of the V-22 and assumes that this control surface is equipped for high deflection rate operation such as flutter suppression. This flap configuration was not changed in any of the studies in Chapter 4. Airloads used were unsteady in the more specific sense, that is, quasi-steady, wake feedback, and apparent mass terms were included. PWAKE supplies a full control input matrix for flap deflection angle, rate, and acceleration, but only the deflection angle was used in the aeroservoelastic study. The wake model itself bases on incompressible potential flow; compressibility effects at high subsonic Mach numbers in the airloads calculation, however, were approximately accounted for by a Glauert correction to the 2D lift curve slope (fixed at 2π). Due to favorable results from the sample case, the pressure difference from circulatory lift in equation (3.22) was assumed to be concentrated at the aerodynamic half chord of the wing ("Lifting Line"), which reduced the computational effort involved in solving equations (3.28) significantly.

The structural dynamic subsystem in PWAKE is described by natural frequency, generalized mass, and mode shape inputs. Chordwise, spanwise, and beamwise modal deflections for five modes were specified at structural chord leading and trailing edge of eleven spanwise locations. The structural chord leading edge and trailing edge location were fixed at 5% and 55% of the local aerodynamic chord. Aerodynamic planform

deflections for airloads were extrapolated with the surface splining technique from /Harder and Desmarais 72/.

The structural modes are symmetric so that only the cosine partition (3.17) of the wake system was used. Based on results from the sample case, sufficient convergence for the tiltrotor wing case was also expected to be achieved with a maximum number of 13 harmonics, M = 13, on the azimuth. The full system included therefore 56 wake states. From the 66 modes of the coupled system, eigenvalues for which the ratio of structural to wake partition in the associated eigenvector was less than 10, were not considered. This number is an arbitrary choice; however, the separation of wake-type from structural modes for this configuration was even more pronounced than in the sample case, so that the choice is not critical. The system order is hence reduced to that of the original structural system. Refer to Appendix C.4. for a description of the sample case, convergence of the wake model with M, a discussion of the "filtering" technique, and the structure of the coupled airframe structure-wake system; and to Appendix C.2 for the relations leading to the total number of wake states.

Data sets previously defined in Section 3.1. can now be partitioned further. The result is summarized in Table 3.5.

Table 3.5: Tool Input / Output - "pwake"

Tool:		pwake	
Given / Assumptions:		incompressible potential flow approximate compressibility consideration in inner problem wake system order, location of structural wrt. aerodynamic wing planform	
Input		Output	
dyn	airframe dynamic system [airframe natural frequencies, generalized masses, mode shapes]	aeo	wing / aerodynamics coupled generalized system [system, gust, control, wing/rotor and wing/fuselage coupling matrices]
geo	wing, fuselage, wing / fuselage configuration		
siz			
mis	limit speed condition		

3.2.4. Aircraft Dynamic Plant Model ("acp")

3.2.4.1. Methods and Programs for Tiltrotor Aeroelastic Analysis

The review of previous research on tiltrotor aeroelasticity in Section 1.2 revealed that these studies were primarily focused on investigation of the proprotor whirl phenomenon in high-speed forward flight from a rotorcraft approach; the problem was solved at the source by dynamically tuning the rotor or applying rotor controls. The airframe was modeled as a cantilevered, homogeneous beam with quasi-steady aerodynamic damping which was directly included in the analysis program (/Nasu 86/, /Johnson 74/, /Nixon 92/). For a closer investigation of the effect of airframe aeroelasticity on proprotor whirl, a modular approach is more promising. Bell's DYN4, its successor, the Aeroelastic Stability Analysis for Proprotors, ASAP /Popelka et al. 85/, the Proprotor Aeroelastic Stability Analysis, PASTA /Kvaternik 73/, and the Comprehensive Analytical Model of Rotorcraft Aerodynamics and Dynamics, CAMRAD /Johnson 80b/, include airframe dynamics in modal form in the rotor analysis. The information required includes generalized mass, natural frequency, modal damping, and modal deflections at the rotor hub. CAMRAD has been used to couple rotor dynamics with results of structural /van Aken 91/ or aeroelastic analyses /Popelka et al. 85/ from MSC/NASTRAN (/NASTRAN 83/, /NASTRAN 87/). Aeroservoelastic analyses of tiltrotor aircraft with MSC/NASTRAN mode shape inputs to ASAP were performed by /Parham and Chao 89/. CAMRAD/JA and PASTA are limited to real mode shape vectors, and airframe aerodynamic forces are included in form of real damping coefficients /Johnson 88/. ASAP and DYN4 have also been used previously using real mode shape information from NASTRAN (/Popelka et al. 85/, /Parham and Chao 89/). /Parham and Chao 89/ pointed out that this approach accounts for these forces only in an approximate manner: Unsteady aerodynamics add not only

damping, but also apparent mass and coupling between the structural modes. A non-diagonal damping matrix can, generally speaking, not be diagonalized by the eigenvectors of the undamped system. Moreover, simultaneous diagonalization of mass, damping, and stiffness matrix is in general not possible, so that use of one "modal damping" coefficient per eigenform is only an approximation.

One accurate approach to including airframe aeroelasticity in the coupled rotor/ airframe analysis is the use of a non-diagonal matrix of aerodynamic influence coefficients in a second-order airframe model. In this representation, however, the modal characteristics of the airframe / aerodynamics system are not apparent. Natural frequency and damping of the airframe subsystem alone, however, might contain information which is valuable to the dynamist. In a modal analysis, the system is transformed to first order "state-space" form before solving for its eigenvalues. It appeared to be the most logical step to use the information obtained from modal analysis of the first order system directly for coupling with the rotor subsystem, instead of attempting a re-transformation to second order form. PASTA had been obtained by Georgia Tech's School of Aerospace Engineering from Dr. Raymond Kvaternik at the NASA Langley Research Center, and was therefore chosen as the platform for this approach. A description of the coupling procedure used in the new code, the Aircraft Plant Model, ACP, is given in Appendix D.4.

Recent research in tiltrotor aeroelasticity included detailed modeling of the rotor's elastic properties (/Nixon 92/, /Chattopadhyay and Narayan 92/). PASTA features a rigid-blade model with separate hinge-spring systems for flap and lag motions, and a table input for blade pitch dependent parameters as elastic coupling coefficients, blade natural frequencies, δ_3 angle and "Hub Rock Ratio" (slope of out-of-plane contribution to the first inplane mode, which affects pitch-flap coupling through the pitch horn geometry, δ_3 /Gaffey 69/). Control system or torsional flexibility of the blade are not included. /Popelka

et al. 85/ showed in comparisons of wind tunnel stability tests with CAMRAD and DYN4 results (which is similar to PASTA) that both Resources exhibit comparable predictive capabilities despite the rotor model simplifications in DYN4. Good agreement with experimental data, however, was only achieved after inclusion of elastic coupling terms in the formulation, in particular pitch-lag.

Van Aken's results (/van Aken 91/) show that the first chordwise airframe mode can contribute significantly to the flutter mode, and kinematic coupling with the rotor coning mode was expected. PASTA's collective modes, however, are not coupled in the manner described above, which caused some concern about the accuracy of PASTA's stability prediction. As a result, the rotor model was modified to incorporate the two spring-system arrangement first introduced by /Ormiston and Hodges 72/ in both collective and cyclic modes. Changes of the blade's dynamic characteristics and pitch-flap coupling with pitch were modeled through rotation of one of the flap-lag spring systems with pitch, and assumption of a given pitch horn geometry, respectively. Refer to Appendix D.1. for a more detailed description of the rotor model.

Modeling of rotor collective lag, also called the rotor speed degree of freedom, brings up the issue of engine dynamics modeling. In the PASTA model, wing tip roll (spanwise slope of vertical deflections at the tip) and rotor rotation are decoupled, representing a wind-milling or unpowered system with no torque transfer between rotor and airframe. The transmission / engine inertia is assumed to be very large, so that the transmission output shaft speed is constant. /Johnson 75/ showed that for symmetric airframe modes this "autorotation" condition is a good approximation for the powered case (rotor rotational speed change in antisymmetric modes result in oscillatory torque loading on the interconnect shaft, which adds stiffness to the drive system). /Nixon 92/ supported this finding for low forward wing sweep angles, but noted that below -30° wing sweep the

windmilling case was non-conservative for the wing-rotor configuration used. In this research, only symmetric modes were considered. Based on center of gravity location considerations, wing sweep angles as small as those investigated by Nixon were not expected. Hence, the wind-milling condition was used.

Use of a rigid-blade model does not allow physical design of the rotor per se. The model is a simplified representation of the rotor, which, if properly tuned, exhibits dynamic characteristics comparable to the low-order dynamics of the real rotor system. Hence, the actual rotor design for performance, dynamic characteristics, and structural integrity is performed off-line, and then translated into an equivalent rigid-blade model. In terms of the objectives of flexibility and modularity in this research, this approach is clearly preferable to a fully integrated rotor / airframe code. For future extensions it is therefore recommended to include a Tool for rotor design and optimization. In order to limit the scope of this research, however, this option was not pursued. As outlined in Section 3.1, Section 3.2.1.2, and Appendix A.4, rotor aerodynamic designs for a constant and a variable diameter configuration were given and hardcoded in VASCOMP table form. Slightly more variability was permitted for the rotor dynamics, by allowing rotor natural frequency placement within certain bounds, as outlined in the next subsection. /Wernicke and Gaffey 67/ showed that flapping restraint alone ($\omega_\beta > 1$) might lead to excessive oscillatory blade loads in maneuvers. Hence, pitch flap coupling was also allowed to vary, where changes in δ_3 with pitch through pitch link geometry were considered (Appendix D.1).

Another issue of closer investigation was the inclusion of airframe rigid-body degrees of freedom. Proprotor whirl flutter is a low frequency aeroelastic instability, and might couple into the aircraft's short period oscillation /Kvaternik 73/. Previous approaches which used cantilevered wing models are therefore non-conservative. PASTA

features an option for rotor / rigid body coupling incorporating stability derivatives which account for quasi-steady airframe aerodynamics (including tail and fuselage influences). These latter contributions, however, were not included for aircraft center of gravity displacements due to elastic modes, as in a free-free configuration. When converting PASTA to coupling of subsystems in state-space form, the aircraft "rigid body" modes and the associated tail and fuselage aerodynamic forces were considered as another subsystem, which was coupled with the elastic modes through the modal deflections of the aircraft's center of gravity.

The coupling process as described so far is purely structural. Flow field interactions between rotor and airframe are another source of coupling. Previous research on this effect in tiltrotor forward flight treated two separate cases: First, wing aerodynamic force perturbations due to rotor-induced flow fluctuations are addressed. /McVeigh et al. 88/ investigated the time-averaged flow field around a wing / rotor configuration. Good correlation between analysis and experiment was achieved by assuming a fully contracted rotor wake. This result would indicate that dynamic rotor-wing interactions at the low thrust coefficients and high inflow conditions encountered by a proprotor in cruise are negligible. Wing-rotor interactions caused more attention. /DeTore and Gaffey 70/ detected large 3/rev hub shear forces in wind tunnel tests of a three-bladed rotor. They attributed these unexpected oscillatory loads to the rotor's passing through the upwash field in front of the wing, but more so to the divergence of the streamlines in this region. /Schillings and Reinesch 87/ emphasized the importance of both wing circulation and thickness effects on wing-rotor interaction. In conclusion, aerodynamic coupling is primarily a vibration and resonance problem, which could possibly be encountered in a simplified way by avoiding airframe frequencies close to the blade passing frequency, n/rev, where n is the number of blades. A more detailed treatment must incorporate a

detailed surface model of the airframe. Including such a necessarily unsteady model in the present simulation model was considered beyond the scope of preliminary design, and aerodynamic interactions between rotor and wing were neglected.

At this state, the model was applicable to stability investigations of free-flight tiltrotor configurations. PASTA had not been written for control system design, so that swash plate and airframe controls, as well as disturbance (gust) effects had not been included. These elements were added by extracting proper elements from the existing matrices; in particular terms affecting rotor pitch for swashplate controls, and elements associated with horizontal and vertical deflections in the damping matrix for gust inputs. Appendix C.2. describes these extensions more in detail.

3.2.4.2. The Linear Tiltrotor Dynamic Plant Model in ACP

ACP models a tiltrotor's aeroelastic system in airplane configuration. A state-space representation of the airframe subsystem (eigenvalues, control input matrix, gust input matrix, and modal deflections at rotor hub and aircraft center of gravity) is coupled with a rigid-blade rotor model which includes coupling effects from blade elasticity and control system geometry, and fuselage/tail aerodynamics. The eigenvalue problem is solved, and the state-space system matrices in generalized form are output. Control inputs include rotor collective pitch, longitudinal cyclic pitch, lateral cyclic pitch, elevator deflection, and up to three airframe controls. Measured system outputs are the modal deflections at the aircraft center of gravity and the rotor hub.

The preprocessor to ACP generated blade static moments and moments of inertia based on the rotor blade mass and separate assumed mass distribution for constant diameter and VDTR cases, see Appendix D.1. Since the rotor model features a central hinge for all rotor modes, blade inertial properties were assumed to be identical inplane and out-of

plane. It was assumed that the lead-lag and flapping motion of a rotating, cantilevered blade were decoupled at 0° collective pitch at 75% of the rotor radius. Based on this assumption, and given the blade inertial properties, rates of springs at the rotor hub were calculated in order to match frequency goal inputs. This spring system was assumed to rotate with pitch. Out-of-plane stiffness of a second, pitch-independent spring system was calculated in a similar way, for a gimbal mode goal frequency. The inplane stiffness of this system was fixed at a value of 2.75×10^6 ft-lb/rad, based on estimations regarding geometry of the rotor drive shaft.

The airframe subsystem, as supplied by PWAKE, as represented by five pole pairs, included wing aerodynamics (Section 3.2.3.3.). Hence, the relevant stability derivatives, $c_{m\alpha}$ and $c_{L\alpha}$ (or $-c_{z\alpha}$ in Etkin's notation /Etkin 82/, which was used in PASTA) included only tail and fuselage contributions. No additional constraints or boundary conditions were imposed on the system. The system was set up, solved, and the associated generalized system output for one flight condition only, as determined by true air speed, speed of sound, density, and rotor RPM. Damping of the coupled modes was combined in a KS function, equation (3.9), in order to reduce the output size. In total, the system included six rotor degrees of freedom (longitudinal and lateral cyclic flapping, longitudinal and lateral cyclic lead-lag, collective flapping/coning, and collective lag/rotor rotation), five airframe degrees of freedom, three rotor control inputs (longitudinal, lateral cyclic pitch, and collective pitch), one "fuselage" control input (elevator), one "airframe" control input (trailing edge flap), and two gust inputs (horizontal and vertical gust).

A discussion of the bounds imposed on nondimensional, uncoupled frequencies of the rotor is necessary at this point. The normalized natural frequency of the first flapping mode, ω_β, was interpreted as an indicator for the blade stiffness, and hence for the blade and hub loads which might occur in operation. /Young and Lytwyn 67/ calculated an

optimal flapping frequency for proprotor stability between 1.1 and 1.2/rev (these results were also supported by the work of /Wernicke and Gaffey 67/); /Ganguli and Chopra 92/ constrained ω_β for a helicopter aeroelastic optimization to be placed between 1.08/rev and 1.18/rev; and /Caramaschi 91/ reports 1.3/rev for the EUROFAR vehicle's flexbeam proprotor. In this study, ω_β was permitted to vary between 1.0/rev and 1.5/rev. A similar constraint was formulated for the inplane frequency, ω_ζ, based on air / ground resonance considerations. This phenomenon can be entirely avoided by placing ω_ζ at or above 1/rev (see for example /Bielawa 92/). /Gaffey 69/ reported that for this condition positive pitch-flap coupling (negative δ_3) has a stabilizing effect on the inplane degree of freedom of coupled flap-lag motion. The EUROFAR lead-lag frequency was placed at 1.5/rev /Caramaschi 91/. Since ω_β was expected to reach values around 1.1/rev based on the findings of Young and Lytwyn, the bounds for ω_ζ were placed at 1.25/rev and 1.7/rev in consideration of frequency separation requirements.

A summary of data considered for this Tool, and their association with the previously defined data sets, is included in Table 3.6.

Table 3.6: Tool Input / Output - "acp"

Tool:		acp	
Given / Assumptions:		rigid blade (RB) rotor model and rotor vacuum natural frequency bounds	
Input		Output	
aeo	wing / aerodynamics coupled dynamic system; coupling matrices	apd	coupled airframe / rotor aeroelastic system (aircraft plant model): system, control, gust, measured output matrices
geo	wing and rotor layout		
mis	limit speed condition	rdy	cruise condition rotor dynamics
rdy	RB vacuum frequencies		
rgo	rotor controls layout		
sae	airframe stability / control derivatives		
siz	rotor and wing dimensions		
wgt	rotor blade mass		

3.2.5. Flutter Suppression Control System Design ("csd")

3.2.5.1. Review of Linear Quadratic Regulator Theory

In agreement with the general philosophy presented in this work, the focus in representation of control system design is on providing an approach which allows enough flexibility to allow future enhancements. A very simple method incorporating Linear Quadratic Regulator (LQR) Theory was chosen to demonstrate how more advanced techniques could be added to the analysis. The use of LQR must not be interpreted as an attempt to fully exploit the potential of active control; it merely serves as a simplistic proof-of-concept technique.

Consider the linear, time-invariant dynamic system

$$\begin{aligned} \dot{x} &= Ax + Bu + Gw \\ y &= Cx \end{aligned} \tag{3.28}$$

with the state vector, x, control vector, u, disturbance vector, w, and output vector, y. According to Optimal Control Theory, the cost functional, J,

$$J = \int_0^\infty \left(x^T Q x + u^T R u \right) dt \tag{3.29}$$

is minimized when using a linear state-feedback law of the form

$$u = -R^{-1} B^T K_\infty \, x \tag{3.30}$$

K_∞ is the unique positive-semidefinite solution of the Algebraic Riccati Equation (ARE),

$$K_\infty A + A^T K_\infty - K_\infty B R^{-1} B^T K_\infty + Q = 0 \tag{3.31}$$

if [A,B] is stabilizable and [A,C] is detectable. Under these conditions, the closed-loop system

$$\dot{x} = \left(A - BR^{-1}B^{T}K_{\infty}\right) x \tag{3.32}$$

is asymptotically stable. The state weighting matrix, Q, is commonly chosen as

$$Q = C^{T} C, \tag{3.33}$$

(as used in the present approach), but can be any positive semi-definite matrix. /Safanov and Athans 77/ have shown that if the control weighting matrix, R, is chosen to be of the form

$$R = \rho I \tag{3.34}$$

then the feedback law of equation (3.32) guarantees at least 6 dB gain margin and 60° phase margin in each input channel. According to MIL-A-8870, an aircraft system with a stability augmentation or flutter suppression controller must be free of instabilities at speeds up to 1.15 times the limit speed, V_L, and exhibit exactly these robustness criteria in all loops of the flight control system up to V_L /Parham and Chao 89/. In other words: Stability requirements according to MIL-A-8870 specifications are inherently satisfied by solving the deterministic linear quadratic control problem.

It is important to note that full-state feedback as in equation (3.32) generally can not be implemented in reality, because only very few states can be measured directly. The Linear Quadratic Gaussian problem (LQG) therefore also includes the design of an observer which uses the available system output signals (e.g. from accelerometers at different locations of the aircraft) together with control input information to create an optimal estimate of the states. "Optimal" in this context means that the deviation of the state

estimates from the actual states, integrated over an infinite time interval, is minimized. Such a Linear Quadratic Gaussian (LQG) design in general does not exhibit the same robustness characteristics as the LQR alone /Doyle 78/. /Doyle and Stein 79/ showed, however, that by properly placing the observer poles, the full-state feedback robustness can be completely recovered (Loop Transfer Recovery, LTR). For the purpose of this study it is recognized that this result can be achieved by LTR, but the actual process is not performed. Instead, it is assumed that the complete state vector is available, and a the Linear Quadratic Regulator is designed. This is similar to the approach to flutter suppression controller design for tiltrotors previously used by /Frick and Johnson 74/.

3.2.5.2. Design Constraints and Implementation

LQR theory guarantees stability, but the system's state responses to an external disturbance like a vertical gust might exceed passenger comfort levels or even structural limits. If these goals are met by varying the weights in Q and R, the required control system activity could be beyond the system's physical capabilities. Hence, constraints must be imposed on certain state and control responses to gust inputs. The metric commonly used for this purpose is the root mean square (rms) response /Frick and Johnson 74/,

$$\sigma_{\beta} = \left(2\int_0^{\infty} |H(s)|^2 F_w(s)\, ds \right)^{1/2} \tag{3.35a}$$

$$\sigma_{\dot{\beta}} = \left(2\int_0^{\infty} s|H(s)|^2 F_w(s)\, ds \right)^{1/2} \tag{3.35b}$$

$$\sigma_{\ddot{\beta}} = \left(2\int_0^{\infty} s^2|H(s)|^2 F_w(s)\, ds \right)^{1/2} \tag{3.35c}$$

for the variable, β (either system response or control input signal), and its first and second time derivative, respectively, where H(s) is the transfer function from the disturbance (gust) input to β. The vertical gust is described by the von Kármán Spectrum,

$$F_w(s) = \frac{\sigma_w^2 L_w}{2\pi V_0} \frac{1 + 8/3\left[1.339\left(s\, L_w/V_0\right)\right]^2}{\left\{1 + \left[1.339\left(s\, L_w/V_0\right)\right]^2\right\}^{11/6}} \tag{3.36}$$

with rms gust velocity, σ_w, and gust wave length, L_w. V_0 is the aircraft limit velocity. If severe gusts are assumed (probability of exceedance 10^{-5}), the numerical values for the gust spectrum at cruise altitude (25,000 ft) are L_w = 2,500 ft and σ_w = 20 ft/sec according to Mil-F-8785C. In order to impose a rather stringent constraint, the rms vertical airframe accelerations in this condition, checked at the rotor hub, the aircraft center of gravity, and the pilot station were not to exceed 0.2g, a value equivalent to "moderate" turbulence in subjective pilot's ratings (/Notess 63/). For simplicity, the pilot station was placed at a constant longitudinal offset from the center of gravity (20 ft). At the same time, elevator and flaperon rms rates were not to exceed 15 rad/sec, and the Euclidian Norm of the rms rotor control rates (collective, longitudinal and lateral cyclic pitch) was limited to 10 rad/sec.

For quick implementation, and in order to expedite future extensions in this discipline, the LQR design algorithm was programmed in MATLAB™. A large number of modern control system design techniques is already available in its Toolboxes, and current controls research relies heavily on this versatile Resource. Hence, improvements of the simple approach followed should be easy to implement. Input are the aircraft's system matrix, A, control input matrix, B, gust input matrix, G, and output matrix, C, as well as the "gain" (equivalent to $1/\sqrt{\rho}$) and parameters σ_w and L_w from equation (3.36). Output are the system and controls responses as outline above. A stabilizability / detectability

check is included to ensure stability of the closed-loop system, equation (3.32). This information was also included in Table 3.7.

Table 3.7: Tool Input / Output - "csd"

Tool:		csd	
Given / Assumptions:		full-state feedback, LQR design	
Input		Output	
apd	coupled airframe / rotor aeroelastic plant model	csd	airframe rms accelerations and control rates rms gust response
csd	"gains" for flaperon, elevator, swashplate controls; gust model parameters		

3.2.6. Objective Function and Constraint Generator ("OBJ")

This Tool provides the option of constructing an objective function or composite constraints using output from several Tools. Additionally, optimization algorithms commonly requires constraint information in a standard, normalized form for numerical conditioning reasons. These conversion are also performed here such that a violated constraint is positive, and the order of magnitude of the constraint value is 1.

The single objective function used in this research is the Productivity Index, PI [kts], which is calculated from payload weight, W_{pay} [lb], range, R [nm], block time (terminal-to-terminal time), t_{block} [h], operating weight empty, W_{oe} [lb], and mission fuel weight, $W_{f,miss}$ [lb],

$$PI = \frac{W_{pay}\left(R/t_{block}\right)}{W_{oe} + W_{f,miss}} \tag{3.37}$$

All the relevant data for the objective function were supplied by the Tool "vascomp." A total of 17 constraints were considered in the tiltrotor Design Simulation Model. These constraints may be grouped into geometric, center of gravity location, table lookup, static load margin of safety, open loop system damping, and closed loop system gust response constraints. Geometric and cg location constraints for aircraft and helicopter configuration are depicted in Fig. 3.9 and 3.10, respectively.

Geometric constraints refer to rotor-airframe clearance in aircraft configuration. FAR 23.771 / 25.771 requires that no primary controls are located within +/- 5° of the propeller plane:

$$c_{grc} = 1 - \frac{2\left(x_r - l_c\right)}{\left(b + D_f\right)\sin(5°)} \tag{3.38}$$

The dimensions are defined in Fig. 3.9; all lengths are in [ft]. Propeller / wing clearance of at least 1 ft was checked at tip and root of the rotor for 15° flapping angle:

$$c_{grwt} = 1 + x_r - x_w + R\sin(15°) + \left(\tfrac{b}{2} - R\right)\left(\frac{(1-\tau)c_{root}}{2b} - \tan(\Lambda)\right) \tag{3.39}$$

$$c_{grwr} = 1 + \xi_{rr}\, c_{tip} \tag{3.40}$$

where x_w denotes the distance from the fuselage nose to the intersection of fuselage center line and wing quarter chord line, b is the wing span, R the rotor radius in cruise configuration, τ is the wing taper ratio, c_{root} and c_{tip} are the wing root and tip chord, respectively, Λ is the wing quarter chord sweep angle, and ξ_{rr} is the ratio of aft chordwise offset of the rotor hub from the wing leading edge, divided by the tip chord (compare also with Fig. A.2). It was furthermore required that the rotor maintained at least one foot distance from the fuselage and nacelle with 15° flapping angle:

$$c_{grf} = 1 + \tfrac{1}{2}(D_f - b) + R \tag{3.41}$$

$$c_{grn} = 1 + x_r - x_n + \tfrac{1}{2}\left[(1-\eta_{en})b\sin(15°) + l_{nac}\right] - \left[\tfrac{1}{2}b(\eta_l - \eta_{en})\right]^2;$$

$$\eta_l = \max(\eta_{en}, 1 - 2R/b) \tag{3.42}$$

Here, x_n is the nacelle center of gravity (cg) location from the fuselage nose, l_{nac} is the nacelle length, and η_{en} is the ratio of spanwise nacelle cg location to wing semi span. The second term creates a smooth transition between cases in which the nacelle cg is located within a rotor radius from the wing tip, and those in which the nacelle does not interfere with the rotor.

Constraints on the aircraft cg location are primarily determined by data generated in "vascomp." The control capacity limit is exceeded when the distance between cg and wing

aerodynamic center, normalized by the mean aerodynamic chord, denoted by $\xi_{ac\text{-}cg}$, is less then the minimum distance, $\xi_{ac\text{-}cg,\ min}$. If the center of gravity is located in front of the wing aerodynamic center, $\xi_{ac\text{-}cg,\ min} < 0$, then the proper constraint formulation is

$$c_{cgc} = \xi_{ac-cg} / \xi_{ac-cg,min} - 1 \tag{3.43}$$

Including one quarter chord cg travel as an additional margin of safety, the static stability constraints in aircraft configuration is defined as

$$c_{cgs} = 1 + 4\left(c_{m\alpha} / c_{L\alpha}\right) \tag{3.44}$$

A detailed analysis of helicopter mode static stability was considered beyond the scope of this research. However, a simplified representation was used to check the aircraft's stability in 45 kts forward flight,

$$c_{cgs,h} = 1 + 4\left(c_{m\alpha} / c_{L\alpha}\right) + 4\left(\xi_{ac-cg,h} - \xi_{ac-cg}\right) + 8\left(c_{m\alpha,R} / c_{L\alpha}\right) \tag{3.45}$$

Note the third term and the fourth term in (3.45), which are related to cg shift from aircraft to helicopter configuration, and rotor pitching moment sensitivity with angle of attack, respectively (refer to Appendix A.2. for an estimation of the rotor contribution). A final constraint originating in "vascomp" is an upper limit on the rotor thrust coefficient to solidity ratio, (c_T/σ), which is given by the highest value available in the VASCOMP rotor tables (numerical values are $(c_T/\sigma)_{max}$ = 0.17 and 0.16 for constant and VDTR, respectively):

$$c_{cts\,max} = \left(\frac{c_T}{\sigma}\right) \Big/ \left(\frac{c_T}{\sigma}\right)_{max} - 1 \tag{3.46}$$

Structural integrity in the 2g-jump take-off condition is given if the failure criterion, $S_{T,cr}$, is less than one (Section 3.2.2.2.),

$$c_{sjt} = S_{T,cr} - 1 \tag{3.47}$$

The open-loop dynamic system (without control feedback) is considered stable, if the critical (minimum) damping , D_{cr}, is larger than the limit damping, D_{min}, at the limit speed, V_L. D_{min} was set to 0.1% critical damping to ensure stability of the final design.

$$c_{oldmp} = D_{min} - D_{cr} \tag{3.48}$$

Finally, constraints were imposed on the closed loop system response to gusts of 7.5 ft/sec ms velocity and 2500 ft wave length (see Section 3.2.5.2.). Airframe accelerations were limited to a_{max} = 0.5g rms magnitude, swashplate controls rms activity to $r_{swp,max}$ = 10 rad/sec, and fixed wing controls activity to $r_{fw,max}$ = 15 rad/sec. Accelerations were checked at the airframe cg, cockpit station (located 20 ft in front of the cg), and rotor hub:

$$c_{acgacc} = a_{acg}/a_{max} - 1; \quad c_{cptacc} = a_{cpt}/a_{max} - 1; \quad c_{rotacc} = a_{rot}/a_{max} - 1 \tag{3.49}$$

Similarly, control system activity was checked for flap, elevator, and combined swash plate rates:

$$c_{frte} = r_f/r_{fw,max} - 1; \quad c_{erte} = r_e/r_{fw,max} - 1; \quad c_{srte} = r_s/r_{swp,max} - 1; \tag{3.50}$$

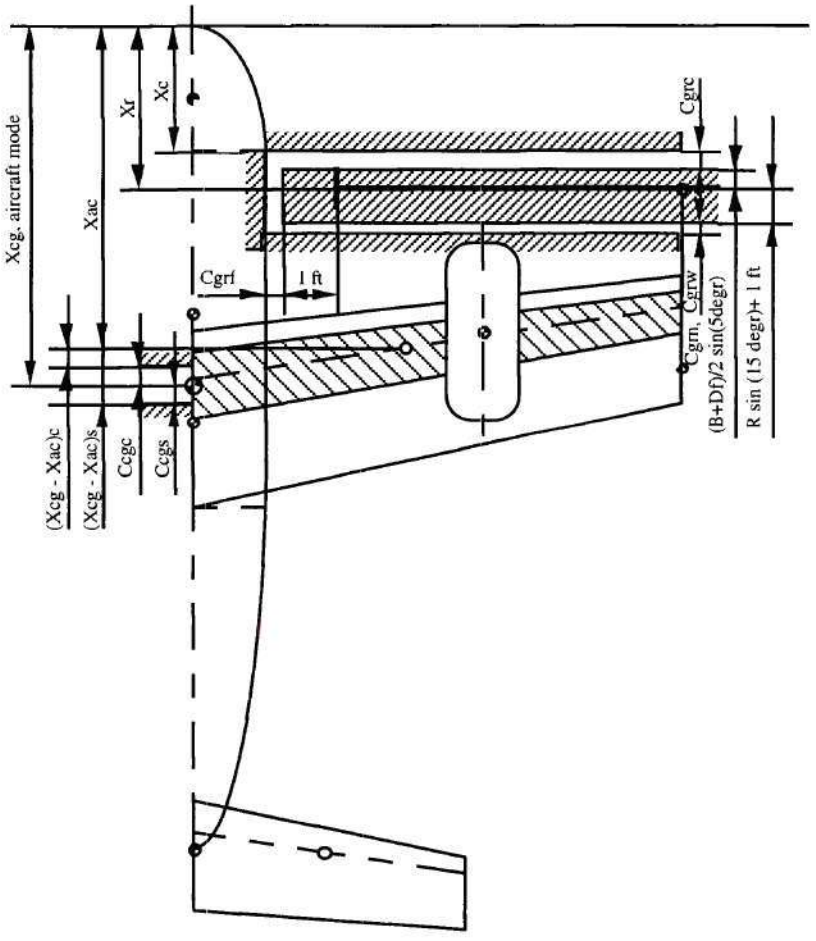

Fig. 3.9: Geometric and Center of Gravity Constraints,

Aircraft Configuration

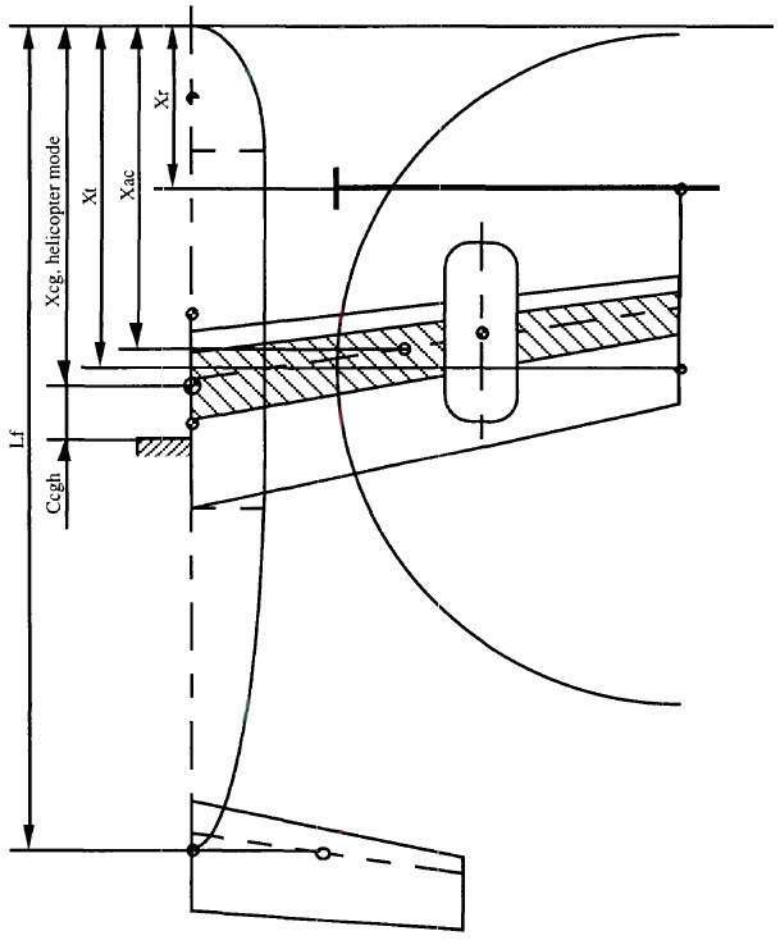

Fig. 3.10: Center of Gravity Constraint, Helicopter Configuration

Table 3.8: Tool Input / Output - "OBJ"

Tool:			OBJ
Given / Assumptions:			-
Input		Output	
apd	min. damping - coupled plant	apd	min. damping constraint
csd	gust response accelerations and	csd	gust response constraints
	control rates	eco	Productivity Index
eco	block time	siz	geometric / cg location
geo	wing, fuselage, and rotor layout		constraints
mis	payload, range	str	structural integrity constraint
rgo	extension ratio, solidity, $(c_T/\sigma)_{max}$		
sae	stability derivatives		
siz	dimensions		
str	KS of static failure criteria		
wgt	fuel, empty weight		

3.2.7. Optimization ("OPT" ["GSE"])

Application of decomposition principles is an essential part of this research. As a result, an optimization strategy was selected which demonstrates utilization of decomposition in ANALYSIS and SENSITIVITY tasks. This method is the Global Design Space approach, GDS, in which locally generated sensitivities are used in the Global Sensitivity Equations, GSE, to generate first order design space information, which in turn is used by a gradient-based optimization engine for determination of a one-dimensional search direction (see Section 1.2). This strategy has also been used in Sections 2.2.2. and 2.2.3. as an example for application of the recomposition technique described in that chapter. In addition to functional operators for Circuit iteration and local sensitivity analysis, only a GSE solver and an optimization engine are required.

The Tool "GSE" is simply a solver for linear systems of equations and utilizes an off-the-shelf LU-decomposition scheme. A commercial Resource, the Design Optimization Tools Package, DOT /DOT 93/, was used for search direction determination and line search solution. The optimization problem as formulated in Section 3.1. translates into a constrained, single objective optimization task, for which a Modified Method of Feasible Directions, MMFD, Sequential Linear Programming, SLP, and Sequential Quadratic Programming, SQP, are offered by DOT. The MMFD was primarily used to reach the feasible region for highly unfeasible initial designs with a large number of design variables, whereas the SLP algorithm proved to be very robust for less complex design tasks. The SQP method was not used.

"OPT" and "GSE" process constraint and objective function information as outlined in Section 3.2.6. Output are design variables, which must not be output of any Tool. The determination of these variables are determined by analyzing the unique data input/output

structure in the Level II Recomposition, outlined in the following section. Table 3.9 therefore provides only general statements from the Level I Decomposition, Fig. 3.1 and 3.2, for decision variable outputs.

Table 3.9: Tool Input / Output - "OPT"

Tool:		OPT	
Given / Assumptions:		-	
Input		Output	
apd	open loop stability constraint	csd	*free control system data*
csd	gust response constraints	geo	*free wing, fuselage, rotor*
eco	Productivity Index		*geometric configuration*
siz	geometric and cg location	mis	*free mission data*
	constraints	rgo	*free rotor geometry*
str	structural integrity constraint	rdy	*free rotor dynamics data*

3.3. Level II Recomposition: Data Coupling Matrix Assembly

The Level II Decomposition left the Design Simulation Model nearly complete disassembled. The final decomposition step is to identify single Attributes. If this tedious task is to result in an efficient data transfer structure, however, the connections between the contributing analyses must be considered. Recomposition aspects are more pronounced at

this step than in the other decomposition steps. Due to the emphasis on an efficient approach in this research, this task was considered part of the system re-assembly. The total number of Attributes generated by this procedure is 186 for the present case. The case of wing shape representation shall serve as an examples for the considerations involved, and the procedure followed. "Shape" refers here to the wing description as a three-dimensional body, excluding inner structure and aerodynamic cross section definitions.

Information regarding the outer shape and dimension of the wing can be found in the input / output relations of five Contributing Analyses: "vascomp," "elaps," "pwake," "acp," and "OBJ." In order to reduce the number of finite-differencing steps necessary in the sensitivity analysis, the dimension of this set of data should be kept small. Representations of the shape differ significantly, however. VASCOMP's input set is a good example for an efficient approach: With aspect ratio, taper ratio, quarter chord sweep, and thickness-to-chord ratio, the shape of a wing with trapezoidal planform is completely described. Wing loading as input, and gross weight as output determine the dimension, so a total of six data items is needed. ELAPS, on the other hand, requires eight values alone to describe the planform using the trapezoid's corner coordinates, and two more to capture the wing thickness (constant and linear term in spanwise direction). The description in PWAKE contains only five items (aspect ratio, sweep, taper, thickness-to-chord ratio, area), which is the minimum required.

The set finally chosen is shown in Table 3.10, which is a row partition of the Data Coupling Matrix, DCM. Wing loading was retained as a necessary nondimensional descriptor for performance purposes. As indicated by the Input / Output Indicator value of 2 in the column "vascomp," wing span (bwing) is an output of "vascomp," and was used as the dimension carrier for wing description. Also, no columns in the "geo" set partition shown contain a "2," indicating that they are not generated within the model, and therefore

must be supplied externally. Hence, all non-dimensional wing descriptors may serve as decision variables. Finally, "0"s in several columns show that not the full description is required in all Contributing Analyses. In these cases, the opportunity to reduce input sets based on disciplinary knowledge was exploited. PWAKE, for example, incorporates thin airfoil theory in its airloads model, so that the airfoil thickness, tovc, is not required.

Level II Compatibility is hence established by carefully examining CA input requirements, matching them with the contents of Intuitive Data Sets, and identifying the Input / Output Indicators for each single data item in the set (rows in the DCM) and each CA (columns in the DCM).

Table 3.10: Wing Shape Description

Set	Variable	...	vascomp	elaps	pwake	acp	csd	OBJ
...	...		...	...	...	...	...	...
geo	ar	...	1	1	1	1	0	1
	...	...	...	...	...	...	...	...
	phi	...	1	1	1	0	0	1
	tau	...	1	1	1	1	0	1
	tovc	...	1	1	0	0	0	0
	...	...	...	...	...	...	...	...
	wl	...	1	0	1	1	0	0
	...	...	...	...	...	...	...	...
siz	bwing	...	2	1	1	1	0	1
	...	...	...	...	...	...	...	...

Input / Output Indicator Values: 0 - not used; 1- input; 2 - output; 3 - input and output

3.4. Level I Recomposition: Process Execution Code Generation and DCM+

3.4.1. Process Execution Code

As noted in Section 2.2, Level I Recomposition for the ANALYSIS task (zeroth order design space information) could have been performed without detailed knowledge of the contents of each Intuitive Data Set. The information required to determine Circuits is fully contained in the Process Intuitive Data Set input / output relations as depicted in Fig. 3.3. The associated N^2 Diagram, Fig. 3.11, was derived from matching these sets based on the information contained in the Tool Input / Output relations, Tables 3.2 and 3.4 to 3.9. Contributing Analyses are denoted using the associated Tool names. Only one feedback loop is seen inside the optimization iteration loop. The data item responsible for this iteration loop is the weight of the wing structure, which is generated in "elaps" and used in "vascomp" for aircraft sizing. This CA, in turn, generates the wing dimensions required for calculation of the structural wing weight. Accordingly, "vascomp" and "elaps" form Circuit 1 (C1 in Fig. 3.12). All other Contributing Analyses can be executed in sequence and therefore form their own Circuits.

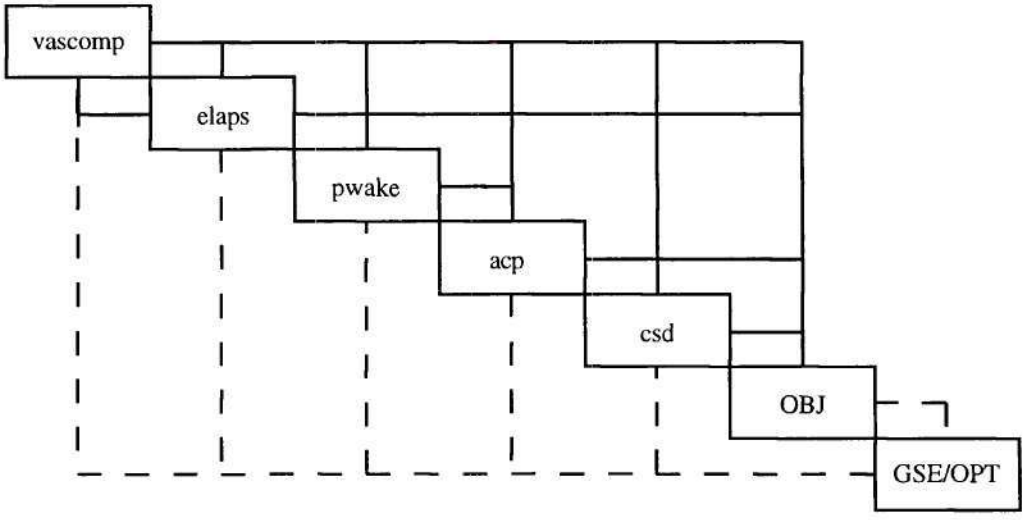

Fig. 3.11: N^2 Diagram, Tiltrotor Case

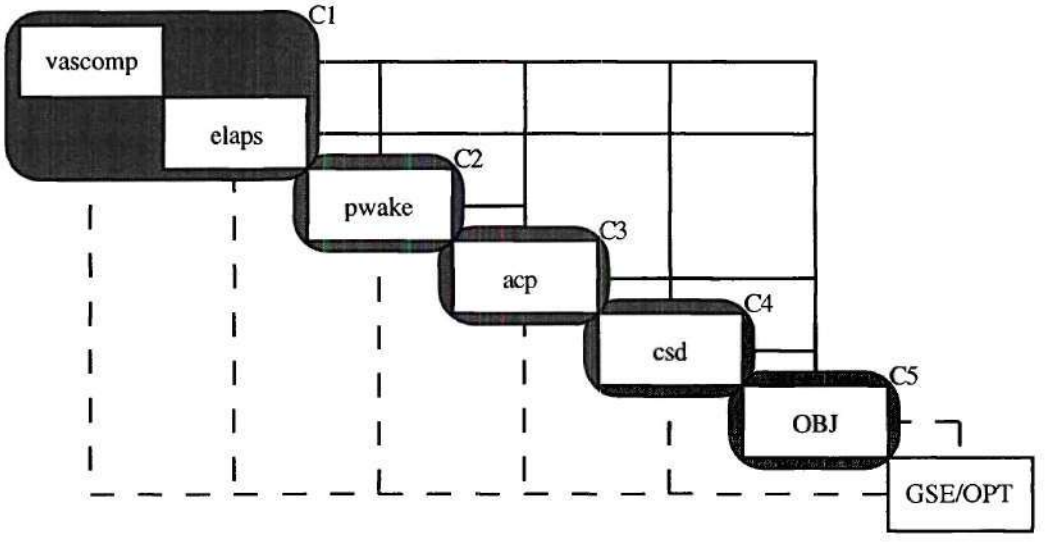

Fig. 3.12: Circuits, Tiltrotor Case

Using the notation introduced in Section 2.2, the Circuits for the ANALYSIS task are defined as follow:

$$C_1 = \{ \text{vascomp, elaps} \} \tag{3.51a}$$

$$C_2 = \{ \text{pwake} \} \tag{3.51b}$$

$$C_3 = \{ \text{acp} \} \tag{3.51c}$$

$$C_4 = \{ \text{csd} \} \tag{3.51d}$$

$$C_5 = \{ \text{OBJ} \} \tag{3.51e}$$

The Contributing Analysis "vascomp" has the longest processing times (3-4 min. on an IBM RS/6000, depending on the initial gross weight guess; numbers refer to CA, not Resource run times - refer to next section). The CA "pwake" is next in computational effort with 2-3 min. user time, followed be "elaps" (about 2 min), "acp" (around 1 min.), and "OBJ" (less than 30 sec.). Hence, if the resources for parallel execution are available, the initial approach might be to define one Sequence per CA in order to achieve high user time efficiency during the SENSITIVITY task. Proceeding along these lines, however, neglects the dimensions of the connections depicted in Fig. 3.11. The control system design CA "csd" serves as a typical example. Table 3.7 shows that only data from the Intuitive Data Sets apd and csd are input. For a system with five airframe aeroelastic modes, six rotor modes, two fixed wing control inputs, three rotor controls inputs, one gust input signal, and three measured output signals (Section 3.2.5.2.), this translates into a total of 682 single data items in the set apd alone[matrix dimensions, first order form, equation (3.28): A(22×22), B(22×5), C(3×22), G(22×1)]. If the generalized form of the system is used, the size can be reduced to less or equal 242 by diagonalization of the system matrix, A.

The number of variable inputs to a Sequence, however, is identical to the number of local sensitivity calculations to be performed. This number is definitely unreasonably large. Additionally, the sensitivities generated do not contain information that can be evaluated ad hoc. For example, the derivative of rms swash plate control rate gust response with respect to the (4,5) element of the control input matrix, B, is not an entity that can be easily interpreted with respect to physical meaning or significance for the optimization process. Hence, this approach was not pursued.

In Section 2.2, data which are considered in the GSE (left hand side of the equation, Eq. (1.1)) were called Behavior Variables. System States were defined as variables which are transferred between Contributing Analyses, but do not enter the GSE (Sequence-internal data transfer only). Eliminating the need to calculate sensitivities for elements in "bulk" data blocks as considered above translates to moving these data from the set of Behavior Variables to the set of States in this terminology. This transfer can be accomplished by combining Contributing Analyses which interchange such bulk data blocks into one Sequence. The result of these considerations was the grouping shown in Fig. 3.13. The associated Sequence definitions are

$$S_1 = \{ \text{ vascomp } \} \tag{3.52a}$$

$$S_2 = \{ \text{ elaps, pwake, acp, csd } \} \tag{3.52b}$$

$$S_3 = \{ \text{ OBJ } \} \tag{3.52c}$$

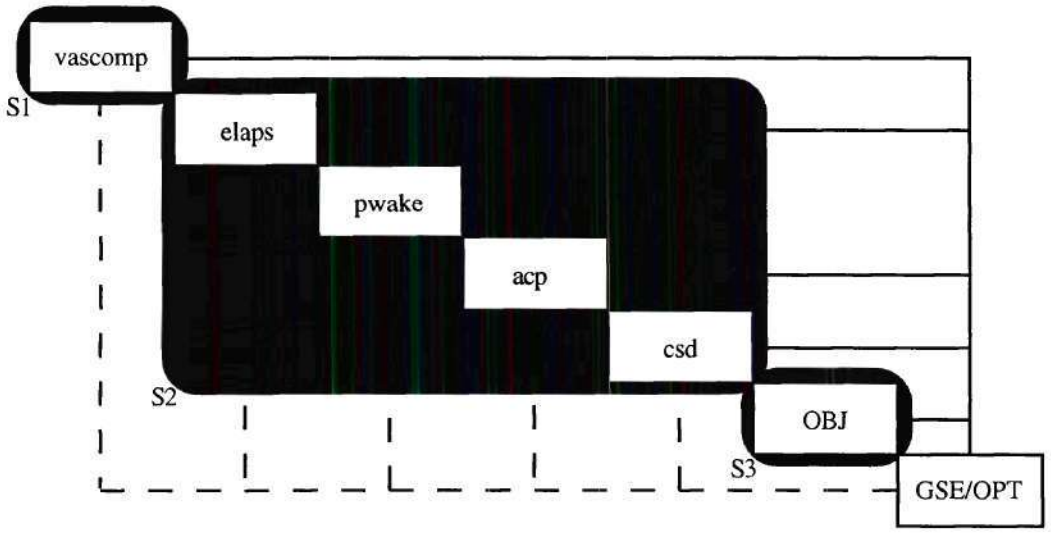

Fig. 3.13: Sequences, Tiltrotor Case

The Problem Execution Code for the tiltrotor case is then of the form

$$
\begin{aligned}
d = \; & SO\,[\\
& \quad SA\,[\; C\,[\, vascomp \parallel elaps \,] \\
& \qquad \Rightarrow C\,[\, pwake \,] \\
& \qquad \Rightarrow C\,[\, acp \,] \\
& \qquad \Rightarrow C\,[\, csd \,] \qquad\qquad (3.53) \\
& \qquad \Rightarrow C\,[\, OBJ \,] \qquad\quad], \\
& \quad SD\,[\; (\quad S\,[\, vascomp \,] \\
& \qquad\quad \parallel S\,[\, elaps \Rightarrow pwake \Rightarrow acp \Rightarrow csd \,] \\
& \qquad\quad \parallel S\,[\, OBJ \,] \quad) \\
& \qquad \Rightarrow GSE \quad\;] \\
& \;\;]
\end{aligned}
$$

Refer to Section 2.2.2.2., equation (2.1) for the notation used.

The establishment of a Sequence structure allowed further reductions of the total set of data required to describe the simulation model. The N^2 Diagram, Fig. 3.11, indicates in combination with the associated Object input / output relations in Tables 3.4 to 3.7 that data flow in Sequence 2 is purely sequential, with structural dynamics data being transferred from "elaps" to "pwake," aeroelastic system data from "pwake" to "acp," and aeroelastic plant model data from "acp" to "csd" (the latter being the case discussed above). All these connections contain "bulk" information, meaning that not all single data items carry physically meaningful information, and are not accessed by other Contributing Analyses. It suffices therefore to tag these bulk data blocks with a unique indicator, and transfer the indicator instead of the entire block.

Table 3.11 shows an example for this procedure, determination of Data Types, and extension of the DCM obtained from Level II Recomposition to the DCM^+. Grouping of CAs in Circuits and Sequences as defined above is included in the first three rows of the DCM^+. In the row partition shown, no Input / Output Indicator value of 1 is located outside the Sequence 2 column partition. This is an indication for exclusive use of these data are in Sequence 2. Exclusive use in one Sequence classifies them as States. Real and imaginary part of the airframe aeroelastic system's eigenvalues are stored as single data items (for simplicity represented by aere_i, aeim_i, where i=1...13 as required) to allow direct access; control, gust, and coupling matrices (bctrl, bgust, cplgfus, cplgrot, cplffus, cplfrot), however, are tagged bulk data. These bulk data blocks can be identified by the Input / Output Indicator value 3 in the column "pwake": An integer "indicator" value for the matrices, called bctrl, bgust, cplfus, and cplrot, respectively, is incremented on each "pwake" execution. This new value is used as a tag attached to the name of a file storing the associated bulk data blocks, creating a unique file name. The CA "acp" then uses the tag in the DCM^+ to re-create this file name and use it as additional input. The

incrementation procedure requires that the indicators bctrl, bgust, cplfus, and cplrot be both input and output. Hence, the Input / Output Indicator value of 3. Effectively, a large number of data has been removed from the DCM$^+$ by this procedure without losing access to them.

Similar consideration were made for all data entries in the DCM. States and Behavior Variables were uniquely determined by identifying Input / Output Indicator location with respect to Circuit and Sequence column partitions. Decision variables were selected from data items showing Input / Output Indicator values of 0 or 1 in the respective row (input only). The complete DCM$^+$ is shown in Appendix E, Table E.1.

Table 3.11: Airframe Aeroelastic Data Representation in the DCM$^+$

Set	Variable	Type	vascomp	elaps	pwake	acp	csd	OBJ
Circuit			1	1	2	3	4	5
Sequence			1	2	2	2	2	3
aeo	aeim_i	2	0	0	2	1	0	0
	aere_i	2	0	0	2	1	0	0
	bctrl	2	0	0	3	1	0	0
	bgust	2	0	0	3	1	0	0
	cplgfus	2	0	0	3	1	0	0
	cplgrot	2	0	0	3	1	0	0
	cplffus	2	0	0	3	1	0	0
	cplfrot	2	0	0	3	1	0	0
...	...	...	...	...	...	...	...	...

Input / Output Indicator Values: 0 - not used; 1- input; 2 - output; 3 - input and output

Data Types: 0 - Constant; 1 - Decision V.; 2 - State; 3 - Behavior V.; 4 - Constraint; 5 - Objective Fct.

3.4.2. Automated Integration Tool

It was mentioned in Section 2.2 that the DCM$^+$, in conjunction with the syntax used in the Problem Execution Code, completely defines individual data transfer between Contributing Analyses and scheduling of CA executions. It was concluded that the problem execution, or, in other words, the solution of equation 3.53, could thus be automated. A Resource, the Design and Optimization Coupling Code, DOCC, was developed and programmed in UNIX shell scripts for performing this task. The choice in favor of shell scripts was made due to the combination of a large library of data filtering tools and job control options offered by standard UNIX shells, such as the programming language awk /Aho et al. 88/. With this respect, DOCC bears some similarity to the HiSAIR/Pathfinder system /Dovi et al. 92/; however, the execution order of Contributing Analyses was programmed in the Pathfinder executive control, which is not the case for DOCC. This section contains an overview of the operation of this code. A detailed description of its implementation, including a comparison with FORTRAN hard-coded optimization for a sample case, can be found in Appendix F.

Fig. 3.14. depicts the flow of operations by DOCC's executive. A comparison with equation (3.53) reveals that the structure follows exactly the syntax of the Problem Execution Code. The first level operator, SO, is paralleled by the OPTIMIZER block in Fig. 3.14; ANALYSIS and SENSITIVITY solvers, SA and SD, are represented by the according executive blocks in the DOCC executive. SA contains sequential execution of Circuit iteration solvers, which, in turn, call Contributing Analyses. Equivalently, DOCC's ANALYSIS block has an iteration loop over the Contributing Analyses nested in a loop over all Circuits. The structure of the SENSITIVITY Block reflects the operation of SD in a similar way.

DOCC was written to exploit coarse grain parallel execution capacities in a network of UNIX workstations connected to a common NFS-mounted file system. In this research, seven IBM RS/6000 workstations under AIX 3.2 in the CAE/CAD Laboratory of Georgia Tech's College of Engineering were used. This setup allows parallel execution of tasks, controlled by one machine. The gray shaded areas in Fig. 3.14 indicate parts of the code which are executed in parallel on different host computers. The choice of host computer is based on compatibility with the Contributing Analysis to be started and the load level. With the parallel execution capability, DOCC's executive loop parallels all features of the Problem Execution Code.

The executive software communicates with a central data base containing the DCM$^+$, information about the process status, available host computers, sensitivities, and variable histories via SQL-compatible scripts /SQL 86/. This connection is indicated in Fig. 3.15 by placement of the executive (containing all three blocks mentions above) and other parts of the integration software directly on the data base block. Choosing scripting for automated data base interrogation has advantages with respect to portability, but is a fairly slow process. This is particularly the case for the data base management system used in this research, the Computer Automated Design Data Base (CADDB, /Herendeen and Ludwig 88/). Communication is performed via the Interactive CADDB Environment, ICE, which slows down data transfer significantly. Specifically during execution of the SENSITIVITY block, a large number of drivers may attempt access to the data base at the same time. In order to improve the speed, each Sequence sensitivity driver downloads part of the DCM$^+$ into a separate, temporary data base in the respective host machine's local disk space. These files are then queried by the generating Sequence sensitivity driver.

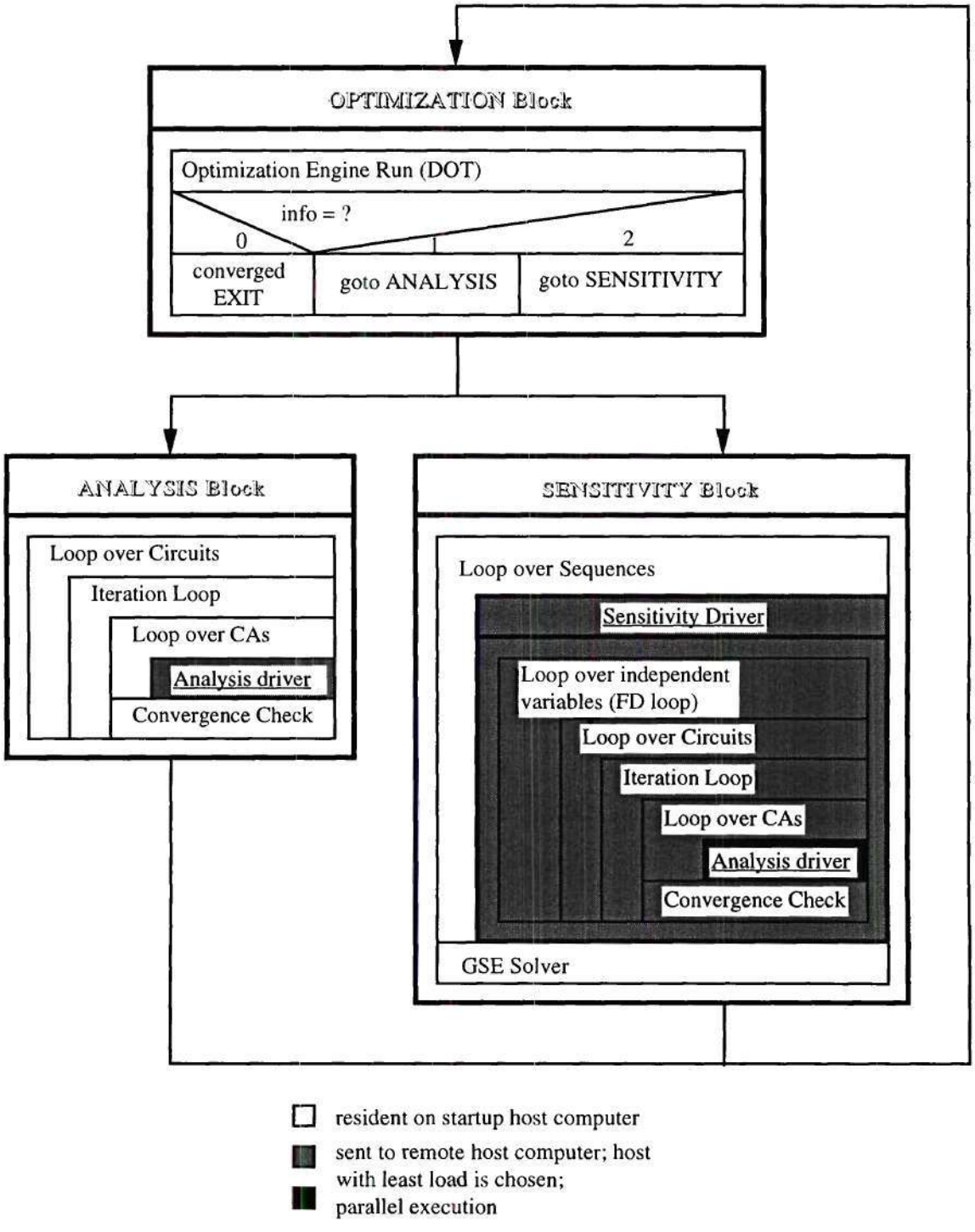

Fig. 3.14: DOCC Executive Control Loop

The executive structure presented is independent of the model problem structure. In DOCC, configuration of the Problem Execution Code as in equation (3.53) is performed by parsing information stored in the DCM^+, as indicated by the small N^2 Diagram and GSE depicted on the data base block. The important detail here is that no reprogramming of the executive loop in Fig. 3.14 is necessary to accommodate a particular Code, but can be accomplished by updating the DCM^+ in the data base. The Problem Execution Code is stored in form of the DCM^+, and DOCC executes a self-configuration based on the information parsed. The ANALYSIS block, for example, obtains the number of Circuits and the Contributing Analyses contained in each Circuit from the second line of the DCM^+ (refer to Table 3.11, for example). The "Analysis Driver" in Fig. 3.14 may then be called for the CA "vascomp." The driver searches the DCM^+ for suitable input by checking the column tagged "vascomp" for Input / Output Indicators of 1. All variables matching this requirement are transferred to "vascomp" for processing. Upon completion of this task, output data are returned to DOCC, and reentered into the DCM^+ by matching the variable "label" (for example aeim_1 in Table 3.11). Similar matching processes are performed in order to download the Sequence-specific temporary data bases.

In addition to parsing operations that determine input and output data for Contributing Analyses, Circuits, and Sequences, the information stored in the DCM^+ is used to reduce the computational effort in Sequence sensitivity analyses by identification of "computational paths" as outlined in Section 2.2. DOCC therefore covers aspects of quasi-procedural programming (/Kroo and Takai 88/), but without the necessity for a separate computational path generator.

As indicated in Fig. 3.15, Contributing Analyses may be added to the framework if the DCM^+ is updated and the proper I/O Filters are provided. Fig. 3.16 is a sketch of the

general form of such a filter, consisting of separate pre- and a postprocessors. This approach eliminates the necessity of modifying Contributing Analysis executables for integration into a Design Simulation Model. According to /Jones et al. 92/, engineers working on the HiSAIR program preferred to have access to these files for data viewing and editing. Within DOCC, programs are executed the very same way they would be run without the framework, that is, input and output files are generated and are accessible for troubleshooting or further analysis. The disciplinary expert is therefore at all times able to assess the performance of his software tool and the progress of the design process from the point of view of the respective discipline by analysis of the complete input and output information in a familiar format.

The "Monitor" in Fig. 3.14 is a user interface which allows observation of a running process, including querying of and process control through the data base. It is a separate utility which may be started from the executive at pre -defined locations in each block, for example after each Contributing Analysis run, or after each completed optimization iteration loop. Using the monitor, execution of a running DOCC case can be paused interactively, and subsequently resumed at the pause position.

Log files are generated by the data base driver, the executive, and the optimizer. The data base log file contains echoes of all data base operations performed during one optimization iteration loop. The executive log file contains time logs of all executive operations, that is block, Circuit, Sequence, Contributing Analysis etc. run start and completion. The optimizer log is the standard DOT output file.

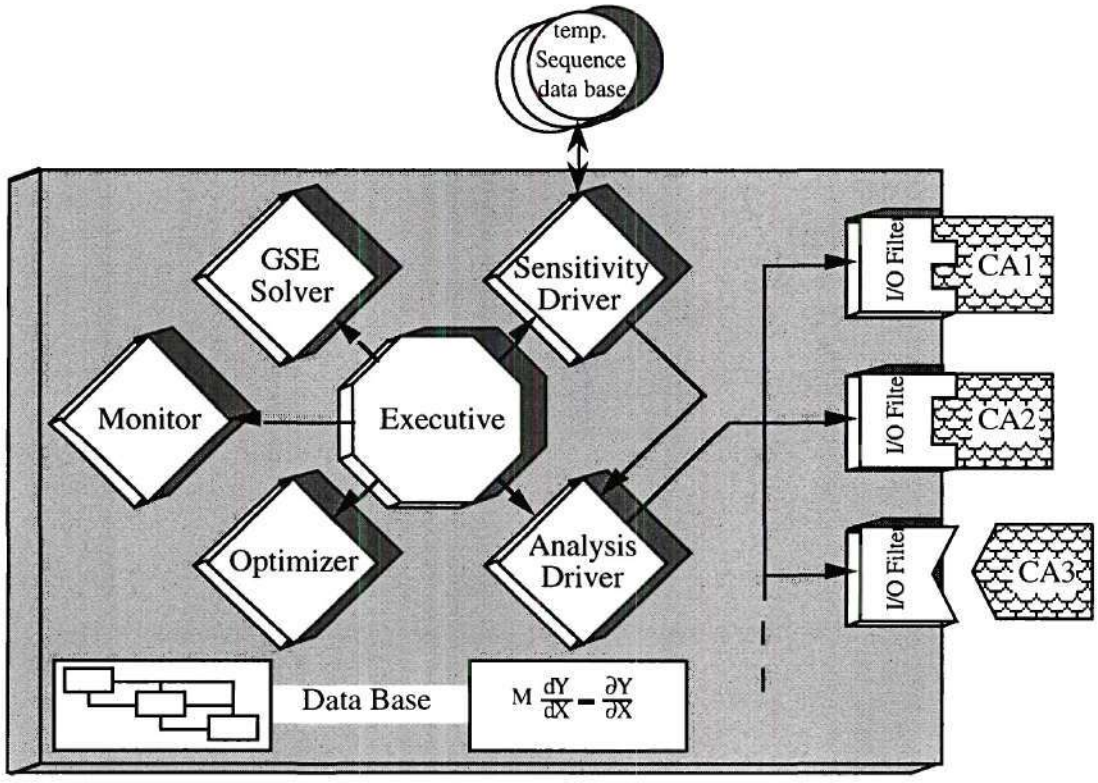

Fig. 3.15: Components of DOCC

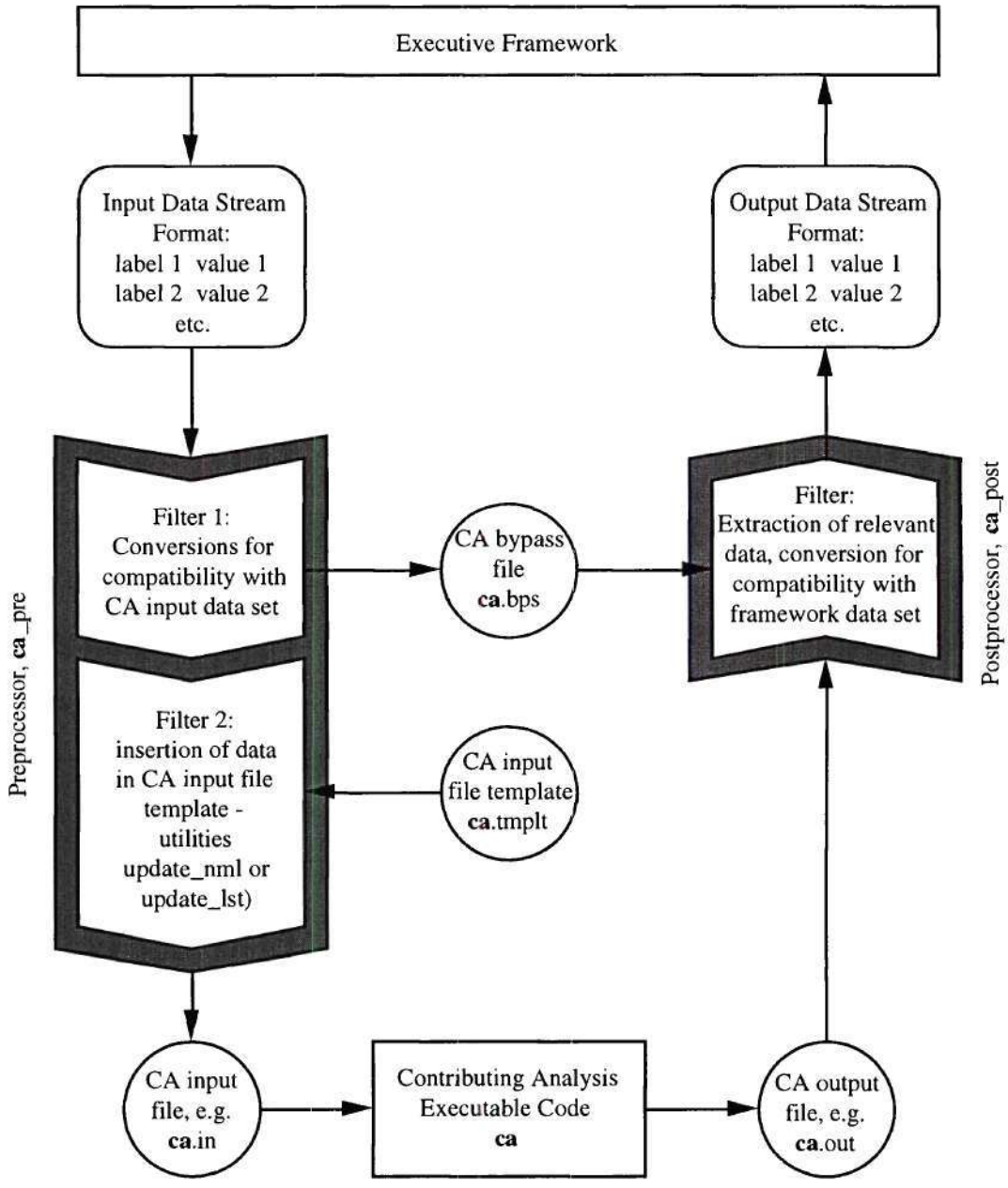

Fig. 3.16: DOCC Input / Output Filter Schematic

CHAPTER IV

TILTROTOR MULTIDISCIPLINARY OPTIMIZATION STUDIES

According to the Problem Definition, Fig. 3.1, effects of the following trades on a PI-optimal tiltrotor design are to be investigated:

(i) conventional rotor system vs. variable diameter design;

(ii) airframe aeroelastic modeling fidelity; and

(iii) passive vs. active aeroelastic stability augmentation.

In order to address these issues, a total of four cases were implemented in DOCC, using three Design Simulation Model accuracies, Fig. 4.1: Conventional and variable diameter tiltrotor designs were compared using the tools "vascomp" and "OBJ" only (i). Since airframe sizing in this model is based on approximate methods internal to VASCOMP, is limited to consideration of geometric and rotor table related constraints, and

was therefore called the "Performance Sizing" model. In order to explore passive means for aircraft stability augmentation by aeroelastic tailoring, a conventional tiltrotor design was generated using the "Performance and Aeroelastic Sizing" model, which includes a complete representation of the aircraft's aeroelastic system (ii). The "Performance and Aeroservoelastic Sizing" model finally incorporates a simple active flutter suppression control system design (iii). Each Design Simulation Model builds upon the previous, lower accuracy model, and adds a set of new Design Variables, Behavior Variables, States, and Constraints which are specific to the Models implemented in added Contributing Analyses.

Initial values for the optimization runs were chosen with reference to previously published data of tiltrotor aircraft designed for the same mission, Table 4.1. The first three designs were obtained by /Schleicher 93/ using an optimization loop included in VASCOMP. The CTR-2000 is the only aircraft with 4-abreast seating, which had been chosen for the present designs. It was therefore selected as the reference configuration, although in its seating layout extra baggage space was located in a 10 ft section around the rotor plane station; this extra section was not included in the current model. All Attribute optimization histories presented in this chapter were normalized by CTR-2000 reference values given in Table 4.1, unless otherwise indicated. No information was available on the wing's internal layout of any of the listed designs, so that initial values for the associated Design Variables were manually adjusted to obtain a wing structure that was feasible with respect to the static load constraint. Attributes are generally referred to by the labels assigned to them; see Appendix E for a glossary of these labels. A complete list of Attributes generated for the designs discussed here is given at the end of this chapter in Table 4.6.

While working with different optimization algorithms it turned out that DOT's Modified Method of Feasible Directions, MMFD, was particularly well suited for guiding an initially unfeasible design towards the feasible region. Once the feasible region was reached, however, very little progress was made in increasing the objective function, PI, and the algorithm converged rapidly to a design very close the location where the feasible region was reached. The Sequential Linear Programming algorithm, SLP, on the other hand, had difficulties reaching the feasible region, but performed excellent inside it. It appeared as if the MMFD's very exact line search attempts to find the next design point in the vicinity of the present one without allowing passing through unfeasible parts of the design space, while the SLP is less selective. As a result, all but one optimization run consisted of an initial pass until convergence in the feasible region using MMFD, and a subsequent restart at this location with SLP (10% move limit).

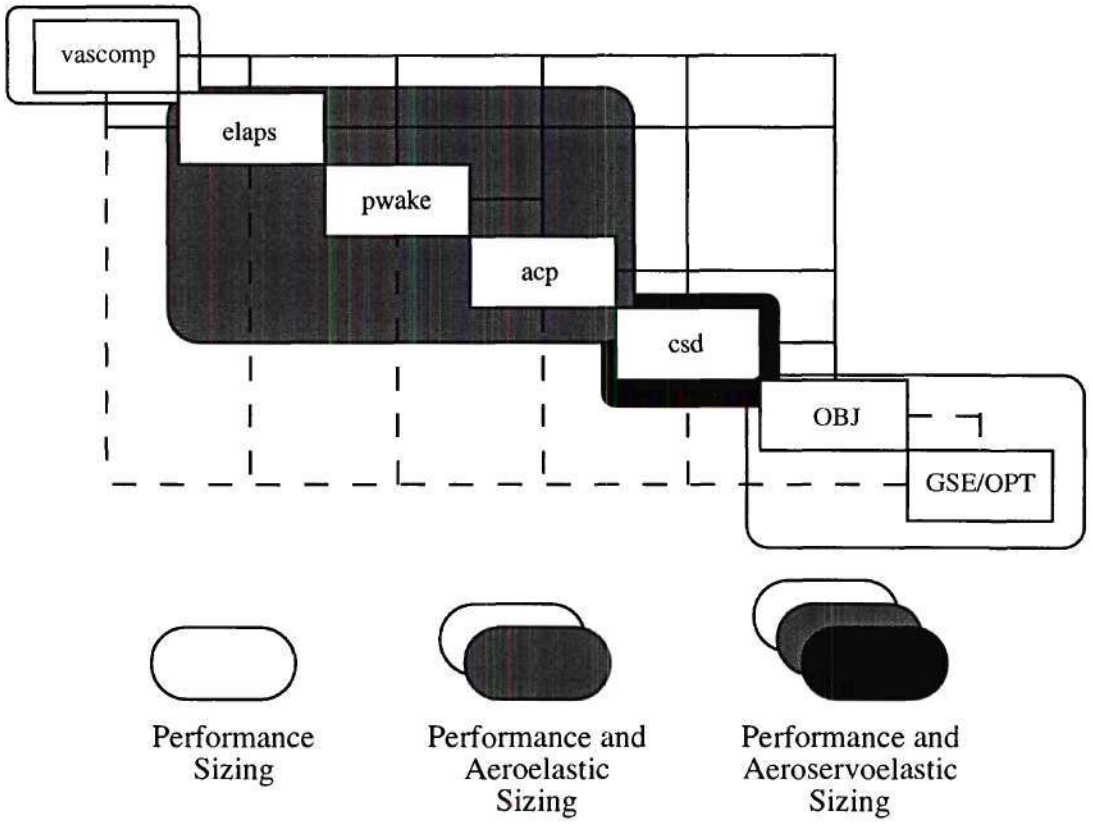

Fig. 4.1: Design Simulation Models

Table 4.1: Baseline Configurations

Attribute*	CTR-22C§ (3 abreast)	NASA CTR (min. GW)§ (3 abreast)	NASA CTR (min. DOC)§ (3 abreast)	**CTR-2000†** **(4 abreast)**
ar	5.5+	6.0	6.0	**6.62**
elpd		(1.35)	(1.35)	**(1.0)**
eltd		(3.0)	(3.0)	**(1.9)**
eten	1.0	1.0	1.0	**1.0**
phi	-6.0°	-6.0°	-6.0°	**-4.0°**
sigma	(0.11)	(0.11)	(0.11)	**0.124**
tau	1.0	1.0	1.0	**1.0**
tovc	0.23	0.24	0.23	**0.20**
vcrs	300 kts at 18,000 ft+	290 kts at 21,400 ft	375 kts at 15,304 ft	**320 kts at 25,000 ft**
vt	790 ft/sec	747 ft/sec	683 ft/sec	**720 ft/sec**
wga	21.0 lb/ft^2	15.4 lb/ft^2	22.8 lb/ft^2	**20.0 lb/ft^2**
wl	124.5 lb/ft^2	89.7 lb/ft^2	133.3 lb/ft^2	**110 lb/ft^2**
xiac				**(0.454)**
xien				**(0.600)**
xirr				**(-0.29)**
xiti				**(0.570)**
wg0	45,578 lb	43,023 lb	45,553 lb	**41,319 lb**
wwstr+wwnst	2,895 lb	2,156 lb		

* refer to Appendix E, Attribute Label Glossary
§ /Schleicher 93/
\+ /Wilkerson and Schneider 88/
† /Lacy and Wilkerson 95/
Values in parentheses were taken from illustrations or are projected

4.1. Performance Sizing

This Design Simulation Model was primarily chosen to verify proper integration of the Tools "vascomp" and "OBJ," which are an integral part of the higher accuracy models. It provided a relatively simple platform for comparative studies between constant and variable diameter-based designs, and allowed direct comparison with previously obtained data using only VASCOMP (/Schleicher 93/). Design Variables included Attributes describing the wing outer shape and size, fuselage geometry, rotor and nacelle location, cruise speed, rotor tip speed, and, to a limited extent, the rotor geometry in the VDTR cases, Table 4.2. Constraints regarding rotor-airframe clearances and center of gravity location were imposed. Additionally, the rotor parameter, c_T/σ, was limited to the maximum value available in VASCOMP's rotor performance tables. Two Circuits and Sequences were chosen: The Contributing Analysis "vascomp" formed Circuit 1 and Sequence 1, and Circuit 2 and Sequence 2 consisted of the Contributing Analysis "OBJ".

Table 4.2: Performance Sizing - Design Variables and Constraints

Design Variables	fuselage/nacelle geometry	elpd, eltd, eten, xien
	conversion axis location	xiti
	rotor geometry (VDTR only)	rbar, sigma
	rotor size, location, etc.	wga, xirr, vt
	wing geometry, size, loc.	ar, phi, tau, tovc, wl, xiac
	cruise speed	vcrs
Constraints	rotor / airframe clearances	cgrc, cgrf, cgrn, cgrwr, cgrwt
	rotor table limit	cctsmax
	static stability	ccgh, ccgs
	control capacity	ccgc

4.1.1. Conventional Rotor System

Distinctly different starting points were chosen for the conventional, fixed diameter rotor design cases in order to explore the structure of the design space: A "low speed" aircraft similar to Schleicher's "minimum gross weight" NASA CTR, Table 4.1; and a "high speed" variant similar to the "minimum DOC" (direct operating cost) design in the same table. Fig. 4.2 shows the objective function histories for both cases; notice the effect of the optimization restart with SLP at iteration 10 in both cases. The "low speed" design converged with a Productivity Index of PI = 74.54 kts, whereas the "high speed" case reached a final value of 76.02 kts. For comparison: Using CTR-2000 weight and performance data from /Lacy and Wilkerson 95/, and the assumption that block speed is equal to cruise speed, this aircraft achieves a slightly higher PI of 77 kts. This assumption is not very realistic, however, since it neglects time spent in taxi, hover, climb and descent. By comparison with the present cases it appears as if block speed on a 600nm mission is approximately 90% of the cruise speed. Under this assumption, the CTR-2000's PI drops to 70 kts. The current results are well within the upper and lower bounds set by these two numbers.

Differences in the convergence behavior are obvious from Fig. 4.2: The "low speed" case produced feasible designs very early, and showed consistent, but small improvements from iteration to iteration. The "high speed" case, on the other hand, exhibits large jumps in the objective function, and passed twice through larger stretches of unfeasible design space. Eventually, it also generated a design with a higher PI. The discussion in the following paragraphs focuses on the interpretation of these observations.

Optimization histories of the most critical constraints are shown in Fig. 4.3 and 4.4. Besides the c_T/σ constraint, cctsmax, the static stability constraints in helicopter mode,

ccgh, and the rotor-nacelle clearance, cgrn, are constantly either active or violated. Since a lot of mass is concentrated in the nacelles, an easy solution for stability problems would be a forward shift of the nacelle center of gravity. This, in turn, might violate the rotor/nacelle clearance constraint. Trade-off between these two constraints is required as the cruise speed, vcrs, is increased in an attempt to improve PI: As the aircraft is resized for a higher cruise speed, horsepower required increases due to increased fuel weight*. As a result, the nacelles grow in size, and extend further towards the rotor disk if the nacelle center of gravity is not moved aft, which again may cause the static stability constraint to be violated. Fig. 4.3 shows that in the "low speed" case, this trade-off was made permanently throughout the optimization as vcrs was increased, Fig. 4.6. The effect is even more apparent through adjustment of the nacelle location, xien, Fig. 4.5, particularly after iteration 10, when the SLP increased vcrs. In the "high speed" case, however, cruise speed and therefore nacelle size are initially high. The associated constraint violation was quickly eliminated by moving the nacelle aft, Fig. 4.5. Since cruise speed experienced only minor reductions (Fig. 4.7), the described trade-off was not necessary until iteration 12, so that more design freedom was retained. Noting the consistent upward trend of the "low speed" case PI up to convergence, it can be speculated that trading off geometric constraints vs. static stability slows down convergence, but that achieving a higher value of PI could be possible. However, starting the optimization at the "high speed" end facilitates convergence. Hence, this approach was followed in all other cases.

---

* In both cases, the critical engine sizing case is the hover OEI (one engine inoperative) condition. Hence, engine size does not grow directly through power required in cruise, but through weight growth as a result of increased fuel flow in cruise.

It is instructive to compare design variable histories, Fig. 4.6 and 4.7, and objective function histories, Fig. 4.3, for identification of the major design drivers. In both cases, the improvement in PI upon restart of the optimization with SLP (iteration 11) coincided with a decrease in the wing taper ratio, tau. It is believed that the reason for this behavior is an associated reduction in induced drag: The effect is much more pronounced for the "high speed case" with its higher wing loading, and is also accompanied by an increase in wing aspect ratio, ar (whereas it decreases in the other case). Both observations support this assertion. Large changes in the wing thickness to chord ratio, tovc, do not appear to be accompanied by correlating PI changes. However, the largest changes of tovc - up or down - coincided with improvements of the objective function. It was concluded that PI is fairly insensitive to tovc itself, but that tovc changes allowed beneficial adjustments of the remaining wing planform design variables. This conclusion is consistent with the well-known trade-off between drag increase and structural weight decrease with increasing wing thickness to chord ratio.

Strong similarities exist between cruise speed, vcrs (final value: 356 kts), disk loading, wga (21.7 / 22.2 lb/ft^2), and tip speed, vt (727 / 735 ft/sec), of the two final designs, and tovc trends indicate that this design variable could also be very similar in both designs, had the optimization been pursued through additional iterations (Fig. 4.6, 4.7). The "low speed" design, however, has approximately 25% less forward sweep, phi, its wing loading is about 20% smaller, and its taper ratio is around 20% higher than that of the "high speed" aircraft. Based on the previous assertion that both designs might converge to a similar objective function value, PI, it was concluded that this design is very sensitive to changes in the former Attributes, but robust to coordinated sweep, aspect ratio, and taper ratio changes.

The planforms of the two designs discussed are depicted in Fig. 4.8, with the outline resembling the CTR-2000's shape. The most obvious differences are the fuselage length (as mentioned in the introductory remarks to this chapter), and the size of the nacelles. It is very likely that the relationship of horsepower installed to nacelle diameter and length in VASCOMP was calibrated against V-22 data. The V-22 aircraft, however, has very large nacelles, in part because of IR suppressors at the engine exhaust. These large nacelles were also added to all designs generated in the course of this research, since no other baseline information was available. It is safe to assume that nacelles on a civil tiltrotor aircraft will be much smaller, similarly to those of the CTR-2000. Since the nacelle size has a significant influence on the aircraft drag, performance improvements from those documented here can be expected. This observation is indicative of a general lack of detailed information about the nacelle size, center of gravity location, and inertial properties. It is desirable to overcome this shortcoming before more detailed studies of civil tiltrotor designs with VASCOMP are begun.

It is furthermore worthwhile to note that both configurations cruise at a speed which is located between the 290 kts and 375 kts of the "minimum gross weight" and "minimum direct operating cost" NASA CTR aircraft designed by /Schleicher 93/ (Fig. 4.8; compare with Table 4.1). This observation indicates that optimization for maximum Productivity Index captures at least part of the operating cost influence, as desired.

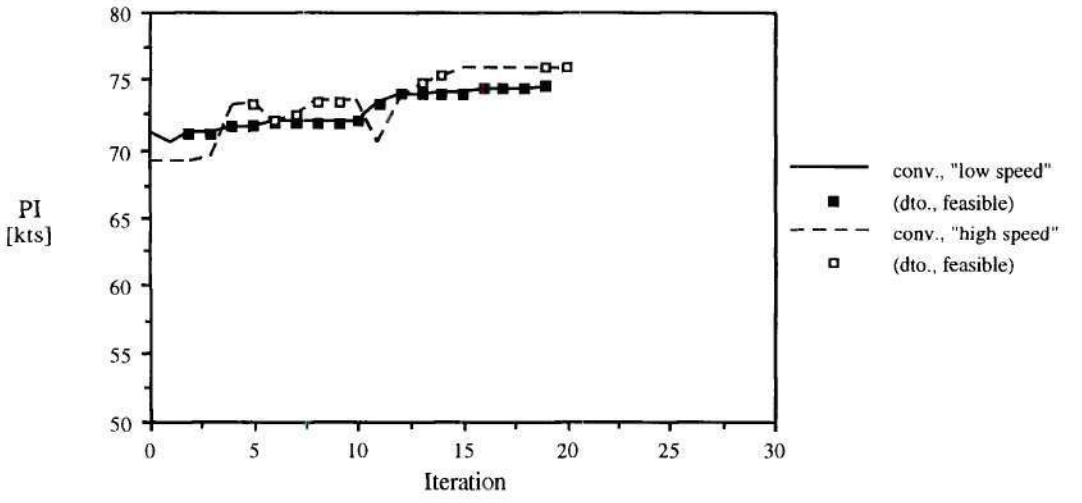

Fig. 4.2: Objective Function Histories, Conventional Rotor Cases

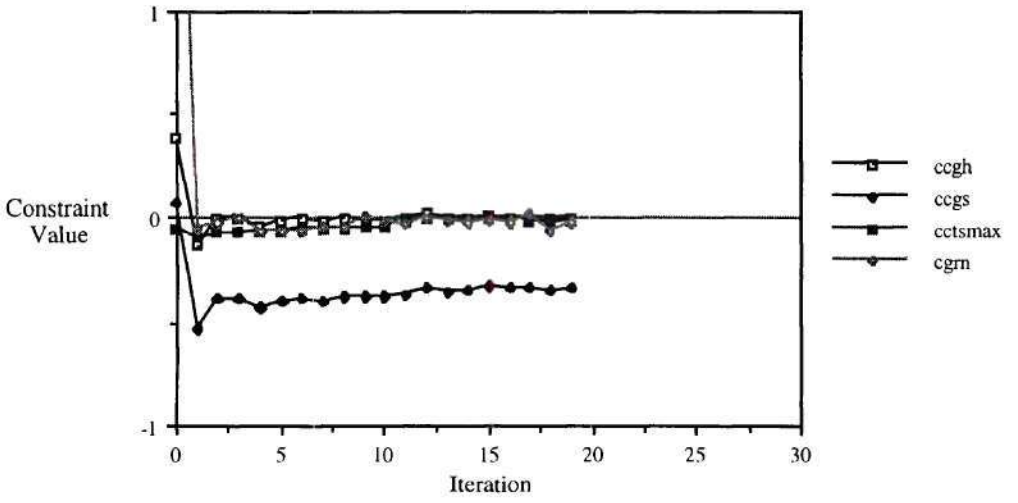

Fig. 4.3: Critical Constraint Histories, Conventional Rotor, "Low Speed" Case

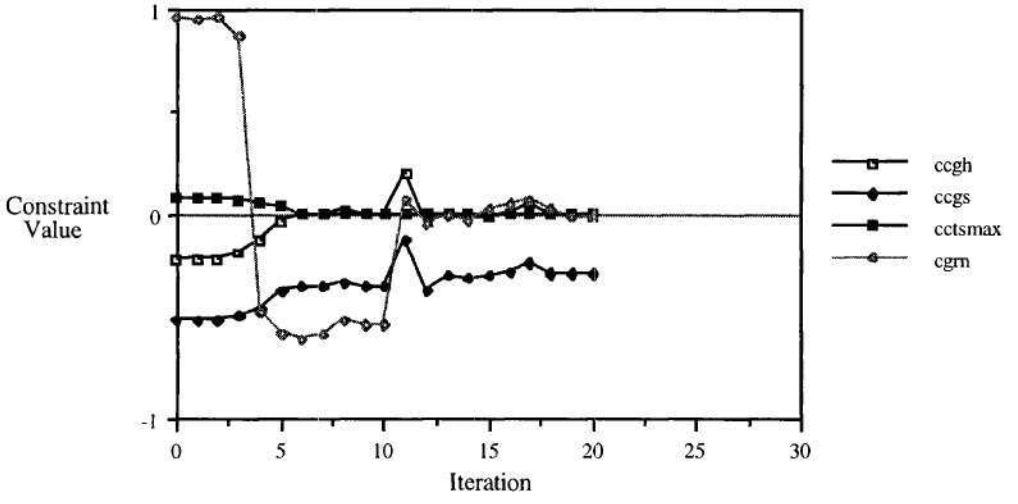

Fig. 4.4: Critical Constraint Histories, Conventional Rotor, "High Speed" Case

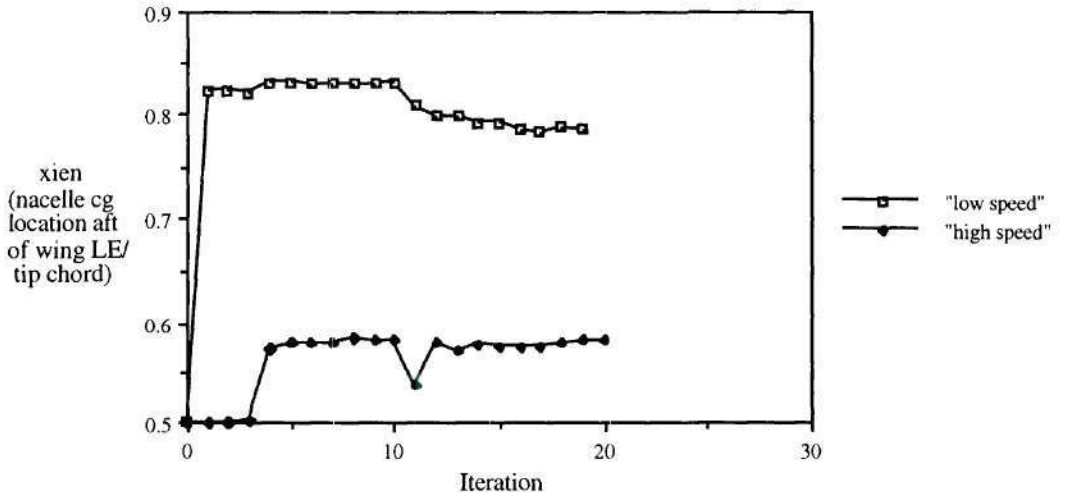

Fig. 4.5 : Nacelle Center of Gravity Location Adjustment

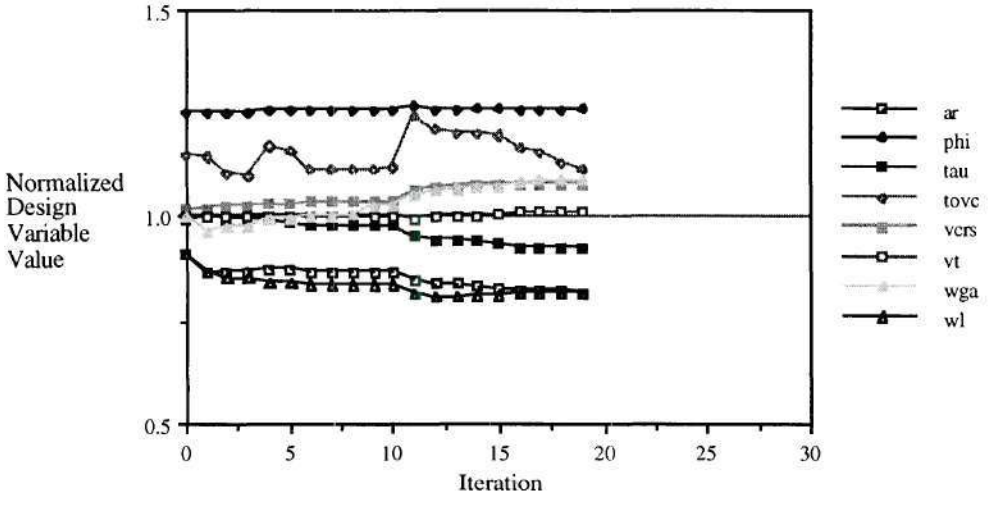

Fig. 4.6: Airframe and Rotor Design Variables, "Low Speed" Case

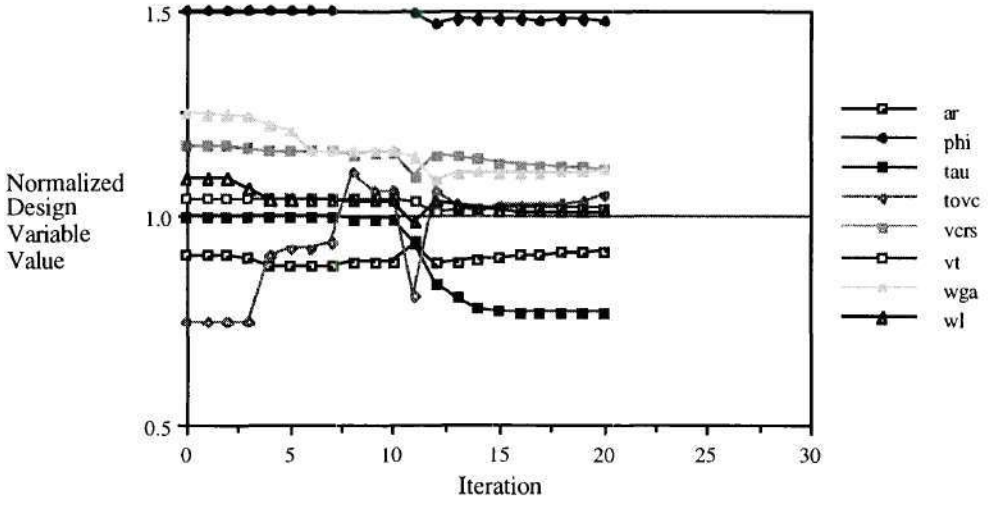

Fig. 4.7: Airframe and Rotor Design Variables, "High Speed" Case

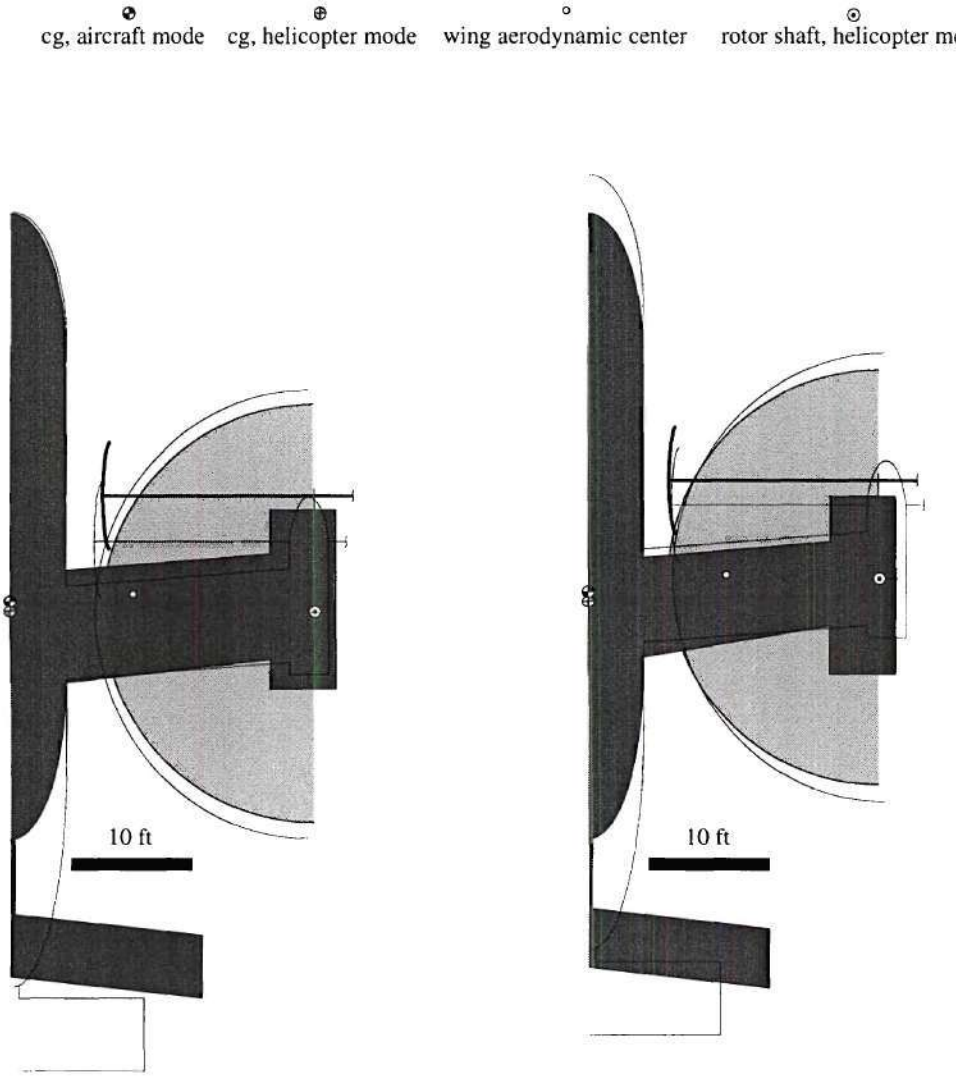

(Outline: CTR-2000)

PI = 74.54 kts	PI = 76.01 kts
WG = 42,341 lb.	WG = 42,536 lb.
vcrs = 345.1 kts	vcrs = 356.5 kts
"low speed"	"high speed"

Fig. 4.8: Planforms, Performance - Sized Configurations with Conventional Rotor System

4.1.2. Variable Diameter Rotor System

Rotor performance considerations suggest that a reduced rotor diameter in cruise and an increased diameter in hover reduce power required in these conditions and eventually improve aircraft performance. Based on this rationale, conventional rotor performance tables were replaced by those for a Variable Diameter Tiltrotor design (VDTR; refer to Appendix A), and rotor weight estimations modified to include 23% retraction mechanism weight increment on a conventional design with the same hover diameter (/Scott 95/). The ratio of cruise to hover rotor diameter, rbar, was added to the list of Design Variables. Trial runs revealed that this Attribute alone does not provide enough design freedom for satisfaction of constraints and objective function increase, so that the rotor solidity, sigma, was also included.

After restart with SLP at iteration 10, the same constraints as in the conventional rotor cases were critical. As shown in Fig. 4.9, the converged VDTR design achieved a Productivity Index of 72.09 kts, which is slightly below those of the conventional rotor designs. Furthermore, rbar was not significantly reduced, but converged to a value of 91.7%. In other words, the final design fits the description of a VDTR aircraft only to a very limited extent. In order to find an explanation for this result, the optimization was repeated with rbar fixed at 66% (as used by /Studebaker and Matuska 93/) and a slightly different set of initial values. After seven SLP iterations and violations of rotor/nacelle, rotor/cockpit, static stability (aircraft), static stability (helicopter), and c_T/σ constraint violations the feasible region was reached, and the optimization converged after 21 iterations with PI = 61.30 kts, more than 15% less than the previous designs.

The rotor weight increment resulting from the VDTR blade retraction mechanism imposes a heavy weight penalty on this configuration (rotor weight accounts for

approximately 9% of a conventional tiltrotor aircraft's gross weight /Schleicher 93/). Since rotor weight is directly related to the rotor hover diameter, it is reduced by increasing the hover disk loading. In order to maintain a feasible c_T/σ, this increase can be compensated for by increasing the rotor hover solidity. Note that in both VDTR cases, sigma was increased significantly before the feasible region was reached (Fig. 4.10, 4.11) and even reached its upper bound in the first case, Fig. 4.10. The design variable sigma, however, stands for the rotor solidity in cruise configuration, that is in the fully retracted blade position. As the blade is extended to the hover configuration, the rotor solidity is reduced (refer to Appendix A). As a result, the closer the extension ratio is to 1.0, the less the drop from cruise to hover solidity. This effect is obviously exploited in the first case (rbar free) in order to achieve satisfaction of the c_T/σ constraint, cctsmax. At the same time, disk loading is increased until sigma reaches its upper bound of sigma = 0.2 in order to reduce the rotor weight further, Fig. 4.10. The resulting configuration can compete with the constant diameter designs in PI (primarily through a 20% cruise speed increase from the "high speed" conventional rotor case, converged design), but is otherwise an unpractical and heavy solution. The PI performance of the VDTR configuration with a fixed extension ratio of 66% on the other hand falls short of that of all conventional designs.

In conclusion: Given the existing rotor performance information from /Studebaker and Matuska 93/ and the constraints imposed on the design through the maximum value of c_T/σ for which data were obtained, a VDTR aircraft cannot compete in PI with conventional tiltrotor configurations due to the large weight penalty resulting from the blade retraction mechanism. Blade retraction would be more feasible if hover performance data were extended to higher c_T/σ. Increasing rotor solidity by adding blades or blade area helps in satisfying cctsmax, but also causes additional weight. Rotor performance deficiencies

compared to the conventional rotor as observed in Appendix A.4 certainly had an amplifying influence on these effects.

Investigation of Design Variable histories in the search for the design drivers reveals similarities to the observations made in the conventional rotor cases: First, the wing thickness to chord ratio, tovc, exhibits initially large oscillations. Second, in both VDTR optimization runs, increases in PI are accompanied by significant reductions in wing taper ratio, tau, and increases in forward wing sweep, phi. The effect is more pronounced in the "rbar free" case (the lower bound for tau is reached), which converges to a wing loading very close to the baseline value of 110 lb/ft^2. In the "rbar = 0.66" case with a converged wing loading of only 100 lb/ft^2, the changes in these Design Variables are much smaller. This observation supports the previously made conclusion that reduction of induced drag is one driver for these design modifications. At cruise speeds of 425 kts (rbar free; M = 0.70 at 25,000 ft) and 405 kts (rbar = 0.66; M = 0.67), compressibility effects are likely to be a contributor to wing sweep increase. The influence can be either direct through drag rise (the airfoils are 17% and 18% thick), or through structural weight growth since the wing design speed (dive speed) increases with cruise speed.

The planforms of the "rbar free" and "rbar = 0.66" designs are compared to the CTR-2000 in Fig. 4.12. High cruise speed in the first case is accompanied by a large forward sweep of the wing, whereas in the second case the large gross weight is expressed in the sheer size of the aircraft's wing. For these two high-powered aircraft (10,133 and 13,267 hp/engine, respectively, compared to 7,290 hp/engine for the CTR-2000 baseline) the oversized nacelles are even more obvious than in the conventional rotor cases (Fig. 4.8).

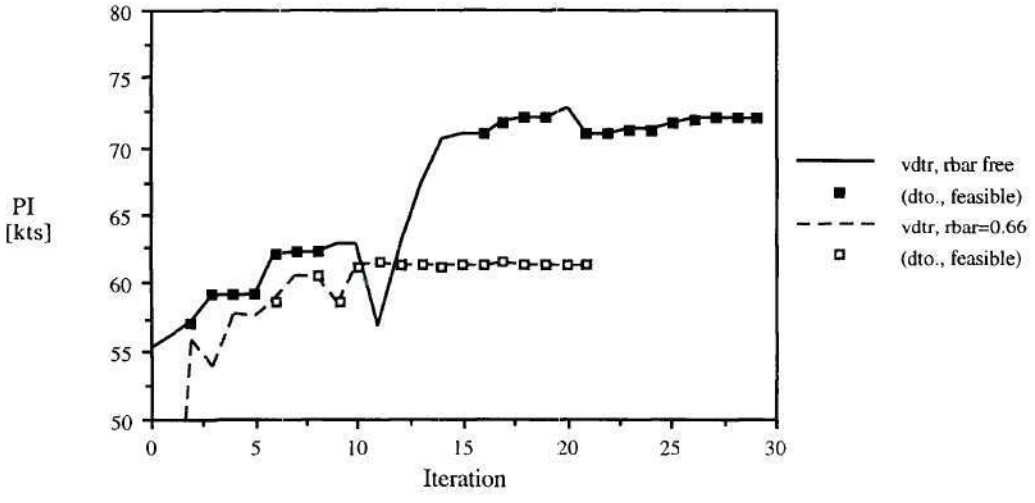

Fig. 4.9: Objective Function Histories, VDTR Cases

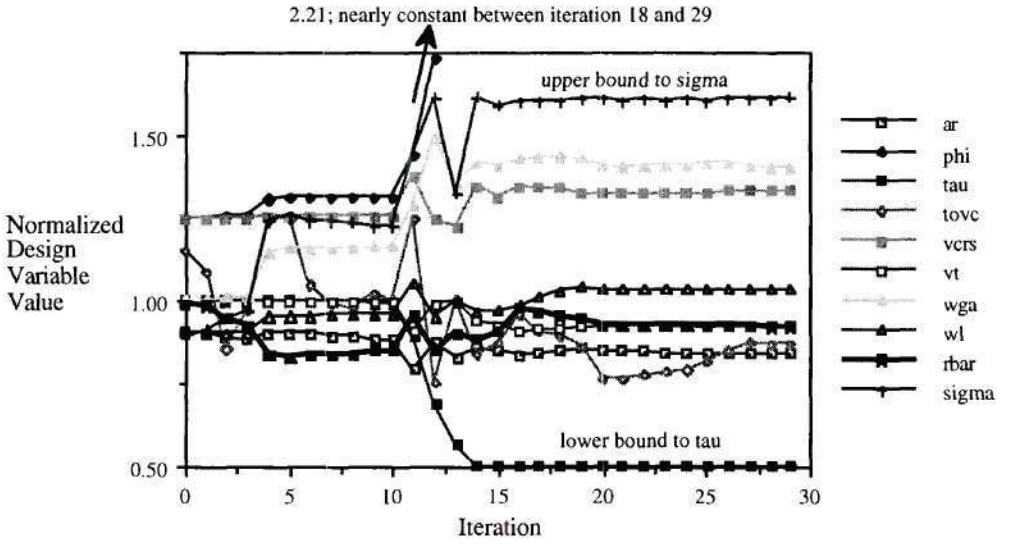

Fig. 4.10: Airframe and Rotor Design Variables, VDTR, rbar free

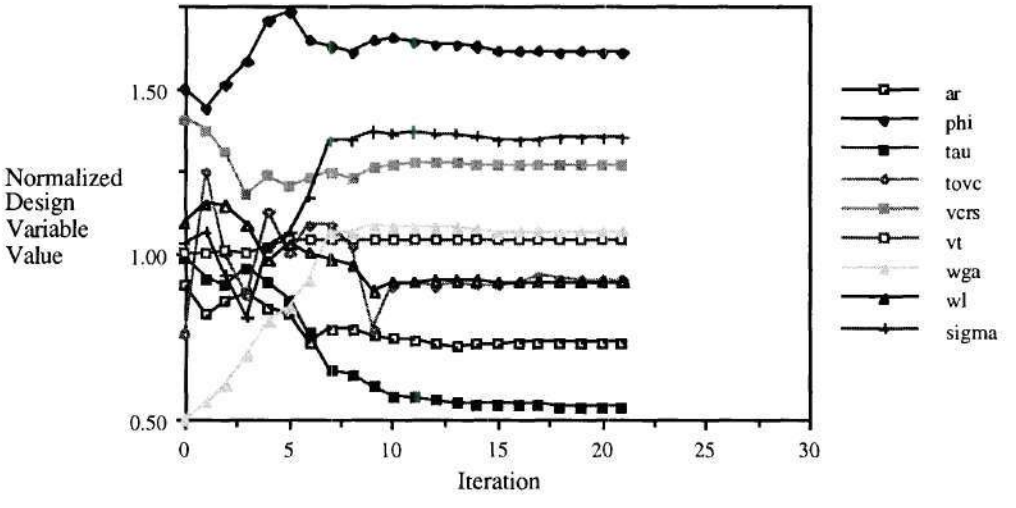

Fig. 4.11: Airframe and Rotor Design Variables, VDTR, rbar = 0.66

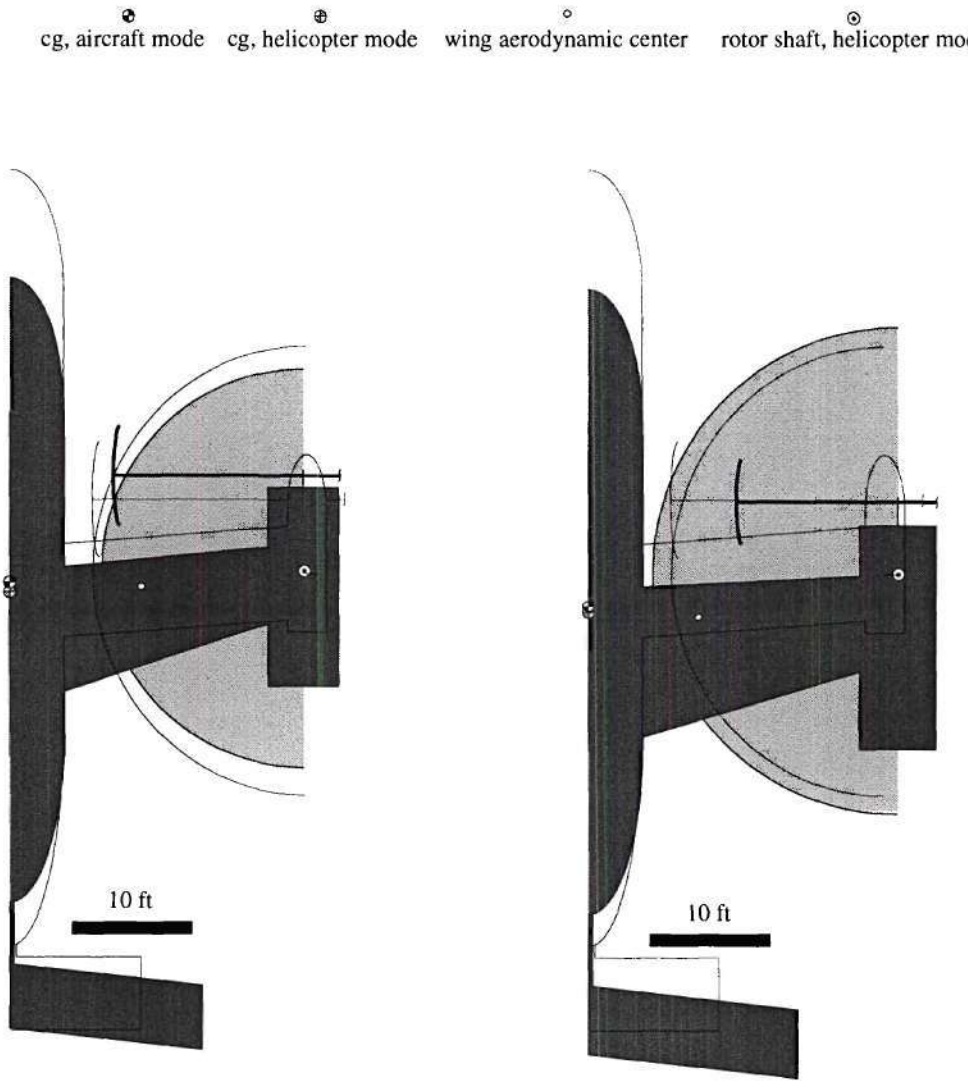

(Outline: CTR-2000)

PI = 72.09 kts	PI = 61.29 kts
WG = 49,455 lb.	WG = 55,819 lb.
vcrs = 425.3 kts	vcrs = 405.2 kts
"rbar free"	"rbar = 0.66"

Fig. 4.12: Planforms, Performance - Sized Configurations with Variable Diameter Rotor System

4.2. Performance and Aeroelastic Sizing

Building on the Design Simulation Model described in the previous section, the Tools "elaps," "pwake," and "acp" were added in order to allow tailoring of inner wing structure and rotor (Table 4.3). Integrity of the wing structure in a 2g jump take-off condition was checked. The dynamic plant model of the tiltrotor aircraft in free-free configuration including symmetric elastic modes of the wing structure (with a rigid fuselage representation), unsteady wing aerodynamics, fuselage and horizontal tail quasi-steady aerodynamics, and rigid-blade aeroelastic rotor modes was generated, and the aeroelastic stability of the aircraft evaluated. The wing was assumed to be filled with mission and reserve fuel in both cases.

The Design Simulation Model features four Circuits and three Sequences. Fig. 4.1 shows an iteration loop between "vascomp" and "elaps," so that these two Contributing Analyses were grouped in Circuit 1. No further feedbacks are present, so that the remaining CAs form separate Circuits. Based on the experiences made with the DOCC sample case (refer to Appendix F), Circuit 1 was opened for the sensitivity analysis: "vascomp" was assigned to Sequence 1. All CAs for aeroelastic modeling were grouped in Sequence 2. "OBJ" finally is the only CA in Sequence 3. A total of 39 Design Variables, 67 States, and 35 Behavior Variables, excluding 11 Constraints, were considered.

Fig. 4.13 shows the objective function history for this case. The MMFD converged after 6 iterations with a feasible, but not competitive design. Except for adjustments made in the first two iteration (before the feasible region was reached), changes in objective function, constraints, and design variables were very small. After restart with SLP, PI improved rapidly and reached a value of 73.64 kts in iteration 17, which is approximately 1.2% below the final value from the "low speed" case using the

Table 4.3: Aeroelastic Sizing - Design Variables and Constraints

Design Variables	wing shear web thicknesses	trib, twlr, twlt, twtr, twtt
	wing skin thicknesses	tpm0t, tpm0t, tp45r, tp45t, tm45r,tm45t,tpm90r,tpm90t
	wing spar cap areas	aclr, aclt, actr, actt
	rotor configuration	beta0, ctrph, delta3, phi0
	rotor dynamics	omefl, omelg, omegim
Constraints	structural integrity (static)	csjt
	aeroelastic stability	coldmp

performance sizing model. Following the development of the constraint values (Fig. 4.14) as the optimization continued and optimization step length was reduced to less than 0.5%, it appeared as if the algorithm had passed through a promising region of the design space into the unfeasible subspace, and would not be able to recover generated constraint violations. The optimization iteration was therefore manually stopped after 18 iterations, and restarted with SLP and an initial move limit of 5%. Seven unfeasible designs were produced before the feasible region was reached again at PI = 71.71 kts. The process was stopped after iteration 28 since the move limits had dropped to 0.31%. The final value of PI for this feasible design was 71.96 kts. Effectively, this optimization run did not generate one design, but a set of feasible alternatives close to local optima.

In the performance sizing cases, the design was driven by PI maximization and the trade-off between geometric and center of gravity location constraints. When detailed modeling of the wing structure and aircraft dynamics are included as in the present case, the associated constraints on structural integrity, csjt, and minimum aeroelastic damping, coldmp, play an additional, important role. As a result, objective function increase and

constraint satisfaction is a more difficult task for the optimization algorithm. The MMFD was very effective in eliminating large initial violations of damping, coldmp, static stability (helicopter), ccgh, and nacelle clearance constraints, cgrn (Fig. 4.14). In these first 6 iterations, a configuration was produced which did not perform very well - PI did not exceed 62 kts. The internal wing structure remained nearly untouched (Fig. 4.15 and 4.16), as wing aspect ratio, ar, and taper ratio, tau, were increased (Fig. 4.17), keeping the wing weight nearly constant (Fig. 4.19). Significant Design Variable changes were limited to a large reduction in cruise speed (vcrs, Fig. 4.17), and an increase in the rotor blade root out-of-plane stiffness at 0° pitch, as signified by the increased nondimensional target frequency, omefl, in Fig. 4.20 (changes in pitch-flap coupling, delta3, control phasing, ctrph, and rotor precone angle, beta0 from their baseline values of 15°, 5°, and 2.5° were barely detectable; these Design Variables were therefore not plotted).

In summary: The MMFD exploited the most powerful means for both increasing damping and eliminating nacelle size and location related constraint violations, which was found in reducing the cruise speed (refer to the previous section regarding the effect on geometric and c.g. location constraints). The result was a feasible, but not competitive design.

Accepting unfeasible solutions appeared to be the key to design improvement, however: PI increased by more than 15% in the first three iterations after the optimization was restarted with SLP and 10% move limits, Fig. 4.13. At the same time, all constraints became either active or violated, Fig. 4.14, as the cruise speed was increased (Fig. 4.17), effectively reversing the trend initiated by MMFD. Simultaneously, a significant drop in wing structural weight can be detected (Fig. 4.19), which is attributed to 15-20% skin thickness reductions in the 0° (Fig. 4.15), 90°, and +/- 45° plies and spar cap areas (Fig.

4.16). PI increase can therefore be related to the combination of speed increase and weight reduction.

Fig. 4.16 shows clearly that wing weight decrease was not the result of indiscriminately weakening of the structure, but of combined material reduction and redistribution. In order to compensate for excessive structural load levels in iteration 8 and 9, the leading edge spar web (twlr, twlt in Fig. 4.16) was strengthened at the expense of the trailing edge member (twtr, twtt). Material was also transferred from the wing tip to the root (last letter "t" and "r" in the Attribute labels in Fig. 4.16; also indicated by outlined vs. solid symbols, respectively). This general tendency was maintained throughout the following iterations. The trend correlates with an increase in wing forward sweep, Fig. 4.18. The following considerations serve as an explanation: The conversion axis location with respect to the wing leading edge was nearly unchanged at about 50% of the aerodynamic chord through all iterations (Fig. 4.21). The structural trailing edge is located at 55% of the aerodynamic chord, so that one would expect strengthening of the trailing edge region. The leading edge spar, however, is located at 5% of the aerodynamic chord, where the airfoil thickness is only approximately 50% of the trailing edge value. In order to accommodate the same shear force, the leading edge web must be thicker. As forward sweep is increased, more shear must be carried by the leading edge region. The observation is therefore consistent with strength considerations.

Beginning at iteration 10, the opposite trend can be observed for the spar cap areas, Fig. 4. 14: Material was moved from the leading edge (aclr, aclt) to the trailing edge (actr, actt). In both cases, the root is strengthened vs. the tip region, as in the case of the spar webs. The initiation of this trend coincided with the beginning of large fluctuations in the aeroelastic damping constraint, coldmp (Fig. 4.14), including significant violations of this constraint at iterations 10, 12, and 15, which are marked in Fig. 4.14-4.21. The first of

these violations (iteration 10) also occurred when the 0° ply orientation skin thickness (Fig. 4.15), and equivalently the wing weight (Fig. 4.19) reached a minimum along the optimization time line, and when reduction of +45° and -45° ply orientation skin thicknesses was stopped (Fig. 4.16). At this point of the tailoring process, the wing material had been reduced so much that both the structural integrity and the aeroelastic damping constraints were violated. Strengthening the trailing edge spar caps appears to have offered the most weight efficient means for compensation. Initial increases in wing weight due to this process (iteration 11, Fig. 4.19), were reduced in following steps by simultaneously reducing the leading edge spar cap areas.

The amplitude of the aeroelastic constraint changes between iterations 9 and 13 is remarkable. The rotor dynamics Design Variables were nearly constant (Fig. 4.20), modifications in the internal structure very small (Fig. 4.15, 4.16), and wing shape and size, rotor size, and speed changes moderate (Fig. 4.17). However, it is noticeable that trend changes in several of the latter Design Variables and the wing forward sweep, phi (Fig. 4.18), preceded both fluctuations. The following interpretation was made: The wing planform parameters were changed at a feasible point in the design space in order to increase the objective function. Given this new direction, the experience that the SLP always moves by a finite, non-zero step, and the observation that aeroelastic stability is very sensitive to small design modifications in this region of the design space, the design invariable violated this constraint in the next iteration. The design now being infeasible, the primary objective became constraint violation reduction, which was accomplished by modifying the wing's inner structure. The feasible region was reached again, and the process began again. This oscillatory behavior was interpreted as being indicative of a "multi-level" type process in this non-hierarchic optimization strategy. "Top level" (wing planform and size) changes for maximization of PI resulted in "lower level" constraint

violations, which were compensated using the "lower level" (wing internal structure) Design Variables. This interpretation suggests that a multilevel optimization procedure is definitely applicable, and might in fact be better suited for this particular problem.

Frequency and damping of the least damped system eigenvalues are plotted in Fig. 4.22. Instability is caused by the highest frequency mode, "B,"of the system, which is not intuitive. The composition of the coupled system eigenvalues for the design in iteration 19 (at a limit speed of 496 kts) is described in Fig. 4.23. Since inplane and out-of-plane blade deflections are highly coupled (refer to Appendix D), cyclic rotor modes are referred to by the ratio of flapping to lead/lag contributions in their mode shapes. Notice that the basic wing mode "wing1" is unstable without the rotor influence, but benefits from being surrounded by highly damped rotor modes in the coupled system. The coupled mode "A" is therefore not likely to be destabilized. Mode "B,"however, is located in the vicinity of the progressing "1 : 1" rotor mode (at 19.9 Hz and 12.59 Hz, respectively), which exhibits the lowest damping of all rotor modes (1.3 %), and can therefore clearly be identified as the source of instability. The fourth wing mode, "wing4,"is much closer in frequency to this rotor eigenform (10.58 Hz or 1.71/rev in vacuum). This mode, however, exhibits negligible wing tip rotations in pitch and yaw (it resembles the first out-of-plane bending mode of the wing, Fig. 4.24). Cyclic rotor modes are characterized by rotor disk tilt in pitch and yaw and rotor inplane center of gravity shifts; "wing4" is therefore kinematically incompatible with these modes. Decoupling of chordwise, beamwise, and rotational degrees of freedom at the wing tip is also a good indication for successful tailoring of the structure.

The second phase of the optimization resulted in significant tailoring of the wing structure. These modifications were triggered by both structural integrity and aeroelastic constraint violations. They allowed an increased cruise speed, which eventually resulted in

a Productivity Index which is comparable in value to those obtained with "Performance-Sizing" only. Note that Design Variables describing the planform and size of the aircraft converge to within +/- 5% of the CTR-2000 baseline values (Fig. 4.17). Significant differences are only detectable for cruise speed (+13%, vcrs in Fig. 4.17) and wing sweep (+63%, Fig. 4.18). A remarkable difference to the "Performance Sizing" cases can be detected in the taper ratio tendency: Instead of consistently increasing, the trend goes towards an almost untapered wing (tau, Fig. 4.17). It is assumed in the higher accuracy model wing torsional stiffness requirements were detected, which were not modeled in the other cases.

In order to test the "shallowness" of the design space in the vicinity of this configuration, the SLP was restarted with initial 10% move limits. An interesting feature of this phase is the reduction of taper ratio, tau, and wing loading, wl, with a simultaneous increase in disk loading, wga, and cruise speed, vcrs (Fig. 4.17). These changes increased the levels of several constraints (Fig. 4.14). In compensation for these constraint violations, the algorithm drove the design back to the vicinity of its starting point, but obviously to a different local optimum. The final configuration cruised at reduced speed, featured a larger aspect ratio, and increased thickness-to-chord ratio (Fig. 4.17). Further wing weight reductions were achieved (Fig. 4.19) while ensuring aeroelastic stability, coldmp (Fig. 4.14). It appears as if this weakening of the structure was made possible through tuning of the rotor's natural frequencies (Fig. 4.20). The overall result was a 2.3% reduction in PI compared to the value achieved in iteration 17 (71.96 kts vs. 73.64 kts). This particular area of the design space obviously contains more than one local optimum with competitive PI values above 70 kts.

A primary reason for including a complete dynamic model of the aircraft in the design process was investigation of the influence of modeling accuracy on the

configurations generated. Of particular interest with this respect is the performance of VASCOMP's wing weight estimation in comparison with the weight calculated by the structural analysis ELAPS. A one-to-one comparison between the two models is virtually impossible due to conceptual differences: In VASCOMP's method (/Schmidt and Dyess 90/) the beamwise, chordwise, and torsional natural frequencies of a cantilevered wing are placed according to empirical data in order to achieve aeroelastic stability. In the present tailoring approach, no constraints are imposed on structural natural frequencies of a free-free configuration, but frequencies and mode shapes are adjusted if the system is unstable. A comparison can therefore be only qualitative. Two configurations which exhibited a maximum of similarity were chosen for closer investigation.

The "low speed" design from the "Performance Sizing" Design Simulation Model and the final configuration using the "Performance and Aeroelastic Sizing" Model were very similar in gross weight and cruise speed, Table 4.4. Coincidentally, the first natural frequencies of the two systems were not far apart from each other. However, the free-free system's degrees of freedom were highly coupled, and even their dominating components did not match the assigned modes of VASCOMP. In terms of mode shape tailoring and frequency tuning, it is evident that VASCOMP's method could possibly generate one feasible wing design, but other feasible, very different configurations are possible through the more detailed methods demonstrated here.

The wing designed using the higher fidelity model was smaller, thinner, and more stretched, which resulted in reduced drag, indicated by a 3% fuel weight reduction. However, the total wing weight exceeded the other configuration's value by more than 500 lb. In fact, the difference in PI between the two aircraft can be almost exclusively attributed to the deviation in wing weight. In order to compare weight data directly, VASCOMP was rerun for the configuration from iteration 28, but with the internal wing weight estimation

selected. The resulting weights are printed in italics in Table 4.4, and do not indicate major differences to the originally obtained data. This finding supports the validity of the weight estimation procedure. Equivalent information for the "low speed" case was estimated based on non-structural weight increments (flaps, fittings, non-load carrying structural weight) as taken from the source code, and pertinent configurational data. These weights (shown in parentheses) were significantly lower. The question arose why this local optimum was not found in the "Performance and Aeroelastic Sizing" process, apart from the well-known fact that no search algorithm guarantees detection of the global optimum. Assuming that VASCOMP's wing weight estimation produces a feasible design, it is believed that matching its dynamic characteristics is not possible with the free-free aircraft model used, as indicated by the differences in natural frequencies and mode shapes indicated in Table 4.4. It was finally concluded that the assumption of a fixed wing root is non-conservative, and has the potential of generating too optimistic designs which may not exhibit the desired stability characteristics in the more realistic free-free configuration.

The planforms of two feasible designs from the second and third phase of the optimization run, respectively, are compared to the CTR-2000 in Fig. 4.25. Note that both aircraft resemble the baseline much more closely than all "Performance Sizing" designs. First, wing and rotor size show better correlation. Second, the designed aircraft's wings have a taper ratio very close to 1.0, unlike the "Performance Sizing" tiltrotors, as previously mentioned in this section.

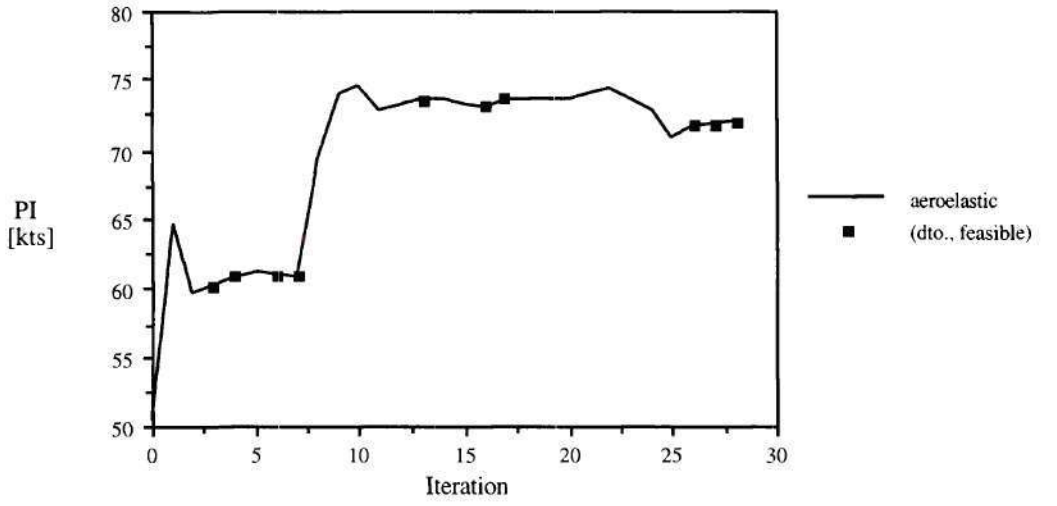

Fig. 4.13: Objective Function History, Performance and Aeroelastic Sizing

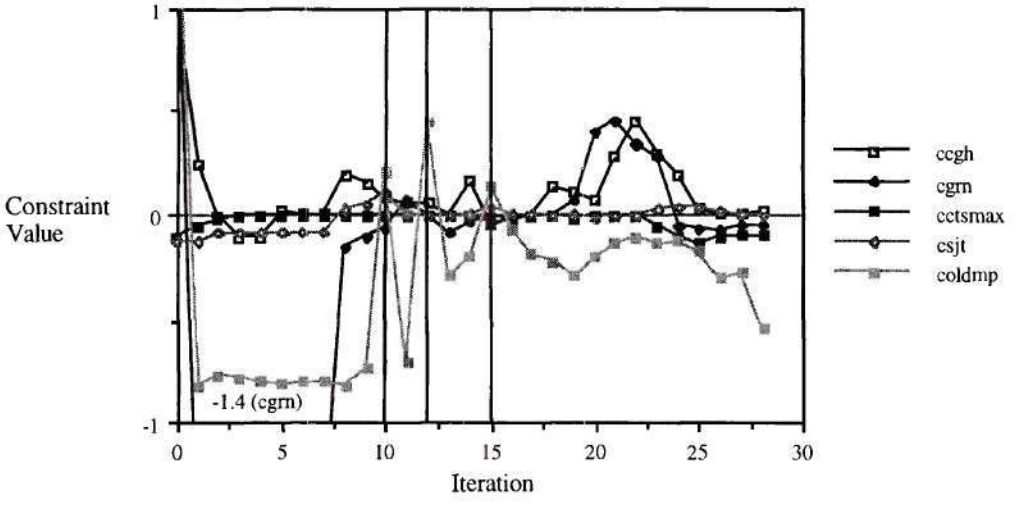

Fig. 4.14: Critical Constraint Histories, Performance and Aeroelastic Sizing

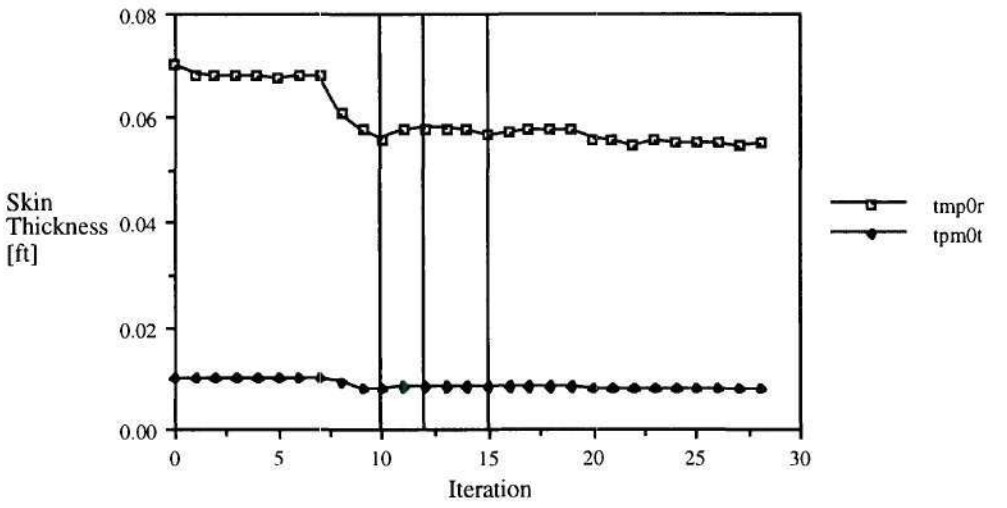

Fig. 4.15: Skin Thickness Histories, 0° Ply Orientation,

Performance and Aeroelastic Sizing

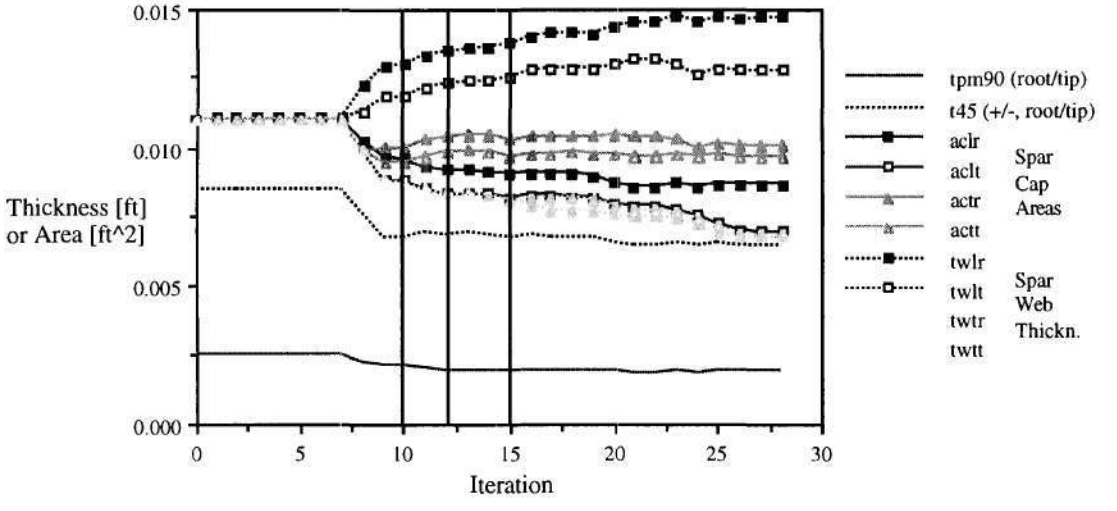

Fig. 4.16: Structural Design Variable Histories, Performance and Aeroelastic Sizing

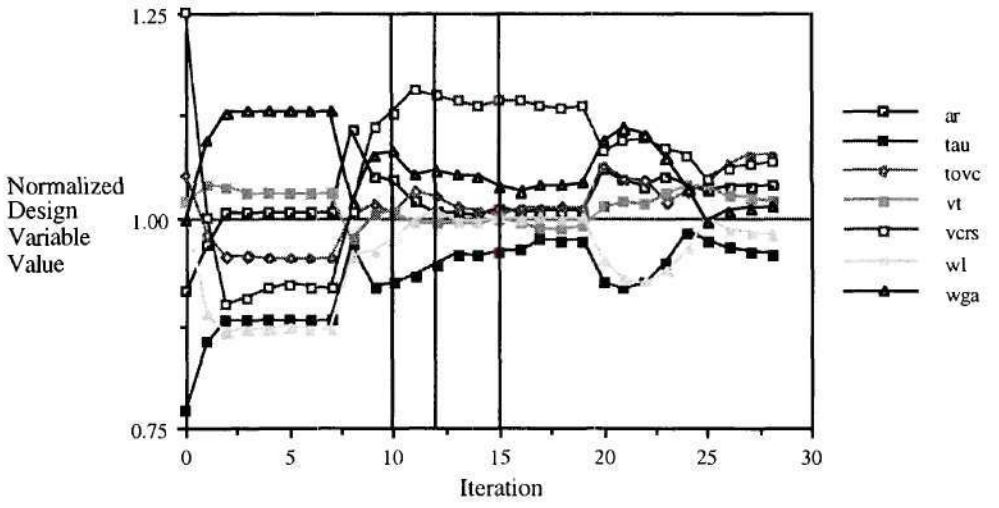

Fig. 4.17: Airframe and Rotor Design Variable Histories,

Performance and Aeroelastic Sizing

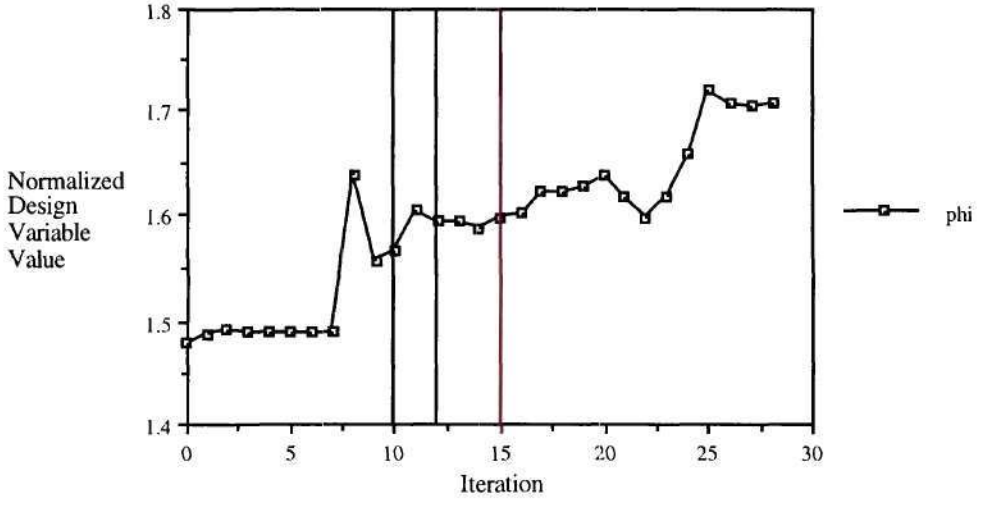

Fig. 4.18: Wing Forward Sweep History, Performance and Aeroelastic Sizing

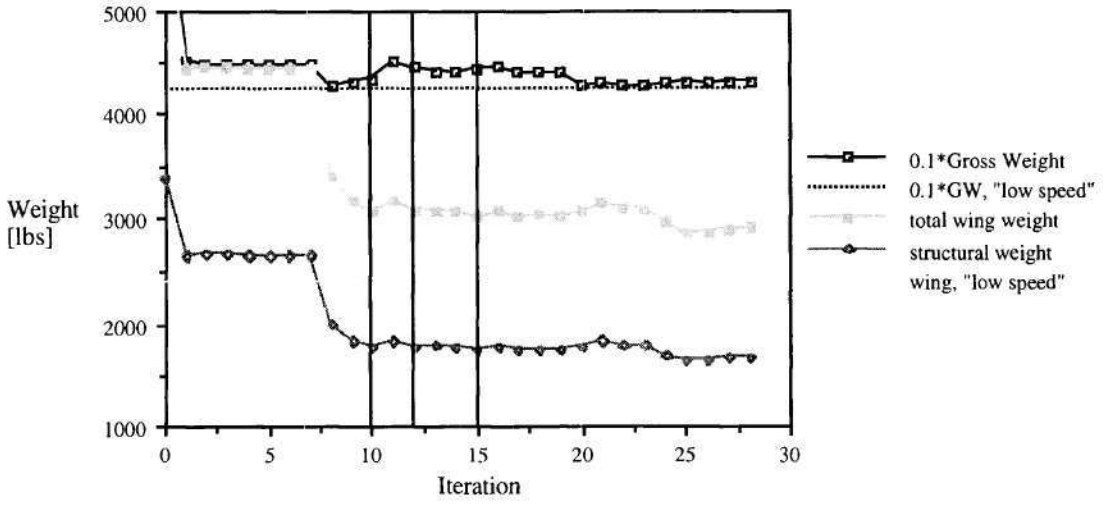

Fig. 4.19: Weight Histories, Performance and Aeroelastic Sizing

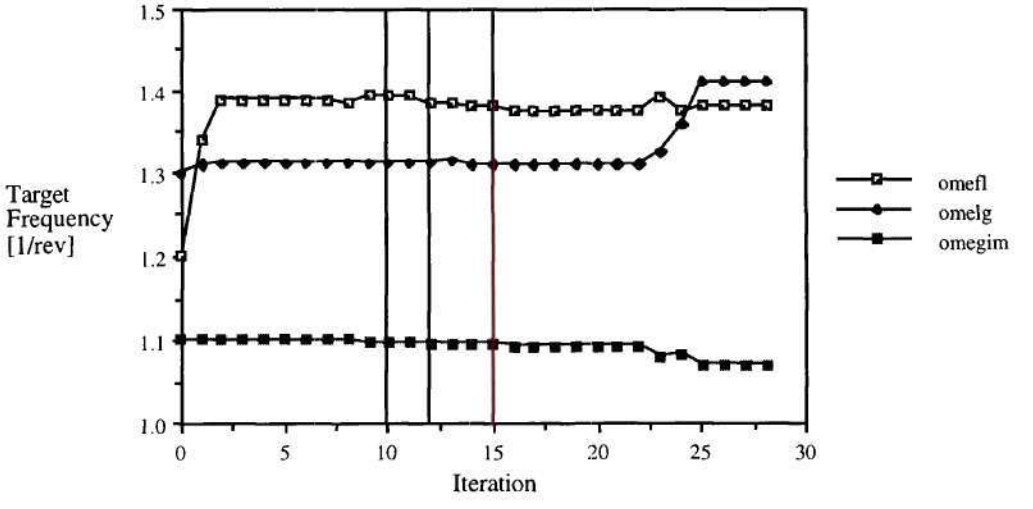

Fig. 4.20: Rotor Dynamics Design Variables, Performance and Aeroelastic Sizing

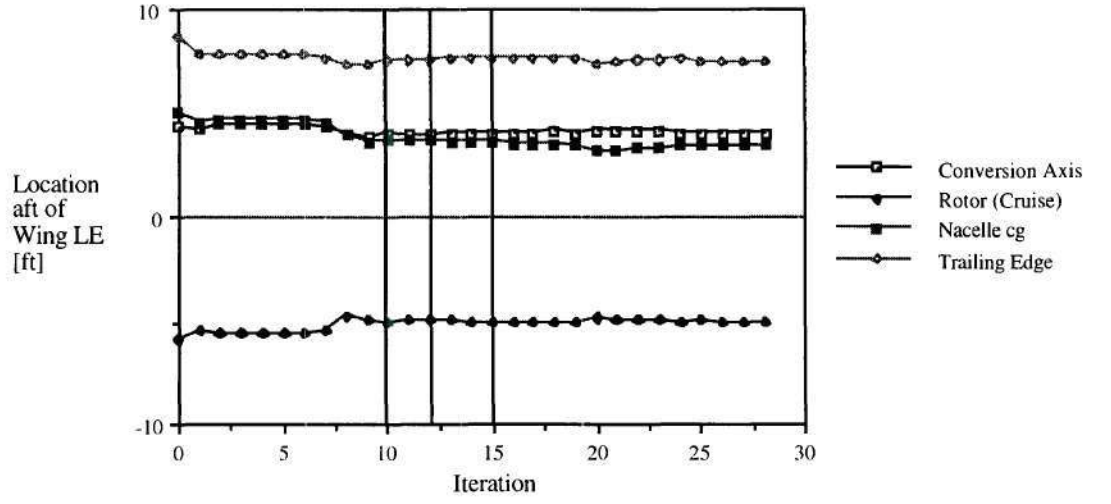

Fig. 4.21: Rotor and Nacelle Location Histories, Performance and Aeroelastic Sizing

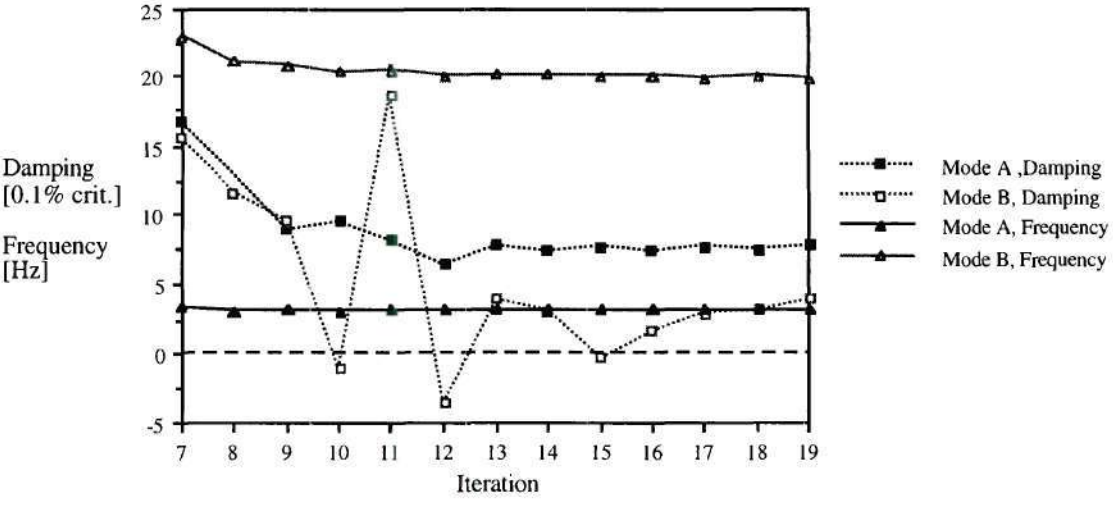

Fig. 4.22: Critical Aeroelastic Modes

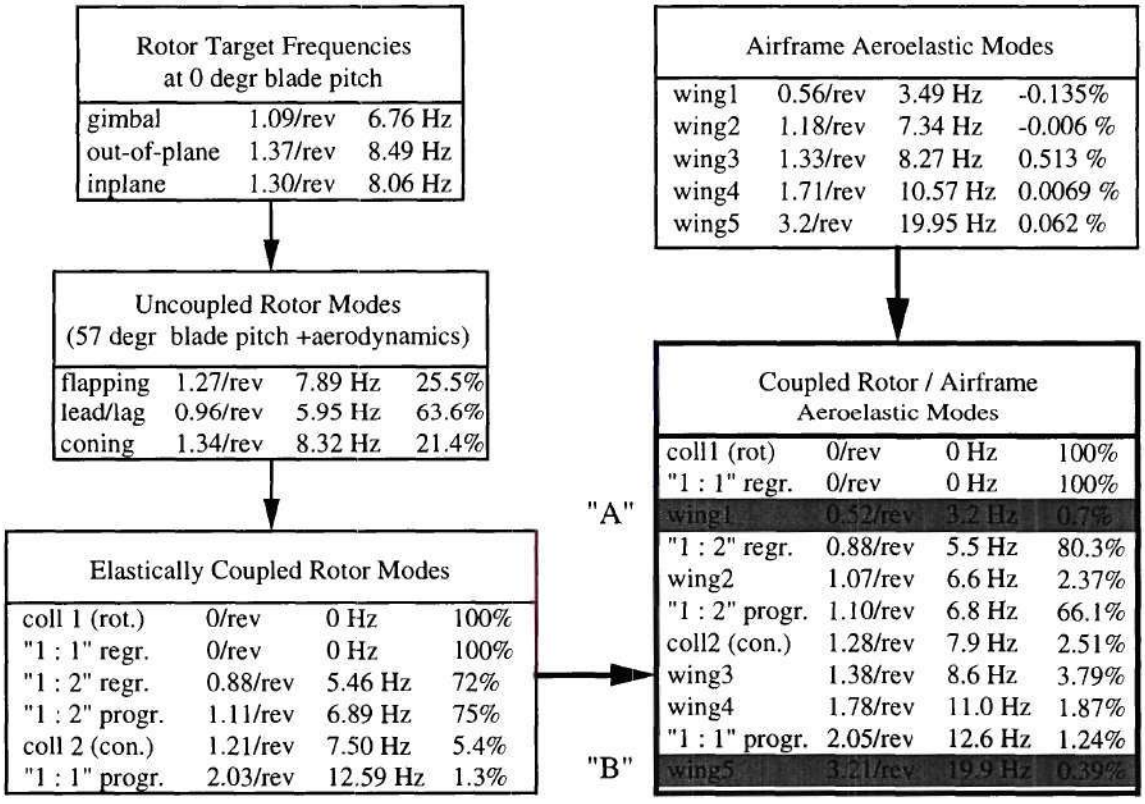

"a : b" denotes the approximate ratio of out-of-plane to inplane deflections in cyclic rotor modes; for example: "1 : 1" regr. is a regressing cyclic mode with similar flapping and lead-lag contributions

Fig. 4.23: Critical Mode Composition

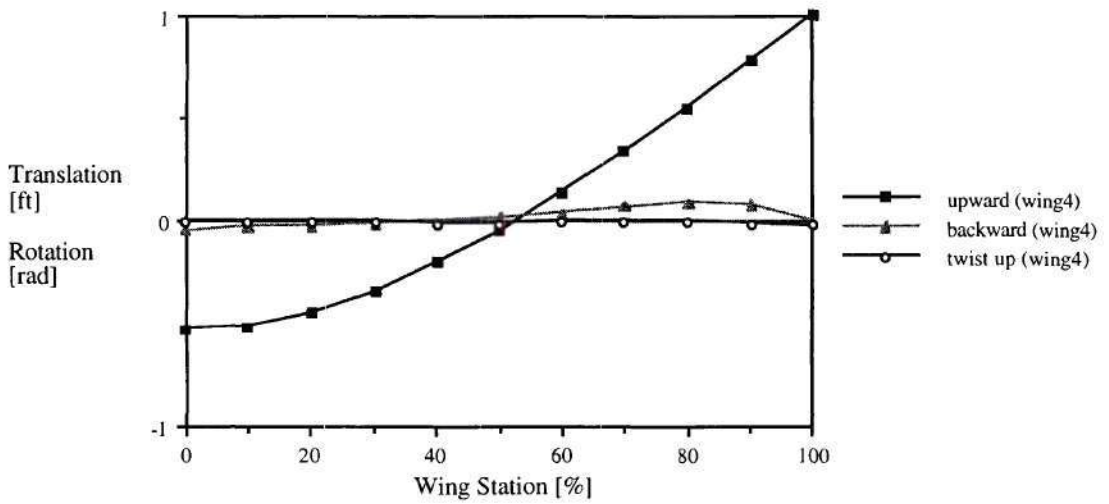

Fig. 4.24: Mode Shape, Mode "wing4" (no aerodynamics)

Table 4.4: Performance Sized vs. Performance and Aeroelastically Sized Aircraft

	Performance Sizing "Low Speed"	Performance & Aeroelastic Sizing, Iteration 28
PI [kts]	74.54	71.96
Block Time, 600nm [hr]	2,008	2,023
OWE [lb]	28,512	29,509
Fuel Weight [lb]	5,689	5,506
Gross Weight [lb]	42,341	43,154
Cruise Speed [kts]	345.1	342.4
Wing Loading [lb/ft^2]	89.31	107.9
Wing Span [ft]	50.6	51.8
Aspect Ratio	5.405	6.893
Thickness-to-Chord Ratio	0.223	0.215
Wing Weight [lb]	2,391	2,922
Wing Str. Weight [lb]	(1,851)	2,492 / *2754.4*
Load Carrying Wt. [lb]	(1,234)	1,661 / *1,754.9*
Wing Frequency 1 [Hz]	3.7 [beam]	3.6 [chord/torsion]
Wing Frequency 2 [Hz]	7.2 [chord]	7.9 [beam/chord/torsion]
Wing Frequency 3 [Hz]	8.4 [torsion]	7.9 [beam/chord/torsion]
Wing Frequency 4 [Hz]		11.0 [beam]

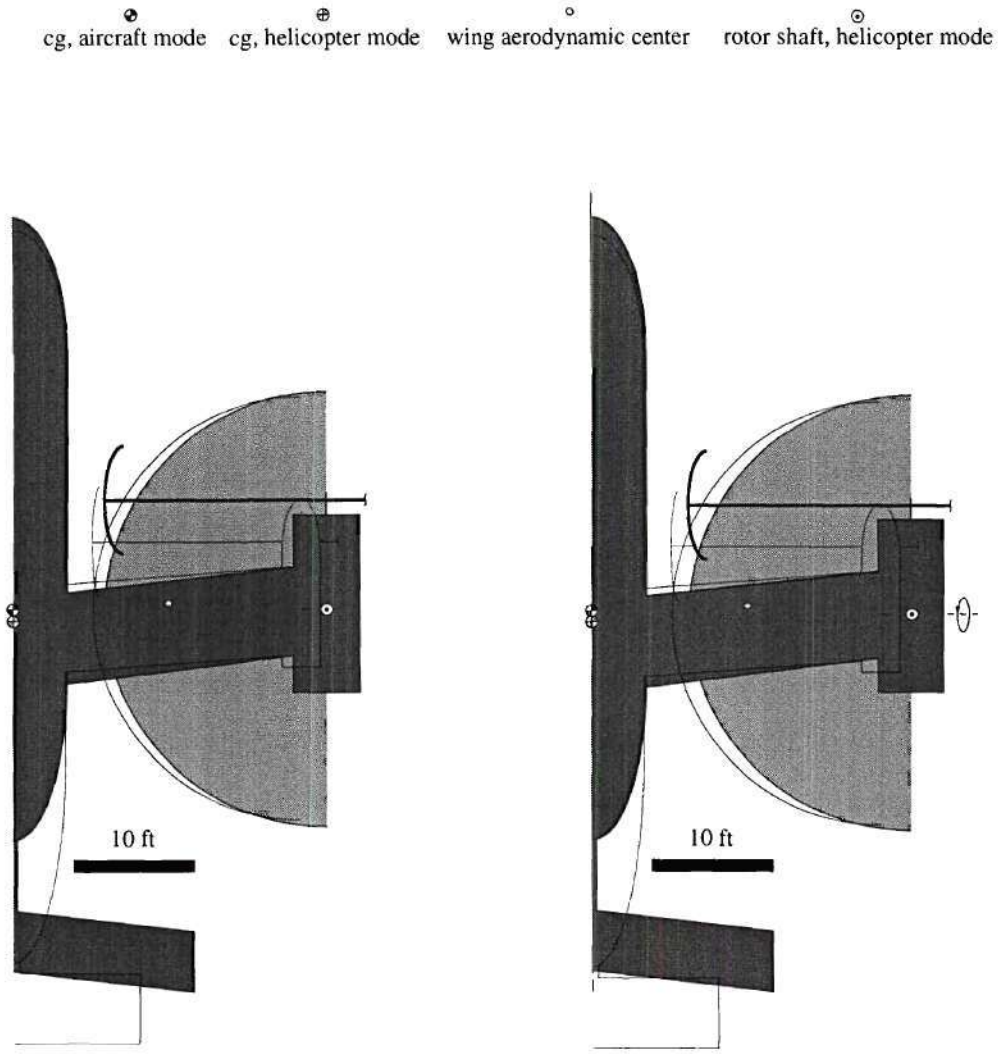

(Outline: CTR-2000)

PI = 73.63 kts	PI = 71.96 kts
WG = 44,095 lb	WG = 43,154 lb
vcrs = 363.9 kts	vcrs = 342.4 kts
Iteration 17	Iteration 28

Fig. 4.25: Planforms, Performance- and Aeroelastically Sized Configurations

4.3. Performance and Aeroservoelastic Sizing

In the most complex Design Simulation Model used in this research, the LQR flutter suppression controller design method described in Section 3.2.5. was added to the "Performance and Aeroelastic Sizing" Model. The resource used for implementation of the LQR algorithm, MATLAB™, was not available on the IBM RS 6000 workstation network used for all other tasks, and the particular host machine also did not belong to the same Network File Server, or NFS-based network. In order to integrate this resource into the Design Simulation Model, a local driver routine was called by DOCC. This driver, in turn, communicated through file transfer protocol, `ftp`, with the remote MATLAB™ host and transferred relevant input files to and output information from the machine to DOCC. Like all other data transfer operations performed by DOCC, this communication process did not require any user assistance except for an initial startup sequence. The Tool for Control System Design, "csd," formed another Circuit, since it generates no information that needed to be fed back into the dynamic plant model, that is, to "vascomp," "elaps," "pwake," or "acp." Due to the large number of input data, "csd" was added to the latter three Tools in Sequence 2. As the most important change to the existing DCM+, the aeroelastic stability constraint, coldmp, was replaced by the rms gust response constraints listed in Table 4.5. This DOCC case was described by 39 Design Variables, 76 States, and 40 Behavior Variables excluding 16 Constraints.

Table 4.5: Aeroservoelastic Sizing - Design Variables and Constraints

Design Variables	"gains" for flaperon, elevator, and swashplate control actuation	gainf, gaine, gains
Constraints	admissible rms control rates admissible rms airframe accelerations	certe, cfrte, csrte ccgacc, ccpacc, crtacc

The primary area of interest in this case is the comparison of "actively controlled" configurations with the "passively controlled" designs described in the previous section. There, structural tailoring commenced after restart with SLP in iteration 7. This aircraft was therefore chosen as the starting point for the "Performance and Aeroservoelastic Sizing" case. Optimization process and final configuration were compared to the equivalent section of the "Performance and Aeroelastic Sizing" case (iterations 7-17).

It had been suspected prior to this investigation that addition of a flutter suppression control system might alleviate stiffness requirements imposed on the structure by aeroelastic stability constraints and allow a light weight wing, with associated benefits for aircraft performance. However, the objective function history, Fig. 4.26, shows a lot of similarity with the passively controlled case, and with a final PI of 73.58 kts, no improvement was detected (compare with PI = 73.64 kts, passively controlled, iteration 17). Aeroelastic stability constraints, in fact, had not contributed to the design process of the passively controlled case during the initial phase (iteration 7, 8, 9), when the largest improvements in PI were made (compare with Fig. 4.13 and 4.14). Center of gravity and static load constraints, however, are violated in both actively and passively controlled cases

during this phase (Fig. 4.14, Fig. 4.27). This is an important observation which will be used in the concluding remarks to this section.

Control rate and airframe acceleration constraints were formulated to yield a value of -1.0 for no rms response, and 0.0 for limit activity (refer to Section 3.2.6.). The former constraints show values between -0.6 and -1.0 throughout the optimization process, indicating that the control system was far from being saturated (dash-dotted lines in Fig. 4.27). This condition was barely affected by the stability of the open-loop system: The open-loop damping constraint from the previous section, coldmp, which was not accounted for in this case, is plotted as a dotted line in Fig. 4.27. Notice that the aircraft was actively stabilized at several iterations and eventually showed neutral stability in this "controller off" condition. Only small reactions to open-loop instability are noticeable, particularly in the elevator rms control rate response, certe. Airframe accelerations, on the other hand, are much more critical and susceptible to the latter influence (the associated constraints are plotted as dashed lines in Fig. 4.27). Vertical accelerations were closest to reaching the 0.2g limit rms value. In iteration 3, the associated constraint, crtacc, reached a level which resulted in its consideration in following SLP steps. In order to reduce this airframe response, the controller "gain" for swashplate controls was increased, Fig. 4.28. Simultaneously, the rotor was dynamically tuned, Fig. 4.32. The combination of both measures resulted in a the desired response reduction. In exception to this observation is the vertical acceleration at the cockpit station, ccpacc, which is also much more susceptible to open-loop system stability (Fig. 4.27). The reason behind this behavior was found in large torsional contributions to most elastic airframe mode considered in the dynamic model. These contributions are indicative of airframe pitch motions about the center of gravity, c.g.. Since the pilot station was located 20 ft in front of the c.g., pitch oscillations contributed significantly to vertical accelerations at this location. Elevator control activity

changes, certe (Fig. 4.27), parallel changes in pilot station accelerations, supporting this interpretation.

Tailoring of the wing's internal structure followed trends similar to those observed in the previous section. However, redistribution of material from the trailing edge spar cap to the leading edge member, and vice versa for the spar webs, was less pronounced, Fig. 4.29. Additionally, transfer of material from the tip to the root of the wing was reduced. In contrast to the previous case, this transfer was detectable for the skin thicknesses of the +/- 45° plies, Fig. 4.30. Furthermore, the -45° ply was strengthened at the expense of the -45° layer. Consider the final configuration's planform, Fig. 4.36. The ply orientation is measured counter clockwise from the spanwise coordinate. The -45° ply supplies fibers which are oriented from the structural box trailing edge at the tip to the leading edge at the root. This direction is also the direction of the main stress flow in the jump take-off condition, since it connects the rotor with the aircraft center of gravity. Hence, it was concluded that this particular trend is a different option for adding bending strength to the wing, which had not been exploited in the previous case.

Wing planform parameters, aircraft size Attributes, cruise speed, and rotor tip speed through the optimization process are plotted in Fig. 4.31. In comparison with the equivalent figure from the "Performance and Aeroelastic Sizing" case (Fig. 4.17), it is apparent that modifications in these Design Variables show less trend changes. This observation was attributed to the lack of an aeroelastic stability constraint, which affected the aircraft planform through the "multi-level" process described in the previous section. The result was a slightly different configuration; the primary differences were seen in an increased wing loading (wl, 114.03 vs. 110.17 lb/ft^2), disk loading (wga, 21.88 vs. 20.83 lb/ft^2), and tip speed (vt, 735.99 vs. 713.25 ft/sec).

Attribute instances describing the rotor dynamics and wing planform for the final configuration of this case, and the equivalent aircraft sized without the flutter controller, are compared in Fig. 4.33. Differences in aspect ratio, ar, and wing sweep, phi, were considered small enough to allow a direct comparison of the internal layout of the two wings. The spar configurations are obviously related, Fig. 4.34. The bar chart also shows clearly a reduced transfer of material from tip to root and leading to trailing edge in the present case ("Aeroservoelastic"; refer to Appendix E for a complete description of the Attributes used in these plots). This effect had been mentioned earlier, like tailoring of the +/- 45° layers which can be seen more clearly in Fig. 4.35. This chart reveals also that skin thicknesses were generally larger in the "aeroservoelastically tailored" wing. As a result, the wing structure is 3.3% heavier (1,795 vs. 1,738 lb). Due to a smaller rotor, however, Empty weight was actually reduced (propulsion weight 9,543 vs. 9,712 lb; Empty Weight 29,272 vs. 29,404 lb). In this light, wing weight reduction appears to be of less importance than initially anticipated.

In summary: The present approach has shown that a flutter suppression control system can be designed for a tiltrotor aircraft, and that even in severe gust conditions at the aircraft's limit speed moderate airframe accelerations are not exceeded. This was accomplished while remaining well inside common operational limits of actuators for aerodynamic control surface and rotor swashplate deflection, and regardless of open-loop system stability. Airframe gust response may become a concern in terms of passenger ride comfort, particularly if the open-loop system is unstable. Anticipated benefits for aircraft performance (PI) due to possible wing weight reductions could not be verified. It was noticed that improvements in PI were achieved primarily by negotiating static stability, static load, and geometric constraints in the variation of wing and rotor planform and size parameters. Internal designs of a passively and an actively controlled wing were very

similar. Judging by the response to respective constraint violations, it appeared as if the main trends - also with respect to the wing weight - were determined by the jump take-off condition. Aeroelastic stability on one hand, and gust response constraints on the other hand resulted in fine tuning of this general concept.

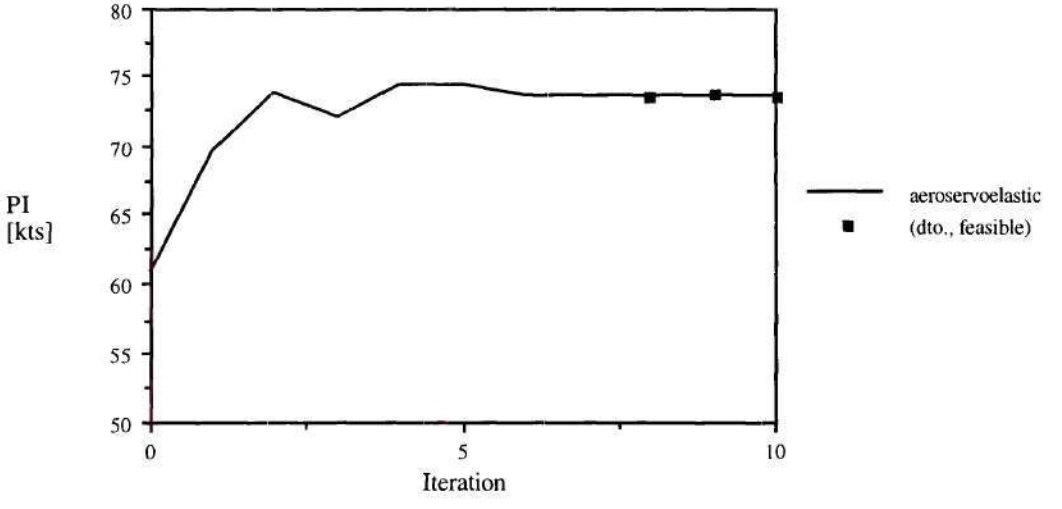

Fig. 4.26: Objective Function History, Performance and Aeroservoelastic Sizing

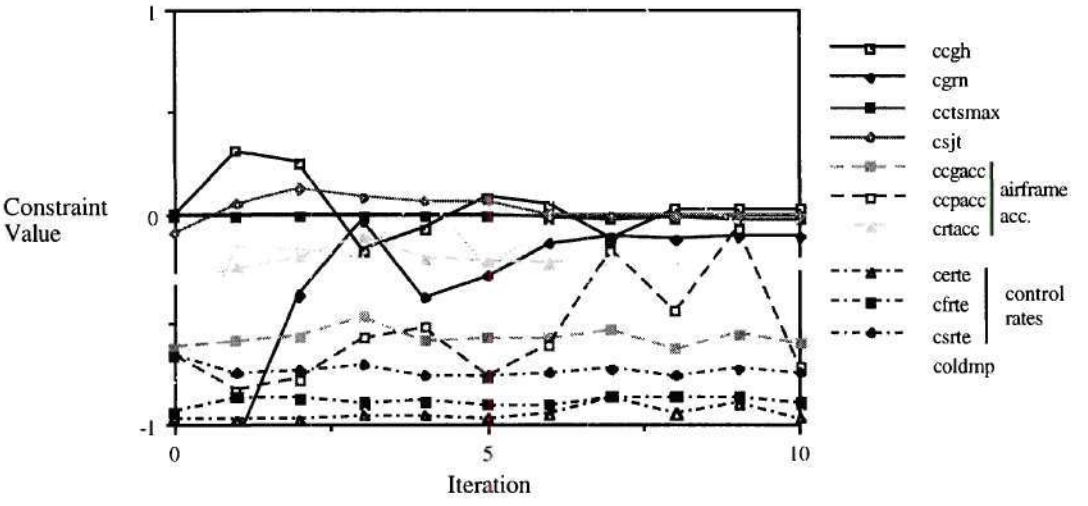

Fig. 4.27: Critical Constraint Histories, Performance and Aeroservoelastic Sizing

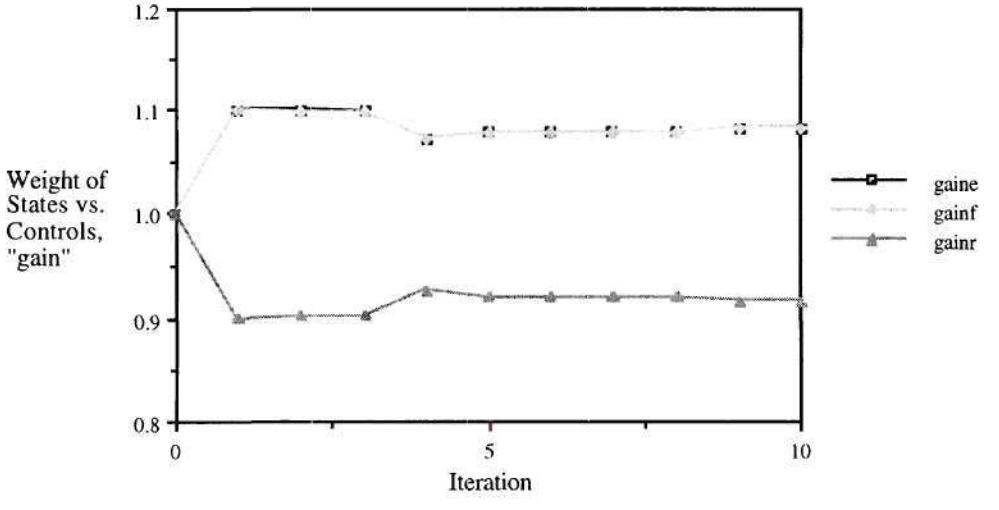

Fig. 4.28: Control System Design Variable Histories

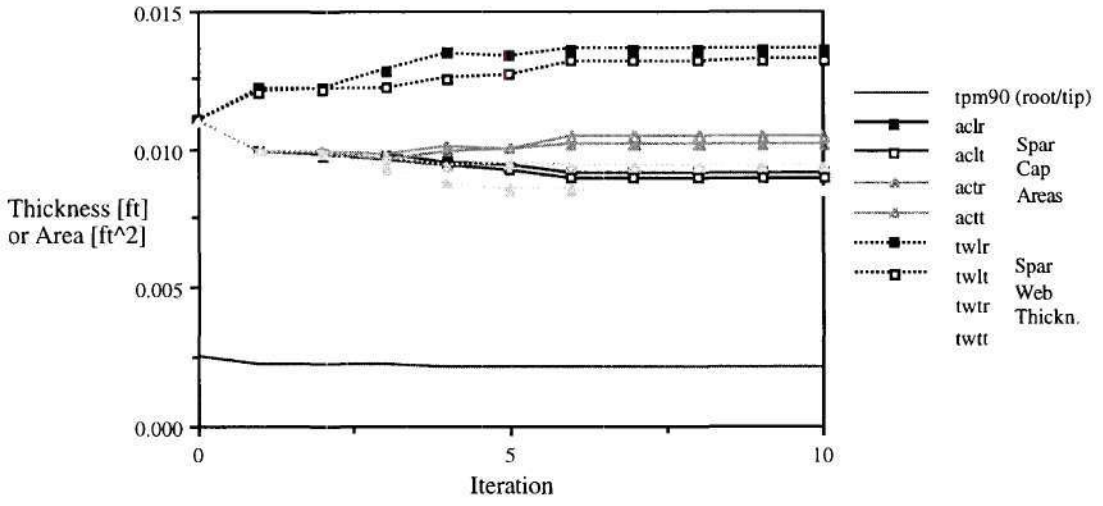

Fig. 4.29: Structural Design Variable Histories, Performance and Aeroservoelastic Sizing

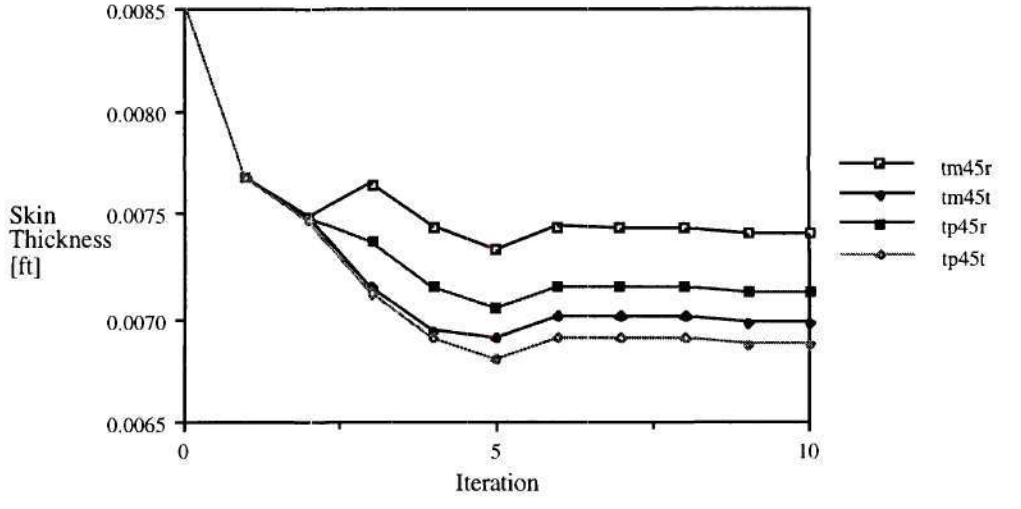

Fig. 4.30: Skin Thickness Histories, +/- 45° Ply Orientation,

Performance and Aeroservoelastic Sizing

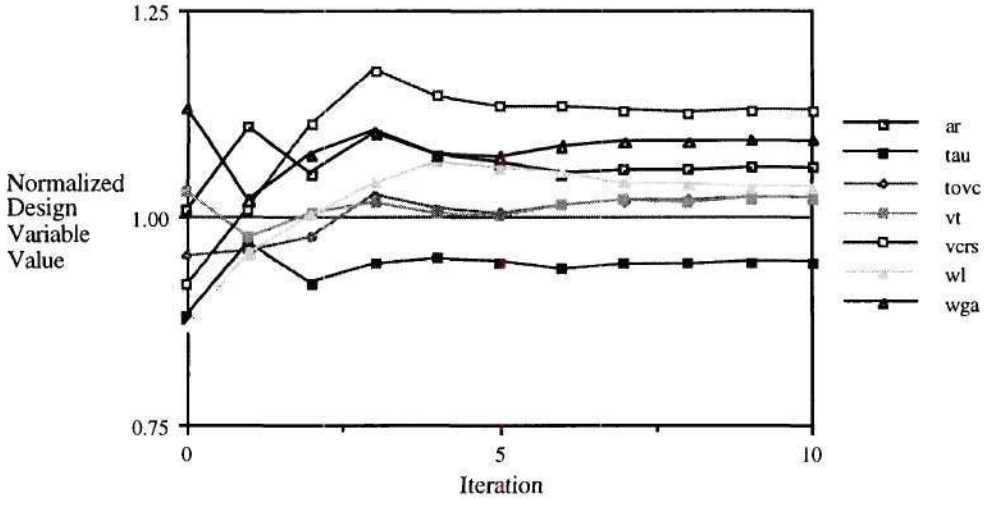

Fig. 4.31: Airframe and Rotor Design Variable Histories,

Performance and Aeroservoelastic Sizing

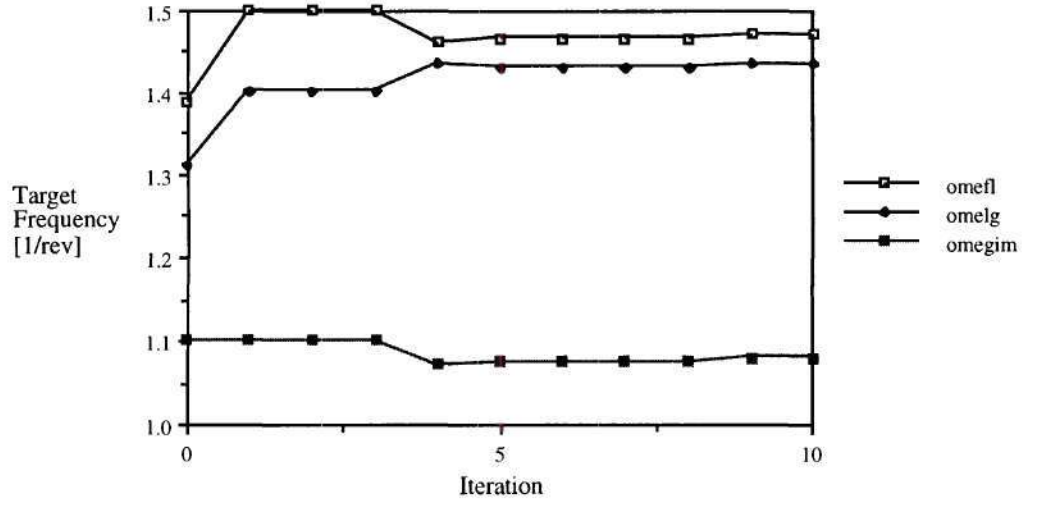

Fig. 4.32: Rotor Dynamics Design Variables, Performance and Aeroservoelastic Sizing

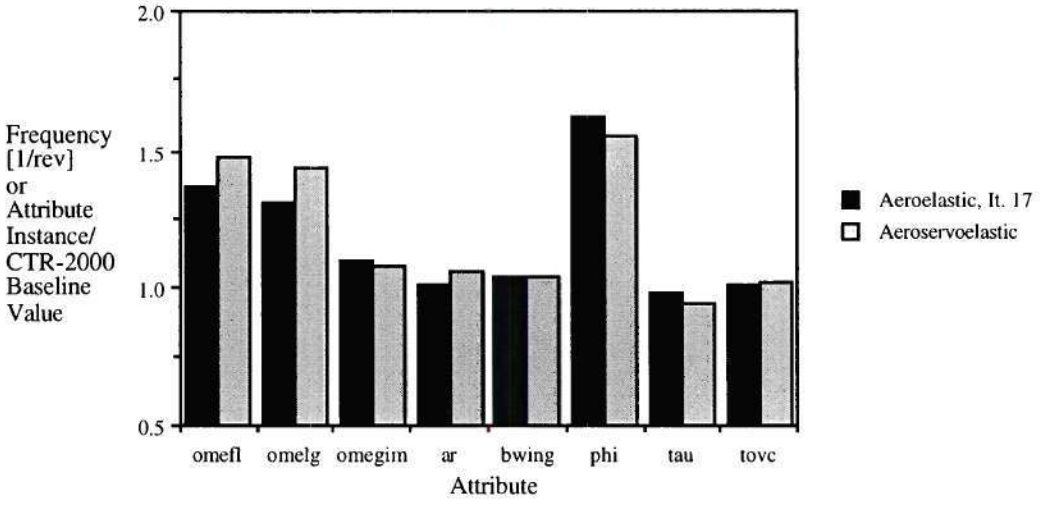

Fig. 4.33: Sensitivity to Control System Inclusion - Rotor Dynamics and Wing Planform

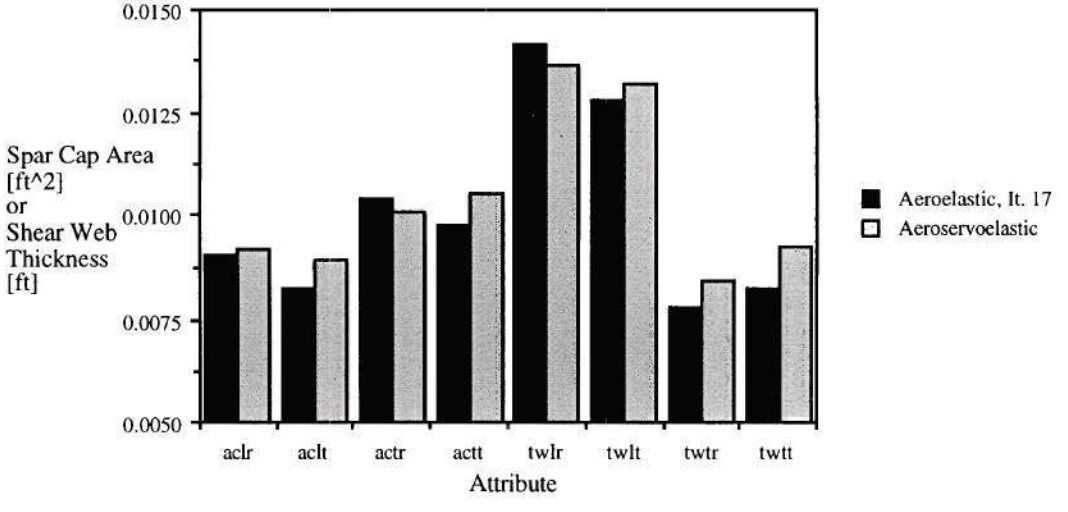

Fig. 4.34: Sensitivity to Control System Inclusion - Spar Configuration

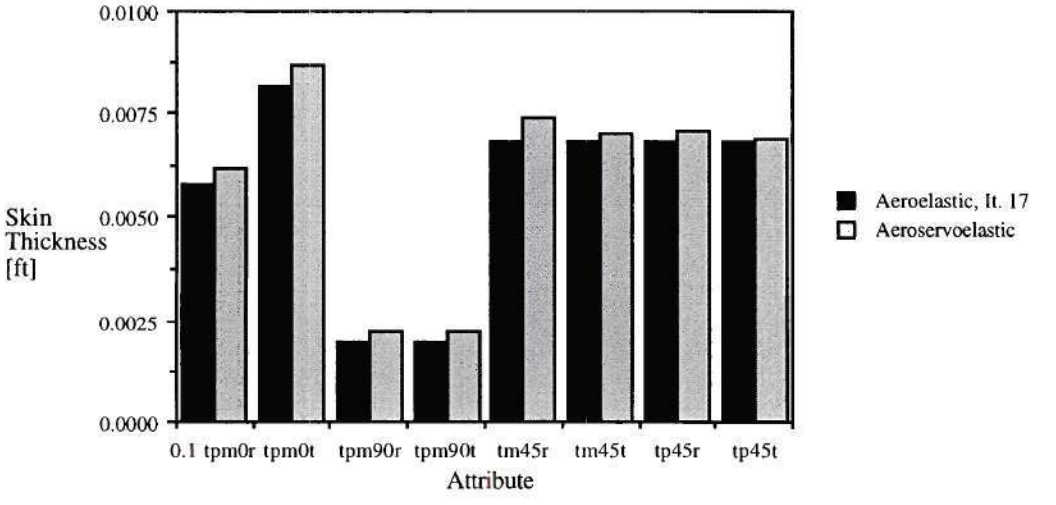

Fig. 4.35: Sensitivity to Control System Inclusion - Skin Thicknesses

cg, aircraft mode cg, helicopter mode wing aerodynamic center rotor shaft, helicopter mode

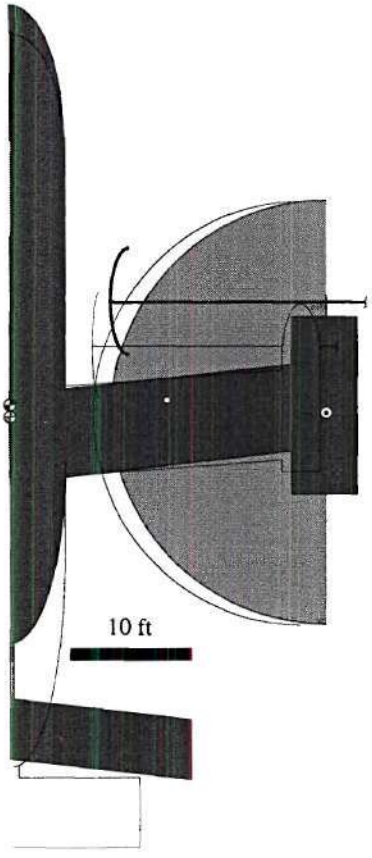

(Outline: CTR-2000)

PI = 73.58 kts
WG = 43,925 lb
vcrs = 361.0 kts

Fig. 4.36: Planform, Performance- and Aeroservoelastically Sized Configuration

Table 4.6: Attribute Instances - Baseline and Generated Designs (1/5)

Attribute	CTR	CTR	NASA	NASA	"low	"high	VDTR	VDTR	Aeroel.	Aeroel.	Aero-
	2000	22C	"GW"	"DOC"	speed"	speed"	"free"	"0.66"	It. 17	It. 28	Servo
acgacc											0.0789
aclr									0.0090	0.0086	0.0091
aclt									0.0082	0.0070	0.0089
acprice					21.11	21.07	23.08	25.35	21.57	21.24	21.57
actr									0.0104	0.0101	0.0101
actt									0.0098	0.0097	0.0105
aeim_1									22.00	22.09	21.85
aeim_2									46.20	43.59	45.08
aeim_3									51.93	52.15	49.60
aeim_4									66.43	63.29	63.62
aeim_5									125.39	119.65	124.73
aere_1									0.03	0.02	0.03
aere_2									0.00	0.00	0.00
aere_3									-0.27	-0.24	-0.23
aere_4									0.00	0.00	0.00
aere_5									-0.08	-0.09	-0.07
affr_1									3.51	3.52	3.49
affr_2									7.35	6.94	7.18
affr_3									8.24	8.28	7.87
affr_4									10.57	10.07	10.13
affr_5									19.97	19.05	19.86
afgm_1									1.07	1.10	1.17
afgm_2									0.01	0.01	0.01
afgm_3									0.17	0.16	0.17
afgm_4									0.01	0.01	0.01
afgm_5									0.00	0.00	0.00
agcr									90.00	90.00	90.00
ar	6.62	5.50	6.00	6.00	5.41	6.06	5.57	4.84	6.69	6.89	7.02
beta0									2.50	2.52	2.39
bwing	49.90	45.80			50.60	48.20	49.20	51.90	51.80	52.50	52.00
ccgacc											-0.61
ccgc					-1.14	-1.27	-0.96	-0.79	-1.11	-1.09	-1.08
ccgh					-0.01	-0.01	0.00	-0.01	0.00	0.02	0.03
ccgs					-0.34	-0.29	-0.50	-0.39	-0.88	-1.00	-1.04
ccpacc											-0.72
cctsmax					0.00	0.00	0.00	0.00	0.00	-0.09	-0.02
cebeta									25.42	27.75	26.07
ceceta									63.73	53.18	52.68

Attributes in italics: Not part of the Attribute list in Appendix E; added for additional information

Table 4.6: Attribute Instances - Baseline and Generated Designs (2/5)

Attribute	CTR 2000	CTR 22C	NASA "GW"	NASA "DOC"	"low speed"	"high speed"	VDTR "free"	VDTR "0.66"	Aeroel. It. 17	Aeroel. It. 28	Aero-Servo
cecon									21.37	22.80	19.76
certe											-0.96
cfrte											-0.90
cgrc					-4.36	-3.40	-1.00	-1.49	-3.69	-3.68	-3.97
cgrf		0.00	1.90	1.20	-2.15	-1.10	-3.69	-6.94	-2.00	-2.30	-2.60
cgrn					-0.02	-0.01	-0.06	0.00	0.01	-0.04	-0.10
cgrwr					-3.51	-3.70	-4.64	-4.95	-4.03	-4.02	-4.05
cgrwt					-2.70	-2.58	-3.98	-4.10	-3.27	-3.31	-3.14
clalpha					4.52	4.74	4.85	4.52	4.91	4.87	4.97
cldelta					-0.08	-0.09	-0.09	-0.09	-0.09	-0.09	-0.10
cmafg					-1.86	-2.45	-1.72	-1.18	-2.69	-2.77	-2.84
cmalpha					-1.52	-1.53	-1.82	-1.57	-2.31	-2.43	-2.53
cmalphr					-0.04	-0.07	0.12	0.09	0.25	0.32	0.35
cmdelta					-0.48	-0.59	-0.54	-0.43	-0.63	-0.65	-0.68
coldmp									-0.19	-0.55	-0.03
cptacc											0.06
crtacc									-1.00	-1.00	-0.23
csjt									0.01	0.00	0.00
csrte									-1.00	-1.00	-0.76
ctrph									5.80	5.80	5.80
dampcr									0.29	0.65	0.13
delta3									15.05	15.35	13.53
dfuse					9.10	9.10	9.10	9.10	9.10	9.10	9.10
doc					16.61	16.25	16.78	19.45	16.41	16.75	16.45
elpd	1.00	1.50			1.25	1.25	1.25	1.25	1.25	1.25	1.25
eltd	1.90	2.00			1.89	1.50	1.50	1.50	1.52	1.59	1.64
elvrate											0.54
etcr									0.40	0.50	0.50
eten					0.97	0.95	0.99	1.00	1.00	1.00	1.00
extdba		85.00	80.00		83.95	84.37	82.27	80.58	82.81	83.54	84.30
flnrate											1.56
fwcrmax											15.00
gaine											1.08
gainf											1.08
gainr											0.92
gsd_1									100.00	100.00	100.00
gsd_10									3.79	57.95	1.87
gsd_11									1.87	2.05	0.33

Attributes in italics: Not part of the Attribute list in Appendix E; added for additional information

Table 4.6: Attribute Instances - Baseline and Generated Designs (3/5)

Attribute	CTR 2000	CTR 22C	NASA "GW"	NASA "DOC"	"low speed"	"high speed"	VDTR "free"	VDTR "0.66"	Aeroel. It. 17	Aeroel. It. 28	Aero-Servo
gsd_12									1.23	0.90	0.14
gsd_13									0.29	0.67	-0.10
gsd_2									100.00	100.00	100.00
gsd_3									100.00	-100.00	43.44
gsd_4									100.00	100.00	93.47
gsd_5									0.77	0.94	1.29
gsd_6									80.35	88.71	1.40
gsd_7									2.40	1.35	4.58
gsd_8									66.03	3.31	3.25
gsd_9									2.48	3.77	54.28
gsf_1									0.00	0.00	0.00
gsf_10									8.54	9.12	10.70
gsf_11									11.03	10.60	13.68
gsf_12									12.66	13.04	19.88
gsf_13									19.94	19.02	19.51
gsf_2									0.00	0.00	0.00
gsf_3									0.00	0.00	0.21
gsf_4									0.00	0.00	2.67
gsf_5									3.23	3.26	3.22
gsf_6									5.49	3.56	6.75
gsf_7									6.62	6.50	8.09
gsf_8									6.84	7.85	8.12
gsf_9									7.91	8.53	10.40
hpinst	14580	13632	11010		15493	15308	20267	26534	15275	14451	15556
ixxnac					112.34	112.72	163.69	231.20	114.90	105.44	114.41
iyyfusg					89691	79427	86542	93904	83928	84414	86770
iyynac					254.78	253.03	392.73	602.37	257.93	233.59	259.47
lfuse	62.40	68.60			55.10	52.40	52.40	52.40	52.50	53.00	53.40
lnac					15.20	15.10	16.90	19.00	15.10	14.70	15.20
mfusg					683.27	685.43	721.72	719.37	696.06	690.27	695.00
mnac					84.21	84.50	106.63	132.09	86.13	81.99	85.76
mrot					61.98	62.64	67.51	83.32	66.35	66.61	65.26
mtcr									9.00	5.00	5.00
mtilt					36.36	37.18	43.89	49.82	39.38	37.70	38.16
mxcr									0.98	0.98	0.98
ombeta									1.27	1.24	1.23
omceta									0.96	1.15	1.18
omcon									1.34	1.35	1.44

Attributes in italics: Not part of the Attribute list in Appendix E; added for additional information

Table 4.6: Attribute Instances - Baseline and Generated Designs (4/5)

Attribute	CTR 2000	CTR 22C	NASA "GW"	NASA "DOC"	"low speed"	"high speed"	VDTR "free"	VDTR "0.66"	Aeroel. It. 17	Aeroel. It. 28	Aero-Servo
omefl									1.37	1.38	1.47
omegim									1.09	1.07	1.08
omelg									1.31	1.41	1.43
phi	-4.00	-6.00	-6.00	-6.00	-5.05	-5.91	-8.85	-6.45	-6.49	-6.83	-6.20
phi0									5.00	5.06	5.00
pi					74.54	76.02	72.10	61.30	73.64	71.96	73.58
plcr									2.00	2.00	2.00
rbar	1.00	1.00	1.00	1.00	10.00	10.00	0.92	0.66	1.00	1.00	1.00
rhvr	18.15	19.00	21.00		17.60	17.45	16.75	20.40	18.35	18.40	17.85
rotacc											0.15
sigma	0.12				0.11	0.11	0.20	0.17	0.11	0.11	0.11
sfcr									2.00	2.00	2.00
swprate											2.44
swprmax											10.00
stcr									1.01	1.00	1.00
tau	1.00	1.00	1.00	1.00	0.92	0.77	0.50	0.54	0.98	0.96	0.95
tblock					2.01	1.96	1.75	1.80	1.93	2.03	1.94
tm45r									0.0068	0.0064	0.0074
tm45t									0.0068	0.0063	0.0070
tovc	0.2000	0.2300	0.2400	0.2300	0.2226	0.2108	0.1738	0.1836	0.2027	0.2157	0.2047
tp45r									0.0068	0.0065	0.0071
tp45t									0.0068	0.0062	0.0069
tpm0r									0.0577	0.0551	0.0617
tpm0t									0.0082	0.0079	0.0087
tpm90r									0.0019	0.0019	0.0022
tpm90t									0.0019	0.0019	0.0021
trib									0.0100	0.0100	0.0101
twlr									0.0141	0.0147	0.0136
twlt									0.0128	0.0128	0.0132
twtr									0.0078	0.0068	0.0084
twtt									0.0082	0.0068	0.0093
vcrs	320.00	300.00	290.00	375.00	345.07	356.45	425.27	405.19	363.96	342.37	360.99
vsafe					473.83	487.49	570.07	545.97	496.50	470.59	492.93
vt	720.00	790.00	747.00	683.00	726.96	735.42	662.34	749.97	713.25	735.77	735.99
controls wt	1734		2216		3407	3430	3802	4410	3578	3555	3545
Empty Wt	27697	31511	29336		27737	27866	32302	36011	29404	28734	29272
wfmiss			3706		4119	4122	5700	7553	4169	3957	4134
wfuel	4631	7269	3999		5689	5755	8327	10893	5776	5506	5738
wg0	41319	47467	43023	45553	42341	42536	49544	55820	44095	43154	43925

Attributes in italics: Not part of the Attribute list in Appendix E; added for additional information

Table 4.6: Attribute Instances - Baseline and Generated Designs (5/5)

Attribute	CTR 2000	CTR 22C	NASA "GW"	NASA "DOC"	"low speed"	"high speed"	VDTR "free"	VDTR "0.66"	Aeroel. It. 17	Aeroel. It. 28	Aero-Servo
wga	20.00	21.00	15.40	22.80	21.74	22.25	28.08	21.31	20.83	20.32	21.88
wing wt		2895	2156		2391	2333	3284	3888	3031	2922	3109
wl	110.00	125.00	89.70	133.33	89.32	111.04	113.72	100.32	110.17	107.96	114.03
woe	28688	32400	30224		28512	28642	33078	36786	30179	29509	30047
wpay	8000				8140	8140	8140	8140	8140	8140	8140
prop. wt	8870				91980	9310	11095	13530	9712	9404	9543
wrbd					144.13	142.10	293.64	348.59	157.85	156.80	150.41
struc. wt	10087				10331	10325	12604	13270	11313	10979	11384
wwgrp					8604	8616	12285	15596	9348	8951	9384
wwinst					524	528	674	814	540	524	538
wwnst					2390	2333	3283	3888	1293	1253	1314
wwstr									1738	1661	1795
xiac	0.45				0.60	0.57	0.49	0.52	0.61	0.61	0.62
xiaccg					0.08	0.19	-0.02	-0.09	0.08	0.07	0.06
xiaccgf					0.26	0.53	0.16	0.01	0.37	0.36	0.32
xiaccgh					0.18	0.29	0.05	-0.03	0.20	0.19	0.19
xiaccgm					-0.56	-0.73	-0.57	-0.40	-0.72	-0.74	-0.77
xicr									1.00	1.00	1.00
xien					0.47	0.58	0.66	0.60	0.46	0.45	0.51
xirr	-0.29				-0.50	-0.68	-0.96	-0.79	-0.66	-0.67	-0.70
xiti	0.60				0.59	0.50	0.37	0.00	0.53	0.54	0.59

Attributes in italics: Not part of the Attribute list in Appendix E; added for additional information

CHAPTER V

CONCLUSIONS AND RECOMMENDATIONS

5.1. Summary of Presented Work

In the introduction to this thesis, two sets of questions were formulated in response to the requirements associated with tiltrotor design. As a prerequisite to detailed studies about this configuration, the following secondary questions were defined:

How can the structure of a design problem be determined in an organized manner?

How can the structure of a design problem be implemented such that it can be easily changed?

In addressing these design methodology-related issues, a structured approach to integration of large, complex design problems has been developed. The method was intended to provide maximum flexibility with respect to modeling accuracy and data flow structure, and proved to possess these characteristics during its application in this research. It is considered to be a tool which facilitates the application of decomposition, subspace

coordination, design space search, and design space exploration methods of Multidisciplinary Design Optimization (MDO) to large, non-academic problems. The central feature is the separation of problem-dependent information - a "program" - and problem-independent functional operators needed in the design process - a "tool box," which forms a programmable structure. The "program" is the extended Data Coupling Matrix, DCM^{+}, which contains information pertinent to the data flow between Contributing Analyses (CAs) of a design problem. Additionally, groups of CAs are identified in the DCM^{+}. These groups, Circuits and Sequences, are operated upon in specific ways - a syntax - by elements of the "tool box," which results in a clearly defined order of execution, the Problem Execution Code. This quasi-mathematical representation for execution of a design problem provides a more structured and functional means for visualization of complex MDO strategies than traditional block diagrams.

The integration methodology was implemented in the Design and Optimization Coupling Code, DOCC, with a maximum of opportunities for user intervention, plenty of accessible information for design process observation, review, and trouble shooting, quick implementation, and portability in mind. The result was an executive software which makes extensive use of UNIX shell data filtering tools and NFS (Network File Server) services. Parallel execution / distributed computing opportunities were exploited in a heterogeneous network of workstations. Generation of traditional Contributing Analysis input and output files proved to be very useful in providing the disciplinary expert with information about an associated tool's operation in a familiar format. This access was essential in location of errors which occurred during early optimization runs that could not be explained with the data provided by the framework alone. In particular, programs with multiple internal iteration loops like traditional aircraft sizing codes are very sensitive to the combination of input parameters, and have the potential to exit ungracefully, generate

erratic data, or even stay in an endless loop if not fed with "reasonable" information. The decision which information is "reasonable" can not be made by an optimization algorithm per se. However, an expert may be able to detect the source of a problem that occurred and prevent it from happening again by adding constraints which the framework is to consider in following program executions.

Data read and write operations take considerable time, particularly on a network of distributed computing resources where the primary storage unit is generally not located on the host machine. Time delays associated with data transfer were substantial, and are estimated to account for about 30% of the total user time in the "Performance and Aeroelastic Sizing" cases (user time was approximately 5h 10 min per SLP iteration at times of low network traffic and low machine load levels). The main contributor to these delays was identified in the Automatic Data Base Inquiry (ADI) procedure used in DOCC.

With this approach, the primary question posed in section 1.3 was addressed:

What is the global impact of rotor design (conventional / VDTR), aeroelastic modeling accuracy and fidelity (tailoring), and active flutter suppression on an economics-related metric of a civil tiltrotor aircraft configuration?

Wilkerson and Schneider concluded their assessment of state-of-the-art tiltrotor dynamic modeling in 1991 in the following way: "A more detailed design and analysis of the wing and rotor, backed by model scale tests, would be necessary to identify the specific combination of design parameters" (/Wilkerson and Schneider 91/). This quote was considered as an incentive for providing such a detailed analysis for use in the present study. The resulting model with aircraft sizing, static stability considerations, airframe structural representation, coupled rotor-airframe aeroelasticity in free-free cruise configuration, and a flutter-suppression-control-system design is arguably the most

comprehensive fully integrated representation used in published tiltrotor optimization studies to date.

A series of optimization runs was performed with models of differing accuracy. Feasible designs which were comparable in size and layout to previously published configurations were produced, which furthered confidence in the tiltrotor model used. The Productivity Index, PI, proved to be an objective function which drove the optimization process more closely to operating cost-optimized configurations than to minimum weight aircraft. As such, it provided a simple, single objective function which captured cost-related trends.

All optimization runs performed were characterized by a permanent conflict of center of gravity location and geometric constraints, more specifically, static stability in helicopter mode and rotor/nacelle clearance in cruise configuration. It appears as if these two constraints leave only a very narrow feasible corridor in the design space for improvement of PI. Cruise speed increases were made so difficult that optimizations with low initial values for cruise speed initial starting points progressed only very slowly. Approaching the feasible region from large speeds resulted generally in faster convergence and higher PI. Considering that the current model employs the sizing trends of the VTOL Aircraft Sizing and Performance Computer Program, VASCOMP (/Schoen et al. 80/), which resulted in nacelles much larger than those of the recently published CTR-2000 civil tiltrotor aircraft with comparable horsepower installed (/Lacy and Wilkerson 95/), it is expected that updated sizing trends have the potential of facilitating negotiation of these two constraints.

Two very different Variable Diameter Tiltrotor (VDTR) optimization cases resulted in configurations which indicated that reducing the rotor size from hover to cruise is not

beneficial. When the optimization algorithm was allowed to modify the ratio of the two rotor diameters, the result was a heavy and fast configuration with very small diameter changes, but with a Productivity Index comparable to those obtained for constant diameter designs. When this ratio was fixed, the design was more than 25% heavier than the conventional configurations generated, and showed a significant 15% shortcoming in PI. These results were attributed to three sources: First, the rotor weight increment for the blade retraction mechanism was estimated at 23% of a conventional rotor weight of the same hover diameter (/Scott 95/), which creates approximately a 2% empty weight penalty. Second, rotor performance tables used in these studies were based on model test data, which were very limited in the c_T/σ range. A combination of these two items was identified as the reason for keeping the rotor diameter nearly unchanged in the first design case. Third, these test data indicated a rotor efficiency deficit up to 10% compared to full scale V-22 rotor performance. Recently published results from analytical variable diameter rotor aerodynamic optimization studies (/Davis et al. 95/) supported the validity of the rotor tables. Granted that limited available data created a disadvantage for this configuration, the trends for the VDTR are not promising. A fair comparison between variable and constant diameter designs, however, will not be possible unless more extensive rotor performance and weight data are available.

The results presented in the previous paragraphs were obtained using VASCOMP only, augmented with static stability and geometric constraint checks (the "Performance Sizing Model"). When Tools for modeling structural integrity, structural dynamics, unsteady airframe aerodynamics, and rotor aeroelasticity were added (the "Performance and Aeroelastic Sizing Model"), the wing structure was tailored to satisfy both structural integrity and aeroelastic stability constraints. The aeroelastic stability constraint, however, was not active for two configurations selected for their performance (PI value), indicating

that this constraint is less restrictive in a completely integrated tiltrotor design process than originally anticipated. Actual "tailoring" occurred only when one of the structural constraints was violated, which caused the optimization process to oscillate between attempted PI improvement through wing size and planform changes in one iteration, and reduction of constraint violation through modification of the internal wing structure in the next. This oscillation, caused by peculiarities of the SLP algorithm used in the optimization engine, was interpreted as "multi-level" type behavior within the non-hierarchic strategy chosen. It was concluded that multi-level optimization is more suitable to the wing tailoring task.

The effect of aeroelastic tailoring on aircraft weight and performance could not be measured directly, since appropriate baseline information has not been published to date. A comparison with the wing weight estimation in VASCOMP, which is based on the method by /Schmidt and Dyess 90/ proved also questionable in detail, since the approaches are too different (cantilevered wing vs. free-free configuration, wing frequency placement vs. tailoring, etc.). However, a qualitative comparison of two very similar configurations designed with either model indicated that VASCOMP's estimation is non-conservative in weight.

Finally, a flutter suppression control system design was added. The constant feedback controller, based on LQR theory, stabilized the aircraft and reduced rms airframe response to severe gust loads to below a level of 0.2g without exceeding control system activity limits. Weight savings had been anticipated based on the expectation that passive stabilization of aeroelastic modes required additional material. The final, actively controlled configuration, however, did not did not show significant lower weight, nor did it achieve a higher PI value than a very similar, passively controlled aircraft. Significant impacts of active vs. passive flutter alleviation on wing planform and wing internal layout were also

not detectable. Rotor frequency tuning was only present when cockpit acceleration levels became active (but never exceeded the limits).

The optimization process was driven by maximization of the objective function, PI, and simultaneous negotiation of rotor/airframe clearance, aircraft static stability (helicopter mode), and rotor performance table limits. Attributes associated with this process are rotor disk loading and tip speed, wing loading, sweep, aspect ratio, and cruise speed. Structural integrity in the 2g jump take-off condition appears were the primary driver for the wing's internal layout and weight. Aeroelastic stability or gust response constraint were responsible for small material redistributions. Interpretation of optimization results was based on trends taken from optimization histories. Very often, this process allowed at most qualitative statements about interdependencies and the "quality" of a particular design. A large number of Design Variables remained unchanged during the design process because they contribute little to the objective function, but primarily to constraints. The following hierarchy of design drivers for tiltrotor optimization for maximum Productivity Index, PI, was identified:

primary: Aircraft configuration and layout Design Variables, affecting PI, highly constrained by negotiation of center of gravity and rotor-nacelle clearance constraints;

secondary: Internal design of the wing, determining wing structural weight, driven by static load constraints;

tertiary: Wing aeroelastic or aeroservoelastic tailoring, rotor frequency placement, controller gains (when applicable), affecting almost exclusively the associated constraints with little effect on the objective function.

Modifications to "lower level" Design Variables were only made when these constraints were violated, that is, when they effectively contributed to progression of the design. At all other times, those subspaces were in an "undefined" state. This lack of "definition" made answering "what if" questions (/Sobieski et al. 88/) very difficult. Certainly, the elements of the Global Sensitivity Equations, GSE, provide this information; but it is desirable to access this information directly through observation of optimization histories. More "definition" could be added through inclusion of metrics other than the top-level objective function in the optimization, in form of multiobjective optimization. One possibility is a multilevel optimization scheme: Given a certain wing planform, "definition" is provided by designing the internal structure of the wing to withstand the jump take-off condition and yield minimum structural weight, then redistributing wing material to obtain a maximum of aeroelastic damping at the limit speed, and finally tuning the gains to minimize rms gust response.

5.2. Conclusions

The following deductions were made in the area of design methodology (secondary questions):

(1) The presented methodology is a viable approach to structured decomposition and flexible integration of large, complex design problems. It bears the potential for future extensions to Multilevel or Concurrent Subspace Optimization (CSSO) strategies, and inclusion of run-time process re-planning.

(2) The implementation of the method in the Design and Optimization Coupling Code, DOCC, demonstrated the feasibility of the flexible architecture. It provides a

blueprint for future applications of this approach with improved efficiency in data transfer and process control tools. Generation of Resource input and output files provided essential information at every state of the design process. Based on the experience gained with the tiltrotor model, the associated time penalties are outweighed by the benefits from increased process transparency - no Resource or Discipline should be treated as a "black box" without access to complete input and output information.

The following conclusions were drawn in the context of tiltrotor modeling and the effect of several trades on PI - the primary question:

(3) Based on limited rotor performance and blade retraction mechanism weight increment data available for this research, Variable Diameter Tilt Rotor (VDTR) designs optimized for maximum Productivity Index, PI, are not competitive with conventional configurations.

(4) The tiltrotor wing weight estimation in VASCOMP (/Schmidt and Dyess 90/) is non-conservative compared to the higher accuracy integrated aeroelastic design method for a free-free configuration. This statement applies both to wing weight estimation and aeroelastic stability.

(5) The effect of aeroelastic stability and gust response limits - separately, for the respective optimization cases - on the final design is small in the fully integrated design model. Aircraft performance poses a more stringent constraint on aircraft speed than stability considerations. Due to the single objective function approach used in this research, Design Variables which affect system damping or gust response were only modified when the respective constraints were violated. This "multi-level" behavior made detection of wing structure tailoring trends difficult.

5.3. Recommendations

The presented implementation of the developed integration methodology and its implementation in the Design and Optimization Coupling Code, DOCC, are considered a proof-of concept, which should be extended and/or modified in future research:

(1) DOCC features frequent checks on the contents of this matrix for CA grouping in order to determine the Problem Execution Code. Design space information (like coupling strengths) can be supplied at run-time to a process planning tool which then revises the initially devised execution order in order to increases the process's efficiency. This would merely require updating the CA grouping in the DCM$^+$, a simple extension to the framework's current operations, which is therefore the first recommendation:

Inclusion of a process planning tool like DeMAID (/Rogers 89/) in DOCC for initial Circuit and Sequence grouping, and run-time process re-scheduling based on coupling strength information obtained from the Global Sensitivity Equations, GSE (following the approach by /Bloebaum 92/).

(2) The presented application of the approach used a non-hierarchic decomposition scheme in which first order system information was supplied to a gradient-based optimization algorithm through local sensitivity analyses and subsequent solution of the GSE. The method is not limited to this strategy, however, if operators and syntax for a new Problem Execution Code are developed. A multilevel optimization scheme is particularly easy to implement by updating the simple Circuit iteration solver to a "daughter" level local optimizer: Feed-forward Behavior Variables supplied to Circuits are equivalent to top-level variables handed down to a lower

level; Circuit iteration variables compare to lower-level local design variables; and driving the Circuit iteration residual is synonymous to minimizing a lower-level objective function*. Multi-level optimization is also suggested for future research in tiltrotor design and optimization. The second recommendation is therefore:

Development of operators and syntax for multi-level optimization, and implementation in DOCC; application of a three-level optimization scheme as described in the previous section to tiltrotor aeroelastic and aeroservoelastic optimization.

(3) DOCC was not programmed with the objective of computational efficiency of its operations. Significant time savings are possible through

replacement of the script-based Automated Database Inquiry (ADI) method by more efficient, direct access procedures offered by most data base management systems.

During assembly of the Tiltrotor Design Simulation Model, the following areas were identified for future improvements:

(4) Performance and Sizing: Replacement of rotor performance tables with an on-line performance analysis in hover and cruise; study of the effect of Variable Diameter Tiltrotor (VDTR) outbound conversion diameter scheduling and conversion profile on transmission size, and integration in the Design Simulation Model; refined VDTR weight increments; update of weight and size trends from the current V-22

---

* There is a difference, because multilevel optimization features feedback of constraint values from lower to upper levels, which is incompatible with the strict Circuit hierarchy. However, local constraint information can be propagated back to the top level optimization if they are formulated as global constraints

baseline - particularly the nacelle size trends appear to be too conservative and should be corrected with turboprop data.

(5) Structures: The validity of structural modes at the upper limit of the frequency spectrum of interest is questionable due to limits on the maximum order of comparison functions used in the Equivalent Laminated Plate Solution, ELAPS (/Giles 89/). It is suggested to use Finite-Element Methods for higher reliability.

(6) Unsteady Airframe Aerodynamics: The Peters/He Finite-State Wake Model has been successfully applied to fixed wing unsteady aerodynamics. Use of the original inflow expansion, however, requires a large number of inflow states, while only a few of the coupled wake modes interact with structural degrees of freedom. An improvement is possible if an expansion can be found which is more suitable for fixed wing reference areas (wing planforms) and allows the numerical efficiency of closed form solution for the wake system's matrix elements.

(7) Aircraft Dynamic Plant Model: The present approach does not include design of the rotor in a strict sense, which could be accomplished by an on-line elastic rotor analysis with physical design parameters. Future models should also include anti-symmetric aircraft modes, in which drive train dynamics are more important.

(8) Flutter Suppression Control System Design: A very simple representation based on Linear Quadratic Regulator Theory was implemented for demonstration purposes. Reduced order feedback of airframe accelerations is suggested as a step towards a more practical controller design.

APPENDIX A

PERFORMANCE AND SIZING ISSUES

A.1. VASCOMP Tail Volume Coefficient Calculation

By equating the limits for front and aft center of gravity location, including a center of gravity travel of Δ times the mean aerodynamic chord,

$$(1+\Delta)\left.\frac{x_{cg}-x_{ac}}{\bar{c}}\right|_{cc} = \left.\frac{x_{cg}-x_{ac}}{\bar{c}}\right|_{s} \qquad (A.1)$$

and then replacing the control capacity limit (subscript cc) expression and the static stability expression (subscript s) by equation {9-40}* and {9-5} in /Torenbeek 82/, respectively, an expression for the required tail volume coefficient can be found:

---

* In Section A.1., equation and page numbers in curly brackets refer to /Torenbeek 82/

$$\overline{V}_h = \frac{-\frac{c_{m0.25}}{c_{L\max}} - \left(1+\frac{1}{1+\Delta}\right)\frac{(c_{m\alpha})_f}{c_{L\alpha}}}{\frac{1}{1+\Delta}\left(\frac{(c_{L\alpha})_h}{c_{L\alpha}}\left(1-\frac{d\varepsilon}{d\alpha}\right)\frac{q_h}{q}\right) - \frac{c_{Lh}}{c_{L\max}}\frac{q_h}{q}} \tag{A.2}$$

The following expressions can be found in the same reference: The ratio of wing moment coefficient about the quarter chord to the maximum lift coefficient for single slotted flaps with no slats in {9-43},

$$\frac{c_{m0.25}}{c_{L\max}} = -0.26\left(1-\frac{1.5\cos\Lambda_{0.25}}{c_{L\max}}\right) \tag{A.3}$$

the ratio of dynamic pressure at the horizontal stabilizer to the free stream value for a T-tail, {p. 325},

$$\frac{q_h}{q} = 0.95 \tag{A.4}$$

the derivative of wing-induced downwash angle at the stabilizer to wing angle of attack, equation {E-52},

$$\frac{d\varepsilon}{d\alpha} = 1.75\frac{(C_{L\alpha})_W}{\pi AR(\tau r)^{0.25}(1+|m|)};\quad r=\frac{2\,l_h}{b};\quad m=\frac{2\,h_h}{b} \tag{A.5}$$

the lift coefficient of the horizontal stabilizer {p. 325},

$$c_{Lh} = -0.35\ AR_h^{1/3} \tag{A.6}$$

the aircraft lift curve slope, equation {9-6},

$$c_{L\alpha} = (c_{L\alpha})_w + (c_{L\alpha})_h\frac{S_h}{S}\left(1-\frac{d\varepsilon}{d\alpha}\right)\frac{q_h}{q};\quad (c_{L\alpha})_{w/h} = \frac{2\pi}{1+\frac{3}{AR_{w/h}}} \tag{A.7}$$

and the fuselage moment coefficient as a function of the fuselage incidence angle, α_f, based on Munk's Airship Theory, derived from equation {E-40},

$$c_{mf} = 1.8\left(1 - 2.5\frac{b_f}{l_f}\right)\frac{\pi}{4}\frac{D_f^2 l_f}{S\bar{c}}\alpha_f \qquad (A.8)$$

If the wing and tail aspect ratio, AR_w (6.0) and AR_t (4.0), wing quarter chord sweep angle, $\Lambda_{0.25}$ (0°), maximum lift coefficient, c_{Lmax} (3.0), wing taper ratio, τ (1.0), ratio of tail area, S_h, to wing area, S (0.4), and the two downwash coefficients in (A.5), m (0.1) and r (1.0), are given, then (A.2) simplifies to an expression which only contains the variables wing area, S, mean aerodynamic chord, $\bar{c}$, fuselage diameter, D_f, and fuselage length, l_f:

$$\bar{V}_h = A + B\frac{D_f^2 l_f}{S\bar{c}} \qquad (A.9)$$

The values given in parentheses describe a 'typical' configuration, which yields A=0.245 and B=0.72 for a required center of gravity travel, Δ, of 0.5. The equivalent values hardwired in VASCOMP are 0.23 and 0.86. From this result it can be deducted that VASCOMP's undocumented internal tail volume coefficient calculation was set up to guarantee these margins.

A.2. Center of Gravity Limits, Helicopter Mode

Center of gravity limits for the aircraft configuration have been derived using the same relations as in the previous section. In helicopter configuration, the center of gravity

moves due to tilting of the nacelles, and each rotor adds a term to the moment coefficient slope expression. For static stability it is required that

$$c_{m\alpha} = \frac{x_{cg,he} - x_{ac}}{\bar{c}} c_{L\alpha} - \left(1 - \frac{d\varepsilon}{d\alpha}\right)\frac{q_h}{q}(c_{L\alpha})_h \overline{V}_h + (c_{m\alpha})_f + 2(c_{m\alpha})_R < 0 \qquad (A.10)$$

Bramwell /Bramwell 76/ {7.54}* expresses the nose-up moment coefficient contribution due to a vertical speed disturbance, as

$$m'_w = -(l - h a_{1s})\frac{\partial t_c}{\partial \hat{w}} + h\left(t_c \frac{\partial a_{1s}}{\partial \hat{w}} + \frac{\partial h_{CD}}{\partial \hat{w}}\right) \qquad (A.11)$$

with l and h being the rotor location aft and above the aircraft center of gravity, respectively, normalized by the rotor radius (the hub is assumed not to transfer any pitching moment from the rotor disk to the shaft). The angle, a_{1s}, is the difference between the longitudinal flapping angle and the longitudinal cyclic pitch angle in trim. Bramwell states that this angle is "small," and gives an example where it is less than 1° {p. 199 and 174, respectively}. As a result, ha_{1s} is small in comparison to l in the first term, and was neglected. The derivatives of the thrust coefficient*, shaft angle, and inplane force coefficient with respect to the disturbance, normalized by the rotor tip speed, are given in {7.79}, {7.81}, and {7.82}, respectively:

$$\frac{\partial t_c}{\partial \hat{w}} = \frac{2\mu}{8\mu + as}; \mu > 0.08$$

$$\frac{\partial a_1}{\partial \hat{w}} = \frac{16\mu^2}{\left(1 - 1/2\mu^2\right)(8\mu + as)} \qquad (A.12a)$$

---

* In Section A.2., equation and page numbers in curly brackets refer to /Bramwell 76/

* Bramwell uses effective rotor area, not disk area for normalization; t_c is equivalent to c_T/σ in more conventional notation

$$\frac{\partial h_{CD}}{\partial \hat{w}} = \frac{4a\mu^2}{8\mu + as} \frac{\theta_0/6\left(1 - 9/2\mu^2\right) + \lambda_D}{1 - \mu^2} \tag{A.12b}$$

which are functions of the advance ratio, μ, blade lift curve slope, a, and rotor solidity, s. Rotor collective pitch in trim can be derived from equation {5.17}:

$$\theta_0 = \frac{\left(4/a + s/(2\mu)\right)t_c - \mu\alpha_{nf}}{2/3\left(1 + 3/2\mu^2\right)} \tag{A.13}$$

with the shaft angle, α_{nf}. Finally, the total disk inflow, λ_D {p. 15}, is calculated by combing equations for induced inflow {p. 158}, inflow {5.15}, and longitudinal flapping angle {5.39}:

$$\lambda_D = \left(\mu\alpha_{nf} - \frac{st_c}{2\mu}\right)\left(1 + \frac{2\mu^2}{1+\mu^2}\right) + \frac{8}{3}\mu\theta_0 \tag{A.14}$$

The following values were assumed in order to explore opportunities for simplifications:

$$x_R = R;\ x_t = 1.7\ R;\ x_{cg,h} = 1.6\ R;\ a = 5.5;\ a_{nf} = 5°$$

Figure A.1 shows that m'_w is approximately linearly dependent of t_c, σ and μ about $t_c = 0.1$, $\sigma = 0.1$ and $\mu = 0.1$. A linear approximation of (A.11) about these values was therefore used, and the location of the rotor with respect to the center of gravity was expressed in terms of the tilt axis, x_t, and rotor hub location in aircraft mode, x_R,

$$l = \frac{x_t + (x_t - x_R)\sin 5°}{R};\ h \approx \frac{x_t - x_R}{R} \tag{A.16}$$

After conversion from Bramwell's helicopter conventions to fixed wing notation (using the more common σ for rotor solidity),

$$(c_{m\alpha})_R = \frac{2\sigma}{\mu}\frac{\pi R^3}{S\bar{c}} m'_w \tag{A.15}$$

this final expression was used in (A.10):

$$(c_{m\alpha})_R = \frac{2\sigma}{\mu}\frac{\pi R^2}{S}\left\{0.6036(\mu-\sigma)\frac{x_{cg,he}}{\bar{c}}\right.$$
$$-\left(0.1427\frac{c_T}{\sigma}-0.1153\,\sigma+0.2667\,\mu\right)\frac{x_R}{\bar{c}} \tag{A.16}$$
$$\left.+\left(0.1427\frac{c_T}{\sigma}+0.4882\,\sigma-0.3369\,\mu\right)\frac{x_t}{\bar{c}}\right\}$$

A.3. Group Masses and Inertias

VASCOMP estimates individual weights for an abundance of components. These point masses can be used for aircraft center of gravity determination, if assumptions regarding the location of these components are made. Those used in this research are summarized in Table A.1, and the associated geometry is depicted in Fig. A.2. Wing/fuselage geometry is completely determined through VASCOMP output data; the chordwise (x-) location of tilt mechanism, rotor, and nacelle are free variables. Fuselage and engine nacelle are important for a subsequent dynamic analyses, and are therefore partially represented by mass homogeneously distributed over a simple geometric body. Engine nacelle rotational inertias were calculated about the roll, pitch and yaw axis; the fuselage inertia was only determined in pitch.

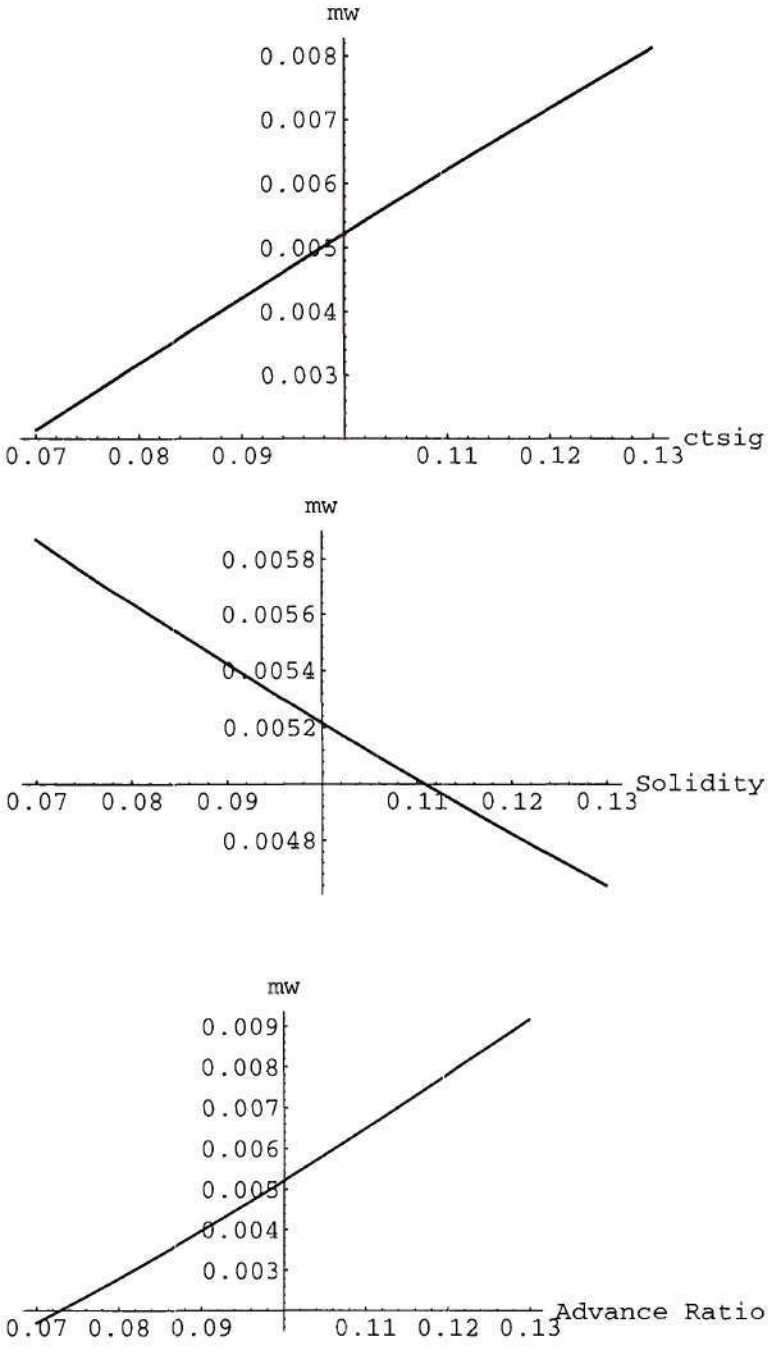

Fig. A.1: Sensitivity of Rotor $c_{m\alpha}$ to Thrust Coefficient, Solidity, and Advance Ratio

Table A.1: Aircraft Group Mass and Inertia Components

Group	CG Location	includes...
Fuselage	x_{fus}, 0 (at 50% of l_f)	evenly distributed over l_f: fuselage structure, fixed useful load, fixed equipment, hydraulics concentrated masses, centered about helicopter configuration cg: landing gear
Cylindrical Part	x_{cyl}, 0 (at 50% of l_{cyl})	evenly distributed over l_{cyl}: payload, cabin acoustic treatment
Wing Group	x_{ac}, 0	concentrated mass: wing structure, fittings, flaps, 50% fixed wing controls, 33% fuel system, fuel
Primary Engine Nacelle	x_n, y_n	evenly distributed in cylinder of 42% nacelle diameter and 35% nacelle length (matches V-22 data from /Sprangers and Stevenson 86/): [for both nacelles combined:] 50% drive system, primary engine section, primary engine acoustic treatment, primary engines, primary engine installation, 66% fuel system
Tilt Mechanism	x_t, b/2	concentrated mass: [for both tip masses combined:] 50% drive system, tilt mechanism
Rotor System	x_r, b/2	concentrated mass: [for both rotors combined:] rotor system, upper controls (swash plate etc.)
Stabilizer	l_f, 0	concentrated mass: horizontal tail, vertical tail, 50% fixed wing controls
Cockpit	x_c, 0	concentrated mass: cockpit controls, SAS

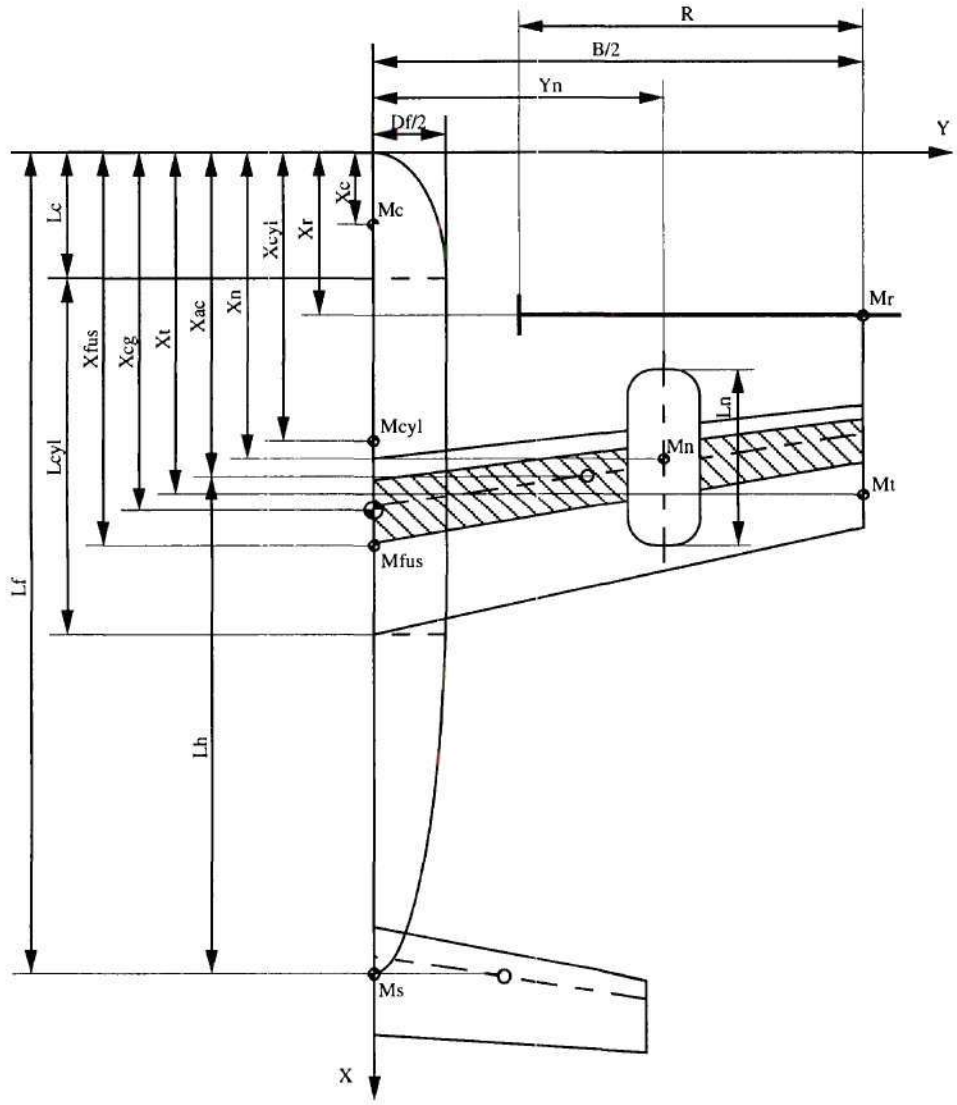

Fig. A.2: Tiltrotor Geometry and Group Mass Locations

A.4. VDTR Rotor Map Generation

A variable diameter rotor features a geometry significantly different from constant diameter designs, in particular a large root cutout in hover, when the blades are fully extended, and smaller twist in cruise. It is therefore doubtful whether rotor efficiency calculations which work reasonably well for conventional configurations perform equally well for this uncommon rotor system. Adopting experimental data, where available, appeared to be a more reasonable approach. This sections describes data conversion and VASCOMP hover and cruise efficiency table generation based on data from a 1/6th-scale VDTR wind tunnel model as reported in /Studebaker and Matuska 93/. Throughout this reference, rotor data are normalized according to the conventions commonly used for helicopter applications. In order to achieve consistency, only geometric data of the fully extended rotor, the hover configuration, were used. The following definitions apply to thrust coefficient (divided by solidity), power coefficient, advance ratio, cruise efficiency, and hover Figure of Merit:

$$\frac{c_T}{\sigma^*} = \frac{T}{\sigma_h \rho \pi \Omega^2 {R_h}^4}; c_P = \frac{550\,HP}{\rho \pi \Omega^2 {R_h}^5}; \mu = \frac{V}{\Omega R_h}; \eta_P = \frac{c_T \mu}{c_P}; FM = \frac{{c_T}^{1.5}}{\sqrt{2} c_P} \qquad (A.17)$$

VASCOMP's hover Figure of Merit table uses the same conventions, hence an equally spaced grid of points can be generated by using a curve fit of the form

$$FM = a + b\left(\frac{c_T}{\sigma^*}\right)^{-1} + c\left(\frac{c_T}{\sigma^*}\right) + d\left(\frac{c_T}{\sigma^*}\right)^2 + e\left(\frac{c_T}{\sigma^*}\right)^3 \qquad (A.18)$$

Fig. A.3 shows that the correlation of this curve fit with the experimental data is excellent. Since data were available for one tip Mach number only, this curve was used for all Mach numbers between 0.5 and 0.9. For comparison, the equivalent curve for a V-22 type rotor as obtained by Schleicher /Schleicher 93/ is also plotted. The efficiency

advantage to the VDTR is significant; this could possibly be attributed to the model scale (V-22 results are supported by full scale data). It was considered to be beyond the scope of this work to investigate the exact reasons for this phenomenon.

Cruise efficiency data preparation requires a few more conversions, since VASCOMP requires input of power coefficient as a function of thrust coefficient and advance ratio, where propeller conventions are used for normalization:

$$\tilde{c}_T = \frac{T}{\rho n^2 D_c{}^4}; \tilde{c}_P = \frac{550\,HP}{\rho n^2 D_c{}^5}; J = \frac{V}{nD_c}; \eta_P = \frac{\tilde{c}_T J}{\tilde{c}_P} \tag{A.19}$$

D_C is the diameter in cruise configuration, and n is the rotor rotational frequency (as opposed to the rotor angular velocity, Ω; the numerical values for a full scale VDTR are σ^*= 0.083, R_h = 24.6 ft, D_C = 32.4 ft, and n = 4.4 Hz /Studebaker and Matuska 93/). The cruise propulsive efficiency data in /Studebaker and Matuska 93/ exhibit significant scatter (Fig. A.4); the trends become more apparent when plotting power coefficient vs. thrust coefficient (Fig. A.5). This representation is also needed for the VASCOMP table, and was therefore used for a curve fit of the form

$$\tilde{c}_P = a + b\tilde{c}_T + cJ + d\tilde{c}_T J + e\tilde{c}_T{}^2 J + f\tilde{c}_T J^2 \tag{A.20}$$

Trial runs with this table showed that in descent the thrust coefficient was smaller than the lowest value for which test results were obtained. Additional data for an advance ratio of J = 0 were therefore derived from hover test data. Using the definition for the hover Figure of Merit and conversions from helicopter to propeller conventions, the static power coefficient (with FM in the denominator being a function of the thrust coefficient according to (A.18)),

$$\tilde{c}_{P,J=0} = \frac{\pi^4}{4}\frac{1}{\sqrt{2}}\frac{\left(\frac{\pi^3}{4}\tilde{c}_T\right)^{1.5}}{FM\left(\pi^3/4\,(\tilde{c}_T/\sigma)\right)} \tag{A.21}$$

as plotted in Fig. A.5, was incorporated in the curve fit. The final curves are plotted as dashed lines in Fig. A.4 and A.5.

The rotor solidity changes during conversion from cruise to hover configuration, and an approximate expression for this effect was obtained. If the effective blade area does not change, the solidity is proportional to $\bar{r}^2$ due to change in disk area, where $\bar{r}$ is the ratio of cruise to hover diameter. The blade area, however, increases linearly with $\bar{r}$ as the inboard blade section is exposed. The following expression matches the values for the rotor design used with $\sigma_c = 0.125$, $\sigma_h = 0.083$, and $\bar{r} = 0.6585$ /Matuska 93/:

$$\sigma_h = \frac{\bar{r}^2}{0.024 + 0.976\bar{r}}\sigma_c \tag{A.22}$$

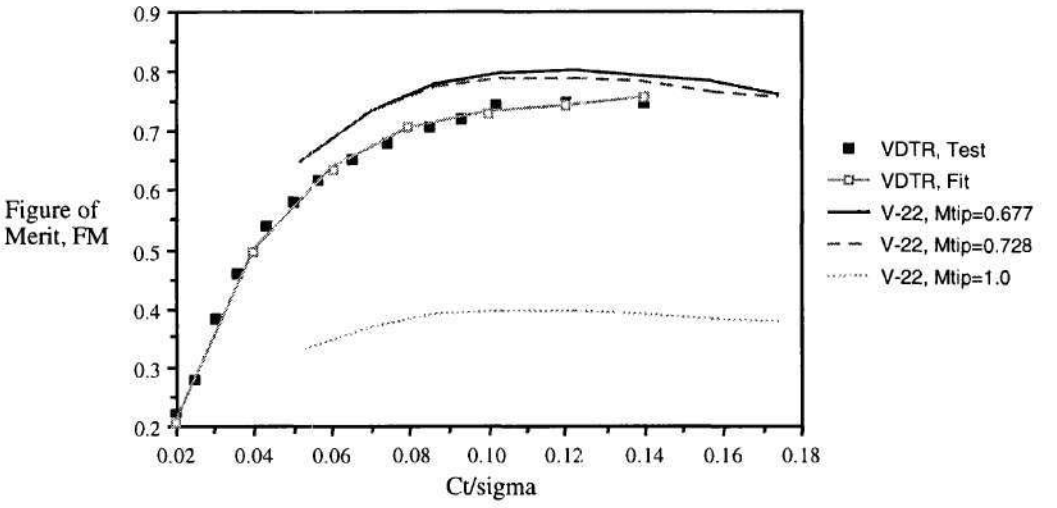

Fig. A.3: VDTR and V-22 Rotor Hover Performance

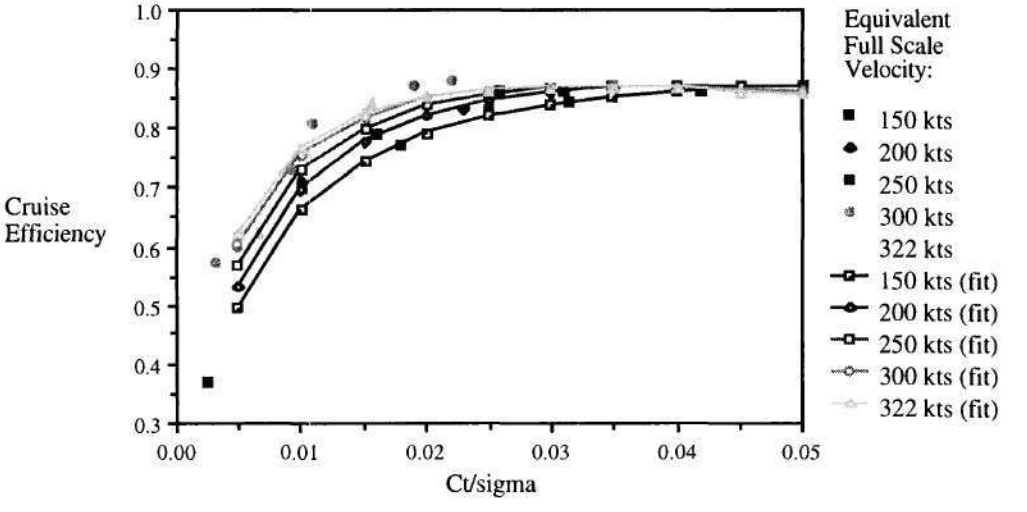

Fig. A.4: VDTR Cruise Propulsive Efficiency -

Test Data vs. Curve Fit

[Normalization according to Equation (A.17)]

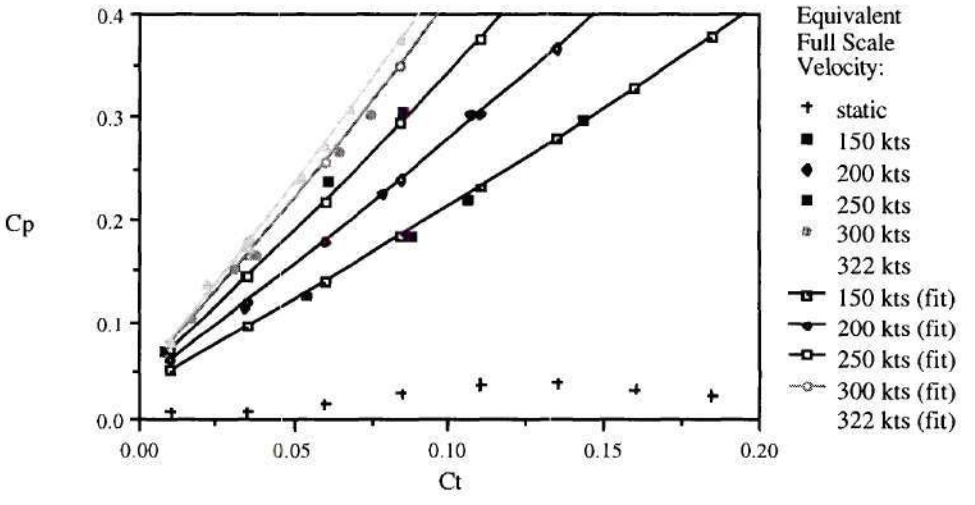

Fig. A.5: VDTR Power and Thrust Coefficient as a Function of Speed - Test Data vs. Curve Fit

[Normalization according to Equation (A.19)]

APPENDIX B

A SIMPLE SHEAR PANEL FOR ELAPS

B.1. Shear Panel Formulation and Inclusion in ELAPS

A shear panel segment perpendicular to the x,y-plane, with its lengthwise coordinate, s, oriented at an angle, ψ, with respect to the chordwise coordinate, x, located between the upper and lower skin of a structural box is considered (see Fig. B.1). Since the displacement in s-direction is

$$t = u\cos\psi + v\sin\psi \tag{B.1}$$

the skin displacements in the panel plane as a function of time, τ, can be described as

$$\begin{Bmatrix} t^u(x,y,\tau) \\ w^u(x,y,\tau) \end{Bmatrix} = \begin{bmatrix} \cos\psi \left\{a_u^u(x,y)\right\}^T & \sin\psi \left\{a_v^u(x,y)\right\}^T & 0 \\ 0 & 0 & \left\{a_w^u(x,y)\right\}^T \end{bmatrix} \begin{Bmatrix} \left\{q_u^u(\tau)\right\} \\ \left\{q_v^u(\tau)\right\} \\ \left\{q_w^u(\tau)\right\} \end{Bmatrix} \tag{B.2}$$

in terms of the planform coordinates and the ELAPS comparison functions introduced in Section 3.2.3.1., equation (3.1). The superscript, u, denotes the set for the upper skin; an identical, independent set exists for the lower skin. For simple harmonic motion,

$$\dot{t}(x,y,\tau) = \omega\, t(x,y,\tau); \quad \dot{w}(x,y,\tau) = \omega\, w(x,y,\tau) \tag{B.3}$$

The corners of the panel element are denoted as depicted in Fig. B.1, with "u" and "l" indicating upper and lower skin, and "a" and "b" the location (x_1,y_1) and (x_2,y_2), respectively. In each triangular subelement, a linear displacement field in the coordinates, s and z, is assumed,

$$t_I(s,z) = a_{0,I} + a_{1,I}s + a_{2,I}z; \quad w_I(s,z) = b_{0,I} + b_{1,I}s + b_{2,I}z \tag{B.4a}$$

$$t_{II}(s,z) = a_{0,II} + a_{1,II}s + a_{2,II}z; \quad w_{II}(s,z) = b_{0,II} + b_{1,II}s + b_{2,II}z \tag{B.4b}$$

The coefficients, $a_{i,j}$ and $b_{i,j}$, in (B.4) are determined using the displacements at the corners and the following normalizations:

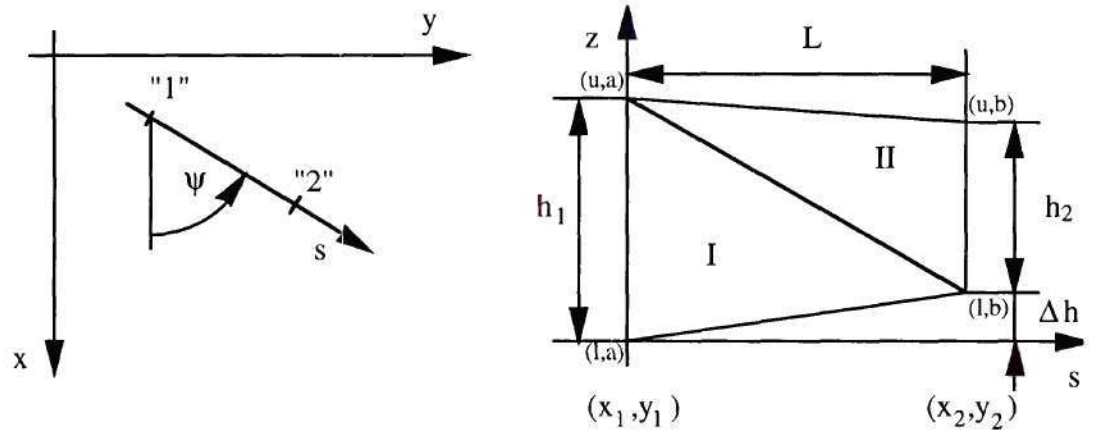

Fig. B.1: Shear Panel Segment Orientation and Geometry

$$\bar{t} = \frac{t}{L}; \quad \overline{w} = \frac{w}{h_1}; \quad \sigma = \frac{s}{h_1}; \quad \zeta = \frac{z}{L} \tag{B.5}$$

The following expressions are obtained for $\bar{t}$ (the equations for $\overline{w}$ are of identical form, with $\bar{t}$ replaced by $\overline{w}$):

$$\bar{t}_I(\sigma,\zeta) = \bar{t}_{l,a} + \left[\left(\bar{t}_{l,b} - \bar{t}_{l,a}\right) - \frac{\Delta h}{h_1}\left(\bar{t}_{u,a} - \bar{t}_{l,a}\right) \right]\sigma + \left(\bar{t}_{u,a} - \bar{t}_{l,a}\right)\zeta \tag{B.6a}$$

$$\bar{t}_{II}(\sigma,\zeta) = \bar{t}_{u,a} - \frac{h_1}{h_2}\left(\bar{t}_{u,b} - \bar{t}_{l,b}\right) + \left[\left(\bar{t}_{l,b} - \bar{t}_{u,a}\right) - \frac{h_1 - \Delta h}{h_2}\left(\bar{t}_{l,b} - \bar{t}_{u,b}\right) \right]\sigma$$

$$+ \frac{h_1}{h_2}\left(\bar{t}_{u,b} - \bar{t}_{l,b}\right)\zeta \tag{B.6b}$$

The shear strain in each of the triangular panel sub-segments is

$$\gamma_{sz,I} = \frac{\partial \bar{t}_I}{\partial \zeta} + \frac{\partial \overline{w}_I}{\partial \sigma} = \bar{t}_{u,a} - \frac{\Delta h}{h_1}\overline{w}_{u,a} - \bar{t}_{l,a} - \left(1 - \frac{\Delta h}{h_1}\right)\overline{w}_{l,a} + \overline{w}_{l,b} \tag{B.7a}$$

$$\gamma_{sz,II} = \frac{\partial \bar{t}_{II}}{\partial \zeta} + \frac{\partial \overline{w}_{II}}{\partial \sigma} = \frac{h_1}{h_2}\bar{t}_{u,b} - \overline{w}_{u,a}\frac{h_1 + \Delta h}{h_2}\overline{w}_{u,b} - \frac{h_1}{h_2}\bar{t}_{l,b} - \left(1 - \frac{h_1 + \Delta h}{h_2}\right)\overline{w}_{l,b} \tag{B.7b}$$

Neglecting all but shear strains, the strain energy in the panel segment, U, is

$$U = \frac{1}{4}A_{66}\,h_1 L\left(\gamma_{sz,I}{}^2 + \frac{h_2}{h_1}\gamma_{sz,II}{}^2\right); \quad A_{66} = \sum_{k=1}^{n}\overline{Q}_{66}(\pm 45^\circ)\,d_k = \overline{Q}_{66}(\pm 45^\circ)\,d \tag{B.8}$$

assuming a +/-45° laminate of k plies, with equal numbers of plies in either fiber orientation. The laminate stiffness in shear, $\overline{Q}_{66}(\pm 45^\circ)$, is based on classical laminate theory (e.g. /Tsai and Massard 87/). U can be directly determined from the corner displacements after inserting equations (B.7). The corner displacements, in turn, are

accessible through the comparison functions for upper and lower skin, equation (B.2) Combining all generalized coordinates from upper and lower skin into one global vector,

$$\left\{q^G\right\}^T = \left\{\left\{q_u^u\right\}^T, \left\{q_v^u\right\}^T, \left\{q_w^u\right\}^T, \left\{q_u^l\right\}^T, \left\{q_v^l\right\}^T, \left\{q_w^l\right\}^T\right\} \tag{B.9}$$

the panel's contributions to the system's stiffness matrix, K, are finally

$$\Delta K_{i,j} = \frac{\partial^2 U}{\partial q_i \partial q_j} \tag{B.10}$$

where the indices, i and j, denote row elements in $\{q^G\}$, and associated rows and columns in the stiffness matrix.

Assuming simple harmonic motion and constant thickness, d, the kinetic energy of the panel segment is

$$T = \frac{1}{2}\rho d\omega^2 \int_I \left(t_I^2(s,z) + w_I^2(s,z)\right) dsdz + \frac{1}{2}\rho d\omega^2 \int_{II} \left(t_{II}^2(s,z) + w_{II}^2(s,z)\right) dsdz \tag{B.11}$$

where the integrals denote integration over the associated panel sub-segment area only. Introducing the panel aspect ratio, AR, as the ratio of L to h_1, and the integrals, I_I and I_{II}, equation (B.11) yields

$$T = \frac{1}{2}\rho d h_1 L^3 \omega^2 \left[\left(I_I(\bar{t}) + (AR)^2 I_I(\bar{w})\right) + \frac{h_2}{h_1}\left(I_{II}(\bar{t}) + (AR)^2 I_{II}(\bar{w})\right)\right] \tag{B.12}$$

with

$$I_I(\bar{t}) = \int_I \bar{t}_I^2(\sigma,\varsigma)\, d\sigma d\varsigma = \frac{1}{12}\left(\bar{t}_{l,a}^2 + \bar{t}_{l,b}^2 + \bar{t}_{u,a}^2 + \bar{t}_{l,a}\bar{t}_{l,b} + \bar{t}_{l,a}\bar{t}_{u,a} + \bar{t}_{l,b}\bar{t}_{u,a}\right) \tag{B.13a}$$

$$I_{II}(\bar{t}) = \int_{II} \bar{t}_{II}^2(\sigma,\varsigma)\, d\sigma d\varsigma = \frac{1}{12}\left(\bar{t}_{u,a}^2 + \bar{t}_{l,b}^2 + \bar{t}_{u,b}^2 + \bar{t}_{u,a}\bar{t}_{l,b} + \bar{t}_{u,a}\bar{t}_{u,b} + \bar{t}_{l,b}\bar{t}_{u,b}\right). \tag{B.13b}$$

The corner displacements are then expressed in terms of the comparison functions according to (B.2) and (B.9). The panel segment's contributions to the system's mass matrix, M, are finally

$$\Delta M_{i,j} = \frac{\partial^2 T}{\partial q_i \partial q_j} \tag{B.14}$$

B.2. Comparison with ASTROS Finite Element Model - Dynamic Analysis

Correlation of this extended equivalent plate analysis, denoted ELAPS* in this section, with the original ELAPS and the finite element analysis in ASTROS was performed using a sample case for a large, swept, high aspect ratio jet transport wing, a sample case from the ASTROS User's Training Workshop /Venkayya et al. 94/. Figure B.2 depicts the geometry of this structure. Some differences between the ELAPS and ASTROS models could not be avoided due to modeling restrictions in ELAPS, as indicated in Fig. B.2. Plate and shear panel thicknesses are listed in Table B.1. Both models include 21 ribs (perpendicular to spars, 0.1 in. thick), which are not shown in Fig. B.2. Shear web masses are included as concentrated masses in the original ELAPS input; rods in ASTROS are modeled as concentrated masses in both ELAPS representations. In the "ELAPS + Shear Panels" (ELAPS*) case, the wing is rotated such that the spars are roughly parallel to the spanwise coordinate, which resulted in a reduced number of comparison functions necessary to reach reasonable convergence. It was observed that convergence also depended on the aspect ratio of the panel elements; choosing the number

of integration intervals - equivalent to the number of panel elements into which a shear panel is divided - such that the aspect ratio is approximately three yielded the best results. The root is clamped in all cases. Since ELAPS allows only planforms with inboard and outboard boundaries in chordwise orientation (parallel to the x-axis), springs approximate proper support conditions in the upgraded ELAPS model.

Fig. B.3 and Table B.2 show comparisons of modal analyses obtained with the three different models. The modes are plotted and listed, respectively, in the order in which they are predicted by ASTROS. The "mode type" refers to the dominant characteristic; for example, "1B" is the first beamwise mode, "2C" the second chordwise mode, and "2T" the second torsional mode. The order of the ELAPS modes 5 and 6 are swapped to more closely resemble the ASTROS mode shapes. Fig. B.3 indicates that inclusion of shear panels improved natural frequency correlation of the torsionally dominated modes by more than 60%. A slight increase in beamwise bending mode frequency is also detectable. One contribution to this effect can be explained as follows: The wing box thickness decreases from root to tip, hence the skins exhibit slight spanwise slopes with respect to the x,y-plane. Since the individual reference planes for each skin are parallel to the x,y-plane (see Section 3.2.3.1.), there are small vertical offsets of the skins with respect to their reference plane. The Kirchhoff kinematic assumptions are still active in each of the skin displacement systems, so this offset adds bending stiffness even if the skin itself is modeled as a membrane.

Another possible reason is the introduction of shear into the triangular subelement through pure bending of the structure: Consider the element in Fig. 3.3, and assume that h_1 and h_2 are constant (no change in crossection). In pure bending without shear, the corners ((l,a), (u,a)) and ((l,b), (u,b)) remain perpendicular to the panel center line. The

deflection of (l,b), however, generates a constant shear deflection in the inscribed subelement I (similarly for subelement II). In a more general interpretation, the deviations are related to the assumption of constant shear deflection in each subelement.

A more practical explanation are the slight differences between the three models. Some ASTROS elements had to be approximately included in ELAPS, as described in the previous paragraph, so that deviations had to be expected.

The generalized masses in Table B.2 give an indication for the correlation of the mode shapes with the ASTROS baseline. The mode shapes are plotted in Figs. B.4 to B.9; the darker lines indicate the trailing edge deflection of the structural box, the lighter lines the leading edge displacements; the dashed lines are the ASTROS baseline results, the solid lines depict displacements calculated with the updated ELAPS*. The maximum order of the comparison functions used in ELAPS* is eight spanwise and three chordwise, since numerical errors in the library routines increase excessively with function order and cause the program to terminate with an error. Note that the mode shapes in Fig. B.8 and B.9 require at least a sixth order polynomial in the normalized spanwise coordinate, y. Correlation can therefore be expected to decrease significantly starting with the sixth mode. The first three modes, however, are in excellent agreement with the ASTROS baseline. Note that the erratic behavior of chordwise deflections for ELAPS* modes 2 and 4 (Fig. B.5b and B.7b) is within 0.1% and 1% of the beamwise deflection, and can therefore be attributed to rounding errors. Deviations of ELAPS leading edge mode shapes from the ASTROS baseline in the outermost 15-20% of the span were attributed to additional mass at the leading edge, resulting from the rotation of the ELAPS coordinate system. Due to geometry modeling limitations, the ELAPS planform featured an small triangular element filling the planform between the actual tip, which is oriented in streamwise direction, and the model's tip, which is parallel to the x-axis (dashed lines in Fig. B.2).

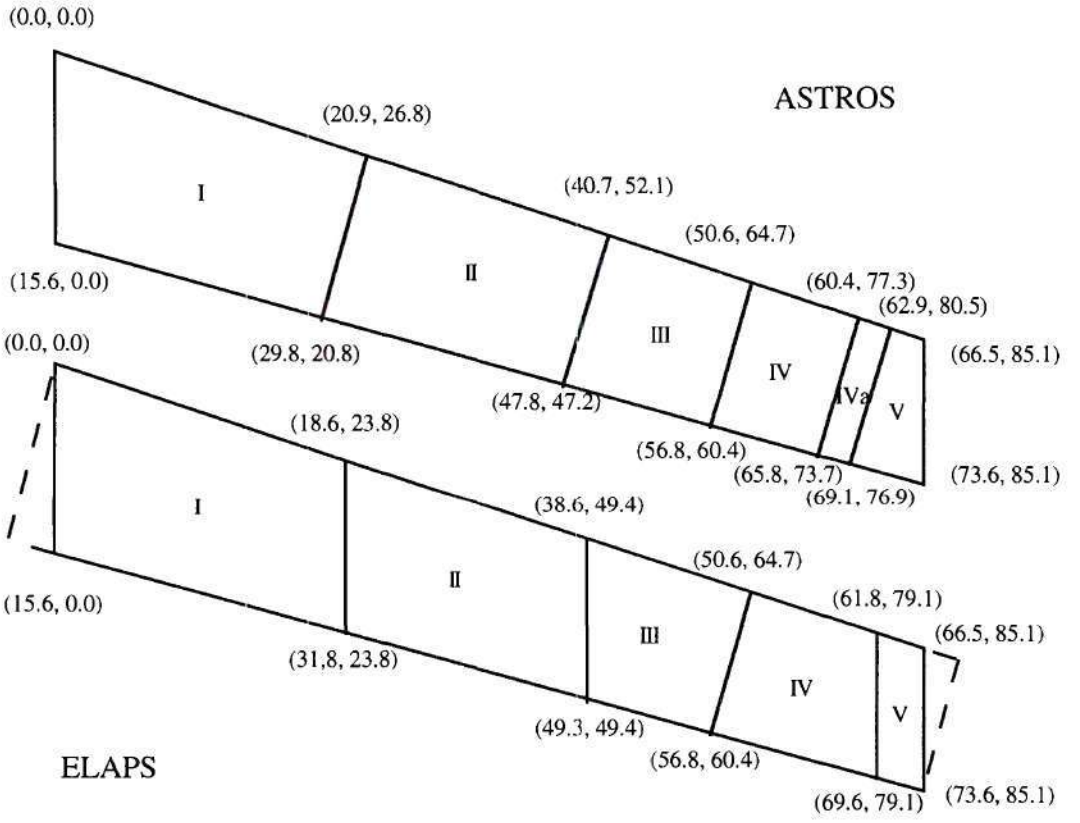

all coordinates in ft

Fig. B.2: Sample Wing Layout in ASTROS and in ELAPS

Table B.1: Sample Wing Internal Layout

	Plate Thickness [in]		Spar Web Thickness [in]	
Segment	ELAPS	ASTROS	ELAPS	ASTROS
I	0.300	0.300	0.200	0.200
II	0.200	0.200	0.160	0.160
III	0.125	0.125	0.120	0.120
IV	0.125	0.125	0.110	0.110
IVa	-	0.125	-	0.100
V	0.100	0.100	0.100	0.100

segment numbers refer to Fig. B.2, not to ELAPS planform segments

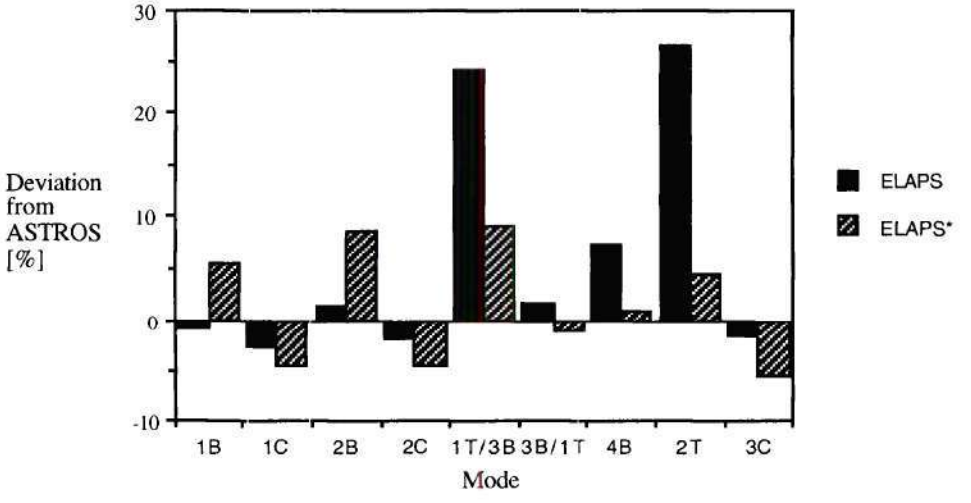

Fig. B.3: Correlation of Natural Frequencies from ELAPS and ELAPS* (with Shear Panels) with ASTROS Baseline

Table B.2: Comparison of Generalized Masses

Mode Type	Baseline Values ASTROS	Deviation original ELAPS	Deviation ELAPS + Shear Panel
1B	120.3	+ 2.1% (1)	+ 2.0% (1)
1C	228.2	+ 1.2% (2)	- 0.4% (2)
2B	95.3	+ 9.3% (3)	+ 12.7% (3)
2C	232.7	+ 11.5% (4)	+ 16.1% (4)
1T / 3B	114.1	- 35.8% (6)	- 52.6% (6)
3B / 1T	138.8	- 26.8% (5)	- 43.0% (5)
4B	68.3	+74.9% (7)	+ 206% (7)
2T	109.6	- 43.7% (8)	- 54.1% (8)
3C	248.3	- 20.3% (9)	- 37.1% (9)

Units: slugs-ft^2;
Mode Normalization: Maximum Translation per Coordinate 1 ft

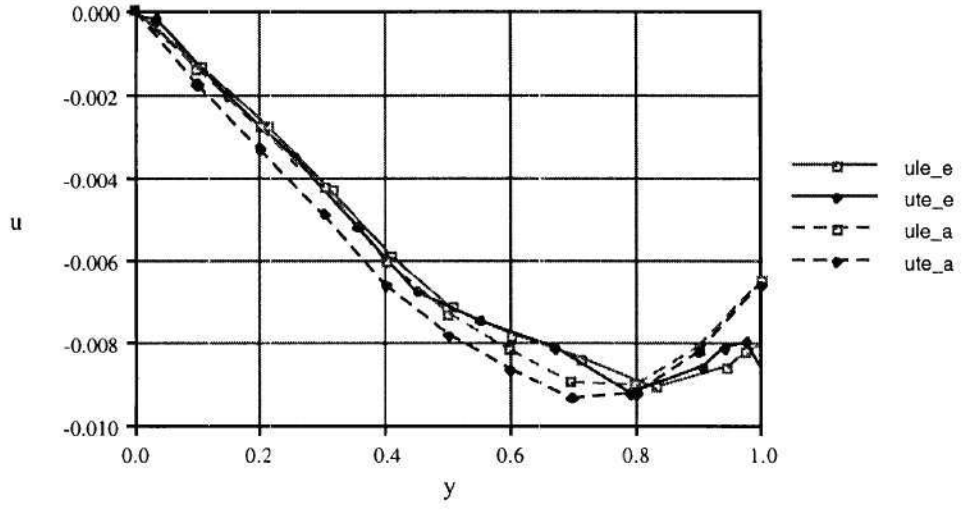

Fig. B.4(a): ELAPS* and ASTROS Mode Shapes, Mode 1

(chordwise deflection)

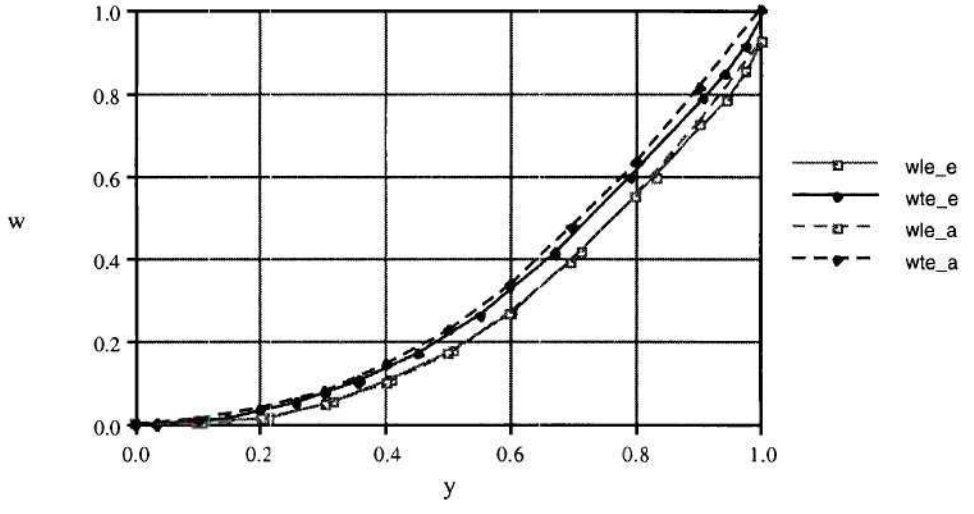

Fig. B.4(b): ELAPS* and ASTROS Mode Shapes, Mode 1

(beamwise deflection)

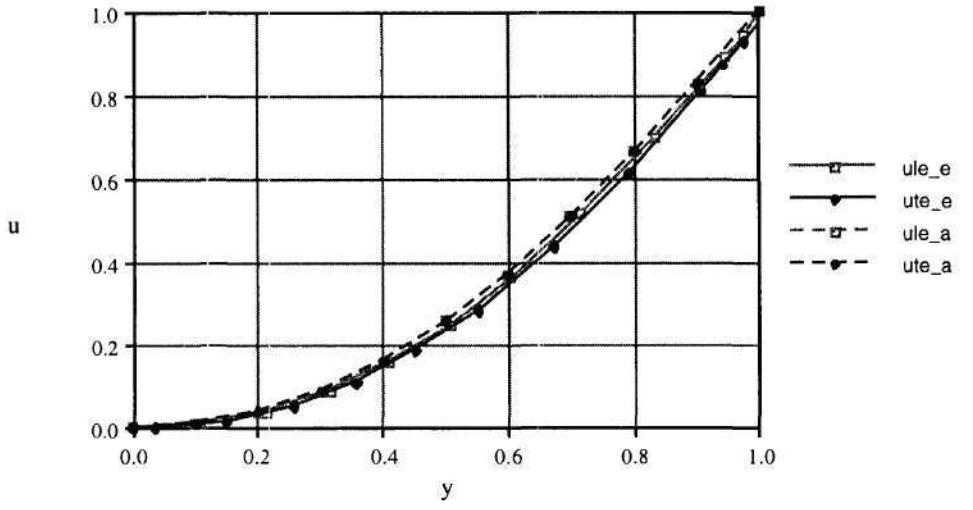

Fig. B.5(a): ELAPS* and ASTROS Mode Shapes, Mode 2

(chordwise deflection)

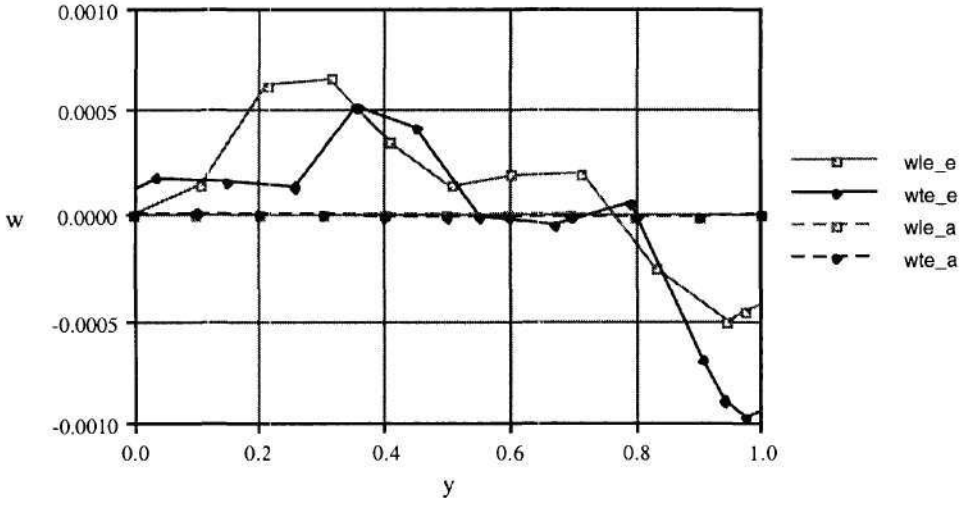

Fig. B.5(b): ELAPS* and ASTROS Mode Shapes, Mode 2

(beamwise deflection)

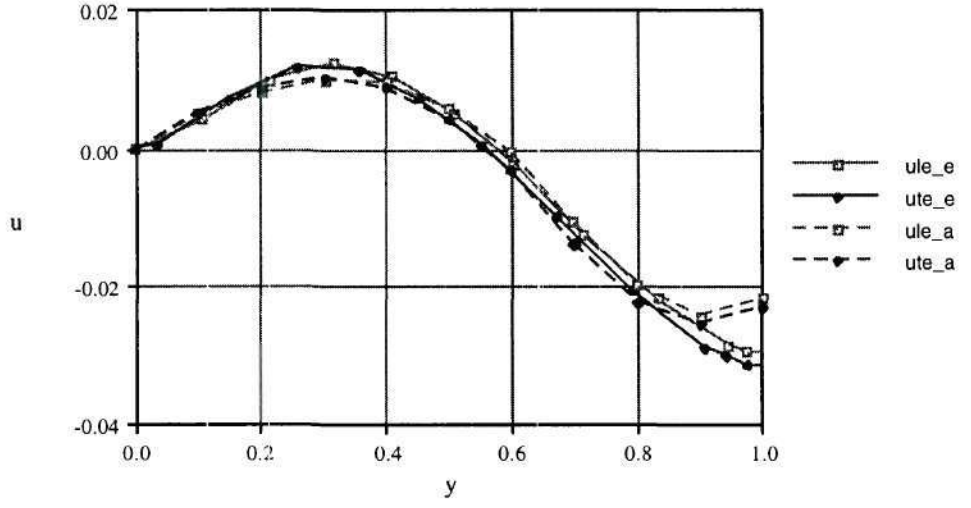

Fig. B.6(a): ELAPS* and ASTROS Mode Shapes, Mode 3

(chordwise deflection)

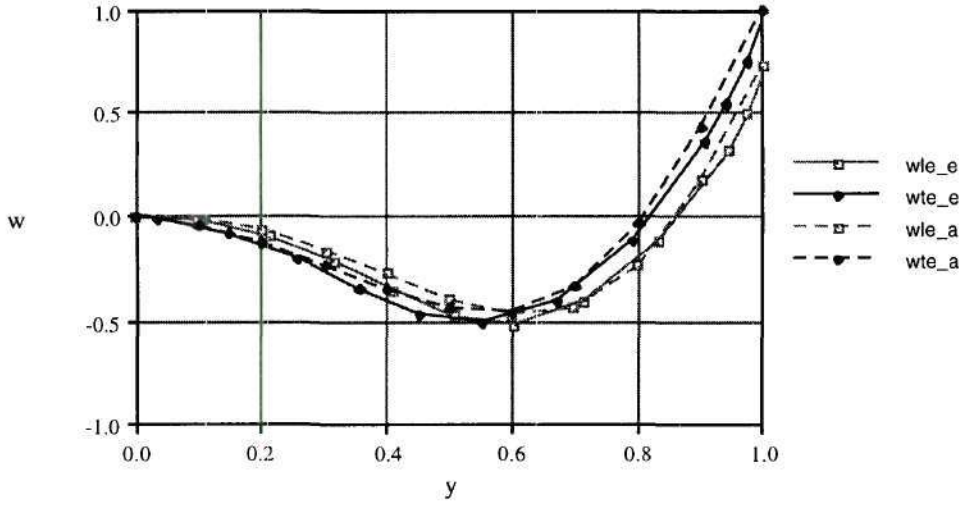

Fig. B.6(b): ELAPS* and ASTROS Mode Shapes, Mode 3

(beamwise deflection)

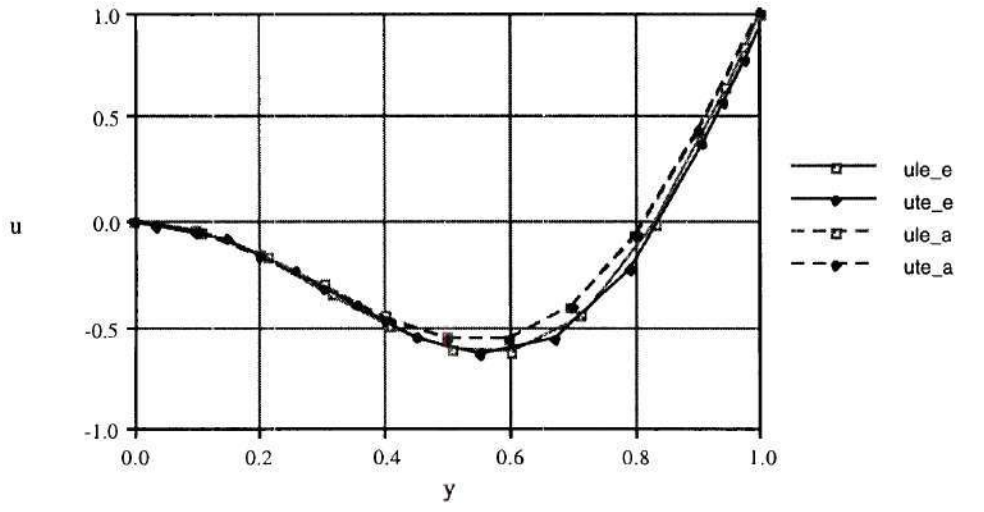

Fig. B.7(a): ELAPS* and ASTROS Mode Shapes, Mode 4

(chordwise deflection)

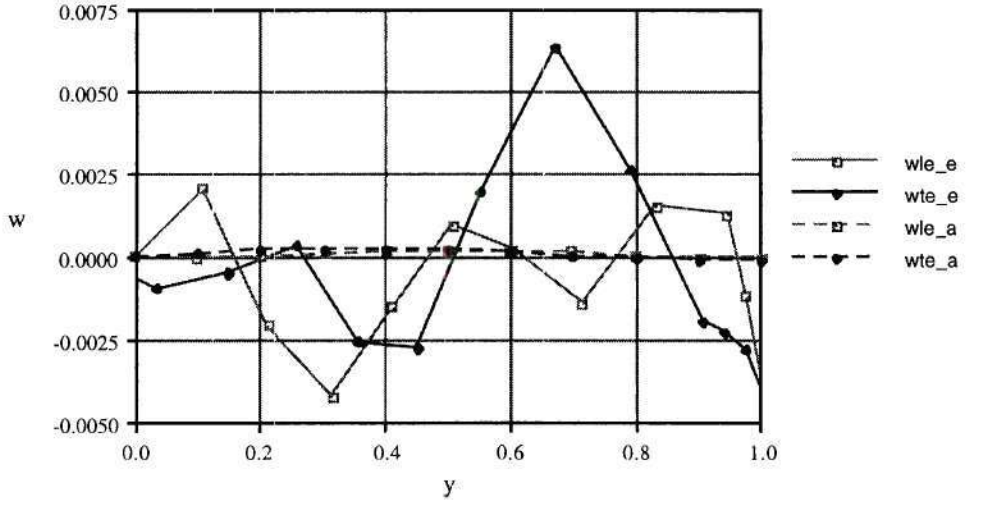

Fig. B.7(b): ELAPS* and ASTROS Mode Shapes, Mode 4

(beamwise deflection)

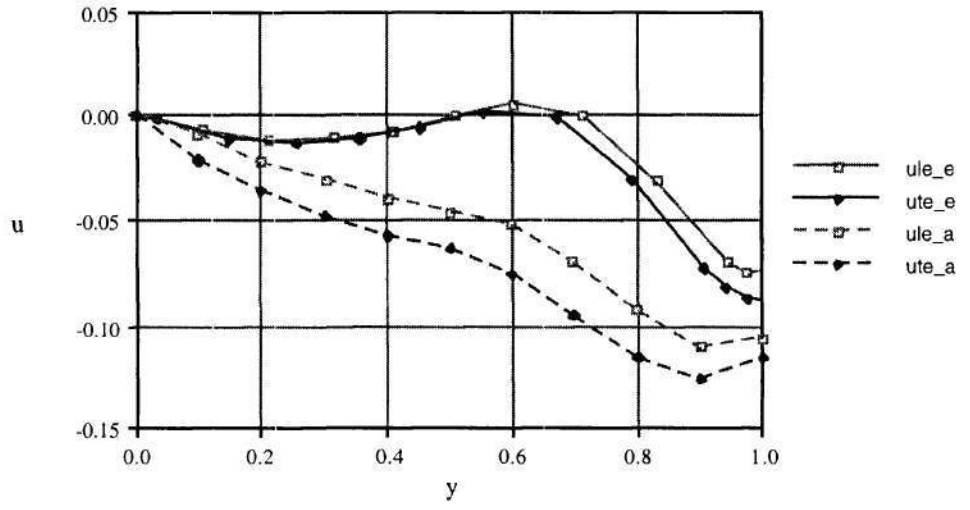

Fig. B.8(a): ELAPS* and ASTROS Mode Shapes, Mode 5

(chordwise deflection)

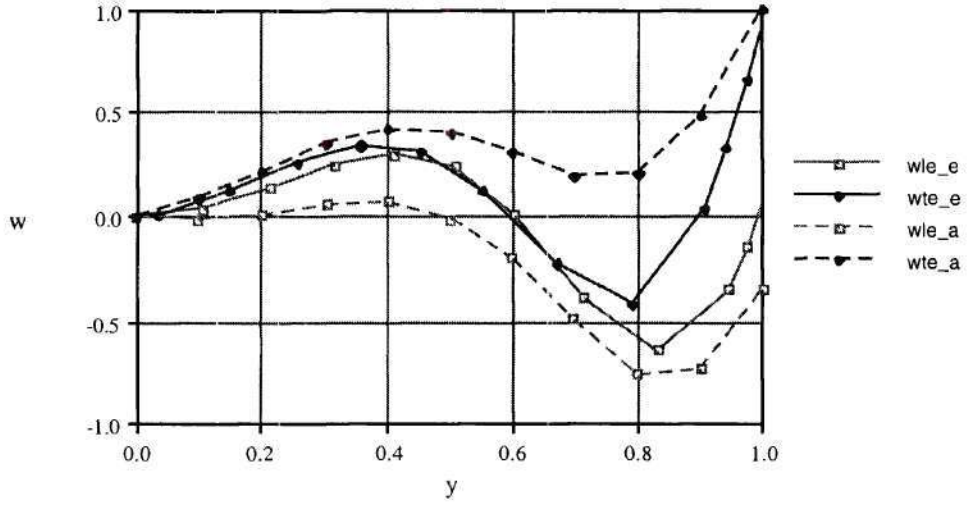

Fig. B.8(b): ELAPS* and ASTROS Mode Shapes, Mode 5

(beamwise deflection)

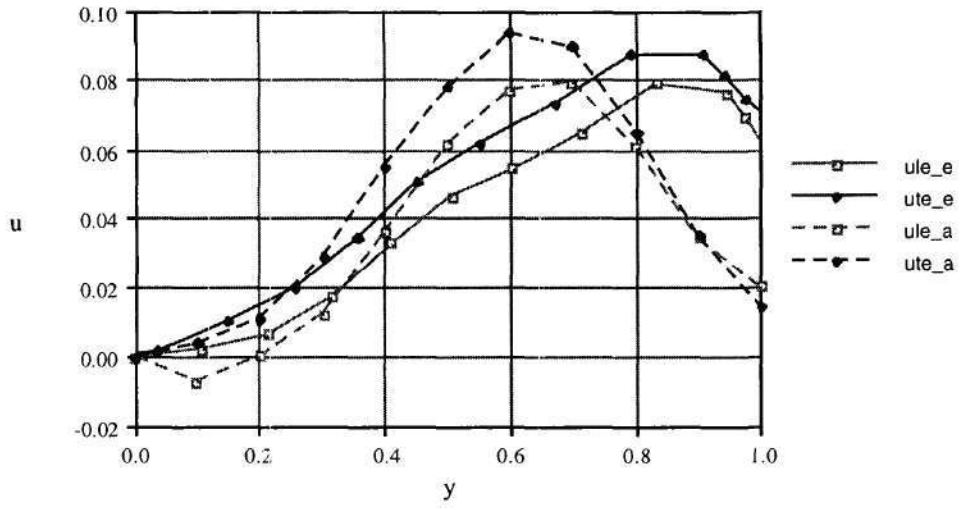

Fig. B.9(a): ELAPS* and ASTROS Mode Shapes, Mode 6

(chordwise deflection)

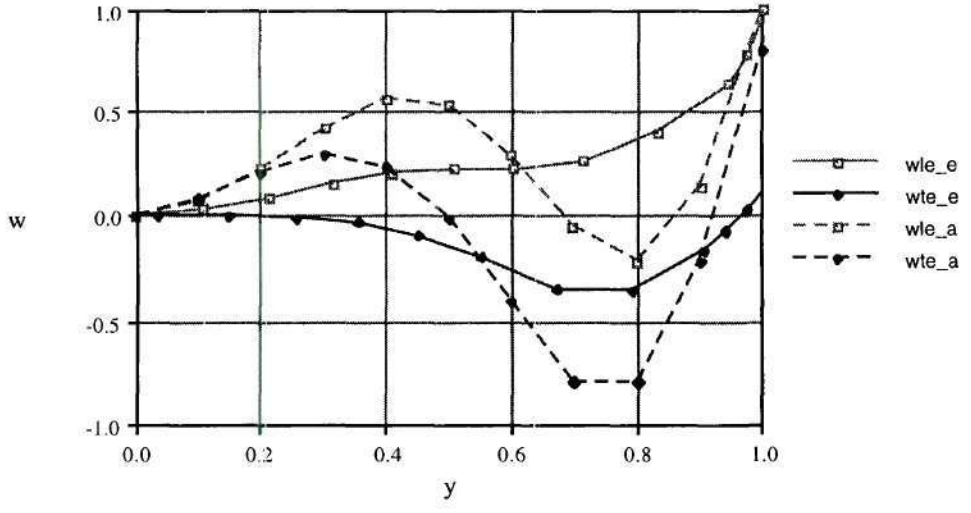

Fig. B.9(b): ELAPS* and ASTROS Mode Shapes, Mode 6

(beamwise deflection)

APPENDIX C

APPLICATION OF A FINITE-STATE WAKE MODEL TO FIXED-WING UNSTEADY AERODYNAMICS

The following sections describe the coupled airframe / unsteady aerodynamics model employed in the Tool "pwake." Unless otherwise noted, all entities shown in figures, tables, and equations in this Appendix are normalized in the following way: Length is divided by the reference disk radius, $\boldsymbol{R}$; velocity by the reference velocity, $\boldsymbol{U}$ (freestream velocity, $\boldsymbol{V_\infty}$); time by $\boldsymbol{R/U}$; frequency by $\boldsymbol{U/R}$; mass and inertia by $\rho\boldsymbol{R^3}$ and $\rho\boldsymbol{R^5}$, respectively; lift per unit length by $\rho\boldsymbol{U^2R}$ (ρ is the air density); pressure or moment per unit length by $\rho\boldsymbol{U^2R^2}$. Terms in bold, italic face denote dimensional entities.

C.1. Airloads Model (Inner Problem)

The airloads model utilizes quadratically cambered, flapped, thin airfoil sections, arranged in streamwise direction on a wing of trapezoidal planform, Fig. C.1. The reference disk was chosen to encompass the entire wing area as depicted; the reference disk radius, $\boldsymbol{R}$, is described by

$$\boldsymbol{R} = \sqrt{\left(\frac{\boldsymbol{S}}{\cos\Lambda}\right)^2 + \boldsymbol{b_{tip}}^2 - 2\frac{\boldsymbol{S}}{\cos\Lambda}\boldsymbol{b_{tip}}\sin\left(\tan^{-1}\left(\tan\Lambda + \frac{\boldsymbol{b_{tip}}}{\boldsymbol{S}}\right)\right)} \qquad \text{(C.1)}$$

with the wing semi-span, $\boldsymbol{S}$, tip chord, $\boldsymbol{b_{tip}}$ (both dimensional) and half chord sweep angle, Λ. The vertical location of the unflapped, deflected airfoil with initial angle of attack, α_0, initial camber, ξ_0 (normalized by the local dimensional semi chord, $\boldsymbol{b}$), elastic twist and camber, α and ξ, and half chord elastic vertical deflection, w, as a function of the Glauert angle, θ, for this configuration is

$$z(\theta,y,t) = w(y,t) - \left(\alpha_0 + \alpha(y,t)\right) b(y)\cos\theta - \left(\xi_0 + \xi(y,t)\right)\left(b(y)\cos\theta\right)^2 \qquad \text{(C.2)}$$

For notational simplicity, the dependency of the normalized spanwise coordinate, y, is dropped in the following expressions. Using equation (C.2), the normalwash, ω, along the airfoil due to airfoil translation (u and w), twist (α and α_0), camber (ξ and ξ_0), external disturbances (V_h and V_v), flap deflection (δ), and steady-state induced angle of attack (α_i) is

$$\omega_{unflapped}(\theta,t) = \left(1 + V_h(t) - u(t)\right)\left(\alpha_0 + \alpha_i + \alpha(t) + 2\left(\xi(t) + \xi_0\right)\cos\theta\right)$$

$$-w^*(t) + b\cos\theta\left(\alpha^*(t) + \xi^*(t)\cos\theta\right) + V_v(t);\ \pi > \theta > \theta_d \qquad \text{(C.3a)}$$

$$\omega_{flapped}(\theta,t) = \omega_{unflapped}(\theta,t) + \left(1 + V_h(t) - u(t)\right)\delta(t) - b\,\delta^*(t)\cos\theta_d;\ 0 < \theta < \theta_d \qquad \text{(C.3b)}$$

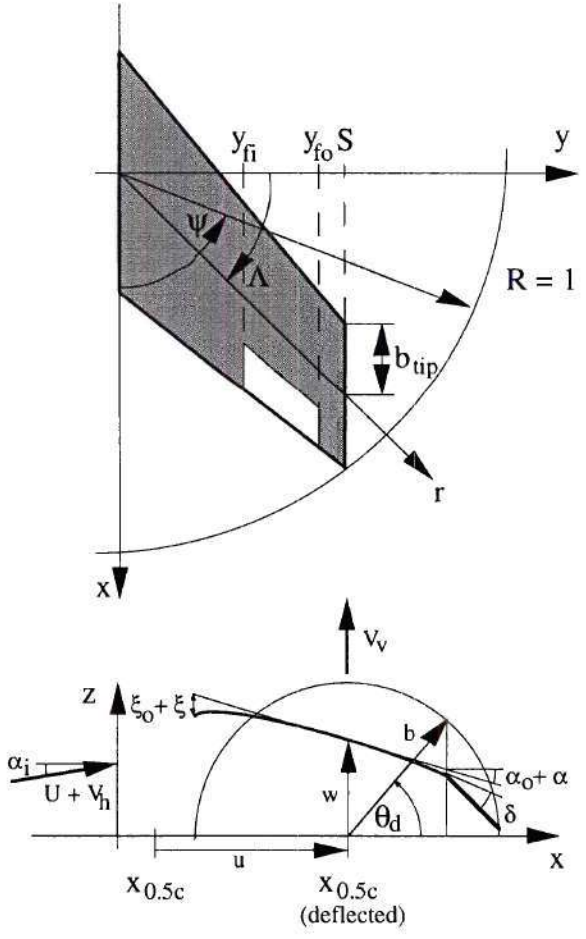

Fig. C.1: Wing / Airfoil Geometry

The asterisk denotes a derivative with respect to non-dimensional time. If this normalwash is expanded into a Fourier Series in the Glauert coordinate, θ, the following linearized coefficients are obtained:

$$\omega_0(t) = -(\alpha_0 + \alpha_i)\, u(t) - w^*(t) + \alpha(t) + \tfrac{1}{2} b\, \xi^*(t)$$

$$+D_0\, \delta(t) + D_{0s}\, b\, \delta^*(t) + V_v(t) + (\alpha_0 + \alpha_i)\, V_h(t) \qquad \text{(C.4a)}$$

$$\omega_1(t) = -\xi_0\, u^*(t) + b\, \alpha^*(t) + 2\xi(t) + D_1\, \delta(t) + D_{1s}\, b\, \delta^*(t) + \xi_0\, V_h(t) \qquad \text{(C.4b)}$$

$$\omega_2(t) = \tfrac{1}{2} b\, \xi^*(t) + D_2\, \delta(t) + D_{2s}\, b\, \delta^*(t) \qquad \text{(C.4c)}$$

$$\omega_i(t) = D_i\, \delta(t) + D_{is}\, b\, \delta^*(t); \quad i > 2 \qquad \text{(C.4d)}$$

where

$$D_0 = \tfrac{1}{\pi}\theta_d; \quad D_{0s} = -\tfrac{1}{\pi}\left(\theta_d \cos(\theta_d) - \sin(\theta_d)\right) \qquad \text{(C.5a)}$$

$$D_1 = \tfrac{2}{\pi}\sin(\theta_d); \quad D_{1s} = \tfrac{1}{\pi}\left(\theta_d - \tfrac{1}{2}\sin(2\,\theta_d)\right) \qquad \text{(C.5b)}$$

$$D_2 = \tfrac{1}{\pi}\sin(2\,\theta_d); \quad D_{2s} = \tfrac{1}{2\pi}\left(\sin(\theta_d) - \tfrac{1}{3}\sin(3\,\theta_d)\right) \qquad \text{(C.5c)}$$

$$D_j = \tfrac{1}{\pi}\tfrac{j-1}{j}\sin(j\,\theta_d); \quad D_{js} = \tfrac{1}{j\pi}\left(\tfrac{1}{j-1}\sin((j-1)\,\theta_d) - \tfrac{1}{j+1}\sin((j+1)\,\theta_d)\right); \quad j > 2 \qquad \text{(C.5d)}$$

The equivalent expressions for the induced inflow Fourier expressions can be obtained by applying the Fourier transformation to the inflow distribution (equation (3.16), here only shown for a symmetric system)

$$\lambda(r, \psi, t) = \sum_{m,n} \frac{\overline{P}_n^m(\nu)}{\nu} \cos(m\psi)\, a_n^m(t) \qquad \text{(C.6)}$$

which results in

$$\lambda_0(y,t) = \sum_{m,n} \lambda_{n;0}^{m;c}(y)\, a_n^m(t); \quad \lambda_1(y,t) = \sum_{m,n} \lambda_{n;1}^{m;c}(y)\, a_n^m(t) \tag{C.7}$$

where (from equation (3.26))

$$\lambda_{j;0}^{r;c}(y) = \frac{1}{\pi}\int_0^\pi \frac{\overline{P}_j^r(\nu)}{\nu}\cos(r\psi)\, d\theta; \quad \lambda_{j;1}^{r;c}(y) = \frac{2}{\pi}\int_0^\pi \frac{\overline{P}_j^r(\nu)}{\nu}\cos(r\psi)\cos(\theta)\, d\theta \tag{C.8}$$

Expressions (C.4) and (C.7) can now be used in the following equations from /Peters and Su 91/ in order to obtain the nondimensional lift, pitching moment about half chord, and drag per unit length (L, M, and D, respectively; D has been linearized):

$$L(y,t) = 2\pi b(y)\left(\omega_0(y,t) + \tfrac{1}{2}\omega_1(y,t) - \lambda_0(y,t)\right) + \pi b^2(y)\left(\omega_0{}^*(y,t) - \tfrac{1}{2}\omega_2{}^*(y,t)\right) \tag{C.9a}$$

$$M(y,t) = \pi b^2(y)\left(\omega_0(y,t) - \tfrac{1}{2}\omega_2(y,t) - \lambda_0(y,t)\right) + \tfrac{\pi}{8} b^3(y)\left(\omega_1{}^*(y,t) - \omega_3{}^*(y,t)\right) \tag{C.9b}$$

$$D(y,t) = -2\pi b(y)\left(\alpha_0 + \alpha_i(y)\right)\left(2\omega_0(y,t) + \tfrac{1}{2}\omega_1(y,t) - 2\lambda_0(y,t) - \tfrac{1}{2}\lambda_1(y,t)\right) \tag{C.9c}$$

The values, $\lambda_0(y,t)$ and $\lambda_1(y,t)$ are the first and second coefficients of the induced inflow Fourier Series in θ (similar to $\omega_0(y,t)$ and $\omega_1(y,t)$). The normalwash coefficients can now also be replaced in the expression for the circulatory lift as given in equation (3.24):

$$L_\tau(y,t) = 2\pi b(y)\left[\left(\omega_0(y,t) + \tfrac{1}{2}\omega_1(y,t)\right) - \left(\lambda_0(y,t) + \tfrac{1}{2}\lambda_1(y,t)\right)\right] \tag{C.10}$$

It is worthwhile to note that $\lambda_1(y,t)$ is found in the circulatory lift, equation (C.10), but not in the complete lift expression, equation (C.6a), which also include non-circulatory contributions. /Johnson 80a/ developed expressions for sums of induced flow Fourier coefficients for a flat wake; based on these expressions, the following equalities can be established:

$$\lambda_1 = -b\left(\lambda_0^* - \tfrac{1}{2}\lambda_2^*\right) \tag{C.11a}$$

$$2(n+1)\lambda_{n+1} = -b\left(\lambda_n^* - \tfrac{1}{2}\lambda_{n+2}^*\right);\ n > 0 \tag{C.11b}$$

Equation (C.11a) applies in the case of total lift calculation, where part of the circulatory contribution (λ_1) is canceled by part of the non-circulatory contribution in from of the negative right-hand-side of equation (C.8a).

C.2. Aerodynamics-Structures Coupling

C.2.1. Structural Dynamics

Consider an undamped wing structural system with the generalized coordinates, q_k, which is excited by a vector of generalized forces, f_k:

$$[MS_u]\{q_k\}^{**} + [KS]\{q_k\} = \{f_k\} \tag{C.12}$$

If the generalized coordinates are associated with N modes of the homogeneous system, then the deflection vector, d, containing the wing half chord chordwise and beamwise deflection, u and w, twist, α, and elastic quadratic camber, ξ, can be expanded in the form

$$\{d\} = \begin{Bmatrix} u(y,t) \\ w(y,t) \\ \alpha(y,t) \\ \xi(y,t) \end{Bmatrix} = \sum_{k=1}^{N} \begin{Bmatrix} u_k(y) \\ w_k(y) \\ \alpha_k(y) \\ \xi_k(y) \end{Bmatrix} q_k(t) \tag{C.13}$$

and the mass and stiffness matrices assume a diagonal form,

$$[MS_u] = \text{diag}\,(m_k); \quad [KS] = \text{diag}\,(m_k \omega_k{}^2) \tag{C.14}$$

where m_k are the generalized masses of the undamped system modes, equation (C.13), and ω_k are the associated natural frequencies, normalized according to the conventions described at the beginning of this Appendix. It is assumed at this point that the wing structure is analyzed for one half wing only. Neglecting effects of aerodynamic forces on quadratic camber, the generalized forces, f_k, are in the form

$$f_k(t) = \int_0^S \left[u_k(y)\, D(y,t) + w_k(y)\, L(y,t) + \alpha_k(y)\, M(y,t)\right] dy + \sum_l \left\{WU_k^l\right\}^T \left\{F^l\right\} \tag{C.15}$$

which includes aerodynamic contributions and the influence of discrete external forces at location l, $\{F^l\}$, where $\left\{WU_k^l\right\}$ are the structural deflections and rotations at location l in mode k. Full expansion of the drag, lift and moment terms according to equation (C.9) and substitution of the normalwash and induced inflow Fourier coefficients by equations (C.4) and (C.7), respectively, converts the structural system, (C.12) into a dynamic system with both structural and inflow states:

$$\text{diag}\,(m_k)\{q_k\}^{**} + \text{diag}\,(m_k \omega_k{}^2)\{q_k\} = [MSS]\{q_j\}^{**} + [DSS]\{q_j\}^{*} + [KSS]\{q_j\}$$

$$+ [KIS]\left\{a_n^m\right\} + \left[\{CS2\}\,\{CS1\}\,\{CS0\}\right]\begin{Bmatrix} \delta^{**} \\ \delta^{*} \\ \delta \end{Bmatrix} \tag{C.16}$$

$$+ \left[\{GS1V\}\,\{GS1H\}\,\{GS0V\}\,\{GS0H\}\right]\begin{Bmatrix} V_v^{*} \\ V_h^{*} \\ V_v \\ V_h \end{Bmatrix} + \sum_l \left[WU^l\right]^T \left\{F^l\right\}$$

The matrix and vector elements are found by collecting the appropriate terms, and are listed below. Superscripts and subscripts indicate the location within that matrix. Since the inflow coefficients are determined by a combination of subscript (n, radial polynomial order) and superscript (m, azimuthal harmonics order), indices before a comma stand for the row, after the comma for the column. Except for the initial angle of attack and camber, a_0 and x_0, all terms in the integrals are functions of the spanwise coordinate, y. The explicit denotation of this dependency has therefore been dropped.

$$MSS^{k,j} = 2\pi\int_0^S b\left\{-\tfrac{1}{2}b\left[w_j + (\alpha_0+\alpha_i)\,u_j + \tfrac{1}{8}b^2\xi_j\right]w_k - \left[\tfrac{1}{8}b\,u_j + \tfrac{1}{16}b^2\alpha_j\right]b\,\alpha_k\right\}dy \tag{C.17}$$

$$DSS^{k,j} = 2\pi\int_0^S b\left\{-2(\alpha_0+\alpha_i)\left[-(\alpha_0+\alpha_i+\tfrac{1}{2}\xi_0)\,u_j - w_j + \tfrac{1}{4}b\,\alpha_j + \tfrac{1}{2}b\,\xi_j\right]u_k + \left[-(\alpha_0+\alpha_i+\xi_0)\,u_j - w_j + \tfrac{1}{2}b\,\alpha_j + b\,\xi_j\right]w_k + \left[-\tfrac{1}{2}(\alpha_0+\alpha_i)\,u_j - \tfrac{1}{2}w_j + \tfrac{1}{4}b\,\xi_j\right]b\,\alpha_k\right\}dy \tag{C.18}$$

$$KSS^{k,j} = 2\pi\int_0^S b\left\{-(\alpha_0+\alpha_i)\left[2\alpha_j + \xi_j\right]u_k + \left[\alpha_j + \xi_j\right]w_k + \tfrac{1}{2}b\,\alpha_j\,\alpha_k\right\}dy \tag{C.19}$$

$$KIS^{k,m}_{-,n} = -2\pi\int_0^S b\,\lambda^{m;c}_{n;0}\left\{-2(\alpha_0+\alpha_i)\,u_k + w_k + \tfrac{1}{2}b\,\alpha_k\right\}dy \tag{C.20}$$

$$CS2^{k,-} = 2\pi\int_{y_{fi}}^{y_{fo}} b^3\left\{\tfrac{1}{2}\left[D_{0s} - \tfrac{1}{2}D_{2s}\right]w_k - \tfrac{1}{16}\left[D_{1s} - D_{3s}\right]b\,\alpha_k\right\}dy \tag{C.21}$$

$$CS1^{k,-} = 2\pi\int_{y_{fi}}^{y_{fo}} b^2\left\{-2(\alpha_0+\alpha_i)\left[D_{0s} - \tfrac{1}{4}D_{1s}\right]u_k + \tfrac{1}{2}\left[2D_{0s} + D_{1s} + D_0 - \tfrac{1}{2}D_2\right]w_k + \tfrac{1}{2}\left[D_{0s} - \tfrac{1}{2}D_{2s} - \tfrac{1}{8}D_1 + \tfrac{1}{8}D_3\right]b\,\alpha_k\right\}dy \tag{C.22}$$

$$CS0^{k,-} = 2\pi\int_{y_{fi}}^{y_{fo}} b\left\{-2(\alpha_0+\alpha_i)\left[D_0 + \tfrac{1}{4}D_{1s}\right]u_k + \left[D_0 + \tfrac{1}{2}D_1\right]w_k + \left[D_0 - \tfrac{1}{2}D_2\right]b\,\alpha_k\right\}dy \tag{C.23}$$

$$GS1V^{k,-} = \pi \int_0^S b^2 \, w_k \, dy \tag{C.24}$$

$$GS1H^{k,-} = 2\pi \int_0^S b^2 \left\{ \tfrac{1}{2}(\alpha_0 + \alpha_i) w_k - \tfrac{1}{8} \xi_0 \, b \, \alpha_k \right\} dy \tag{C.25}$$

$$GS0V^{k,-} = 2\pi \int_0^S b \left\{ -2(\alpha_0 + \alpha_i) u_k + w_k + \tfrac{1}{2} b \, \alpha_k \right\} dy \tag{C.26}$$

$$GS0H^{k,-} = 2\pi \int_0^S b \left\{ -2(\alpha_0 + \alpha_i)\left(\alpha_0 + \alpha_i + \tfrac{1}{2}\xi_0\right) u_k + \left(\alpha_0 + \alpha_i + \xi_0\right) w_k \right.$$

$$\left. + \tfrac{1}{2}(\alpha_0 + \alpha_i) b \, \alpha_k \right\} dy \tag{C.27}$$

C.2.2. Wake Dynamics

For cases symmetric about the aircraft center line, the wake system can be described using the cosine partition only (equation (3.17)):

$$\left[M^c\right]\left\{a_j^r\right\}^* + \left[N^c\right]\left\{a_j^r\right\} = \tfrac{1}{2}\left\{\tau_n^{m,c}\right\} \tag{C.28}$$

The superscript, m (or r), and subscript, n (or j), of the wake forcing function denote the number of azimuthal harmonics and the order of the radial expansion of the induced flow distribution, equation (C.6), respectively. The normalized associated Legendre functions of the first kind, $\overline{P}_n^m$, in (C.6) are only defined for n > m, and (C.6) only models a pressure discontinuity on the reference disk for (n+m) odd. As a result, only the combinations n = m+1, n = m+3, n = m+5, etc. are considered, which suggests partitioning of wake system matrices and vectors by harmonics number, m, and ordering the elements within each partition by polynomial order, n. The inflow expansion, equation (C.6), contains strictly speaking an infinite number of terms; in a practical application, however, this series is truncated by choosing the maximum order of azimuthal harmonics,

M, such that n = m+1, n = m+3, n = m+5, ..., n = M or M+1, and m = 0, 1, 2, ... , M (cosine partition; the sine partition lacks m = 0 terms).

The "wake mass matrix," $[M^c]$, is of the following form (/Peters and He 87/):

$$\left[M^c\right] = \text{diag}\left(\frac{2}{\pi} H_n^m\right); \quad H_n^m = \frac{(n+m-1)!!\,(n-m-1)!!}{(n+m)!!\,(n-m)!!} \tag{C.29}$$

where the double factorial is a short hand notation for the product

$$j!! = j(j-2)(j-4)(j-6)\ldots(2 \text{ or } 1); \quad (-1)!! = 1;\, 0!! = 1;\, (-3)!! = -1 \tag{C.30}$$

Calculation of the "wake damping matrix," $[N^c]$, is more involved. The general form of this matrix is

$$\left[N^c\right] = \left[\tilde{L}\right]^{-1} \tag{C.31}$$

with the matrix elements

$$\tilde{L}_{n,j}^{m,r} = \begin{cases} \dfrac{(-1)^{\frac{n+j-2r}{2}}}{\sqrt{H_n^m\, H_j^r}} \dfrac{2(2n+1)(2j+1)}{(j+n)(j+n+2)\left[(j-n)^2-1\right]} & r+m \quad \text{even} \\ \dfrac{\pi}{2\sqrt{H_n^m\, H_j^r}} \dfrac{\text{sgn}(r-m)}{\sqrt{(2n+1)(2j+1)}} & r+m \quad \text{odd}; \quad j = n \pm 1 \\ 0 & r+m \quad \text{odd}; \quad j \neq n \pm 1 \end{cases} \tag{C.32}$$

These expressions are a closed form representation of the L-operator in equation (3.14a). A closed form solution of the inversion in equation (C.31) for an infinite number of terms was reported by /Wang 92/:

$$\left(N^c\right)_{n,j}^{m,r} = \begin{cases} \dfrac{\sqrt{(2n+1)(2j+1)H_n^m H_j^r}}{\pi^2} \dfrac{(-1)^{\frac{n+j-2}{2}} 2(2r+1)(2m+1)}{(r+m)(r+m+2)\left[(r-m)^2-1\right]} & \text{I} \\ \pm(-1)^{\frac{n+j-1}{2}} \dfrac{\sqrt{(2n+1)(2j+1)H_n^m H_j^r}}{\pi} \dfrac{\operatorname{sgn}(r-m)}{2} & \text{II} \\ 0 & \text{III} \end{cases} \qquad \text{(C.33)}$$

according to the cases described in Table C.1. Both (C.32) and (C.33) are only valid if M approaches infinity, which casts some doubt on their validity if M is restricted to some finite value. The question whether to invert the truncated $\tilde{L}$ matrix (C.32), or to truncate the inverted $\tilde{L}$ matrix (C.33), has not been resolved yet. It has been observed, however, that both approaches yield identical results if M is odd for the cosine partition, and if M is even for the sine partition. Since the selection of odd M is not a prohibitively restricting condition for the symmetrical cases considered, the latter approach using equation (C.33) was chosen. A more detailed discussion of the issues involved and the general structure of the matrix N^c can be found in /Wang 92/, pages 32 - 37.

Table C.1: Closed Form Inversion Matrix Element Cases

Case	Cosine Partition	Sine Partition
I	r and m odd	r and m even
II	$r = m \pm 1$	$r = m \pm 1$
	m even: $j > n$; m odd: $j < n$	m even: $j < n$; m odd: $j > n$
	positive sign	negative sign
III	all others	all others

The wake forcing functions (the right hand side vector in equation (C.28)) were expanded in Section 3.2.3.2. for a chordwise pressure distribution of the form 1/sin θ:

$$\tau_n^{m,c}(t) = 2\int_{-S}^{S} b(y)\lambda_{n;0}^{m;c}(y)\left(\omega_0(y,t) + \tfrac{1}{2}\omega_1(y,t)\right) dy$$

$$-2\int_{-S}^{S} b(y)\lambda_{n;0}^{m;c}(y) \sum_{r,j}\left(\lambda_{j;0}^{r;c}(y) + \tfrac{1}{2}\lambda_{j;1}^{r;c}(y)\right)a_j^r(t)\, dy \qquad \text{(C.34)}$$

The normalwash Fourier coefficients, ω_0 and ω_1, can be substituted by expressions in the structural states, q_k, and wake states, a_r^j, according to equations (C.4):

$$\begin{aligned}\left[M^c\right]\left\{a_n^m\right\}^* + \left[N^c\right]\left\{a_n^m\right\} = \tfrac{1}{2}\Bigg(& \left[DSI\right]\left\{q_k\right\}^* + \left[KSI\right]\left\{q_k\right\} \\ & + \left[KII\right]\left\{a_j^r\right\} \\ & + \left[\{CI1\}\ \{CI0\}\right]\begin{Bmatrix}\delta^* \\ \delta\end{Bmatrix} \\ & + \left[\{GI0V\}\ \{GI0H\}\right]\begin{Bmatrix}V_v \\ V_h\end{Bmatrix}\Bigg)\end{aligned} \qquad \text{(C.35)}$$

The right hand side matrix elements are for the complete system with two half-wings (denoted by the factor ***2***):

$$DSI_{n,-}^{m,k} = \boldsymbol{2}\cdot 2\int_0^S b\left\{\left(\lambda_{n;0}^{m;c} - \tfrac{1}{2}\lambda_{n;1}^{m;c}\right)\left[-\left(\alpha_0 + \alpha_i + \xi_0\right)u_k - w_k\right.\right.$$

$$\left.\left. + \tfrac{1}{2}b\left(\alpha_k + \xi_k\right)\right]\right\} dy \qquad \text{(C.36)}$$

$$KSI_{n,-}^{m,k} = \boldsymbol{2}\cdot 2\int_0^S b\left\{\left(\lambda_{n;0}^{m;c} - \tfrac{1}{2}\lambda_{n;1}^{m;c}\right)\left(\alpha_k + \xi_k\right)\right\} dy \qquad \text{(C.37)}$$

$$KII_{n,j}^{m,r} = -\boldsymbol{2}\cdot 2\int_0^S b\left\{\left(\lambda_{n;0}^{m;c} - \tfrac{1}{2}\lambda_{n;1}^{m;c}\right)\left(\lambda_{j;0}^{r;c} + \tfrac{1}{2}\lambda_{j;1}^{r;c}\right)\right\} dy \qquad \text{(C.38)}$$

$$CI1_{n,-}^{m,-} = \mathbf{2}\cdot 2\int_{y_{fi}}^{y_{fo}} b^2 \left\{\left(\lambda_{n;0}^{m;c} - \tfrac{1}{2}\lambda_{n;1}^{m;c}\right)\left[D_{0s} + \tfrac{1}{2}D_{1s}\right]\right\} dy \tag{C.39}$$

$$CI0_{n,-}^{m,-} = \mathbf{2}\cdot 2\int_{y_{fi}}^{y_{fo}} b \left\{\left(\lambda_{n;0}^{m;c} - \tfrac{1}{2}\lambda_{n;1}^{m;c}\right)\left[D_{0} + \tfrac{1}{2}D_{1}\right]\right\} dy \tag{C.40}$$

$$GI0V_{n,-}^{m,-} = \mathbf{2}\cdot 2\int_{0}^{S} b \left\{\left(\lambda_{n;0}^{m;c} - \tfrac{1}{2}\lambda_{n;1}^{m;c}\right)\right\} dy \tag{C.41}$$

$$GI0V_{n,-}^{m,-} = \mathbf{2}\cdot 2\int_{0}^{S} b \left\{\left(\lambda_{n;0}^{m;c} - \tfrac{1}{2}\lambda_{n;1}^{m;c}\right)\left[\alpha_0 + \alpha_i + \xi_0\right]\right\} dy \tag{C.42}$$

C.2.3. Coupled Airframe-Wake System

Coupling between the structural system, equation (C.16), and the wake system, equation (C.35), is provided through presence of wake states in the structural forcing function and structural states in the wake forcing functions. Combination of these two systems yields the coupled system dynamics in first order (state-space) form:

$$\begin{Bmatrix} \{q_k\} \\ \{q_k\}^* \\ \{a_n^m\} \end{Bmatrix}^* + \begin{bmatrix} 0 & -I & 0 \\ [MS]^{-1}([KS]-[KSS]) & -[MS]^{-1}[DSS] & -[MS]^{-1}[KIS] \\ -\frac{1}{2}[M^c]^{-1}[KSI] & -\frac{1}{2}[M^c]^{-1}[DSI] & [M^c]^{-1}\left([N^c]-\frac{1}{2}[KII]\right) \end{bmatrix} \begin{Bmatrix} \{q_k\} \\ \{q_k\}^* \\ \{a_n^m\} \end{Bmatrix} =$$

$$\begin{bmatrix} \{0\} & \{0\} & \{0\} \\ [MS]^{-1}[CS2] & [MS]^{-1}[CS1] & [MS]^{-1}[CS0] \\ \{0\} & \frac{1}{2}[M^c]^{-1}[CI1] & \frac{1}{2}[M^c]^{-1}[CI0] \end{bmatrix} \begin{Bmatrix} \delta^{**} \\ \delta^{*} \\ \delta \end{Bmatrix} + \sum_l \begin{bmatrix} 0 \\ [MS]^{-1}[WU^l]^T \\ 0 \end{bmatrix} \{F^l\}$$

$$+ \begin{bmatrix} \{0\} & \{0\} & \{0\} & \{0\} \\ [MS]^{-1}[GS1V] & [MS]^{-1}[GS1H] & [MS]^{-1}[GS0V] & [MS]^{-1}[GS0H] \\ \{0\} & \{0\} & \frac{1}{2}[M^c]^{-1}[GI0V] & \frac{1}{2}[M^c]^{-1}[GI0H] \end{bmatrix} \begin{Bmatrix} V_v^* \\ V_h^* \\ V_v \\ V_h \end{Bmatrix} \tag{C.43}$$

where

$$[MS] = [MS_u] - [MSS] \tag{C.43a}$$

or shorter:

$$\{x\}^* = [A]\{x\} + [B]\{u\} + [G]\{w\} + \sum_l \left[W^l\right]\left\{F^l\right\} \tag{C.44}$$

Up to this point, all entities were nondimensional according to the conventions given at the beginning of this Appendix. The structural state vector, $\{q_k\}$, and control vector $\{u\}$, do not carry any dimension in any case. The wake states, $\left\{a_n^m\right\}$, and the gust vector, $\{w\}$, however, are normalized by the reference speed, $\boldsymbol{U}$. Natural frequencies obtained from the homogeneous system are normalized by $\boldsymbol{U/R}$. For easier interpretation and use of the coupled system in other analyses like control system design, it might be more appropriate to use a dimensional form of (C.44):

$$\{\dot{\boldsymbol{x}}\} = [\boldsymbol{A}]\{\boldsymbol{x}\} + [\boldsymbol{B}]\{\boldsymbol{u}\} + [\boldsymbol{G}]\{\boldsymbol{w}\} + \sum_l \left[\boldsymbol{W}^l\right]\left\{\boldsymbol{F}^l\right\} \tag{C.45}$$

Bringing the dimensions into the system can be visualized by one-by-one (or Hadamard) multiplication of matrix elements by dimension carriers; in the following expressions, vector and matrix partitioning is identical to that displayed in equation (C.43), and the dimension carriers are assumed to fill the entire vector and matrix partitions indicated:

$$\{\boldsymbol{x}\} = \begin{Bmatrix} \{q_k\} \\ \{\dot{q}_k\} \\ \left\{a_n^m\right\} \end{Bmatrix} = \begin{Bmatrix} \{1\} \\ \{U/R\} \\ \{1\} \end{Bmatrix} \otimes \{x\}; \quad \{\boldsymbol{u}\} = \begin{Bmatrix} \ddot{\delta} \\ \dot{\delta} \\ \delta \end{Bmatrix} = \begin{Bmatrix} (U/R)^2 \\ U/R \\ 1 \end{Bmatrix} \otimes \{u\}; \quad \{\boldsymbol{w}\} = \begin{Bmatrix} \dot{V}_v \\ \dot{V}_h \\ V_v \\ V_h \end{Bmatrix} = \begin{Bmatrix} U^2/R \\ U^2/R \\ U \\ U \end{Bmatrix} \otimes \{w\}$$

(C.46a)

$$[\boldsymbol{A}]=\begin{bmatrix}[0] & [1] & [0]\\ \left[(U/R)^2\right] & [U/R] & \left[(U/R)^2\right]\\ [U/R] & [U/R] & [U/R]\end{bmatrix}\otimes[\mathrm{A}]; \qquad [\boldsymbol{B}]=\begin{bmatrix}[0] & [0] & [0]\\ [1] & [U/R] & \left[(U/R)^2\right]\\ [0] & [1] & [U/R]\end{bmatrix}\otimes[\mathrm{B}]$$

$$[\boldsymbol{G}]=\begin{bmatrix}[0] & [0] & [0] & [0]\\ [1/R] & [1/R] & [U/R^2] & [U/R^2]\\ [0] & [0] & [U/R] & [U/R]\end{bmatrix}\otimes[\mathrm{G}]; \qquad [\boldsymbol{W}]=\begin{bmatrix}[0]\\ \left[(U/R)^2\right]\\ [0]\end{bmatrix}\otimes[\mathrm{W}] \qquad \text{(C.46b)}$$

C.3. Chordwise Pressure Integration

The pressure distribution functions used in the wake model originate in work by /Kinner 37/ on circular wings, where the choice of ellipsoidal coordinates is well suited to the planform, Fig. C.2 (a). In conventional fixed wing aerodynamics, however, it is more practical to observe the streamwise distribution first, and then describe spanwise distribution of chordwise integrals such as lift per unit span, or moment per unit span (b). The wake forcing functions, equation (3.18), therefore contain expressions derived in both coordinate systems, which complicates integration. In rotorcraft applications of the wake model, the transformation between the two systems is facilitated by assuming that the free stream direction is approximately perpendicular to each rotor blade's radial coordinate, and the chord is small compared to the radial coordinate. Under these assumptions, the chordwise integration can be approximated by integration along an arc. The approximation becomes invalid in the vicinity of the rotor hub (c), which is an acceptable limitation for rotorcraft aeroelasticity, where the inboard region of the blades contribute only a small part to the overall aerodynamic forces. In low aspect ratio fixed wing cases, however, the region in which the approximation does not hold covers a large part of the planform, and

the root region may provide more significant contribution to the unsteady aerodynamic loads, for example for free-free structural configurations. In these cases, a rigorous integration in cartesian coordinates is unavoidable.

These considerations translate into three different solution techniques for the integrals,

$$\lambda_{j;0}^{r;c}(y) = \frac{1}{\pi}\int_0^{\pi} \frac{\bar{P}_j^r(\nu)}{\nu}\cos(r\psi)\,d\theta; \quad \lambda_{j;1}^{r;c}(y) = \frac{2}{\pi}\int_0^{\pi} \frac{\bar{P}_j^r(\nu)}{\nu}\cos(r\psi)\cos(\theta)\,d\theta \tag{C.47}$$

For very large aspect ratios, the lifting surface planform may be approximates by a line at the half chord, at which all aerodynamic loads are concentrated (in the following text referred to as "lifting line" approximation). In this case, the integral is reduced to an evaluation of the integrand at the half chord:

$$\lambda_{j;0}^{r;c}(y) = \frac{\bar{P}_j^r(\nu_0(y))}{\nu_0(y)}\cos(r\psi_0); \quad \lambda_{j;1}^{r;c}(y) = 0 \tag{C.48}$$

where

$$\nu_0(y) = \sqrt{1 - y^2\left(1 + \tan^2\Lambda\right)}; \quad \psi_0 = \tfrac{\pi}{2} - \Lambda \tag{C.49}$$

A second approach is to express the normalized associated Legendre functions, $\bar{P}_j^r$, and the azimuth angle, ψ, approximately in terms of the variable of integration. The azimuth angle can be approximated by

$$\psi \approx \psi_0 + \tilde{\psi}(y)\cos\theta; \quad \tilde{\psi}(y) = \frac{b(y)\cos^2\Lambda}{y} \tag{C.50}$$

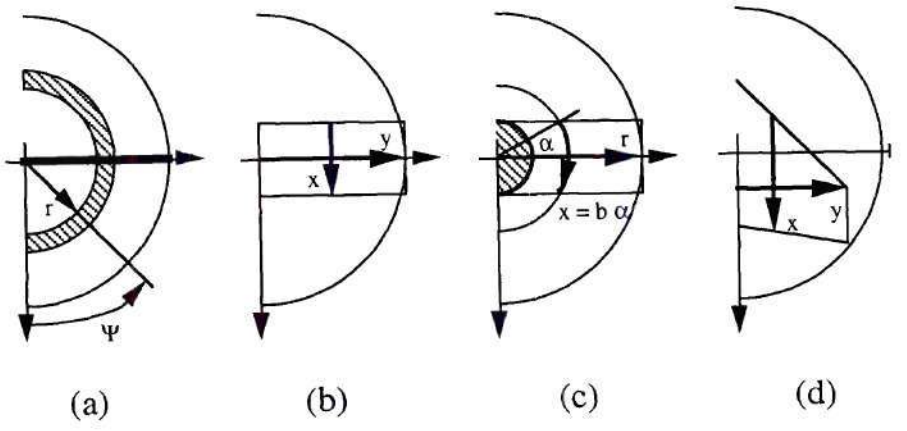

Fig. C.2: Coordinate Systems for Integration

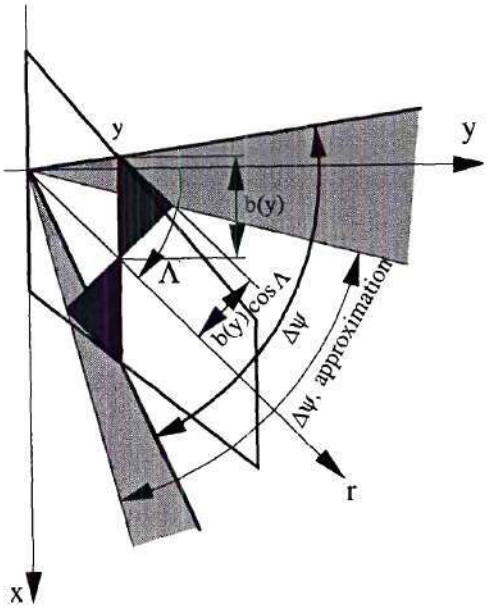

Fig. C.3: Integration Interval Error, High Aspect Ratio Approximation

Fig. C.3 depicts that for backward swept wings the azimuth interval spanned by (C.50), "$\Delta\psi$, approximation," is smaller and shifted backward compared to the actual interval, "$\Delta\psi$." The error increases with wing sweep, Λ, and effectively limits the validity of (C.50) to small sweep angles. It is advantageous to expand the Legendre functions similarly in a Taylor series in terms of $\cos\theta$:

$$\frac{\bar{P}_j^r(\nu(y,\theta))}{\nu(y,\theta)} \approx \frac{\bar{P}_j^r(\nu_0(y))}{\nu_0(y)} + \frac{\partial\nu}{\partial(\cos\theta)}\frac{\partial}{\partial\nu}\left(\frac{\bar{P}_j^r(\nu(y,\theta))}{\nu(y,\theta)}\right)\Bigg|_{\nu=\nu_0}\cos\theta + \ldots$$

$$= p_{j;0}^{r;c}(y) + p_{j;1}^{r;c}(y)\cos\theta + \ldots \qquad \text{(C.51)}$$

with

$$p_{j;0}^{r;c}(y) = \frac{\bar{P}_j^r(\nu_0)}{\nu_0} \qquad \text{(C.52)}$$

and

$$p_{j;1}^{r;c}(y) = -\frac{b(y)\, y \tan\Lambda}{\nu_0}\left[\frac{\bar{P}_j^r(\nu_0)}{\nu_0}\left(\frac{j\nu_0}{\nu_0^2-1} - \frac{1}{\nu_0}\right) - \frac{\sqrt{\frac{j+1}{j}\left(j^2-r^2\right)}}{\nu_0^2-1}\frac{\bar{P}_{j-1}^r(\nu_0)}{\nu_0}\right] \qquad \text{(C.53)}$$

where ν_0 is still a function of y according to (C.49) (the argument was dropped for simplicity). With this particular choice of expansion, each term of the series (C.51) results in an integral which can be solved in closed form in terms of Bessel functions of the first kind:

$$\lambda_{j;0}^{r;c}(y) = p_{j;0}^{r;c}(y)\, J_0\left(r\,\tilde{\psi}(y)\right)\cos\left(r\,\psi_0\right)$$

$$- p_{j;1}^{r;c}(y)\, J_1\left(r\,\tilde{\psi}(y)\right)\sin\left(r\,\psi_0\right) \pm \ldots \qquad \text{(C.54)}$$

$$\lambda_{j;I}^{r;c}(y) = \quad -2\, p_{j;0}^{r;c}(y)\, J_1\left(r\,\tilde{\psi}(y)\right)\sin\left(r\,\psi_0\right)$$

$$+\, p_{j;I}^{r;c}(y)\left[J_0\left(r\,\tilde{\psi}(y)\right) - J_2\left(r\,\tilde{\psi}(y)\right)\right]\cos\left(r\,\psi_0\right) \mp \ldots \qquad \text{(C.55)}$$

If only the first terms of (C.54) and (C.55) are used, the resulting wake forcing functions are identical to those previously suggested by /Peters and He 87/ for rotorcraft applications and by /Nibbelink 92/ for fixed wing cases. This expression is referred to as "high aspect ratio" approximation in the following text.

Finally, the integrals (C.47) may be solved directly in streamwise coordinates. Due to the relations between ellipsoidal and streamwise coordinates,

$$\nu(y,\theta) = \sqrt{1 - y^2\left(1 + \tan^2\Lambda\right) - \left(b\cos\theta\right)^2}\,; \quad \psi(y,\theta) = \arctan\left(\frac{y}{y\tan\Lambda + b(y)\cos\theta}\right) \qquad \text{(C.56)}$$

the integrand is not a simple function of the variable of integration, θ, and no closed form solution was found. Numerical integration, however, involves repetitive evaluation of the normalized associated Legendre functions, which is computationally very intensive. Previous computational implementations of the wake model used Legendre function recurrence relations to obtain $\overline{P}_j^r$ for general r and j from a few basis functions (proper operation up to r = 1000 and j = 1399 was demonstrated, /He and Peters 88/). The functions are power series, with the limited number of terms, depending on the difference between j and r (recall: j > r). In the case of numerical integration, only relatively few a priori known r, j pairs are used in evaluation of the $\overline{P}_j^r$, but this process is repeated a large number of times. As a result, the additional computational effort involved in determining the coefficients of these power series once for the entire program run is warranted by subsequent time savings in multiple evaluation of $\overline{P}_j^r$. Such a representation has been developed based on the generating formulas

$$P_j(x) = \frac{1}{2^j j!}\frac{d^j}{dx^j}\left[\left(x^2-1\right)^j\right]; \quad P_j^r(x) = \left(1-x^2\right)^{r/2}\frac{d^r}{dx^j}P_j(x) \tag{C.57}$$

by collecting factors and coefficients produced in differentiations and multiplications:

$$\overline{P}_j^r(x) = B\sum_{k=0}^{q+s}\overline{b}_{j,k}^r\, x^{j-2k}$$

$$B = \begin{cases} 1 & r \text{ even} \\ \dfrac{\sqrt{1-x^2}}{x} & r \text{ odd} \end{cases}$$

$$q = \mathrm{Int}\left(\frac{j-r}{2}\right); \quad s = \mathrm{Int}\left(\frac{r}{2}\right) \tag{C.58}$$

$$\overline{b}_{j,k}^r = (-1)^r\left(\frac{(j+r)!}{(2j+1)(j-r)!}\right)^{-\frac{1}{2}}\sum_{i=\max(0,k-q)}^{\min(k,s)}\frac{(-1)^{s+k}\,s!}{i!\,(s-i)!\,(k-i)!\,2^{k-i}}\sum_{l=0}^{q-(k-i)}\frac{C_{r+(k-i)+l}^{r+j}}{2^i\,l!}$$

$$C_0^b = 1; \quad C_a^b = 0 \quad \forall\, a<0; \quad C_1^2 = 1;$$

$$C_a^b = C_a^{b-1} + (b+1-2a)\,C_{a-1}^{b-1} \quad \forall \quad 0 < a < \mathrm{Int}\left(\frac{b}{2}\right)$$

Although equation (C.58) looks hopelessly complex, it can be programmed very efficiently. In a comparison with the algorithm from /He and Peters 88/, $\overline{P}_j^r$ was calculated for r = 0,..., 21 (a total of 132 function evaluations). The new algorithm was approximately 30% faster, including preparation of the coefficients, $\overline{b}_{j,k}^r$, in equation (C.58). For high orders of r and j it is recommended to use the original representation, since inaccuracies in calculation of the coefficients of alternating sign, high order terms may result in large errors.

C.4. Wake Pole Structure and Model Order Reduction Studies

The order of the wake system, equation (3.17), can be fairly large (between 56 and 132 between the minimum number for which reasonable convergence was achieved in the sample problem, and the maximum order used). The computational effort involved in solving such a system is less of a concern as the computer time needed to set it up, in particular the forcing function integrals, equation (C.48) (see previous section). It has therefore been attempted to reduce the number of wake modes based on wake pole structure and tendency to coupling with structural modes. In these studies, the large transport aircraft wing structural system described in Appendices B.2 and C.6 was used (quarter chord sweep of 36°, taper ratio of 0.44, aspect ratio of 7.57, wing area 4006 ft^2 - modal analysis using ASTROS). The success of these efforts was limited. Observations made are summarized in this section and should be understood as an inspiration for follow-up research rather than a presentation of complete explanations.

C.4.1. Open-Loop System

Fig. C.4 depicts the non-dimensional eigenvalues of the uncoupled, open-loop wake system,

$$\left[M^c\right]\left\{a_n^m\right\}^* + \left[N^c\right]\left\{a_n^m\right\} = 0 \tag{C.59}$$

for a maximum number of harmonics, M, from 3 to 21. The first observation is that all modes are stable and located within a semi circle around the origin with increasing radius as M increases. The overlay of different fidelity models allows detection of certain characteristics which are otherwise hidden in an apparently amorphous accumulation of

poles: (1) The group of eigenvalues closest to the imaginary axis shows the smallest variation with M. If M is increased, the lowest order poles in this group are almost identical, while higher frequency eigenvalues are added. Eventually, these "lowest damping" eigenvalues appear to be located equidistantly on an almost straight line which intersects the real axis at approximately 2 U/R. (2) Similarly, "lowest frequency" eigenvalues concentrate at an imaginary part of approximately 2 U/R, indicating some symmetry in the overall eigenvalue structure. The grouping is not as pronounced in this case, since the clusters stretch in real direction as one proceeds into the stable half plane.

(3) Modes located further from the imaginary axis exhibit a similar structure, which is more difficult to identify, however. A large number of modes may be grouped along lines which are more and more curve into the stable half plane when moving away from the imaginary axis (as indicated for M = 19). Furthermore, as M is increased, these "strings" expand to higher imaginary parts along certain corridors, which are sketched in Fig. C.4.

Wake eigenvalues in Fig. C.4 and C.5 are normalized by U/R. A constant frequency, undamped structural mode would converge from +/- j∞ to the origin if U is increased from 0 to ∞. For very low U, apparent mass terms are dominating aerodynamic forces; for high U, wake feedback is negligible. In an intermediate velocity range, wake-induced feedback is an important factor. Assuming no interference of wake and structural system, this range would be determined by the highest and lowest wake mode imaginary parts. As pointed out before, the highest value - the boundary between apparent mass term domination and wake influence - is a function of the wake model order. The lowest value, however - the limit of wake feedback, and transgression to quasi-steady aerodynamics - is independent of the model order, and equal to approximately 2 U/R. The interpretation of this value is facilitated if the definition of the reduced frequency, k, from is recalled:

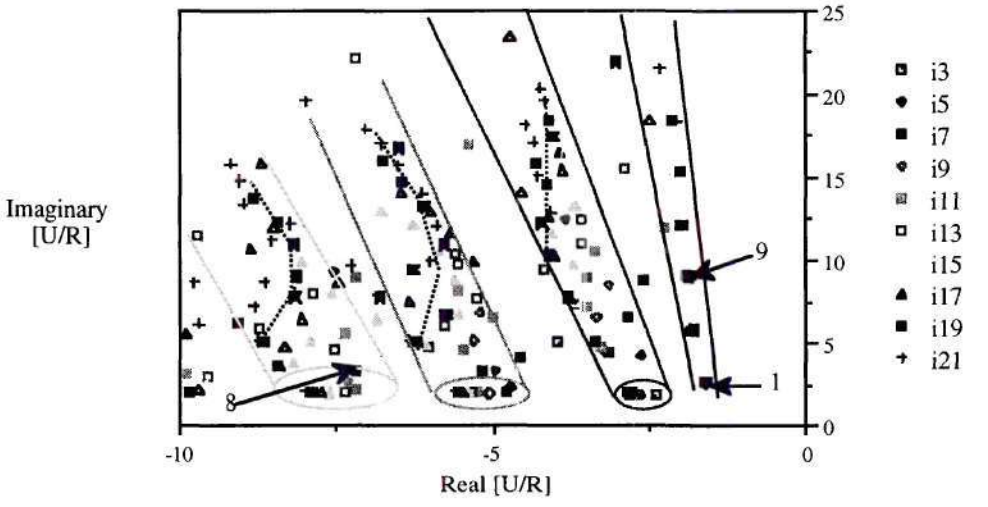

Fig. C.4: Open-Loop Wake Pole Structure (a)

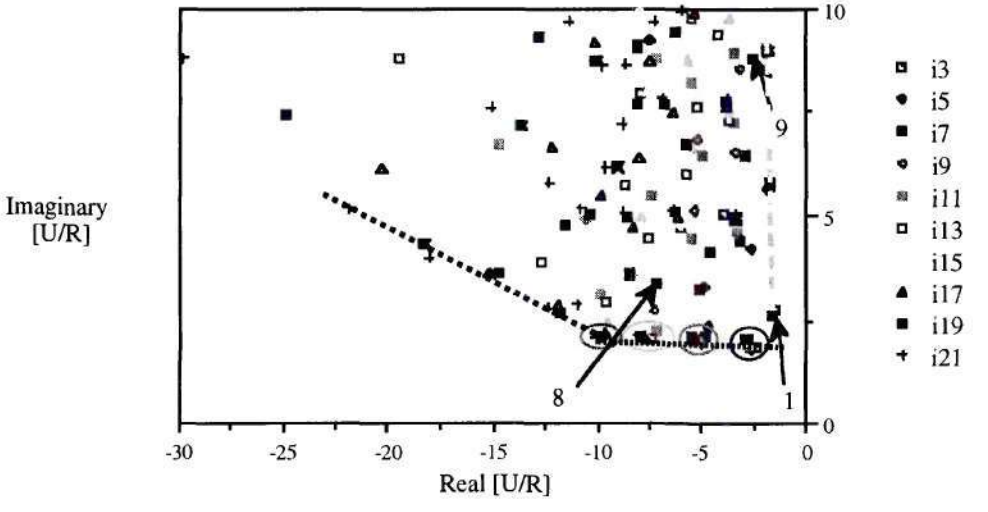

Fig. C.5: Open-Loop Wake Pole Structure (b)

$$k = \frac{\omega\, b}{U} \approx \frac{1}{AR}\frac{\omega}{(U/R)} \tag{C.60}$$

assuming a rectangular wing planform just fitting in the reference plane, that is with a span of 2R. For a wing with an aspect ratio, AR, of 10, the limit reduced frequency obtained this way is k = 0.2, which is an acceptable value for the transition from unsteady to quasi-steady aerodynamics. Unfortunately, this value appears to be more coincidental than fundamental: First, equation (C.60) yields that k approaches 0 as the aspect ratio is increased. This means that for nearly two-dimensional cases the wake feedback contributes to aerodynamic forces at very low reduced frequencies, which is a paradox observation. Second, interference between structure and wake changes the pole structure, as shown in the Appendix C.4.2. Third, coupling between dynamic systems is not based exclusively on natural frequency proximity. Another important factor is compatibility of the mode shapes; consider for example a wing with uncoupled bending and torsion modes. If the wing is excited by a force through the shear center, no energy is transferred into the torsional degree of freedom, even if the force oscillates at the torsional mode natural frequency. Similarly, only those wake modes which are close to structural eigenvalues in frequency and exhibit a mode shape which may be excited by a structural deflection will actually couple with structural dynamics. Based on these considerations, some "typical" mode shapes were analyzed for their characteristics.

Fig. C.6, C.7 and C.8 show amplitudes of mode shapes associated with the wake modes "1," "8" and "9" (M = 7), respectively, which are marked in the wake eigenvalue plots, Fig. C.4. and C.5 (the notation refers to the position of the eigenvalues in a list sorted by increasing distance from the origin). The coordinate system in these plots complies with fixed wing conventions; the free stream velocity vector, U, points in positive

chordwise direction, x, and positive spanwise coordinates, y, indicate the right half wing (seen in flight direction, or opposite to the free stream direction). No attention should be paid to the numerical values of the amplitudes, which were chosen to depict acceptably scaled mode shape plots. Note the differences between the "low frequency" mode "8" and the "low damping" mode "9." Mode "8" shows very large inflow amplitudes at the reference disk edges, compared to those at the disk center. This highly damped, low frequency mode represents primarily a large amplitude oscillation of a small air mass. In the case of mode "9," however, the inflow amplitude peak is concentrated at the rear end of the disk, and much less pronounced. Thus, this high frequency, low damping mode consists mainly of an oscillation of the entire air mass passing through the reference disk.

A lifting, finite span wing in steady-state flow induces a downstream induced flow field with distinct peaks at the wing tips. In a similar fashion, an oscillating pressure distribution creates in general* a tip vortex of oscillating strength. It can therefore be concluded that wake modes which exhibit large induced flow amplitudes in the vicinity of the wing tip (like mode "8," Fig. C.7.) are much more likely to couple with structural vibrations compared to those with less spanwise inflow amplitude variation, Fig. C.6 and Fig. C.8.

---

* ...unless the spanwise slope of the pressure distribution at the wing tip is zero at all times - a very specific case.

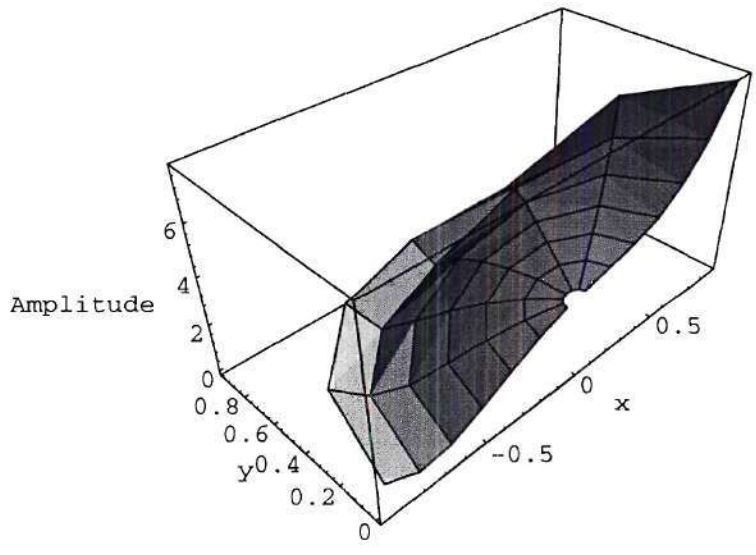

Fig. C.6: Amplitude, Wake Mode "1" (M = 7)

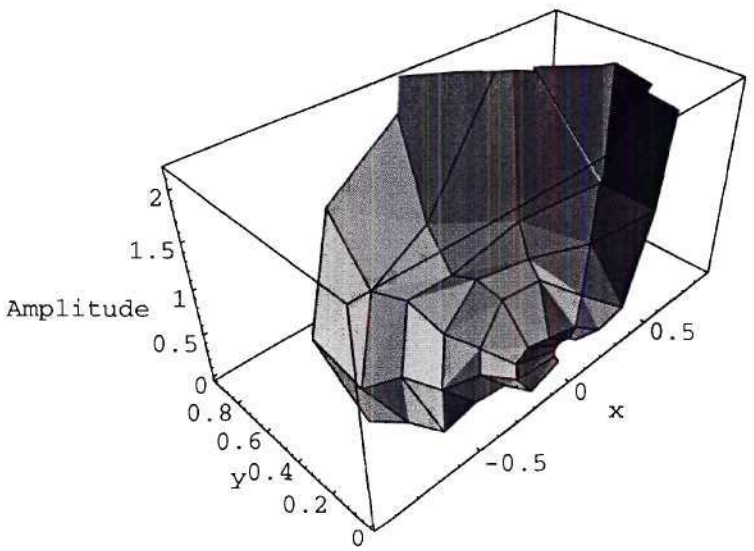

Fig. C.7: Amplitude, Wake Mode "8" (M = 7)

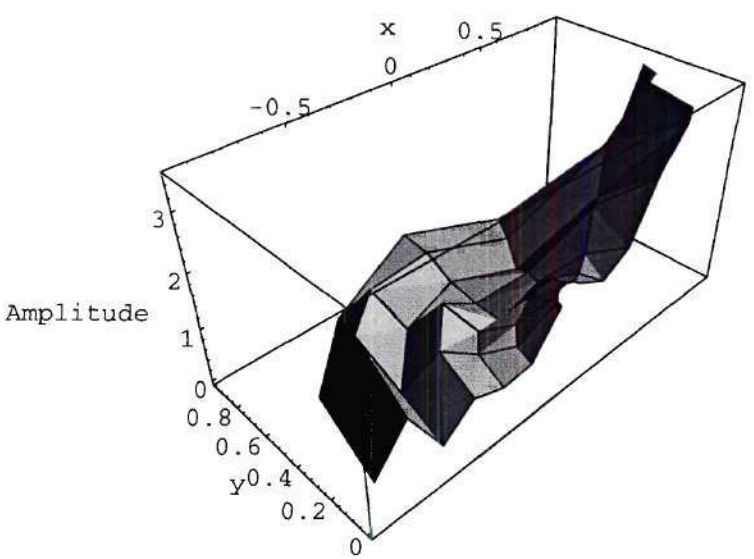

Fig. C.8: Amplitude, Wake Mode "9" (M = 7)

C.4.2. Closed-Loop System

The previous section explicitly excluded any interference between wake and structure, and concentrated on identification of potential coupling mechanisms. This section addresses actual coupling phenomena detected in the sample case described in the introduction to Appendix C.4., the relation to the observations made before, and conclusions drawn with respect to possible model order reduction.

For a direct comparison, the open-loop wake eigenvalues and wake-dominated eigenvalues from the closed loop system using two different chordwise integration techniques (refer to Appendix C.3.) are plotted in Fig. C.9. The majority of poles exhibit a significant shift. The plot, however, is too busy to allow further conclusions. In order to explore the effect of wake-structure coupling more in detail, the area was subdivided in quadrants denoted by the roman numerals in Fig. C.9. The density, ρ, was then varied in small steps from very small values to the sea level value, the rationale being that ρ provides a means for changing the wake mass with respect to the fixed generalized masses of the structural modes. If ρ is set to a very small value, then structure-wake coupling exceeds wake-structure feedback, and the structural modes are very close to their locations from the undamped (uncoupled) case. For very large density values, the structural mass is small with respect to the wake mass, and the wake modes are close to the uncoupled wake eigenvalues. Note that the latter case is not identical to that of equation (C.59), since the uncoupled wake dynamics include wake-wake feedback through the KII terms, see equation (C.35).

The only eigenvalues which are located on the imaginary axis for $\rho = 10^{-6}$ slugs/ft^3 in Fig. C.10 to C.13 (numerical integration) can be identified as the structural modes, which exhibit increasing damping, both due to interference with the wake and quasi-steady

aerodynamics. From the other, wake-dominated modes, only a relatively small number moves from their open-loop position. Fig. C.10 and C.13 in particular show that within the frequency range of the structural modes, some wake eigenvalues remain nearly constant (boxed; including the "low damping" modes described in the previous section) , while other couple with structural dynamics (encircled).

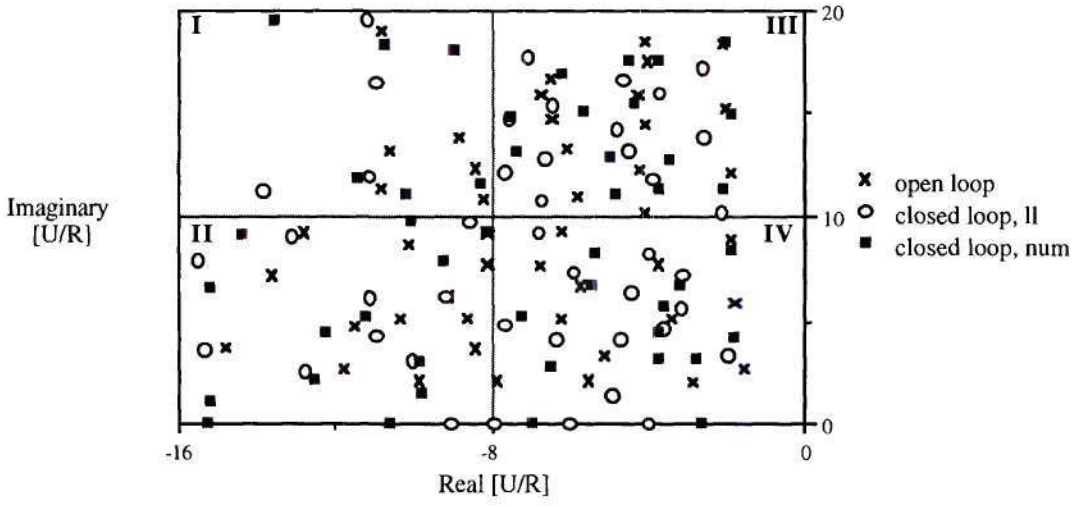

Fig. C.9: Open-Loop and Closed-Loop Wake Modes,

M = 19, U = 800 ft/sec

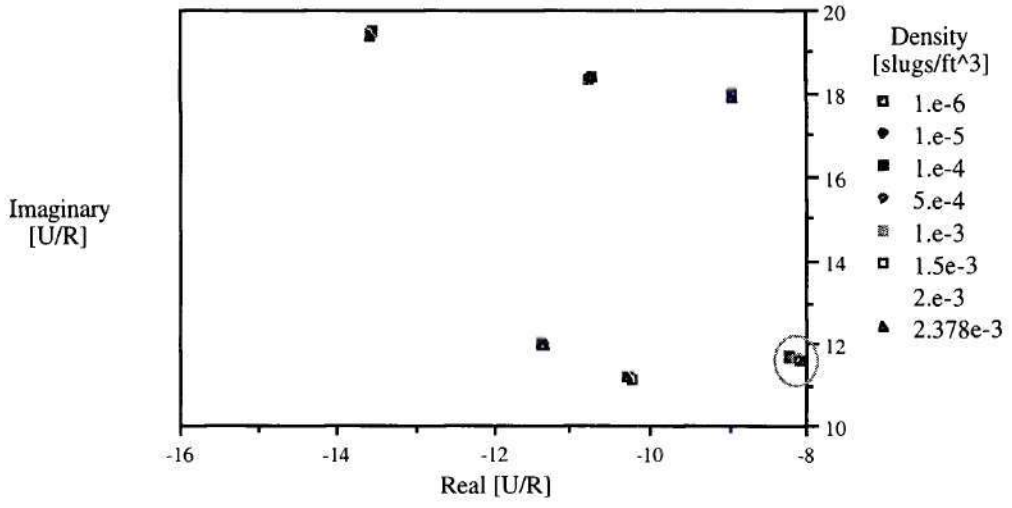

Fig. C.10: Wake-Structure Coupling Effect on Pole Structure - Quadrant I

M = 19, U = 800 ft/sec

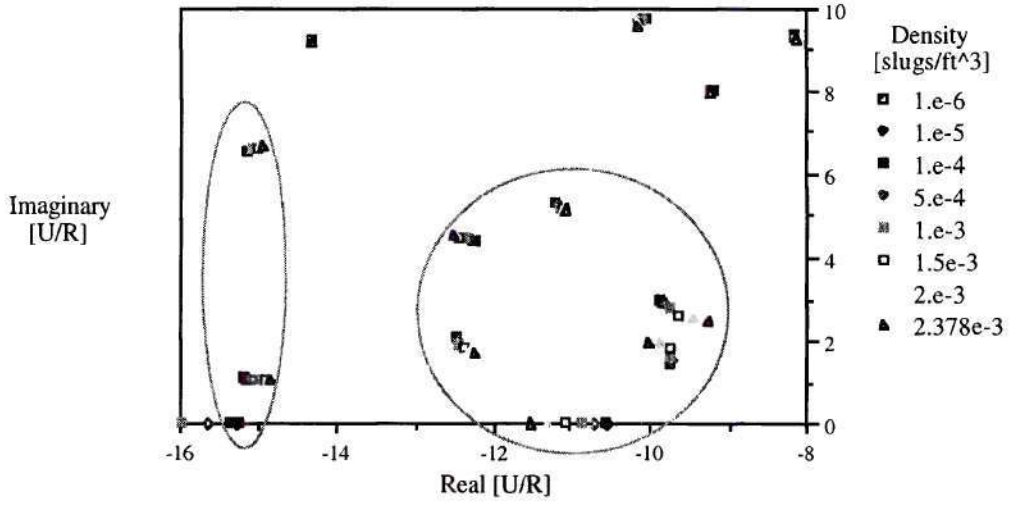

Fig. C.11: Wake-Structure Coupling Effect on Pole Structure - Quadrant II

M = 19, U = 800 ft/sec

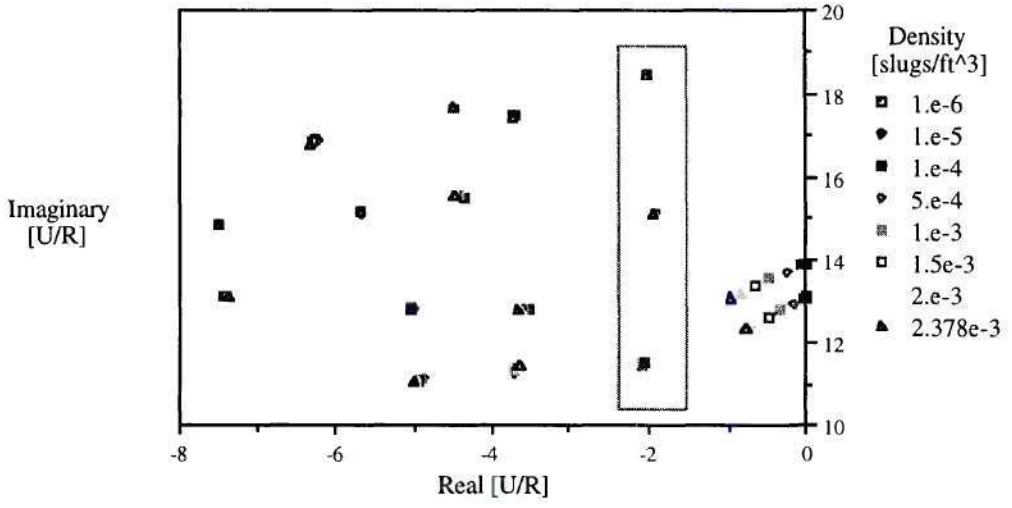

Fig. C.12: Wake-Structure Coupling Effect on Pole Structure - Quadrant III

M = 19, U = 800 ft/sec

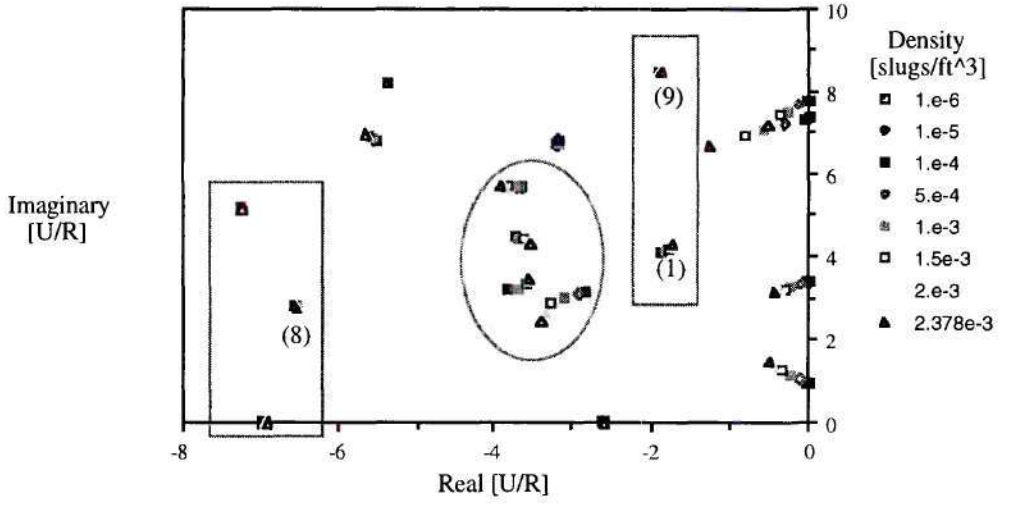

Fig. C.13: Wake-Structure Coupling Effect on Pole Structure - Quadrant IV

M = 19, U = 800 ft/sec

A general interpretation of the wake mode behavior is not possible, since wing geometry, natural frequencies and mode shapes affect the sample case observations made so far. However, for the encircled eigenvalues in Fig. C.11 a physical explanation supporting this observation can be found: The flutter critical mode is the lowest frequency mode permitting energy transfer from aerodynamics into the structure (in the sample case the first two modes couple to yield the flutter mode); hence, the associated structural mode shape includes only a small number of node lines. Wake modes which couple with this eigenform therefore likewise exhibit a low order spanwise inflow distribution. The spanwise inflow distribution in the wake model is determined by the radial shape functions, the normalized associated Legendre functions, $\overline{P}_n^m(\nu)/\nu$, where $\nu = \sqrt{1-\left(\frac{y}{R}\right)^2}$ at an azimuthal position, ψ, of $\pi/2$. These functions have (n - m) zeros between y = -1 and y = 1. In conclusion, modes which couple with the flutter mode are expected to be dominated by wake states, a_n^m, with a small difference between the polynomial index, n, and the harmonics index, m.

In order to identify wake state contributions to wake-dominated modes, a graphical representation according to Fig. C.14 was chosen. Note that as a result of the (m, n) ordering scheme (refer to Appendix C.2.2.), combinations exist at the location marked with squares. The relative magnitude of eigenvector elements is depicted by the gray shade, with black representing the largest values. These plots have been prepared for 25 wake modes and placed in the pole plot at the proper location, Fig. C.15. Remaining poles are shown as black circles. The encircled modes from Fig. C.12 - which coupled noticeably with structural modes - clearly feature a concentration along the line n = m+1, and little contribution from wake states with n > m+1, as postulated in the previous paragraph. The

difference n - m, called the number nodes, n', can therefore be used to reduce the number of wake states required by dropping all wake states with $n - m > n'$.

In conclusion: There is a connection between wake mode composition out of wake states, pole location, and potential coupling with structural modes. The inflow expansion, equation (C.6), however is not well suited for matching a fixed wing perturbation induced flow field; wake modes therefore comprise a relatively large number of significant wake state contributions, and the wake model order required to achieve convergence is high. Three options may be considered for model order reduction:

First, choice of an inflow expansion better suited for fixed wing applications, possibly based on the observations made. In this case, the wake model may have a small order to begin with. However, selection of such a set is not a trivial task if closed form solutions for the wake matrices, M^c and N^c, are to be used as in the case of the present expansion (equations (C.29), (C.32), and (C.33); refer to /He 89/ for details of the derivation). The numerical effort involved in calculating the wake matrix elements may outweigh model order reduction advantages if such closed form solutions cannot be found.

Second, use of the original expansion and elimination of wake states which do not contribute significantly to coupled wake-structure modes, as described above for wake node number considerations. This approach relies on a priori knowledge of the characteristics of these modes, and is therefore problem specific.

Third, utilization of the complete wake model, modal analysis of the coupled system, followed by system order reduction based on wake state contribution to the coupled wake modes. Unless aerodynamic coupling phenomena are investigated, the important information is the contribution of structural modes to coupled wake-structure

eigenvectors. Hence, one may reduce the system order by dropping coupled eigenvalues which are dominated by wake states ("filtering"). The latter two options were pursued.

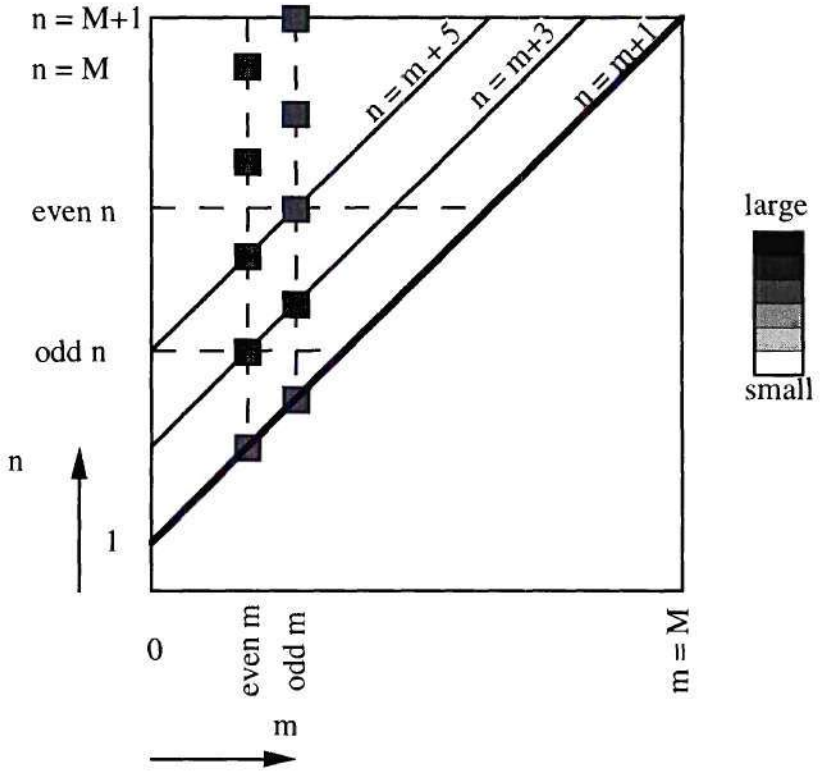

Fig. C.14: Representation of Wake State Contributions

(M odd)

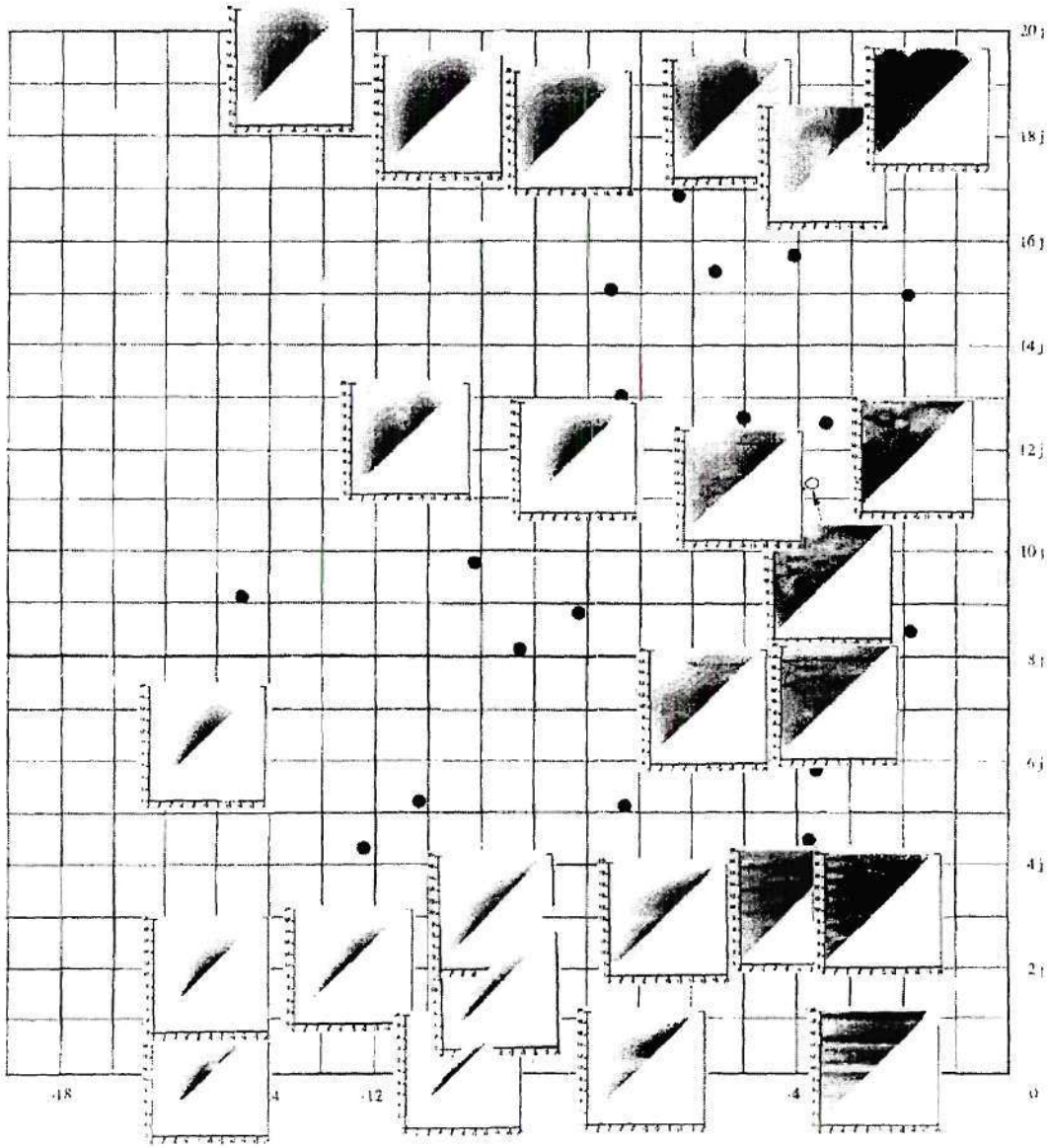

Fig. C.15: Wake State Contribution to Wake-Dominated Poles, and Pole Location

C.5. Implementation - the Program PWAKE

Both the dimensional and nondimensional form of the coupled airframe/wake system (Appendix C.2) have been implemented in the program PWAKE. Input are the flight condition, wing and flap geometry, initial angle of attack and camber, spanwise slope of the steady-state induced flow distribution, natural frequencies, generalized masses, and mode shapes of the undamped structure, and the wake model order. Based on modal structural deflections in chordwise and beamwise deflections at 11 spanwise stations, for a specified number of chordwise locations at each station, a surface splining technique (/Harder and Desmarais 72/) is used to obtain the aerodynamic semi chord beamwise and chordwise deflections, w and u, twist, α, and quadratic camber, ξ (geometric and elastic). Wake forcing function integrals, equation (C.48) are determined using either the lifting line simplification, high aspect ratio approximation (first [constant] term only of the expansion, equation (C.54)/(C.55)), or numerical integration. Normalized associated Legendre functions may be calculated either with the algorithm by /He and Peters 88/ or equation (C.58). Output are coupled system eigenvalues and eigenvectors, possibly for a velocity sweep, and state-space generalized system matrices for a selected velocity. These matrices include the system dynamics matrix, control and gust input matrices, and modal deflection matrices at up to five locations, which are rigidly connected to a given point in the structure. Required deflections and slopes are determined using the surface spline mentioned above. Model order reduction may be performed by "inflow node" limitation, coupled mode "filtering" based on a user-supplied criterion (see Appendix C.4.2.), or a combination of both. Generalized system matrices are separately output in a file format which allows to load them into MATLAB™ for subsequent control system design.

C.6. Correlation of PWAKE with a Doublet-Lattice Method

In order to compare the performance of the Finite-State Wake Model with baseline results from a conventional fixed wing unsteady aerodynamics model, the high aspect ratio jet transport wing sample case from the 1994 ASTROS User Training Workshop, /Venkayya et. al. 94/, which was already used in verification of ELAPS modification, was implemented in PWAKE and ASTROS (Fig. C.16). In order to eliminate influences resulting from different structural models, ASTROS mode shapes, natural frequencies, and generalized masses were input into PWAKE. The ASTROS baseline results, Fig. C.17, were generated in a complete aeroelastic analysis run with a finite-element analysis of the structure, followed by a p-k iteration using the Doublet-Lattice Method in ASTROS. The critical phenomenon is coupling of the first and second lowest frequency modes at approximately 925 ft/sec. Flutter occurs at 1090 ft/sec, at a reduced frequency of k = 0.23. Previous results obtained with a two-dimensional version of the wake model indicated that this value marks approximately the range up to which the wake model performs properly* , which underscores the validity of this case as a benchmark test.

The importance of wake feedback effects becomes obvious when considering the characteristics of the system using quasi-steady aerodynamics only, Fig. C.18. Coupling of the first two structural modes does not occur, and the flutter speed is overpredicted by approximately 15%.

---

* Convergence of the chordwise inflow slope, λ_1, is slow; in the "lifting line" model, it is identical to zero. /Peters et al. 94/ showed that neglecting λ_1 in the Theodorsen Function results in very small errors up to approximately k = 0.3.

Adding a low order wake system degrades the result. Fig. C.19 depicts clearly that the second and third mode couple for M = 3, and that the system is stable up to 1400 ft/sec. The plot shows all modes of the coupled wake-structure system. Uncoupled wake modes feature velocity-proportional natural frequencies and constant damping (refer to Appendix C.4.1.). Similarly, wake-dominated modes of the coupled system exhibit the same characteristics (dashed lines in Fig. C.19), so that wake modes which couple with structural eigenforms can be identified by frequency branches which deviate from frequency proportionality with increasing or decreasing speed, and damping branches which show fluctuations in the same velocity range, but are otherwise fairly constant. The behavior was initially used to separate "wake-type" and "structure-type" modes. A closer investigation of the associated eigenvectors revealed that choosing a limit ratio, ε_{smodes}, and requiring for the structural and wake partitions of the eigenvectors, x_s and x_w, of dimension n_s and n_w, respectively, that

$$\frac{\sqrt{x_s{}^T x_s}}{\sqrt{x_w{}^T x_w}} \frac{n_w}{n_s} > \varepsilon_{s\,modes} \qquad \text{(C.61)}$$

performs exactly the same task. All following plots were generated using this technique, which facilitated comparison with the ASTROS results significantly. Modes which satisfy the criterion (C.61) only for a small velocity range are not plotted. Also, a rigorous analysis of modal frequency crossovers was not performed. Instead, branches were continued after such couplings to closely resemble the ASTROS baseline plots.

For M = 13 (56 wake states), the system behavior converged to that of the baseline results. Note strong coupling between a wake mode and the third structural (first torsional) mode. Convergence problems of the algorithm used for numerical integration of the chordwise integrals, equation (C.8), were encountered with increasing polynomial and

harmonics order, n and m, respectively. These became more severe when approaching the wing root, in particular for the integrals associated with inflow slope, $\lambda_{n;1}^{m;c}$. The impact of these numerical instabilities becomes apparent when comparing the results obtained using full numerical integration, Fig. C.20, numerical integration with $\lambda_{n;1}^{m;c} = 0$ for all (n,m), Fig. C.21, and lifting line approximation, Fig. C.22: Simplification of the model actually improved correlation with the ASTROS baseline. The flutter speed in Fig. C.22 is only 6% higher than that obtained with ASTROS. It was concluded that the lifting line model is more efficient and more accurate - since not subject to numerical instabilities - for this case.

Increase of the model order to M = 21 (132 wake states) reduced the predicted flutter speed to 3% below the ASTROS value, but did not improve overall correlation significantly (Fig. C.23), and therefore did not justify the increased computational effort. Excluding all wake states with $n' = n - m \leq 5$ reduced the wake order by approximately 30% while retaining acceptable accuracy, thus showing the viability of this approach (Fig. C.24). However, correlation is not much improved compared to Fig. C.22 (M = 13, lifting line model), and the wake model order is 60% higher.

In conclusion: For moderate to high aspect ratio wings, deviations associated with simplifications for the lifting line model are overcompensated by numerical problems with more "accurate" pressure distribution models. A maximum number of azimuthal harmonics, M = 13, and a lifting line model represented the best trade-off between accuracy and computational efficiency (model order). As a result , this PWAKE configuration was used in the tiltrotor Design Simulation Model.

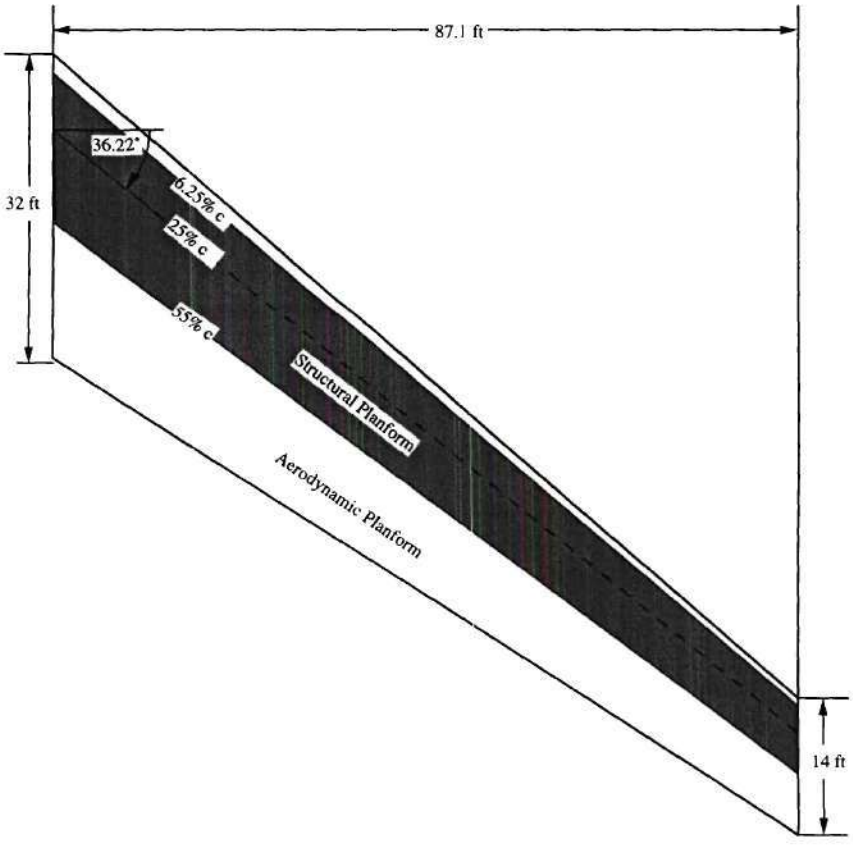

Fig. C.16: Sample Case Wing Planform

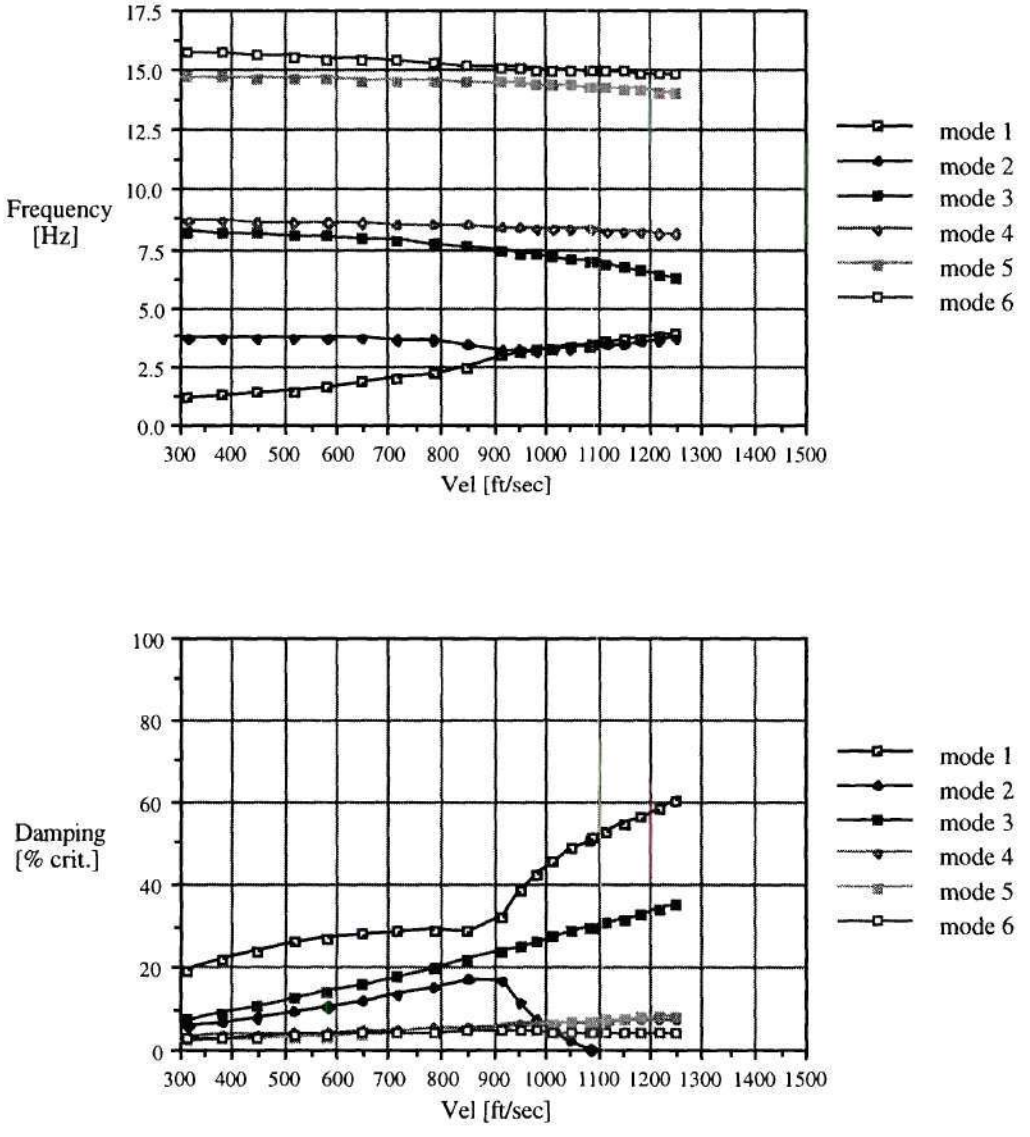

Fig. C.17: ASTROS Baseline Results

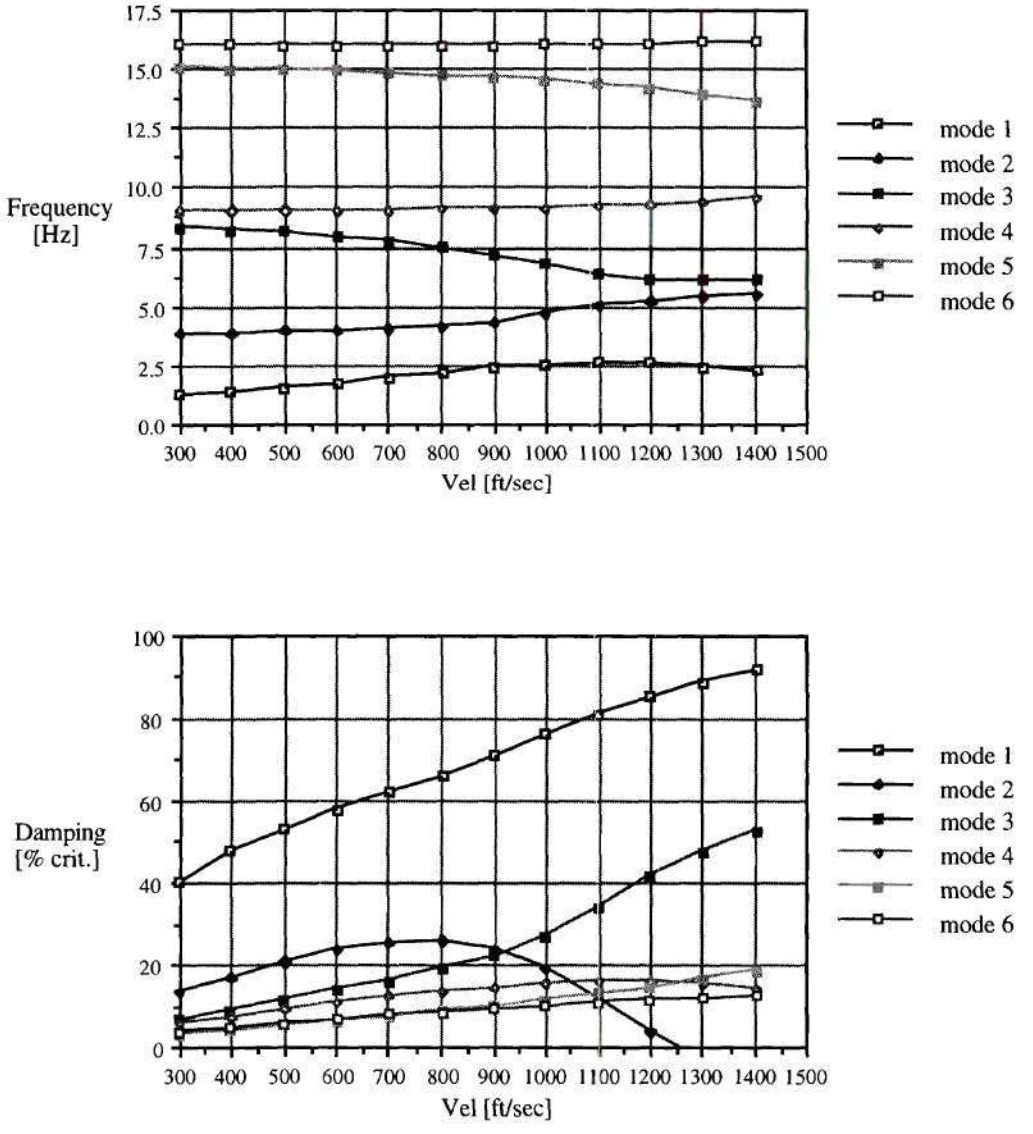

Fig. C.18: PWAKE, Quasi-Steady Aerodynamics

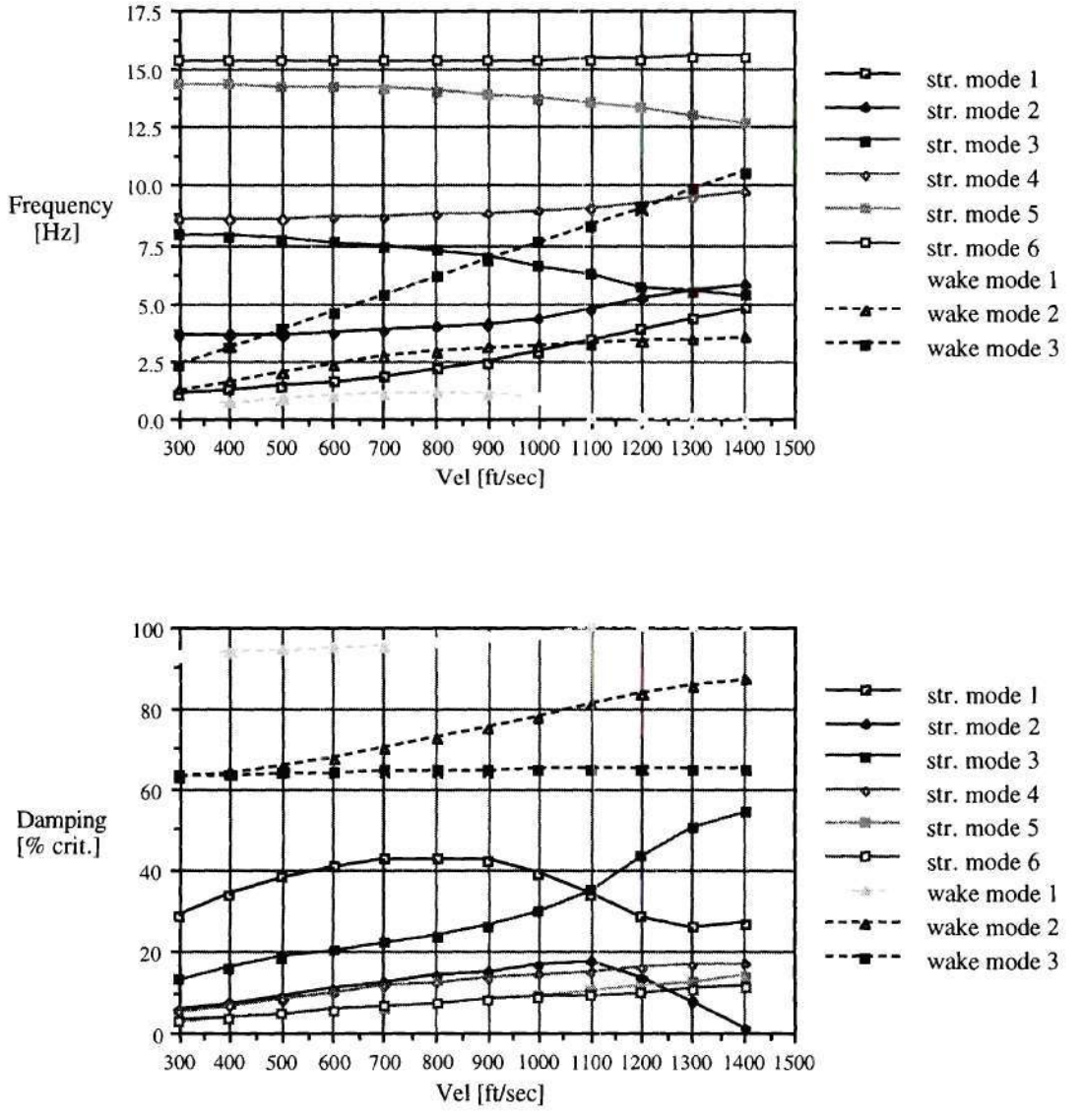

Fig. C.19: PWAKE, M = 3, Numerical Integration

(3 wake states)

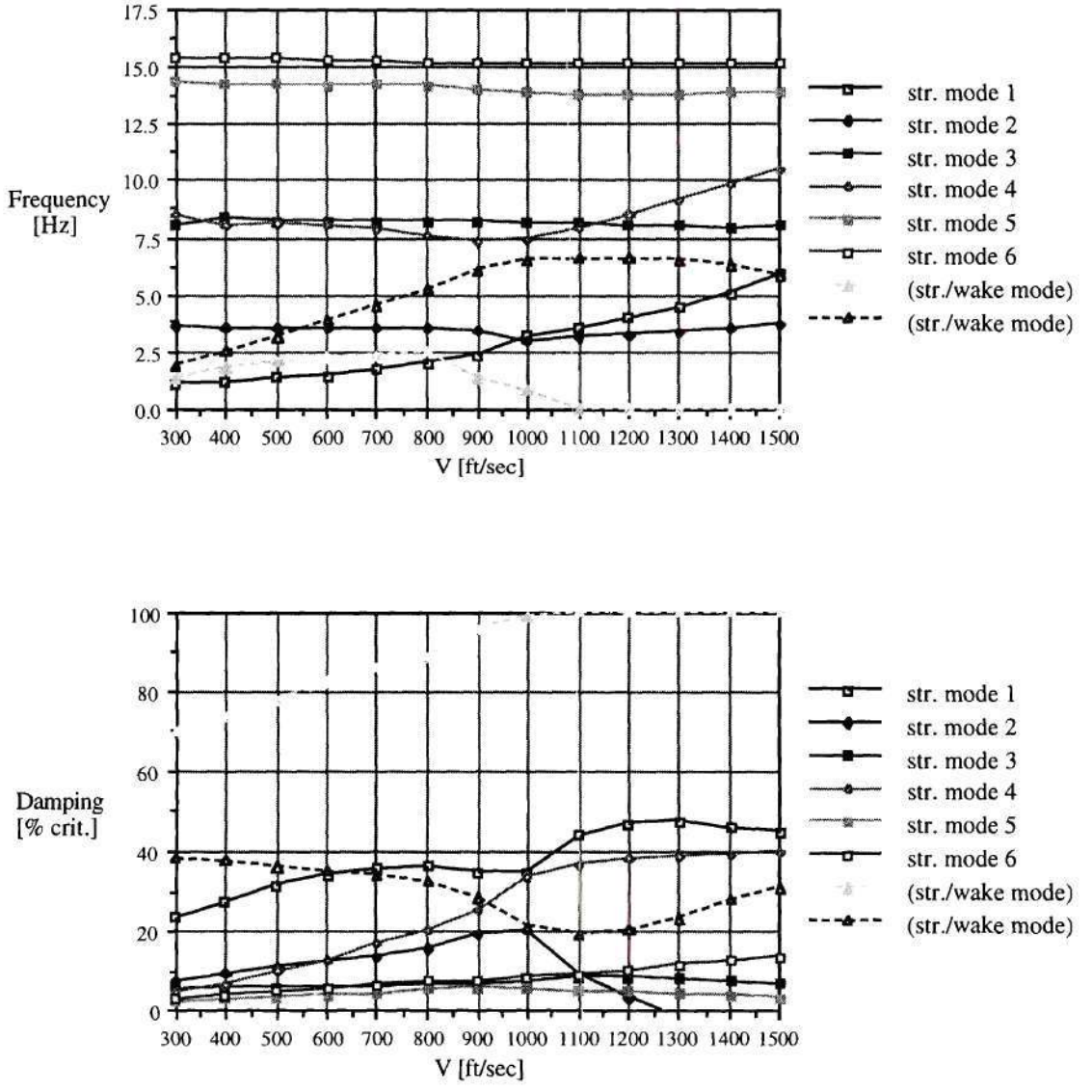

Fig. C.20: PWAKE, M = 13, Numerical Integration

(56 wake states)

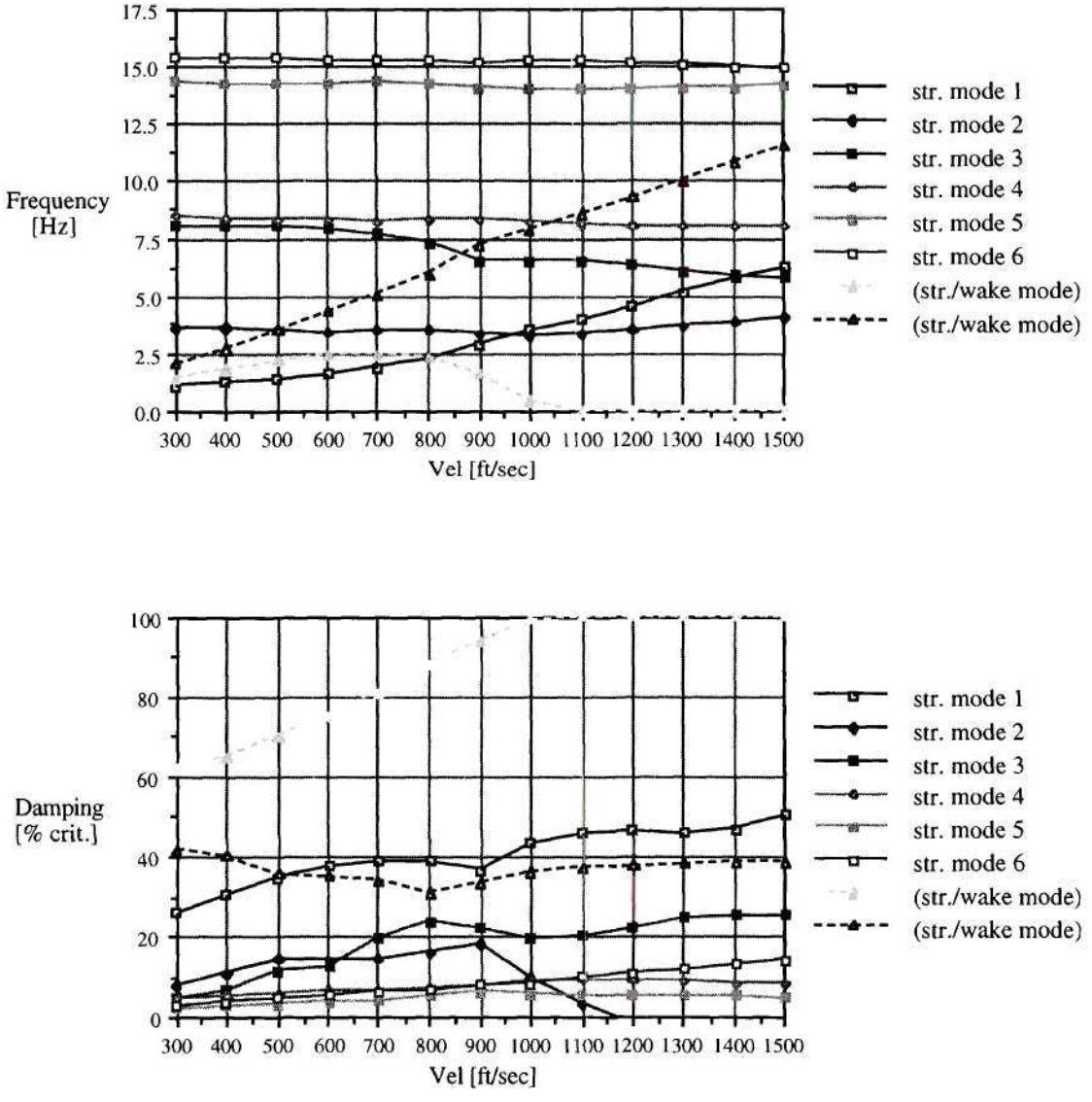

Fig. C.21: PWAKE, M = 13, Numerical Integration, λ_1 neglected

(56 wake states)

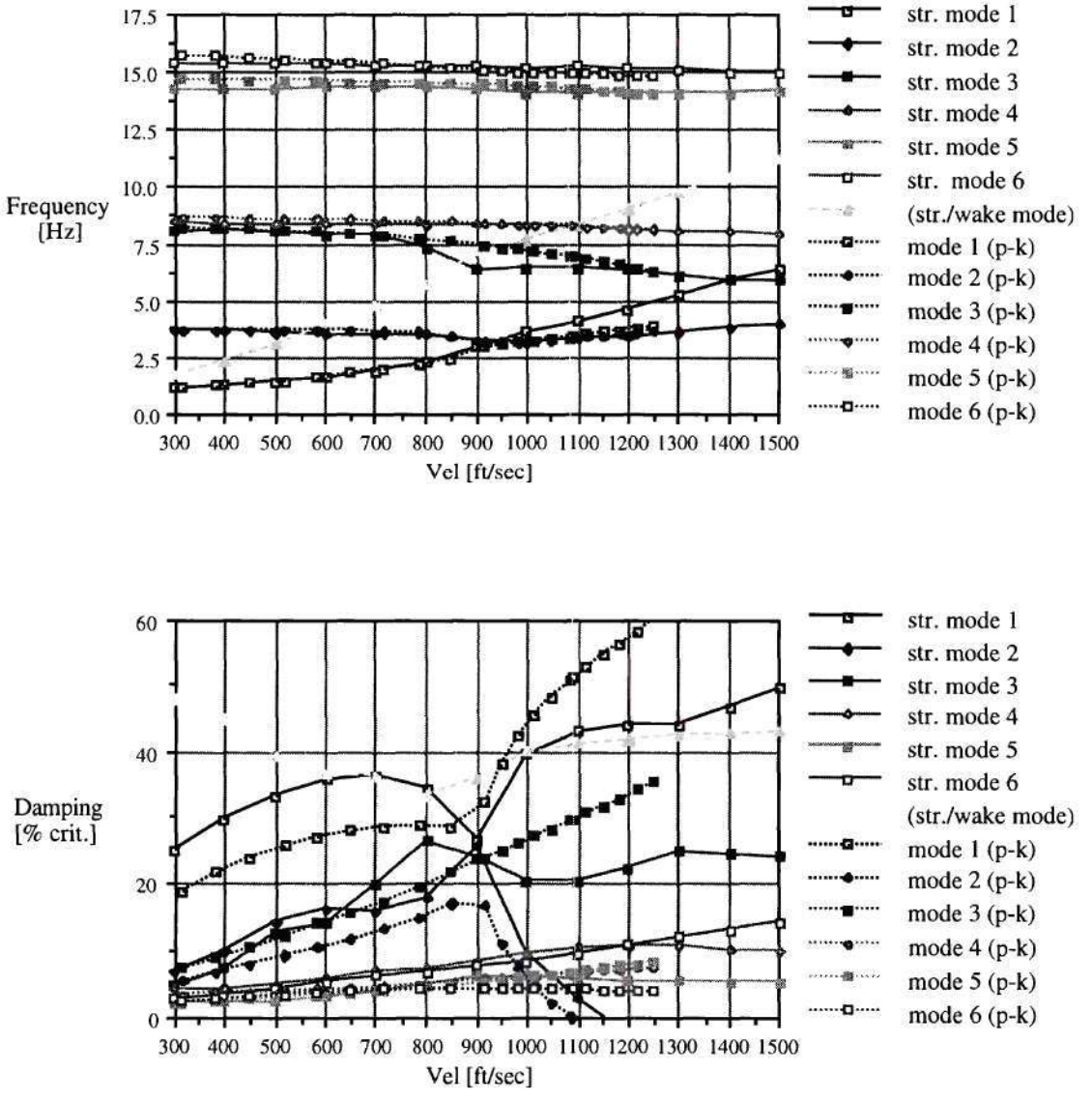

Fig. C.22: PWAKE, M = 13, Lifting Line Approximation (56 wake states)

and ASTROS p-k Method Baseline Results (dashed)

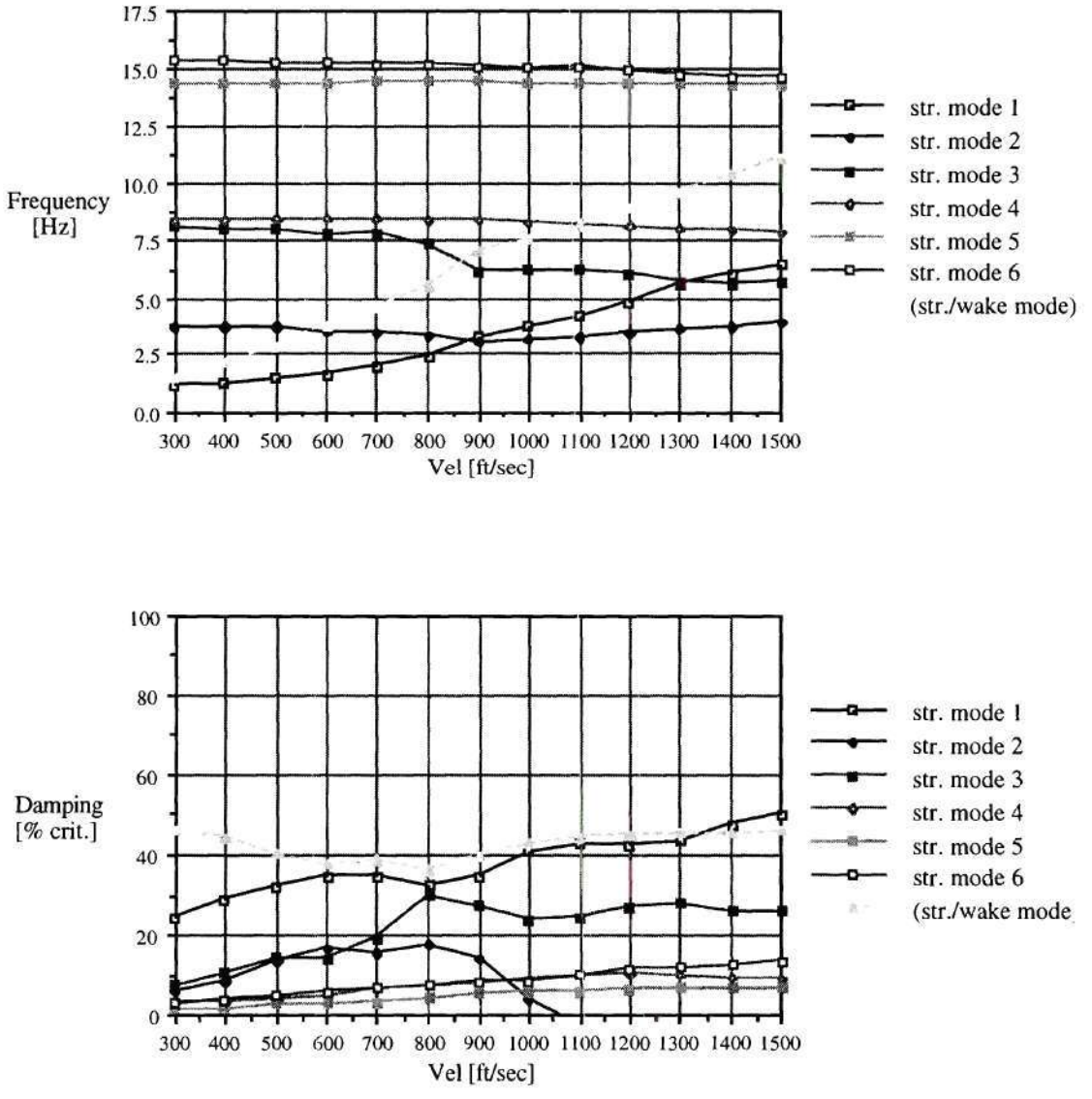

Fig. C.23: PWAKE, M = 21, Lifting Line Approximation

(132 wake states)

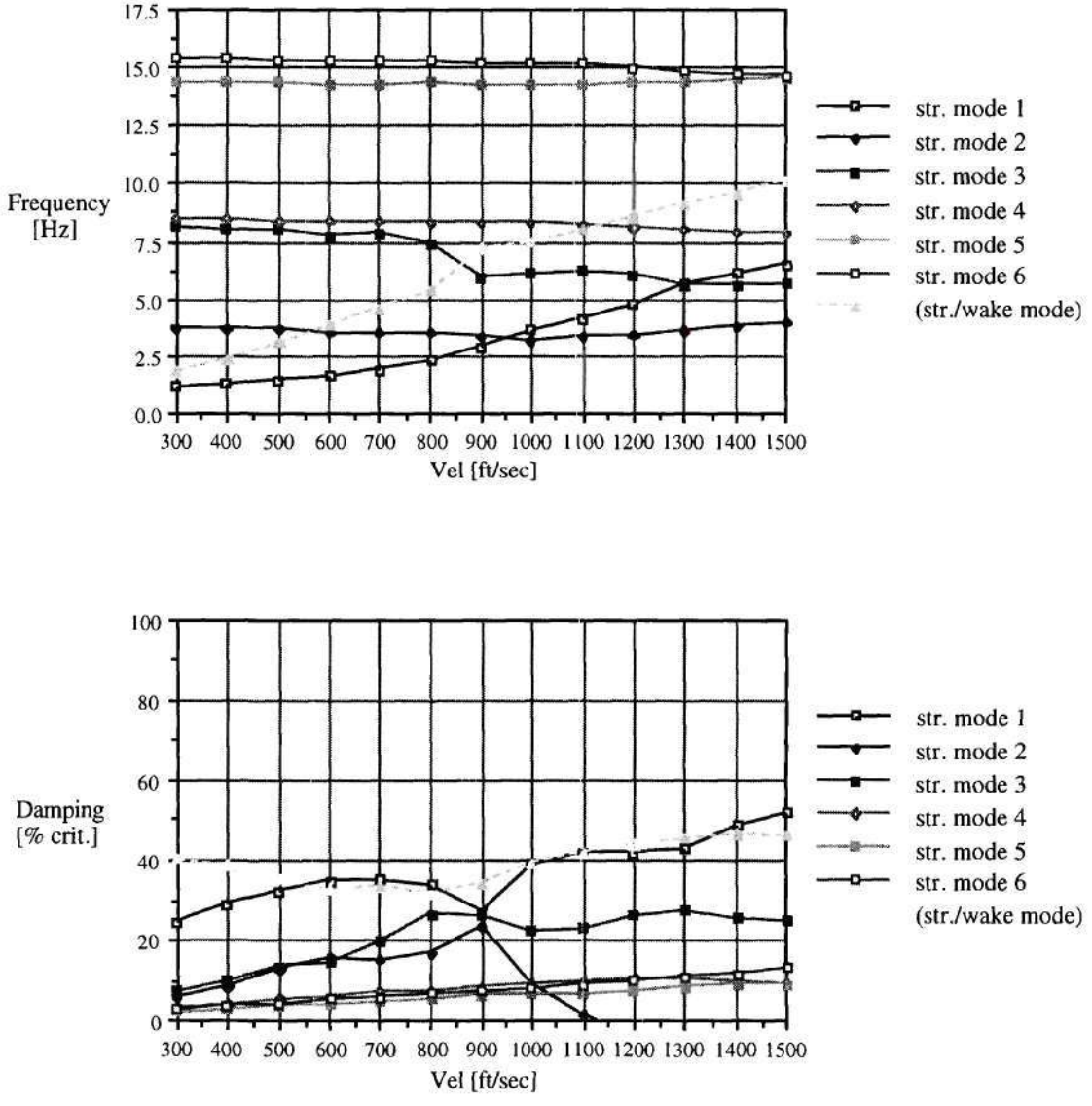

Fig. C.24: PWAKE, M = 21, Lifting Line Approximation, n' = 5

(90 wake states)

APPENDIX D

LINEAR DYNAMIC PLANT MODEL FOR TILTROTOR AIRCRAFT

Based on considerations presented in Section 3.2.4.1., the Proprotor Aeroelastic Stability Analysis, PASTA /Kvaternik 73/, was chosen as baseline analysis program for modeling proprotor aeroelasticity and coupling with airframe elastic and rigid body degrees of freedom. This Appendix describes a rotor blade static moment and inertia estimation based on blade weight, which was added to an external preprocessor, and development of the tiltrotor Aircraft Plant Model, ACP, from PASTA.

D.1. Blade Inertial Property Estimation

Rotor blade weight is provided by the contributing analysis for performance and sizing, VASCOMP. If the distribution of mass per unit radius is known, then the blade's static moment, S, and moment of inertia, I, can be computed. The simplifying assumption

that S and I are identical for flapping and lead-lag motion was made, based on the fact that the rotor model used did not employ and equivalent hinge offset). Since the blade mass, m_{blade}, is the integral of this distribution over the blade, the two missing entities can be directly expressed in terms of this value. Denoting the maximum value of mass per unit length as a function of nondimensional radius, $\overline{m}(r)$ (normalized by the hover radius, R) by $\overline{m}_{max}$, the following distribution was assumed for the constant diameter rotor:

$$\overline{m}(r) = \overline{m}_{max},\ 0 \le r \le 0.3; \quad \text{linear from } \overline{m}_{max} \text{ to } 0.2\overline{m}_{max} \text{ in } 0.3 < r \le 1 \tag{D.1}$$

which resulted in the following expressions:

$$S_{blade,c} = 0.3274\ m_{blade}\ R; \quad I_{blade,c} = 0.1534\ m_{blade}\ R^2 \tag{D.2}$$

For the variable diameter case, it was assumed that the inboard and outboard part of the blade have the same, constant mass distribution. In cruise configuration, the outer, "blade" partition slides completely over the inner, "torque tube" component of the rotor blade, leaving only room for the hub (assumed to be 5% of the hover rotor radius). In the interval of overlap, the mass per unit length is twice as large as in the remaining areas:

$$\begin{aligned} &\overline{m}(r) = 0.5\,\overline{m}_{max}, \quad 0 \le r \le 0.05 \ \text{ and } \ 1.05 - \bar{r} < r \le \bar{r} \\ &\overline{m}(r) = \overline{m}_{max}, \quad 0.05 < r \le 1.05 - \bar{r} \end{aligned} \tag{D.3}$$

where $\bar{r}$ is the extension ratio, the ratio of cruise to hover radius. The resulting static moment and mass moment of inertia of the blade about the hub in cruise configuration are

$$\begin{aligned} &S_{blade,v} = \left(0.55 - 1.05\bar{r} + \bar{r}^2\right) m_{blade}\ R; \\ &I_{blade,v} = \tfrac{1}{3}\left(1.1575 - 3.3075\bar{r} + 3.15\bar{r}^2\right) m_{blade}\ R^2 \end{aligned} \tag{D.4}$$

D.2. Rotor Dynamics

The rotor is represented in PASTA by a six degree of freedom model with coning and rotor rotation as collective, and longitudinal and lateral flapping and lead/lag as cyclic modes. A rigid blade representation with individual equivalent hinge offsets and hinge springs for each mode is used in the coning and cyclic flapping and lead/lag mode representations; in the rotor rotation mode, the blades are assumed to be rigidly mounted to the shaft. Indirect coupling between cyclic modes via blade pitch is introduced through pitch-flap and pitch-lag coupling coefficients, and the "hub rock ratio" (/Gaffey 69/), which accounts for blade pitch changes in elastic lag modes due to out-of-plane blade root deflections and pitch-flap coupling (δ_3). All these data may be input in form of a table as a function of collective blade pitch angle.

Two considerations led to replacement this rotor model. First, in order to provide an acceptable representation, a rotor dynamics table mentioned in the previous paragraph must be provided. Such a table may be based on existing data, or could be supplied by an external analysis employing an elastic blade model. The first option means that the rotor design cannot be changed, which is incompatible with the desire to tune airframe and rotor dynamics simultaneously. The second option requires inclusion of an additional Contributing Analysis for detailed rotor design, which was considered beyond the scope of this research. Second, the existing model did not employ elastic coupling between in-plane and out-of-plane modes per se. Previous studies have shown that both flapping and lead-lag degrees of freedom may contribute to the whirl mode (/Nixon 92/), so that consideration of couplings is of particular importance. Furthermore, whirl flutter modes may include large chordwise wing bending contributions (/van Aken 91/), which is

expected to couple kinematically with the rotor coning mode. Hence, coupling between rotor rotation and coning may have significant influence on whirl stability.

The present approach is to allow rotor dynamic tuning and inclusion of elastic coupling through utilization of the rigid blade model introduced by /Ormiston and Hodges 72/, Fig. D.1. Given the rotor angular velocity, Ω, blade inertia about the hub, I, and the "hub" and "blade" spring stiffnesses, $K_{\beta h}$ through $K_{\zeta b}$, elastic coupling between lead/lag and flapping can be calculated as a function of the blade pitch angle, θ, which also denoted the relative angular offset of the two hinge/spring systems. The elastic out-of-plane and inplane root moments are described by

$$M_{\beta\,\text{elastic}} = -\frac{1}{\Delta}\left[K_\beta + R\left(K_\varsigma - K_\beta\right)\sin^2\theta\right]\beta + \frac{1}{2\Delta}\left[R\left(K_\varsigma - K_\beta\right)\sin 2\theta\right]\varsigma \qquad \text{(D.5a)}$$

$$M_{\varsigma\,\text{elastic}} = \frac{1}{2\Delta}\left[R\left(K_\varsigma - K_\beta\right)\sin 2\theta\right]\beta - \frac{1}{\Delta}\left[K_\varsigma - R\left(K_\varsigma - K_\beta\right)\sin^2\theta\right]\varsigma \qquad \text{(D.5b)}$$

which shows the coupling between the two degrees of freedom. In equations (D.5), the following abbreviations were used in accordance with /Ormiston and Hodges 72/:

The combined stiffnesses from both spring systems for $\theta = 0$,

$$K_\beta = \frac{K_{\beta b}\,K_{\beta h}}{K_{\beta b} + K_{\beta h}}; \quad K_\varsigma = \frac{K_{\varsigma b}\,K_{\varsigma h}}{K_{\varsigma b} + K_{\varsigma h}} \qquad \text{(D.6)}$$

the coupling ratio, R, which is 0.0 if the dynamic properties do not change with pitch, and 1.0 if only the "blade" spring system exists:

$$R = \frac{K_\beta}{K_{\beta b}} = \frac{K_\varsigma}{K_{\varsigma b}} \qquad \text{(D.7)}$$

and the denominator term, Δ,*

$$\Delta = 1 + R(1-R)\frac{\left(K_\varsigma - K_\beta\right)^2}{K_\varsigma K_\beta}\sin^2\theta \qquad (D.8)$$

Collective and cyclic modes represent different situations for a gimbaled rotor system, Table D.1: Based on symmetry considerations, the "hub" degrees of freedom do not contribute to collective flapping and cyclic lead/lag. For simulation of this effect, the respective spring stiffnesses in equation (D.6) approach infinity. Hence, the gimbal spring stiffness, K_{gimbal}, appears only in the cyclic flapping degrees of freedom, and the rotor shaft stiffness, K_{shaft}, is only found in the collective lead/lag term. The elastic "blade" spring stiffnesses, $K_{\beta\,elastic}$ and $K_{\zeta\,elastic}$, occur in all stiffness expressions.

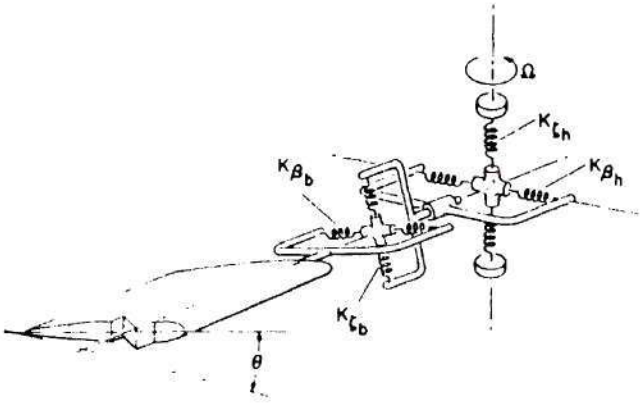

Fig. D.1: Rigid Blade Model with two Hinge/Spring Systems
(both systems are located at the hub, and are only separated for clarity;
from /Ormiston and Hodges 72/)

---

* based on re-derivation of the system dynamics; this term is the only expression which is different from those given in /Ormiston and Hodges 72/

Root spring stiffness terms in PASTA were replaced by the expressions in equations (D.1), and cross-coupling terms added. In order to allow size-independent tuning of the rotor, the natural frequencies per revolution are used as input (except for the rotor shaft stiffness). The associated hinge stiffnesses are calculated based on standard centrally hinged rigid blade expressions for decoupled gimbal tilt, lead/lag and flapping motion. The following parameters were therefore used for simplified rotor frequency placement: First out-of-plane natural frequency per revolution of the elastic blade, with the root rigidly attached to a hub rotating at constant angular velocity; first inplane natural frequency per revolution with the same boundary conditions; and rotor gimbal tilt natural frequency, assuming a "rigid rotor disk" (no blade flexibility).

Pitch-flap coupling through a given pitch link geometry was included in the model. Consider the situation at zero blade pitch angle, θ, Fig. D.2(a). The pitch horn is oriented at an angle, φ_0, with respect to the blade reference chord line. In consideration of the radial offset, b, of the pitch horn from the rotor center, and the length, l, of the pitch horn, the pitch-flap coupling parameter for this configuration, $\bar{\delta}_3$, is

$$\bar{\delta}_3 = \tan^{-1}\left(\frac{b}{l\cos\varphi_0}\right) \tag{D.9}$$

For non-zero blade pitch, δ_3 can be calculated using $\bar{\delta}_3$ and φ_0 (Fig. D.2 (b)), so that these two values are sufficient for description of the pitch link geometry effect on pitch-flap coupling change with collective pitch (and therefore qualify as design variables):

$$\delta_3 = \tan^{-1}\left(\tan\bar{\delta}_3 \frac{\cos\varphi_0}{\cos(\varphi_0 - \theta)}\right) \tag{D.10}$$

Table D.1: Individual Spring Stiffnesses, Rigid Blade Model

	Collective $I_{rotor} = n_b\, I_{blade}$	Cyclic $I_{rotor} = \frac{n_b}{2} I_{blade}$
flapping	 $K_{\beta b} = n_b\, K_{\beta elastic}$ $K_{\beta h} \rightarrow \infty$	 $K_{\beta b} = \frac{n_b}{2} K_{\beta elastic}$ $K_{\beta h} = K_{gimbal}$
lead / lag	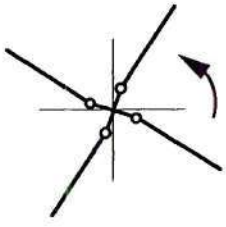 $K_{\varsigma b} = n_b\, K_{\varsigma elastic}$ $K_{\varsigma h} = K_{shaft}$	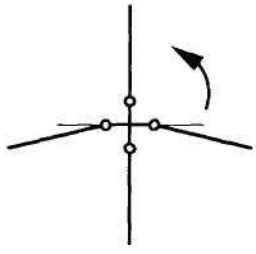 $K_{\varsigma b} = \frac{n_b}{2} K_{\varsigma elastic}$ $K_{\varsigma h} \rightarrow \infty$

n_b: number of blades per rotor; $n_b \geq 3$

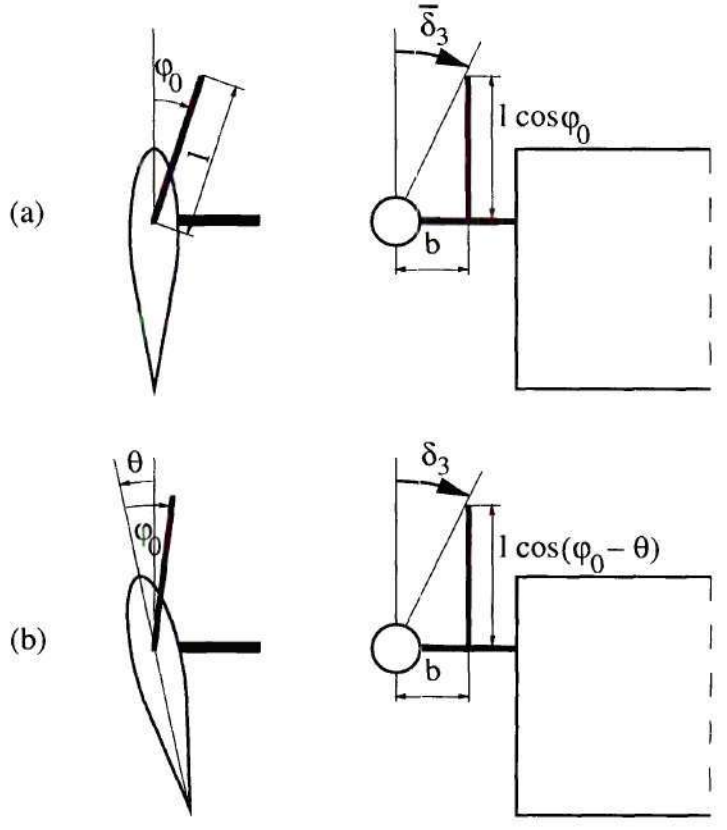

Fig. D.2: Pitch Link Geometry

D.3. Control and Gust Input

The baseline code, PASTA, was designed to perform modal analysis of the undisturbed, passively damped rotor / airframe system. Hence, it does not include provisions for gust response investigations and active control inputs. Control and gust input matrix elements, however, can be derived from existing terms in PASTA:

The system dynamics are initially derived for uncoupled rotor and airframe systems in the program . Rotor / nacelle degrees of freedom are the six rotor hub (nacelle) motions in translation (x, y, and z) and rotation (ϕ_x, ϕ_y, and ϕ_z), rotor coning, a_0, longitudinal and lateral flapping, a_1 and b_1, shaft elastic twist, ϕ'_x, and, lateral and longitudinal lead/lag, c_1 and d_1 (Fig. D.3; rotor disk is shown for no nacelle rotation). At this stage, gust input terms can be easily identified in the rotor aerodynamic expressions from /Kvaternik 73/, or directly in the source code: A horizontal gust velocity, V_h, creates the same perturbation velocities as rotor translation in negative z-direction, $-\dot{z}$; similarly, V_v terms are of the same form as $\dot{x}$ terms. PASTA's rotor aerodynamics model includes cyclic blade pitch changes through swashplate/nacelle coupling, Fig. D.4. If no coupling exists, then the swashplate pitches with the shaft ($K_1 = 0$). Is the swashplate rigidly coupled to some support ($K_1 = 1$), then pylon pitch, ϕ_y, causes the swashplate to be tilted with respect to the shaft axis, and longitudinal cyclic pitch, δ_l, identical to the negative pylon pitch angle is introduced. Similarly, pylon yaw, ϕ_z, results in negative lateral cyclic pitch, δ_a, for a lateral gain of $K_2 = 1$. Hence, cyclic perturbation pitch, $\Delta\theta_{cyc}$, is described by

$$\Delta\theta_{cyc} = -K_1 \phi_y \cos\psi - K_2 \phi_z \sin\psi = \delta_l \cos\psi + \delta_a \sin\psi \qquad (D.11)$$

so that cyclic pitch control terms can easily be identified by locating expressions multiplied by $-K_1\phi_y$ and $-K_2\phi_z$, respectively.

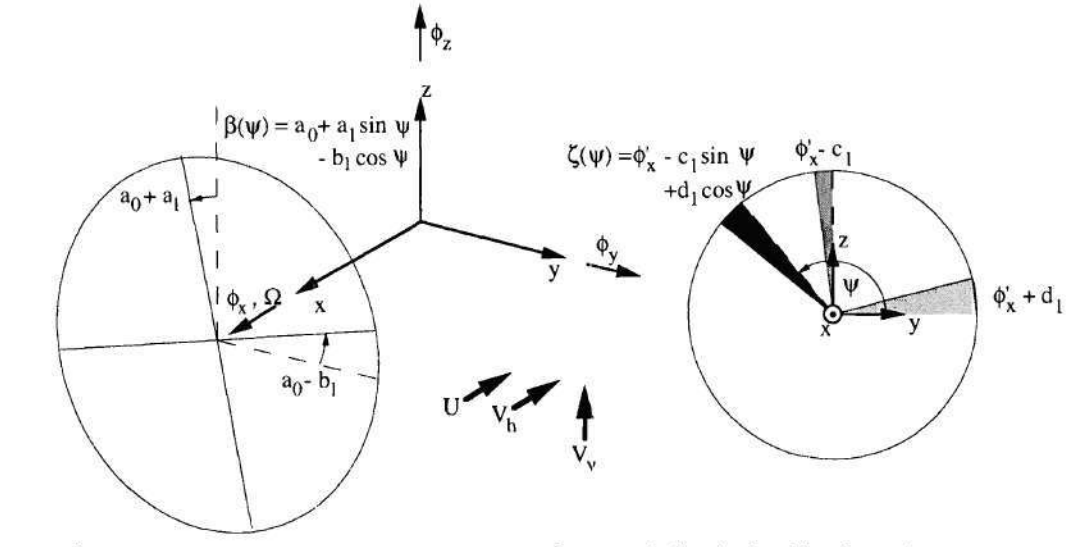

a_0: coning
a_1: longitudinal tip path plane tilt (positive about y)
b_1: lateral tip path plane tilt (positive about z)

ϕ'_x: rotor shaft twist (positive about x)
c_1: longitudinal rotor c.g. motion (positive in z-dir.)
d_1: lateral rotor c.g. motion (positive in y-dir.)

Fig. D.3: Rotor / Nacelle Degrees of Freedom

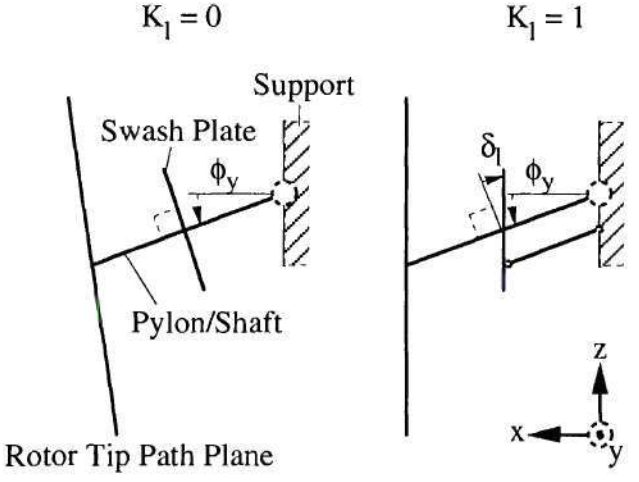

Fig. D.4: Swash Plate / Pylon Coupling

D.4. Subsystem Coupling

Coupling of dynamic subsystems by enforcement of geometric compatibility and force equilibrium at the subsystem interfaces is a well-known procedure and is frequently applied, for example, in finite-element analyses. In the present case, however, the airframe subsystem includes aerodynamic damping, which in general does not allow a description in mass, damping and stiffness only, but may require higher order time derivative terms. A state-space representation is most commonly used or these systems. The coupling procedure must account for this fact, in particular since the rotor subsystem in PASTA is represented in second order form, with a singular mass matrix.

The following subsection reviews aspects of generalized dynamic system description in state-space with respect to opportunities for reduction of necessary data. The actual coupling procedure as implemented in ACP is described in Appendix D.4.2.

D.4.1. General Considerations

Consider the state-space representation of a homogeneous second order dynamic system with degrees of freedom, $\{y\}$, and system matrix, [A],

$$\begin{Bmatrix} \{y\} \\ \{\dot{y}\} \end{Bmatrix}^{\bullet} = [A] \begin{Bmatrix} \{y\} \\ \{\dot{y}\} \end{Bmatrix} \tag{D.12}$$

Let the deflections of this system be described as a series in the modal deflection vectors, $\{\psi_i\}$,

$$\{y\}(t) = \sum_i \{\psi_i\}\, q_i\, e^{\lambda_i t} \tag{D.13}$$

where λ_i are the associated eigenvalues. Then the state-space system deflections are

$$\begin{Bmatrix}\{y\}\\ \{\dot{y}\}\end{Bmatrix}(t)=\sum_i \begin{Bmatrix}\{\psi_i\}\\ \lambda_i\{\psi_i\}\end{Bmatrix} q_i\, e^{\lambda_i t}=\sum_i \{x_i\}\, q_i\, e^{\lambda_i t} \tag{D.14}$$

with the eigenvectors of the system in state-space form, $\{x_i\}$, so that for complex conjugate pole pairs, $(\lambda_i, \bar{\lambda}_i)$,

$$[A]\{x_i\}=\lambda_i\{x_i\};\quad [A]\{\bar{x}_i\}=\bar{\lambda}_i\{\bar{x}_i\} \tag{D.15}$$

Expansion of complex eigenvalues and eigenvectors in real and imaginary parts in the form

$$\begin{aligned}\lambda_i &= u+iv\\ \{\psi_i\} &= \{a\}+i\{b\}\\ \{x_i\} &= \{c\}+i\{d\}\end{aligned} \tag{D.16}$$

and insertion of these expression into equation (D.15) yields for the real and imaginary parts of this equation, respectively,

$$[A]\{c\}=\{c\}u-\{d\}v;\quad [A]\{d\}=\{c\}v+\{d\}u \tag{D.17}$$

Rewriting equations (D.15) and (D.17) in the following form shows more clearly that these are equivalent representations:

$$[A]\left[\{x\}\{\bar{x}\}\right]=\left[\{x\}\{\bar{x}\}\right]\begin{bmatrix}\lambda_i & \\ & \bar{\lambda}_i\end{bmatrix} \tag{D.18}$$

$$[A]\left[\{c\}\{d\}\right]=\left[\{c\}\{d\}\right]\begin{bmatrix}u & v\\ -v & u\end{bmatrix} \tag{D.19}$$

The matrix of eigenvectors is commonly referred to as the modal matrix; the second matrix on the right hand side of equations (D.18) and (D.19) shall be called the generalized

system matrix. A complete description of (D.12) requires both the modal matrix and the generalized system matrix, which contains the eigenvalues on its main diagonal (D.18) or its real and imaginary parts in 2×2 blocks (D.19). Note that (D.19) is a purely real representation, which allows more compact storage and data transfer. Additionally, it can be shown that

$$\{c\} = \begin{Bmatrix} \{a\} \\ \{a\}u - \{b\}v \end{Bmatrix}; \quad \{d\} = \begin{Bmatrix} \{b\} \\ \{a\}v + \{b\}u \end{Bmatrix} \tag{D.20}$$

so that the system (D.12) is completely described by the real and imaginary parts of its eigenvalues (u, v) and the upper partition of its real modal matrix ({a}, {b}; the lower partition can be reconstructed according to (D.20)). For a system with n degrees of freedom, the total number of real data required, N_{min}, is

$$N_{min} = 2n + 2n^2 \tag{D.21}$$

whereas the equivalent value for equation (D.18), N, with a fully populated, complex modal matrix is

$$N = 2n + 2(2n)^2 \tag{D.22}$$

The real representation using (D.20) is much more compact, which is an important factor with respect to data transfer infrastructure in multidisciplinary optimization tasks, and was therefore used in the input and subsystem coupling procedures of ACP.

D.4.2. System Coupling

D.4.2.1. Airframe / Aerodynamics System

Consider the airframe / aerodynamics system from Appendix C, equation (C.45), in its generalized form:

$$\{\dot{q}_{ae}\} = [AM]\{q_{ae}\} + [BUU]\{u_s\} + [BGG]\{w\} + \sum_{l}\left[WF^{l}\right]\left\{F^{l}\right\} \tag{D.23}$$

with the system's normal coordinate vector, $\{q_{ae}\}$, airframe control surface control vector, $\{u_s\}$, gust vector, $\{w\}$, external force vector at location l, $\{F^l\}$, and the generalized system, control, gust and force input matrices, respectively, which are calculated from the expressions derived in Appendix C using the modal matrix, [X], as

$$\begin{aligned}
[AM] &= [X]^{-1}[\boldsymbol{A}][X] \\
[BUU] &= [X]^{-1}[\boldsymbol{B}] \\
[BGG] &= [X]^{-1}[\boldsymbol{G}] \\
\left[WF^{l}\right] &= [X]^{-1}\left[\boldsymbol{W}^{l}\right]
\end{aligned} \tag{D.24}$$

The airframe deflections at location l, $\{d^l\}$, are a function of the system normal modes according to

$$\left\{d^{l}\right\} = \left\{x^{l}, y^{l}, z^{l}, \phi_x^{l}, \phi_y^{l}, \phi_z^{l}\right\}^{T} = \left[WG0^{l}\right]\{q_{ae}\} \tag{D.25}$$

where, again in reference to Appendix C,

$$\left[WG0^{l}\right] = \left[\left[WU^{l}\right] \quad [0] \quad [0]\right][X] \tag{D.26}$$

Note that the associated matrix for the first deflection time derivative, $\left[WG1^{l}\right]$,

$$\left\{\dot{d}^l\right\} = \left[WG1^l\right]\left\{q_{ae}\right\} \tag{D.27}$$

can be derived from $\left[WG0^l\right]$ in the same fashion as demonstrated in the previous section for the lower partition of the real representation of the modal matrix. It assumed that the matrices in (D.23) and (D.25) have been generated using the real representation of the modal matrix as described in the previous section, and are supplied to the coupling procedure. Three sources for external forces, acting at two location of the airframe, can be identified for the dynamic tiltrotor model:

(i) Support springs and dampers at the aircraft center of gravity - This feature is included in PASTA to allow proper modeling of aeroelastic windtunnel models. Support springs and dampers are assumed to act independently in the six rigid body degrees of freedom, so that the associated stiffness and damping matrices with elements k^{sup} and d^{sup}, respectively, are diagonal (using equations (D.25) and (D.27) to eliminate the physical deflections at the center of gravity and their first time derivative):

$$\left[WF^l\right]\left\{F^l\right\} = \left[WF^{cg}\right]\left(-\text{diag}\left(k^{sup}\right)\left[WG0^{cg}\right] - \text{diag}\left(d^{sup}\right)\left[WG1^{cg}\right]\right)\left\{q_{ae}\right\} \tag{D.28}$$

(ii) Airframe quasi-steady aerodynamic forces at the aircraft center of gravity - Airframe mass, damping, and stiffness matrices filled with flight dynamic stability derivatives in Etkin's notation (/Etkin 82/) are assembled in PASTA and were used to investigate the effect of rotor forces on aircraft rigid body degrees of freedom. In the current approach, airframe inertias and wing aerodynamic forces have already been included in the airframe aeroelastic model (free-free configuration). The existing stiffness, and damping matrices, [ASR] and [ADR], respectively, can be used for inclusion of aerodynamic loads on tail and fuselage due to airframe elastic deflections though if wing contributions are eliminated from the stability derivatives. A gust input matrix, [AGR], has

been derived in a fashion similar to that described in Appendix D.3, and the horizontal force and pitch contributions of elevator deflection, u_{cg}, have been added in the vector {ACR}. The resulting generalized force at the center of gravity is

$$\left[WF^2\right]\left\{F^2\right\} = -\left[WF^{cg}\right]\left(\left[ASR\right]\left[WG0^{cg}\right]+\left[ADR\right]\left[WG1^{cg}\right]\right)\left\{q_{ae}\right\}$$

$$+\left[WF^{cg}\right]\left\{ACR\right\}u_{cg}+\left[WF^{cg}\right]\left[AGR\right]\left\{w\right\} \qquad (D.29)$$

(iii) Hub loads at the rotor attachment point - inertial and aerodynamic forces and moments enter the airframe at the rotor hub:

$$\left[WF^3\right]\left\{F^3\right\} = \left[WF^h\right]\left\{F_x^h, F_y^h, F_z^h, M_x^h, M_y^h, M_z^h\right\}^T \qquad (D.30)$$

The moment transmitted by the rotor shaft, M_x^h, requires special consideration. Strictly speaking, this moment acts as an external forcing function to the engine dynamics, which, in turn, couple into airframe dynamics. An engine model, however, is not included. Instead, it is assumed that the output shaft perturbation torque at the hub, M_x^h, follows a first order relationship in the engine housing rotation about the shaft axis, ϕ_x, and the rotor's rotational degree of freedom, ϕ_x':

$$M_x^h = K_\phi\left(\phi_x' - \phi_x\right) + C_\phi\left(\dot{\phi}_x' - \dot{\phi}_x\right) \qquad (D.31)$$

This relationship can be interpreted in the following way: Given an unlimited power source which generates a constant angular velocity with respect to its housing, the coefficients, K_ϕ and C_ϕ, are the stiffness and damping of the shaft connecting this source to the rotor hub. For antisymmetric airframe modes, a more practical explanation is possible. In this case, the interconnect shaft between the two rotors of a tiltrotor aircraft is subject to oscillatory torque loads, and the coefficients in equation (D.31) are equivalent to the stiffness and damping of the drive system from the rotor hub to the center of the

fuselage. /Johnson 75/ showed that for symmetric airframe modes, on the other hand, the moment transmitted between rotor and airframe, M_x^h, is very small, so that the powered case can be approximated by the windmilling (or autorotating) condition. Subsequently, a very small value is chosen for K_ϕ (but larger than zero, to avoid introduction of a rigid body degree of freedom), and C_ϕ may be set to zero.

If the engine is assumed to be rigidly mounted to the airframe, then the engine housing deflection can be replaced by the airframe normal modes:

$$M_x^h = K_\phi \phi_x' + C_\phi \dot{\phi}_x' - \left(K_\phi \left\lfloor WG0_{(4)}^h \right\rfloor + C_\phi \left\lfloor WG1_{(4)}^h \right\rfloor \right) \{q_{ae}\} \tag{D.32}$$

where the subscript, (4), denotes the fourth row of the respective matrix, which is associated with ϕ_x (see equation (D.25)). The total generalized force at the rotor hub can be divided into a torque contribution and the effect of the remaining force vector, $\{F^h\}$:

$$\left[WF^3\right]\left\{F^3\right\} = \left\{WF^{h,(4)}\right\}\left(K_\phi \phi_x' + C_\phi \dot{\phi}_x'\right) - \left\{WF^{h,(4)}\right\}\left(K_\phi \left\lfloor WG0_{(4)}^h \right\rfloor + C_\phi \left\lfloor WG1_{(4)}^h \right\rfloor\right)\{q_{ae}\}$$
$$+\left[WF^{h*}\right]\left\{F^h\right\} \tag{D.33}$$

The superscript, (4), stands for the fourth column of $[WF^h]$. This column was then omitted in $\left[WF^{h*}\right]$, which is denoted by the asterisk. After inclusion of all external force expressions, the airframe / aerodynamics system equation (D.23) takes the following form:

$$\{\dot{q}_{ae}\} = [AM']\{q_{ae}\} + \left\{WF^{h,(4)}\right\}\left(K_\phi \phi_x' + C_\phi \dot{\phi}_x'\right)$$
$$+\left[[BUU] \quad \left[WF^{cg}\right]\{ACR\}\right]\begin{Bmatrix}\{u_s\}\\ u_{cg}\end{Bmatrix} + \left[[BGG] + \left[WF^{cg}\right][AGR]\right]\{w\} \tag{D.34}$$
$$+\left[WF^{h*}\right]\left\{F^h\right\}$$

The original system dynamics matrix, [AM], is modified in the following way:

$$
\begin{aligned}
[AM'] = [AM] \\
&- \left(\left[WF^{cg} \right] \mathrm{diag}\left(k^{sup} \right) \left[WG0^{cg} \right] + \left[WF^{cg} \right] \mathrm{diag}\left(d^{sup} \right) \left[WG1^{cg} \right] \right) \\
&- \left(\left[WF^{cg} \right] [ASR] \left[WG0^{cg} \right] + \left[WF^{cg} \right] [ADR] \left[WG1^{cg} \right] \right) \\
&- \left(K_\phi \left\{ WF^{h,(4)} \right\} \left\lfloor WG0^{h}_{(4)} \right\rfloor + C_\phi \left\{ WF^{h,(4)} \right\} \left\lfloor WG1^{h}_{(4)} \right\rfloor \right)
\end{aligned}
\tag{D.35}
$$

D.4.2.2. Rotor / Nacelle System

The dynamics of rotor, nacelle, and rotor blade aerodynamics, including the modification described in Appendices D.2 and D.3, can be written in matrix form:

$$
[BM]\left\{ \ddot{x}_{rn} \right\} + [BC]\left\{ \dot{x}_{rn} \right\} + [BK]\left\{ x_{rn} \right\} = [BUR]\left\{ u_r \right\} + [BGR]\{w\} + \left\{ F^h_{rn} \right\} \tag{D.36}
$$

The vector of rotor and nacelle degrees of freedom,

$$
\left\{ x_{rn} \right\} = \left\{ a_0, a_1, a_2, b_1, c_1, d_1, \phi'_x, x^h, y^h, z^h, \phi^h_y, \phi^h_z \right\}^T \tag{D.37}
$$

can be partitioned into the rotor degrees of freedom, $\{x_r\}$, in coning, a_0, longitudinal flapping, a_1, lateral flapping, b_1, longitudinal lag (or lateral rotor center of gravity displacement), c_1, lateral lag (or longitudinal rotor cg motion), d_1, and rotor rotation, ϕ'_x:

$$
\left\{ x_r \right\} = \left\{ a_0, a_1, a_2, b_1, c_1, d_1, \phi'_x \right\}^T \tag{D.38}
$$

and the hub displacements,

$$
\left\{ x_n \right\} = \left\{ x^h, y^h, z^h, \phi^h_y, \phi^h_z \right\}^T \tag{D.39}
$$

Note that for compatibility with the airframe dynamics, the external hub force, $\left\{ F^h_{rn} \right\}$, is the negative of the generalized force acting on the airframe at the hub; since this

force depends on airframe deflections only, it affects exclusively the hub displacement partition of equation (D.36). Using equation (D.33), the external force can be expressed in the following form:

$$\left\{F_{rn}^{h}\right\}=\begin{bmatrix}[0]_{5\times n} & [0]_{5\times 6} & [0]_{5\times 6}\\ K_{\phi}\left\lfloor WG0_{(4)}^{h}\right\rfloor+C_{\phi}\left\lfloor WG1_{(4)}^{h}\right\rfloor & \left\lfloor 0,0,0,0,0,-K_{\phi}\right\rfloor & \left\lfloor 0,0,0,0,0,-C_{\phi}\right\rfloor\\ [0]_{5\times n} & [0]_{5\times 6} & [0]_{5\times 6}\end{bmatrix}\begin{Bmatrix}\{q_{ae}\}\\ \{x_r\}\\ \{\dot{x}_r\}\end{Bmatrix}$$

$$-\begin{Bmatrix}[0]_{6\times 5}\\ I_5\end{Bmatrix}\left\{F^{h}\right\} \qquad (D.40)$$

$$=[\Delta AR_1]\begin{Bmatrix}\{q_{ae}\}\\ \{x_r\}\\ \{\dot{x}_r\}\end{Bmatrix}-\begin{Bmatrix}[0]_{6\times 5}\\ I_5\end{Bmatrix}\left\{F^{h}\right\}$$

(n is the order of the airframe / aerodynamics system). The system is finally converted into state-space form:

$$[OM]\begin{Bmatrix}\{x_{rn}\}\\ \{\dot{x}_{rn}\}\end{Bmatrix}^{\bullet}=[SC]\begin{Bmatrix}\{x_{rn}\}\\ \{\dot{x}_{rn}\}\end{Bmatrix}+\begin{bmatrix}[0]_{11\times(n+12)}\\ [\Delta AR_1]\end{bmatrix}\begin{Bmatrix}\{q_{ae}\}\\ \{x_r\}\\ \{\dot{x}_r\}\end{Bmatrix}$$

$$+[BU]\{u_r\}+[BG]\{w\}-\begin{bmatrix}[0]_{17\times 5}\\ I_5\end{bmatrix}\left\{F^{h}\right\} \qquad (D.41)$$

where

$$[OM]=\begin{bmatrix}I_{11} & [0]_{11\times 11}\\ [0]_{11\times 11} & [BM]\end{bmatrix};\quad [SC]=\begin{bmatrix}[0]_{11\times 11} & I_{11}\\ -[BK] & -[BC]\end{bmatrix};$$

$$[BU]=\begin{bmatrix}[0]_{11\times 3}\\ [BUU]\end{bmatrix};\quad [BG]=\begin{bmatrix}[0]_{11\times 2}\\ [BGR]\end{bmatrix} \qquad (D.42)$$

At this stage, it is not possible to bring the system equations into standard form (with an identity matrix on the left hand side), since the left hand matrix, [OM], is singular.

D.4.2.3. Geometric Compatibility

Compatibility of airframe deflections at the rotor hub and the hub deflections in the rotor / nacelle system, $\{x_n\}$, has been previously used to express hub loads in terms of system states. In a rigorous representation, elimination of the redundant vector of hub deflections can be expressed by the transformation:

$$\begin{Bmatrix} \{x_{rn}\} \\ \{\dot{x}_{rn}\} \end{Bmatrix} = [C] \begin{Bmatrix} \{q_{ae}\} \\ \{x_r\} \\ \{\dot{x}_r\} \end{Bmatrix}; \quad [C] = \begin{bmatrix} & I_6 & \\ \left[WG0_*^h\right] & & \\ & & I_6 \\ \left[WG1_*^h\right] & & \end{bmatrix} \tag{D.43}$$

The asterisk in the subscript of $\left[WG0_*^h\right]$ and $\left[WG1_*^h\right]$ denotes that the row pertaining to rotation about the x-axis, ϕ_X, has been omitted from the original matrix. Elimination of the original rotor / nacelle state vector in (D.41) using (D.43), and pre-multiplication by the transpose of [C] yields

$$\begin{aligned} [C]^T [OM][C] \begin{Bmatrix} \{q_{ae}\} \\ \{x_r\} \\ \{\dot{x}_r\} \end{Bmatrix}^{\bullet} &= [C]^T \left([SC][C] + \begin{bmatrix} [0] \\ [\Delta AR_1] \end{bmatrix} \right) \begin{Bmatrix} \{q_{ae}\} \\ \{x_r\} \\ \{\dot{x}_r\} \end{Bmatrix} \\ &+ [C]^T [BU]\{u_r\} + [C]^T [BG]\{w\} - \begin{bmatrix} \left[WG1_*^h\right]^T \\ [0] \\ [0] \end{bmatrix} \{F^h\} \end{aligned} \tag{D.44}$$

The special structure of [C] has been used for simplification of the last term.

D.4.2.4. Equilibrium

Equations (D.34) and (D.44) represent the airframe / aerodynamics and rotor / nacelle dynamics as connected by the rotor shaft moment, M_x^h, which in both cases has been expressed in terms of system states. These two equations are now coupled by eliminating the hub force vector, $\{F^h\}$, in equation (D.44) using equation (D.34). Solution of (D.34) for $\{F^h\}$, insertion of the thus developed expression into (D.44), and collection of terms leads to the following equation:

$$\left([C]^T[OM][C]+\begin{bmatrix}[WFI] & [0] & [0]\\ [0] & [0] & [0]\\ [0] & [0] & [0]\end{bmatrix}\right)\begin{Bmatrix}\{q_{ae}\}\\ \{x_r\}\\ \{\dot{x}_r\}\end{Bmatrix}^{\bullet} =$$

$$\left([C]^T\left([SC][C]+\begin{bmatrix}[0]\\ [\Delta AR_1]\end{bmatrix}\right)+\begin{bmatrix}[\Delta AR_2]\\ [0]\\ [0]\end{bmatrix}\right)\begin{Bmatrix}\{q_{ae}\}\\ \{x_r\}\\ \{\dot{x}_r\}\end{Bmatrix}$$

$$+\begin{bmatrix}[WFI][BUU] & [WFI]\left[WF^{cg}\right]\{ACR\} & \\ [0] & \{0\} & [C]^T[BU]\\ [0] & \{0\} & \end{bmatrix}\begin{Bmatrix}\{u_s\}\\ u_{cg}\\ \{u_r\}\end{Bmatrix} \qquad \text{(D.45)}$$

$$+\left(\begin{bmatrix}[WFI]\left([BGG]+\left[WF^{cg}\right][AGR]\right)\\ [0]\\ [0]\end{bmatrix}+[C]^T[BG]\right)\{w\}$$

where

$$[\Delta AR_2]= \qquad \text{(D.46)}$$

$$\left[[WFI][AM'] \quad [0]_{(n+12)\times 5} \quad K_\phi[WFI]\left\{WF^{h,(4)}\right\} \quad [0]_{(n+12)\times 5} \quad C_\phi[WFI]\left\{WF^{h,(4)}\right\}\right]$$

and

$$[\mathrm{WFI}] = \left[\mathrm{WGI}_*^h\right]^T \left(\left[\mathrm{WF}^{h*}\right]^T \left[\mathrm{WF}^{h*}\right]\right)^{-1} \left[\mathrm{WF}^{h*}\right]^T \tag{D.47}$$

The left hand side matrix of (D.45) can be inverted and the coupled system be brought in standard state-space form. The eigenvalue problem is solved, and the system matrices in terms of the system's normal coordinates (similar to (D.24)) are output for further use, for example in control system design.

APPENDIX E

TILTROTOR SIMULATION MODEL ATTRIBUTE GLOSSARY AND ENHANCED DATA COUPLING MATRIX

Glossary

aag	global system matrix bulk file indicator [1]
accmax	limit, vertical airframe acceleration [g]
acgacc	aircraft center of gravity vertical acceleration (gust response) [g]
aclr	leading edge cap area, root [ft^2]
aclt	leading edge cap area, tip [ft^2]
acprice	aircraft price [10^6 $]
acrs	speed of sound, cruise altitude (25,000 ft) [ft/sec]
actr	trailing edge cap area, root [ft^2]
actt	trailing edge cap area, tip [ft^2]

aeim_"i"	imaginary part, airframe aeroelastic mode "i" (1..."i"...5) [rad/sec]
aere_"i"	real part, airframe aeroelastic mode "i" (1..."i"...5) [rad/sec]
affr_"i"	frequency, airframe undamped mode "i" (1..."i"...5) [Hz]
afgm_"i"	generalized mass, airframe undamped mode "i" (1..."i"...5) [% critical]
afmods	mode shape bulk file indicator [1]
agcr	critical ply angle, static load check [°]
ar	wing aspect ratio [1]
bctrl	airframe control matrix bulk data file indicator [1]
beta0	rotor precone [°]
bgg	global gust matrix bulk file indicator [1]
bgust	airframe gust matrix bulk data file indicator [1]
bug	global control matrix bulk file indicator [1]
bwing	wing span [ft]
ccg	global output matrix bulk file indicator
ccgacc	constraint, aircraft center of gravity vertical acceleration [1]
ccgc	constraint, control capacity, aircraft mode [1]
ccgh	constraint, static stability, helicopter mode [1]
ccgs	constraint, static stability, aircraft mode [1]
ccpacc	constraint, cockpit station vertical acceleration [1]
cctsmax	constraint, maximum (c_T/σ) in VASCOMP Figure of Merit Table [1]
cebeta	flapping damping, cruise, rotor only [% critical]
ceceta	lag damping, cruise, rotor only [% critical]
cecon	coning damping, cruise, rotor only [% critical]
certe	constraint, elevator rate [1]
cfrte	constraint, flaperon rate [1]
cgrc	constraint, propeller / primary controls clearance [1]

cgrf	constraint, propeller / fuselage clearance [1]
cgrn	constraint, propeller / nacelle clearance [1]
cgrwr	constraint, propeller root / wing clearance [1]
cgrwt	constraint, propeller tip / wing clearance [1]
clalpha	aircraft lift curve slope [1/rad]
cldelta	elevator lift per deflection [1/rad]
cmafg	fuselage group pitching moment coefficient slope (about aircraft center of gravity) [1/rad]
cmalpha	aircraft pitching moment coefficient, aircraft mode
cmalpha	rotor pitching moment coefficient slope (per rotor) [1/rad]
cmdelta	elevator pitching moment per deflection (about aircraft center of gravity) [1/rad]
coldmp	constraint, minimum open loop damping [1]
cplffus	airframe/rigid body force coupling matrix bulk data file indicator [1]
cplgfus	airframe/rigid body geometric coupling matrix bulk data file indicator [1]
cplfrot	airframe/rotor force coupling matrix bulk data file indicator [1]
cplgrot	airframe/rotor geometric coupling matrix bulk data file indicator [1]
cptacc	cockpit station vertical acceleration (gust response) [g]
crtacc	constraint, rotor hub vertical acceleration [1]
csjt	constraint, Margin of Safety, 2g jump take-off [1]
csrte	constraint, swash plate controls [Euclidian sum] rate [1]
ctrph	rotor control phasing [°]
ctsmax	constraint, maximum (c_T/σ) (upper limit of FM table in VASCOMP) [1]
dampcr	open-loop stability criterion (KS function of aircraft plant damping) [% critical]
delta3	rotor δ_3 at 0° pitch [°]

dfuse	fuselage diameter [ft]
dmpmin	minimum open loop damping allowed [% critical]
doc	direct operating cost [cents/asm]
elpd	nose fineness ratio (length/diameter) [1]
eltd	tail fineness ratio (length/diameter) [1]
elvrate	elevator rate (gust response) [rad/sec]
etcr	critical spanwise location, normalized by semi-span, static load check [1]
eten	engine nacelle spanwise center of gravity location, divided by semi-span [1]
extdba	500ft sideline external noise [dB(A)]
flnrate	flaperon rate (gust response) [rad/sec]
fwcrmax	limit, fixed wing controls activity (rate) [rad/sec]
gaine	ratio of elevator control to state weighting in LQR design [1]
gainf	ratio of flaperon control to state weighting in LQR design [1]
gainr	ratio of swashplate control to state weighting in LQR design [1]
gsd_"i"	damping, mode "i", generalized aircraft plant system (1..."i"...13) [% crit.]
gsf_"i"	frequency, mode "i", generalized aircraft plant system (1..."i"...13) [Hz]
ixxnac	primary engine nacelle roll inertia [slugs - ft^2]
iyyfusg	fuselage group pitch and yaw inertia [slugs - ft^2]
iyynac	primary engine nacelle pitch inertia [slugs - ft^2]
lfuse	fuselage length [ft]
lnac	nacelle length [ft]
lwgust	gust wave length [ft]
mfusg	fuselage group mass [slugs]
mnac	primary engine nacelle mass [slugs]
mrot	rotor mass (blades, controls, hub) [slugs]

mtcr	critical load check number [1] 1 - maximum stress criterion, in fiber direction 2 - maximum stress criterion, perpendicular to fiber direction 3 - maximum stress criterion, shear 4 - maximum strain criterion, in fiber direction 5 - maximum strain criterion, perpendicular to fiber direction 6 - maximum strain criterion, shear 7 - Hill criterion 8 - Hoffmann criterion 9 - Tsai-Wu criterion
mtilt	tilt axis group mass [slugs]
mxcr	maximum static load criterion [1]
nblds	number of blades [1]
njto	jump take-off load factor [g]
npax	number of tourist class passengers [1]
ombeta	flapping frequency, cruise, rotor only, coupled [1/rev]
omceta	lag frequency, cruise, rotor only, coupled [1/rev]
omcon	coning frequency, cruise, rotor only, coupled [1/rev]
omefl	out-of-plane cantilevered rotating uncoupled blade freq, 0° pitch, vacuum [1/rev]
omegim	gimbal rotating frequency, uncoupled, stiff rotor blade, vacuum [1/rev]
omelg	inplane cantilevered rotating uncoupled blade freq., 0°pitch, vacuum [1/rev]
phi	wing quarter chord sweep angle [°]
phi0	blade pitch angle at which minimum δ_3 is reached [°]
pi	Productivity Index [kts]
plcr	critical plate number, static load check [1]

range	range [NM]
rbar	rotor extension ratio, cruise/hover diameter [1]
rhocrs	density, cruise altitude (25,000 FT) [slugs/ft^3]
rhvr	rotor radius, hover [ft]
rotacc	rotor hub vertical acceleration (gust response) [g]
sfcr	critical surface number, static load check [1] 1 - upper surface/skin 2 - lower surface/skin
sigma	rotor solidity, cruise [1]
stcr	static load criterion (KS function of all Margins of Safety, static load) [1]
swprate	swash plate controls [Euclidian sum] rate (gust response) [rad/sec]
swprmax	limit, swashplate controls activity (rate) [rad/sec]
tau	wing taper ratio [1]
tblock	block time [h]
tm45r	-45° ply thickness, wing root [ft] (reference: spanwise direction)
tm45t	-45° ply thickness, wing tip [ft]
tovc	wing thickness to chord ratio [ft]
tp45r	+45° ply thickness, wing root [ft]
tp45t	+45° ply thickness, wing tip [ft]
tpm0r	0° ply thickness, wing root [ft]
tpm0t	0° ply thickness, wing tip [ft]
tpm90r	90° ply thickness, wing root [ft]
tpm90t	90° ply thickness, wing tip [ft]
trib	rib web thickness [ft]
twlr	leading edge web thickness, root [ft]
twlt	leading edge web thickness, tip [ft]

twtr	trailing edge web thickness, root [ft]
twtt	trailing edge web thickness, tip [ft]
v0gust	rms gust velocity [ft/sec]
vcrs	cruise speed [KTAS]
vsafe	stable speed (controller design speed) [KTAS]
vt	rotor tip speed, hover [ft/sec]
wfmiss	mission fuel weight (no reserves) [lb]
wfuel	total fuel weight [lb]
wg0	initial gross weight [lb]
wga	disk loading, hover [lb/ft^2]
wl	wing loading [lb/ft^2]
woe	operating empty weight [lb]
wpay	payload weight [lb]
wrbd	rotor blade weight [lb]
wwgrp	wing group weight [lb]
wwinst	wing internal installations weight [lb]
wwnst	wing non structural weight (flaps, fittings) [lb]
wwstr	wing structural weight [lb]
xiac	wing aerodynamic center location aft of nose, divided by fuselage length [1]
xiaccg	aircraft center of gravity location aft of wing aerodynamic center, normalized by wing mean aerodynamic chord, aircraft mode [1]
xiaccgf	fuselage group center of gravity location aft of wing aerodynamic center, normalized by wing mean aerodynamic chord [1]
xiaccgh	aircraft center of gravity location aft of wing aerodynamic center, normalized by wing mean aerodynamic chord, helicopter mode [1]

xiaccgm	minimum aircraft center of gravity location aft of wing aerodynamic center, normalized by wing mean aerodynamic chord, helicopter mode [1]
xicr	critical location chordwise (normalized), static load case [1]
xien	primary engine nacelle center of gravity location aft of wing leading edge, normalized by local chord [1]
xirr	rotor location aft of wing leading edge, normalized by local chord, aircraft mode [1]
xisle	structural box leading edge spar location aft of wing leading edge, normalized by local chord [1]
xiste	structural box trailing edge spar location aft of wing leading edge, normalized by local chord [1]
xiti	tilt axis location aft of wing leading edge, normalized by tip chord [1]

Table E.1: Enhanced Data Coupling Matrix DCM+, Tiltrotor Case

Set	Attribute	Type	vascomp	elaps	pwake	acp	csd	OBJ
Circuit			1	1	2	3	4	5
Sequence			1	2	2	2	2	3
aeo	aeim_i	2	0	0	2	1	0	0
	aere_i	2	0	0	2	1	0	0
	bctrl	2	0	0	3	1	0	0
	bgust	2	0	0	3	1	0	0
	cplffus	2	0	0	3	1	0	0
	cplgfus	2	0	0	3	1	0	0
	cplfrot	2	0	0	3	1	0	0
	cplgrot	2	0	0	3	1	0	0
apd	aag	2	0	0	0	3	1	0
	bgg	2	0	0	0	3	1	0
	bug	2	0	0	0	3	1	0
	ccg	2	0	0	0	3	1	0
	coldmp	4	0	0	0	0	0	2
	dampcr	3	0	0	0	2	0	1
	dmpmin	0	0	0	0	0	0	1
	gsd_i	2	0	0	0	2	0	0
	gsf_i	2	0	0	0	2	0	0
csd	accmax	0	0	0	0	0	0	1
	acgacc	3	0	0	0	0	2	1
	ccpacc	4	0	0	0	0	0	2
	certe	4	0	0	0	0	0	2
	cfrte	4	0	0	0	0	0	2
	cptacc	3	0	0	0	0	2	1
	crtacc	4	0	0	0	0	0	2
	csrte	4	0	0	0	0	0	2
	elvrate	3	0	0	0	0	2	1
	flnrate	3	0	0	0	0	2	1
	fwcrmax	0	0	0	0	0	0	1
	gaine	1	0	0	0	0	1	0
	gainf	1	0	0	0	0	1	0
	gainr	1	0	0	0	0	1	0
	lwgust	0	0	0	0	0	1	0
	rotacc	3	0	0	0	0	2	1
	swprate	3	0	0	0	0	2	1
	swprmax	0	0	0	0	0	0	1
	v0gust	0	0	0	0	0	1	0

Input / Output Indicator Values:
0 - not used; 1- input; 2 - output; 3 - input and output
Data Types:
0 - Constant; 1 - Decision Variable; 2 - State; 3 - Behavior Variable; 4 - Constraint; 5 - Objective Function

Table E.1: Enhanced Data Coupling Matrix, DCM+, Tiltrotor Case (cont'd)

Set	Attribute	Type	vascomp	elaps	pwake	acp	csd	OBJ
Circuit			1	1	2	3	4	5
Sequence			1	2	2	2	2	3
...	...		...	...	...	...	...	...
dyn	affr_i	2	0	2	1	0	0	0
	afgm_i	2	0	2	1	0	0	0
	afmods	2	0	3	1	0	0	0
eco	acprice	2	2	0	0	0	0	0
	doc	2	2	0	0	0	0	0
	extdba	2	2	0	0	0	0	0
	pi	5	0	0	0	0	0	2
	tblock	3	2	0	0	0	0	1
geo	ar	1	1	1	1	1	0	1
	elpd	1	1	0	0	0	0	1
	eltd	1	1	0	0	0	0	0
	eten	1	1	1	0	0	0	1
	npax	0	1	0	0	0	0	0
	phi	1	1	1	1	0	0	1
	tau	1	1	1	1	1	0	1
	tovc	1	1	1	0	0	0	0
	wga	1	1	0	0	0	0	1
	wl	1	1	0	1	1	0	0
	xiac	1	1	1	0	0	0	1
	xien	1	1	1	0	0	0	1
	xirr	1	1	1	1	0	0	1
	xiti	1	1	1	1	0	0	1
mis	acrs	0	1	0	1	1	0	0
	range	0	1	0	0	0	0	1
	rhocrs	0	1	0	1	1	0	0
	vcrs	1	1	0	0	0	0	0
	vsafe	3	2	0	1	1	0	0
	wpay	3	2	0	0	0	0	1

Input / Output Indicator Values:
0 - not used; 1- input; 2 - output; 3 - input and output
Data Types:
0 - Constant; 1 - Decision Variable; 2 - State; 3 - Behavior Variable; 4 - Constraint; 5 - Objective Function

Table E.1: Enhanced Data Coupling Matrix, DCM+, Tiltrotor Case (cont'd)

Set	Attribute	Type	vascomp	elaps	pwake	acp	csd	OBJ
Circuit			1	1	2	3	4	5
Sequence			1	2	2	2	2	3
...	...		...	...	...	...	...	...
rdy	cebeta	2	0	0	0	2	0	0
	ceceta	2	0	0	0	2	0	0
	cecon	2	0	0	0	2	0	0
	ombeta	2	0	0	0	2	0	0
	omceta	2	0	0	0	2	0	0
	omcon	2	0	0	0	2	0	0
	omefl	1	0	0	0	1	0	0
	omegim	1	0	0	0	1	0	0
	omelg	1	0	0	0	1	0	0
rgo	beta0	1	0	0	0	1	0	0
	ctrph	1	0	0	0	1	0	0
	ctsmax	0	0	0	0	0	0	1
	delta3	1	0	0	0	1	0	0
	nblds	0	1	0	0	1	0	0
	phi0	1	0	0	0	1	0	0
	rbar	0	1	0	0	1	0	1
	sigma	0	1	0	0	1	0	1
	vt	1	1	0	0	1	0	1
sae	clalpha	3	2	0	0	1	0	1
	cldelta	3	2	0	0	1	0	0
	cmafg	3	2	0	0	1	0	0
	cmalpha	3	2	0	0	0	0	1
	cmalphr	3	2	0	0	0	0	1
	cmdelta	3	2	0	0	1	0	0
	xiaccgm	3	2	0	0	0	0	1

Input / Output Indicator Values:
0 - not used; 1- input; 2 - output; 3 - input and output
Data Types:
0 - Constant; 1 - Decision Variable; 2 - State; 3 - Behavior Variable; 4 - Constraint; 5 - Objective Function

Table E.1: Enhanced Data Coupling Matrix, DCM+, Tiltrotor Case (cont'd)

Set	Attribute	Type	vascomp	elaps	pwake	acp	csd	OBJ
Circuit			1	1	2	3	4	5
Sequence			1	2	2	2	2	3
...	...		...	...	...	...	...	...
siz	bwing	3	2	1	1	1	0	1
	ccgacc	4	0	0	0	0	0	2
	ccgc	4	0	0	0	0	0	2
	ccgh	4	0	0	0	0	0	2
	ccgs	4	0	0	0	0	0	2
	cctsmax	4	0	0	0	0	0	2
	cgrc	4	0	0	0	0	0	2
	cgrf	4	0	0	0	0	0	2
	cgrn	4	0	0	0	0	0	2
	cgrwr	4	0	0	0	0	0	2
	cgrwt	4	0	0	0	0	0	2
	dfuse	3	2	0	1	0	0	1
	lfuse	3	2	1	0	0	0	1
	lnac	3	2	0	0	0	0	1
	rhvr	3	2	0	0	1	0	1
	xiaccg	3	2	1	1	0	0	1
	xiaccgf	3	2	1	0	0	0	0
	xiaccgh	3	2	0	0	0	0	1
str	aclr	1	0	1	0	0	0	0
	aclt	1	0	1	0	0	0	0
	actr	1	0	1	0	0	0	0
	actt	1	0	1	0	0	0	0
	agcr	2	0	2	0	0	0	0
	csjt	4	0	0	0	0	0	2
	etcr	2	0	2	0	0	0	0
	mtcr	2	0	2	0	0	0	0
	mxcr	2	0	2	0	0	0	0
	njto	0	0	1	0	0	0	0
	plcr	2	0	2	0	0	0	0
	sfcr	2	0	2	0	0	0	0
	stcr	3	0	2	0	0	0	1
	tm45r	1	0	1	0	0	0	0
	tm45t	1	0	1	0	0	0	0
	tp45r	1	0	1	0	0	0	0
	tp45t	1	0	1	0	0	0	0
	tpm0r	1	0	1	0	0	0	0
	tpm0t	1	0	1	0	0	0	0
	tpm90r	1	0	1	0	0	0	0
	tpm90t	1	0	1	0	0	0	0
	trib	0	0	1	0	0	0	0
	twlr	1	0	1	0	0	0	0
	twlt	1	0	1	0	0	0	0
	twtr	1	0	1	0	0	0	0
	twtt	1	0	1	0	0	0	0
	xicr	2	0	2	0	0	0	0
	xisle	0	0	1	1	0	0	0
	xiste	0	0	1	1	0	0	0

Table E.1: Enhanced Data Coupling Matrix, DCM+, Tiltrotor Case (cont'd)

Set	Attribute	Type	vascomp	elaps	pwake	acp	csd	OBJ
Circuit			1	1	2	3	4	5
Sequence			1	2	2	2	2	3
...	...		...	...	...	...	...	...
wgt	ixxnac	3	2	1	0	0	0	0
	iyyfusg	3	2	1	0	0	0	0
	iyynac	3	2	1	0	0	0	0
	mfusg	3	2	1	0	0	0	0
	mnac	3	2	1	0	0	0	0
	mrot	3	2	1	0	0	0	0
	mtilt	3	2	1	0	0	0	0
	wfmiss	3	2	0	0	0	0	1
	wfuel	3	2	1	0	0	0	0
	wg0	2	3	0	0	0	0	0
	woe	3	2	0	0	0	0	1
	wrbd	3	2	0	0	1	0	0
	wwgrp	3	2	1	0	0	0	0
	wwinst	3	2	1	0	0	0	0
	wwnst	3	2	1	0	0	0	0
	wwstr	3	1	2	0	0	0	0

Input / Output Indicator Values:
0 - not used; 1- input; 2 - output; 3 - input and output
Data Types:
0 - Constant; 1 - Decision Variable; 2 - State; 3 - Behavior Variable; 4 - Constraint; 5 - Objective Function

APPENDIX F

DESIGN AND OPTIMIZATION COUPLING CODE

(DOCC)

F.1. Overview

The Design and Optimization Coupling Code, DOCC, is a software implementation of the recomposition procedure for the Global Design Space optimization strategy described in Chapter 2, written almost exclusively in UNIX shell scripts. Consistent with this approach, the main executive loop is divided into a system optimizer block, a system analysis block, and a system sensitivity analysis block (Fig. F.1). A circuit iteration solver and a local sensitivity analysis driver complete the set of functional operators suggested. Contributing Analyses, as well as data pre- and post processors are to be supplied by the user. The second primary element of the method, the extended Data Coupling Matrix, DCM^+ (also user-supplied), is stored in an expanded form in a central data base. It is used to direct information flow between Contributing Analyses and reduce computational effort

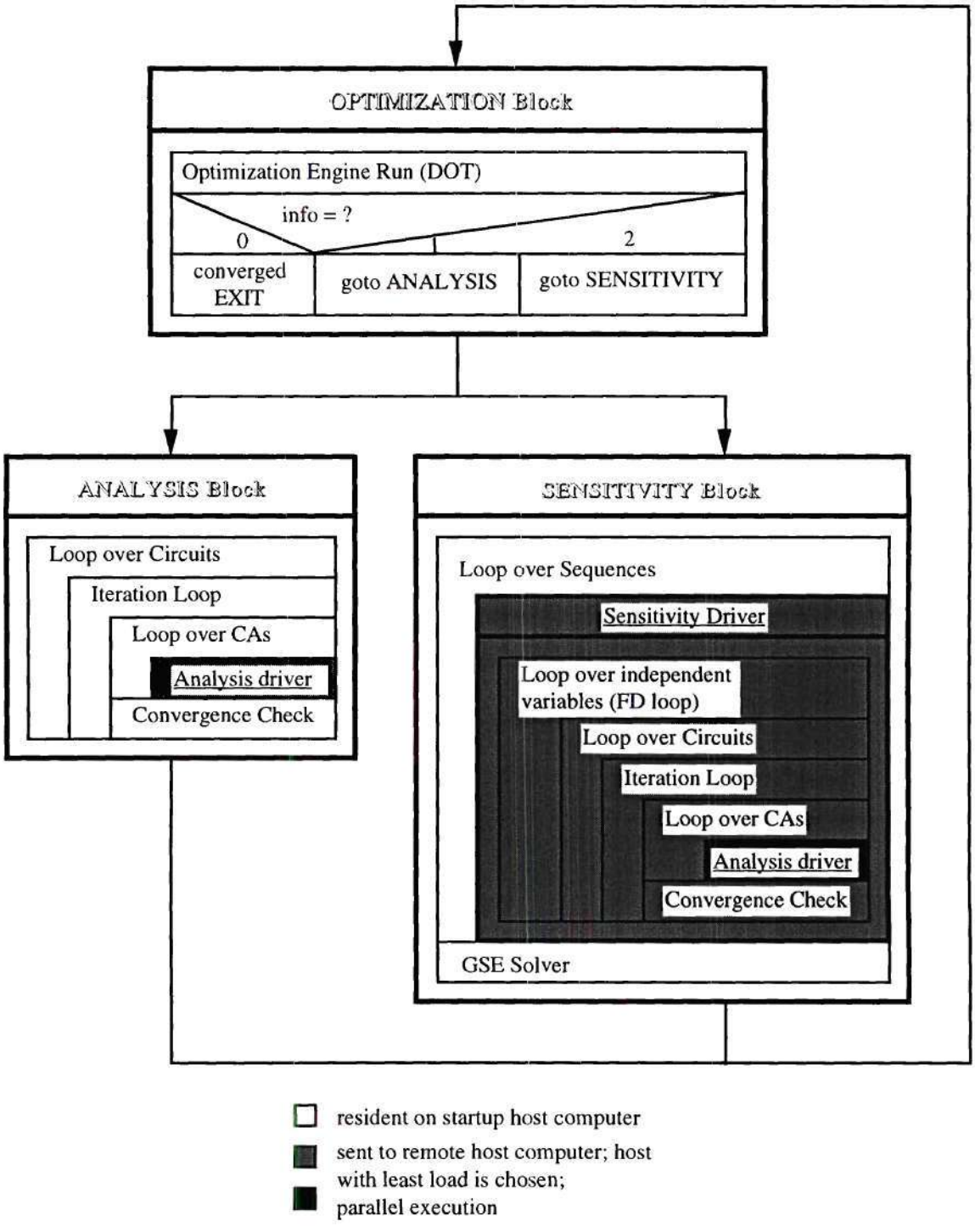

Fig. F.1: Blocks of Executive Loop

in local sensitivity analyses. Coarse grain parallel execution capabilities are exploited where allowed by execution order and available hardware. For this option, a network of host computers running under UNIX, connected to the same NFS-mounted file system is required (NFS = Network File Server).

F.2. Operation

F.2.1. Setup and Configuration

Implementation of a new design task in DOCC requires the following steps:

(1) Problem decomposition: Identification and provision of resources, determination of circuit and sequence grouping;

(2) preparation of an ASCII file containing this information in DCM$^+$ format (see Appendix F.3, descriptions for `conf_DOCC` input);

(3) supply of Contributing Analysis (CA) pre- and post processors (identified by the CA executable name plus the suffix "_pre"/"_post," respectively), which generate CA input from an input stream (into standard input) in the format

Attribute1 value1

Attribute2 value2

etc.,

then filter CA output and generate an output stream in the same format;

(4) Creation of the central database, configuration of design task dependent software.

Execution of item (4) is aided by the utility `conf_DOCC`, which reads the file containing DCM$^+$ information and generates the data base entities described in Appendix F.4. Storage of the DCM$^+$ in the relation "dcmplus" differs slightly from the format presented in Fig. 2.5 in order to allow more convenient parsing operations: Each Attribute is associated with the Contributing Analysis by which it is generated (its source). Hence, Attributes can also be allocated to Circuits and Sequences. In "dcmplus," this information is contained in the Attribute entries, and not in a separate entry like in Fig. 2.5. The direct allocation from Contributing Analyses to Circuits and Sequences is contained in the relation "status."

In an interactive part, `conf_DOCC` prompts the user for the DOT /DOT 93/ optimization method and output print flag, and asks if a minimization or maximization is requested. Using this information and the number of design variables, behavior variables, and constraints from the input table, flags and array sizes are set, and DOT (and driver) and GSE solver are compiled. As a result, these executables are custom sized in order to minimize memory usage.

F.2.2. Execution and Design Process Control

The main executive loop with the blocks OPTIMIZER, ANALYSIS and SENSITIVITY is contained in the script `executive`. The utility `run_DOCC` allows to launch an `executive` job in either an interactive mode or as a "no-hangup" background job. In both cases, the user controls DOCC's operation through the utility `monit`. This script may be started from any host computer in the file system which the `executive` job is using. In the batch mode, this is the only option; in the interactive mode, `monit` is

launched by `executive` at scheduled interrupt locations, depending on the setting of the executive control parameter "ctrl" (refer to the description of the entity "status" in Appendix F.4). The less frequently interrupts are scheduled, the more will the executive software exploit parallel execution opportunities.

`monit` provides an interactive interface with the central data base, which, in turn, is frequently queried by the executive and other utilities. The following operations can be performed:

(i) viewing of current and previous data, including variable histories and the process status (by accessing the data base entity "status");

(ii) changing of the executive control parameter, including sending of a pausing signal which terminates the execution at the next interrupt location (independent of the interrupt schedule), and shuts down all processes in an orderly manner;

(iii) restarting of a paused process, either at the last active block, or for continuation of the process at the exact location where it was previously paused.

The primary reason for this indirect control mechanism via the data base lies in the desire to allow DOCC restarts, which requires a scheduled shutdown of all processes launched by the executive, and completion of data base operations.

F.2.3. Automated Data Base Inquiry (ADI)

A core element of the presented approach is exclusive data transfer between Contributing Analyses through the central data base. Communication with the central data base, henceforth referred to by "ADI," is accomplished by providing appropriate data base

script files with SQL-compatible queries (/SQL 86/). The data base management software ICE (/Herendeen and Ludwig 88/) and its driver routine, `ice_pipe`, are launched on DOCC startup. The driver constantly checks a designated directory for presence of a script file, sends queries line by line to ICE if one is detected, deletes the script after the last query, and returns to the checking mode. Multiple query scripts may be produced at the same time during parallel execution tasks; in order to provide one script file at a time, the utility `spool_db` ensures that a particular script file is only moved to the "pipe" directory if the previous data base query has been completed, that is, if this directory is empty. If the query includes extraction of data from the data base, then the utility `wait_for` loops until the desired data base report file has been generated, and holds the process execution at the respective position until the requested data are available.

F.2.4. Executive, Parsing and Data Flow Operations

DOCC's executive loop is shown in Fig. F.1 for reference. The OPTIMIZER block within `executive` represents the system optimization operation. It is a driver which extracts (identified by the attribute* "type") objective function, constraint, design variable, and behavior variable values from the attribute "new" of the relation "dcmplus" using ADI. This information is supplied to the optimization engine driver, `OPT`, which calls the actual optimization engine, DOT (/DOT 93/). Internal DOT arrays are saved into files and read on restart. At the beginning of a new optimization iteration, global sensitivity information and design variable increments are used to calculate first order behavior variable approximations, in order to speed up convergence in Circuit iteration loops. DOT parameter arrays are finally stored in the relation "optprm" for restart.

---

* a column in a relational entity; not to be confused with the Attribute in the integration terminology

Both the ANALYSIS and SENSITIVITY block begin with ADI for available hosts (from the relation "hosts") and grouping of Contributing Analyses in Circuits and Sequences, respectively. As shown in Fig. F.1, ANALYSIS contains an outer loop over all Circuits, and an inner loop over the Contributing Analyses (CAs) in each Circuit. If parallel execution is allowed by the interrupt schedule, for each CA the host computer with the least load level is selected by the utility `find_host` (it also ensures that the particular CA is executable on the host machine). CAs in one Circuit are then launched in parallel as remote jobs on available host computers, using the CA driver routine `run_ca`, which is equivalent to the "Analysis Driver" in Fig. F.1.

In the ANALYSIS block, `run_ca` uses ADI to extract all Attributes which qualify as inputs to a particular CA by selecting those with an input/output indicator of 1 in the respective field of the relation "dcmplus." The actual numerical value is taken from the attribute "old." The data base report file is filtered, and relevant information converted into the standard format data stream described in Appendix F.2.1. This stream is piped to the CA preprocessor, which generates the CA input file. `run_ca` starts the CA on completion of the input file, and the CA post processor on completion of the CA run. Finally, the post processor output stream is converted into a data base query script, which updates the "new" attribute in "dcmplus." Attributes are in this case identified by matching output stream labels with the attribute "label" in "dcmplus."

After these jobs are launched, `executive` checks for existence of remote shells using the UNIX process status command `ps`, and continues only after all of them have been completed. Then those Attributes in "dcmplus" are identified which are both generated and needed within the Circuit by checking for input / output pairs between all CA pair permutations (using the input/output indicators). The attributes "new" and "old" of these entries are then checked for convergence. If the maximum absolute value of the

difference between these two values, normalized by the reference value in the "ref" field of "dcmplus," is below the limit value "ccrit," then the Circuit iteration is considered converged, and the executive proceeds to the next Circuit. "ccrit" and the maximum number of allowed Circuit iterations, "maxit," may be specified for each Circuit independently in the respective entry of the relation "status."

If the convergence criterion is not satisfied, then the next iteration is initiated by setting "old" equal to "new." This very simple iteration scheme performed satisfactorily in the large majority of situations encountered, since, in general, optimization steps are fairly small and keep the design close to a possible Circuit iteration "root." Provisions have been made for iteration cycling, but divergence may still occur. In order to provide information for dealing with these situations, the convergence criterion and the critical Attribute are echoed to the screen and the log file at each iteration.

The SENSITIVITY block is executed in a different manner. First of all, local sensitivity analyses are launched on remote hosts like CA runs in Circuits. The respective utility, `sens_seq`, extracts sequence-relevant data from "dcmplus" (match of current sequence number and attribute "sequence") and stores it in a temporary file in the host machine's local disk space (/tmp directory); refer to Appendix F.5 for the contents of this file. This "local data base" is then used in all following operations. Only updates on the process status and sensitivity data are communicated to the central data base.

Sequence independent variables are identified as those behavior variables ("type" is larger than 3), which are input to any of the Sequence's CAs, but not generated within the Sequence (the parsing operation is comparable to that described in the paragraph on Circuit convergence). In a simpler procedure, the Sequence's dependent variables are detected as those Attributes which are generated within the Sequence, but not input to any of the

Sequence's CAs. The independent variables are then perturbed in a finite differencing loop by a percent increment, which can be specified for each Attribute individually in the attribute "eps" of the relation "dcmplus." Given this perturbed set, Contributing Analyses allocated to the Sequence are executed. Resulting dependent variable changes are translated into sensitivities, which are normalized by the respective reference values, and stored in the relations "lsens" or "mmat" of the central data base (depending on whether the perturbed independent variable is a design variable or behavior variable, respectively).

Circuit grouping is used twofold in the execution of a given Sequence. First, Circuits are still executed sequentially, and iterations are performed within each Circuit. Differences arise from the fact that CAs of a Circuit may be allocated to different Sequences. In this case, Sequence-specific Circuits are defined. Also, the CA driver, `run_ca`, does not obtain any data from the central data base, but is supplied by `sens_seq` by identical information filtered from the local data base in form of an input stream. Second, for each independent variable it is determined to which Circuit it is an input, starting with the first Circuit in the Sequence. Only the first Circuit to which it is an input, and all following Circuits, are then executed. This procedure can reduce the computational effort involved in calculating local sensitivities significantly by eliminating unnecessary CA executions.

During local sensitivity analyses, the executive is on hold in a waiting loop. When all remote shells have been closed, then it proceeds to solution of the Global Sensitivity Equations, GSE. The associated program is a solver for linear systems of equations, based on LU-decomposition.

F.3. Utilities

`beep`

Type: executable (C source)

Arguments: -

Std. Input: -

Operation: terminal bell - alert for error messages etc. in interactive mode

`conf_DOCC`

Type: C-shell script

Arguments: (1) DCM+ file name = data base name
(2) data base password

Std. Input: -

Operation: (a) creates central data base using DCM+ input file - tabulator delimited ASCII file of Attributes with the columns label, type, ca1...caN, init, lower, upper
where

label	string(8)	Attribute name
type	integer	0 - constant
		1 - design variable
		2 - system state

		3 - behavior variable
		4 - constraint
		5 - objective function
cai	integer	input / output indicator
		0 - Attribute not used
		1 - Attribute is input
		2 - Attribute is output
		3 - Attribute is in- and output
		(column title is executable name; one
		column for each ca, i=1, N)
init	real	initial value
lower	real	lower bound
upper	real	upper bound

first line: column title

second line: Circuit numbers

third line: Sequence numbers

(b) determines array sizes required for GSE solver, `GSE`, and optimization driver, `OPT` (the latter using `set_dot_dim`); interactive: DOT optimization method and output options; modifies template files GSE.tmplt and opt.tmplt accordingly, compiles resulting source code

`executive`

Type: C-shell script

Arguments: -

Std. Input: -

Operation: main executive loop; contains OPTIMIZER, ANALYSIS and SENSITIVITY blocks (see Appendix F.2.4.)

`find_host`

Type: C-shell script

Arguments: (1) executable name
(2) directory in which executable is stored; executable might also be in a subdirectory with the name of the operating system/machine for which it was compiled

Std. Input: vector of host computers

Operation: returns least loaded host computer from the host computer input list which can execute the code in the input list, and the exact directory in which the executable can be found

`GSE`

Type: executable
FORTRAN source, automatically generated from template file "GSE.tmplt" and compiled by `conf_DOCC`

Arguments: -

Std. Input: -

Operation: reads GSE matrix elements from central data base report, solves GSE, writes data base script fro inserting global sensitivities

`ice_pipe`

Type: executable (C source)

Arguments: -

Std. Input: -

Operation: starts ICE (/Herendeen and Ludwig 88/) and opens a pipe to its standard input
checks data base input directory for presence of files; if a file is found, it is assumed to be a data base script file; when this file has been completely written (checked using `wait_til_full`),then each line is sent through the pipe to ICE; file is then deleted

`launch_ca`

Type: Korn shell script

Arguments: (1) name of file containing CA input data in standard format
(2) CA executable name
(3) name of host computer designated for CA run
(4) local directory
(5) directory containing DOCC utilities
(6) data base input directory
(7) host computer on which `executive` is running
(8) exact directory in which CA executable is located
(9) current host computer

Std. Input: -

Operation: launches run_ca in standard input mode as background job (remote, if required); occasionally, the file (argument 1) can not be accessed via the file server; this utility detects such a situation and attempts again until the operation is successful

`monit`

Type: C-shell script

Arguments: (1) Operation mode flag
none monitor active DOCC process (data base pipe open)

-a monitor active DOCC process - called from within `executive`

-p access data base (data base pipe closed)

Std. Input: -

Operation: menu-based (interactive) monitoring and control of DOCC processes and accessing of central data base (see Appendix F.2.2.)

`nuname`

Type: C-shell script

Arguments: (1) file name
(2) directory name

Std. Input: -

Operation: checks if the file (argument 1) is located in a subdirectory of (2) with the current operating system name
returns the operating system name if the file is found
returns 1 if the file is found in (1)
returns 0 if file is not found in these directories

OPT

Type: executable
FORTRAN source, automatically generated from template file "opt.tmplt" and compiled by `conf_DOCC`

Arguments: -

Std. Input: -

Operation: driver for optimization engine DOT (/DOT 93/)

`patch_db`

Type: C-shell script

Arguments: -

Std. Input: -

Operation: connection to the central data base (the data base pipe) is not very stable; this utility detects such a broken pipe and re-establishes the connection; checks for broken pipes as long as `executive` is in the machine's process list

`run_DOCC`

Type: Bourne shell script

Arguments: (1) Operation mode flag

-i interactive mode

-b background job

Std. Input: -

Operation: driver for `executive`; creates log file "run.log" of all standard output and standard error echoes; must be supplied in background mode with a file "startup" containing menu

inputs, in particular setting of the executive control parameter to 0 (no scheduled interrupts)

`run_ca`

Type: C-shell script

Arguments: (1) CA executable name
(2) designated host computer name
(3) local directory
(4) directory containing DOCC utilities
(5) data base input directory
(6) host computer on which `executive` is running
(7) exact directory in which CA executable is located

Std. Input: (a) dummy vector with one element ⇒ ANALYSIS mode; or
(b) Attribute input vector: Label, num. value, label, num. value, ..., file name containing this list, designated file name (temporary) for CA output list in same format
⇒ SENSITIVITY mode

Operation: CA driver; extraction of CA input data from central data base (ANALYSIS mode only); generation of CA input file using CA preprocessor; CA run; extraction of CA output data using CA post processor; updating of relation "dcmplus" in central data base (ANALYSIS mode), or generation of

output list file (SENSITIVITY mode); updating of "status" in central data base

`sens_seq`

Type: C-shell script

Arguments: (1) Sequence number
(2) local directory
(3) directory containing DOCC utilities
(4) data base input directory
(5) host computer on which `executive` is running
(6) optimization iteration number
(7) executive control parameter
(8) jump flag:
1 - returning from scheduled `monit` call; 0 - not
(9) first finite differencing step
(10) first circuit
(11) host computer name

Std. Input: host computer and CA grouping vector:
number of Sequences; number of host computers; host computer names; for each CA: Sequence number, Circuit number, CA name, CA index, max. number of Circuit iterations, Circuit convergence criterion

Operation: creation of temporary Sequence data base file; finite differencing (FD) loop over all independent variables;

detection of unnecessary Circuit executions at each FD step; Circuit iterations; calculation of normalized local sensitivities; spooling of sensitivities to central data base
on restart: find restart location (FD step and last executed Circuit)

`set_dot_dim`

Type: executable (FORTRAN source)

Arguments: -

Std. Input: (1) number of design variables
(2) number of constraints
(3) DOT optimization method indicator (see /DOT 93/)

Operation: driver for DOT subroutine DOT510, which calculates requires dimensions of working arrays to be supplied to DOT in its subroutine form; returns (a) required dimension of real working array, (b) required dimension of integer working array; used by `conf_DOCC` to update array dimensions in the DOT driver routine's template file "opt.tmplt," which is then compiled to generate `OPT`

`spool_db`

Type: C-shell script

Arguments: (1) data base script file name
(2) local directory

(3) directory containing DOCC utilities

(4) data base input directory

Std. Input: -

Operation: moves script file (1) into the data base "pipe directory" (4), if the latter is empty; script (1) is assumed to be located in the host machine's local disk space, /tmp, and begins with "tscript_"; only the part of the name following this prefix is input in (1)

`status_menu`

Type: C-shell script

Arguments: -

Std. Input: -

Operation: sends every 10 seconds a status query to the central data base and displays it in a formatted, task-specific form; called by `monit` as a process monitoring option, particularly when launched from a machine other than that running `executive`

`update_lst`

Type: Korn shell script

Arguments: (1) old file name (to be updated)

(2) new file name (updated)

Std. Input: stream - variable name, numerical value, optional add. locator, CR, variable name, etc. of variables to be updated

Operation: utility to be used in CA preprocessors
updates a set of variables in a formatted input file; the lines in this file are assumed to have the following format:
list of values (the actual input); list of labels; comments (containing additional locators)
these fields must be separated by semi-colons!
the position for replacing a particular numerical value is located by matching both the variable name and the additional locator (if given); one-dimensional array elements can be specified by appending the array index to the variable name, enclosed by colons

`update_nml`

Type: C-shell script

Arguments: (see `update_lst`)

Std. Input: (see `update_lst`)

Operation: equivalent to `update_lst`, for namelist input files
additional locators and specific input file format not required

`wait_for`

Type: C-shell script

Arguments: (1) file name
(2) local directory
(3) directory containing DOCC utilities
(4) data base input directory
(5) host computer on which `executive` is running
(6) delete flag

Std. Input: -

Operation: used to hold process until a requested data base report file is generated
loops until the file (1) is found in the local disk space of the machine running executive (5); then transfers the file to the current directory (2); deletes the file if the flag (6) is set to "d"

`wait_til_full`

Type: C-shell script

Arguments: -

Std. Input: -

Operation: loops until the string "end_of_file" is found in any file in the data base input directory; used by `ice_pipe` to determine when a script file has been written completely

F.4. Data Base Entities

Computer Platforms

Entity: hosts

Description: Contains available host computers

Attributes:

NAME	TYPE	DESCRIPTION
name	String (12)	Host Computer

Optimizer Start / Stop Parameters

Entity: optprm

Description: Contains DOT parameters (see DOT manual)

Attributes:

NAME	TYPE	DESCRIPTION
indx	Integer	Index of vectors
rprm	Real single precision	Real parameters (20)
iprm	Integer	Integer parameters (20)

DOCC Process Status

Entity: status

Description: Contains information on case progress

Attributes:

NAME	TYPE	DESCRIPTION
circuit	Integer	Circuit to which CA is assigned
sequence	Integer	Sequence to which CA is assigned
nsens	Integer	SENSITIVITY: Number of local sensitivity analyses performed in this Sequence
nexec	Integer	ANALYSIS: Number of executions of CA in current ANALYSIS block SENSITIVITY: Circuit converged (1/0)
tnexec	Integer	Number of CA executions since case start
nprocc	Integer	Number of CA in ANALYSIS Circuit
nprocs	Integer	Number of CA in SENSITIVITY Circuit
process	String (8)	CA executable code name
active	String (12)	'inact' - CA not running '(host computer name)' - host running CA 'done' - CA run completed 'complete' - Sequence FD loop completed (SENSITIVITY only)
ctrl	Integer	Executive control parameter: Pause after 0 - complete optimization run 1 - optimization iteration step 2 - executive block 3 - Circuit (A) / Sequence(S) 4 - Circuit It. (A) / Sequence FD Step (S) 5 - CA run (A) / Circuit in Sequence (S)
info	Integer	Indicator for current executive block: 0 - optimization start/end 1 - ANALYSIS 2 - SENSITIVITY
maxit	Integer	Permitted circuit iterations
ccrit	Real Single Precision	Circuit iteration convergence criterion
conv	Real Single Precision	Current circuit convergence

Data Input / Output Compatibility

Entity: dcmplus

Description: Contains the Enhanced Data Coupling Matrix (DCM^+)

Attributes:

NAME	TYPE	DESCRIPTION
indx	Integer	Unique data index number
circuit	Integer	Circuit which source CA is assigned to
sequence	Integer	Sequence which source CA is assigned to
label	String (8)	Unique data label
type	Integer	Data type: 0 - Constant 1 - Design variable 2 - System State (not used in GSE) 3 - Behavior Variable (used in GSE) 4 - Constraint 5 - Objective function
"CA1" ... "CAi" ... "CAn"	Integer	Data source and destination: 0 - Data not used in this CA 1 - Data is input to this CA 2 - Data is produced by CA ("CAi" is data source) ["CAi" must be replaced by actual CA executive code name (one attribute per CA = n attributes)]
init	Real Single Precision	Value at beginning of current opt. iteration
lower	Real Single Precision	Lower bound
upper	Real Single Precision	Upper bound
eps	Real Single Precision	SENSITIVITY finite differencing step width
id	Integer	Data index; unique in the "type"
old	Real Single Precision	Previous iteration data value
new	Real Single Precision	Current iteration data value
step	Integer	Current optimization iteration number
ref	Real Single Precision	Reference value used for normalization (sensitivities; optimization alg.); value from 0th ANALYSIS run

Global Sensitivity Equation

Entity: gsens

Description: Contains elements of current global sensitivity derivative matrix

Attributes:

NAME	TYPE	DESCRIPTION
step	Integer	Current optimization iteration number
yindx	Integer	Dependent (behavior) variable id row number in matrix
xindx	Integer	Independent (design) variable id column number in matrix
val	Real single precision	Element value - normalized sensitivity, multiplied by ratio of reference values of independent to dependent variable

Entity: lsens

Description: Contains elements of current local sensitivity derivative (RHS) matrix

Attributes:

NAME	TYPE	DESCRIPTION
step	Integer	Current optimization iteration number
yindx	Integer	Dependent (behavior) variable id row number in matrix
xindx	Integer	Independent (design) variable id column number in matrix
val	Real single precision	Element value - normalized sensitivity, multiplied by ratio of reference values of independent to dependent variable

Entity: mmat

Description: Contains elements of current local sensitivity derivative (LHS) matrix

Attributes:

NAME	TYPE	DESCRIPTION
step	Integer	Current optimization iteration number
rindx	Integer	Dependent (behavior) variable id row number in matrix
cindx	Integer	Independent (behavior) variable id column number in matrix
val	Real single precision	Element value - normalized sensitivity, multiplied by ratio of reference values of independent to dependent variable

Variable Histories

Entity: glog

Description: Contains elements of previous global sensitivity derivative matrices

Attributes:

NAME	TYPE	DESCRIPTION
step	Integer	Optimization iteration number
yindx	Integer	Dependent (behavior) variable id row number in matrix
xindx	Integer	Independent (design) variable id column number in matrix
val	Real single precision	Element value - normalized sensitivity, multiplied by ratio of reference values of independent to dependent variable

Entity: llog

Description: Contains elements of previous local sensitivity derivative (RHS) matrices

Attributes:

NAME	TYPE	DESCRIPTION
step	Integer	Optimization iteration number
yindx	Integer	Dependent (behavior) variable id row number in matrix
xindx	Integer	Independent (design) variable id column number in matrix
val	Real single precision	Element value - normalized sensitivity, multiplied by ratio of reference values of independent to dependent variable

Entity: mlog

Description: Contains elements of previous local sensitivity derivative (LHS) matrices

Attributes:

NAME	TYPE	DESCRIPTION
step	Integer	Optimization iteration number
rindx	Integer	Dependent (behavior) variable id row number in matrix
cindx	Integer	Independent (behavior) variable id column number in matrix
val	Real single precision	Element value - normalized sensitivity, multiplied by ratio of reference values of independent to dependent variable

Entity: vlog

Description: Contains previous values of optimization variables

Attributes:

NAME	TYPE	DESCRIPTION
step	Integer	Optimization iteration number
indx	Integer	Unique variable index
value	Real single precision	Value

F.5. Data Files

Use of files was limited as much as possible in order to reduce data access times. A certain minimum number of files was considered benificial for troubleshooting purposes, however. Since all files are removed on proper operation and shutdown of DOCC, existence and contents of files aids in pinpointing the problem area. In order to facilitate this process, a consistent terminology for file names was used.

Placeholders

ca Contributing Analysis executable name [string]

cix Contributing Analysis index (SENSITIVITY) [integer]

nseq Sequence number (SENSITIVITY) [integer]

nidp Local finite differencing loop number (SENSITIVITY) [integer]

nstep	Optimization iteration number [integer]
rmode	`monit` observation mode [integer] - 1 - scheduled break, called from executive; 2 - data base closed; 3 - data base open, process running

Prefixes

tfile*	interim file
tscript*	data base script file (data base input)
treport*	data base report file (data base output)

Suffixes

*.a	produced by `run_ca`
*.flg	flag file
*.flgm	flag file, produced by `monit`
*.m	produced by `monit`
*.s	produced by `sens_seq`
*.t	general temporary file

Files Generated by `ice pipe`

db.log	data base echo; refreshed every optimization iteration
db_log.nstep.gz	compressed data base log file from previous optimization iteration nstep

Files Generated by `executive`

• OPTIMIZATION Block

Scripts:

/tmp/tscript_optin.t	extraction: DOT parameters, input
/tmp/tscript_optf.t	insertion: DOT parameters, output
/tmp/tscript_fini	data base and pipe stop
/tmp/tscript_begin	data base and pipe restart

Reports:

/tmp/treport_OPT.in	DOT parameters, input
/tmp/treport_ctrlstat.t	executive control parameter

Flags:

/tmp/treport_opt.flg	DOT parameters, input extracted
/tmp/treport_opt.flg	DOT parameters, output inserted

• ANALYSIS Block

Scripts:

/tmp/tscript_platf.t	extraction: available computer platforms
/tmp/tscript_circnum.t	extraction: circuits
/tmp/tscript_maxcirc.t	extraction: max. circuits number
/tmp/tscript_cav.t	extraction: CAs
/tmp/tscript_convc.t	extraction: Circuit convergence criteria
/tmp/tscript_cca.t	extraction: executive control parameter
/tmp/tscript_ccheck.t	extraction: executive control parameter
/tmp/tscript_convc.t	extraction: previous, current iteration variables
/tmp/tscript_convupd.t	insertion: iteration number, convergence; update previous to current iteration variables

/tmp/tscript_iterupd.t	update nsquare: circuit 'inactive'; extraction: executive control parameter
Reports:	
/tmp/treport_platfav.t	available computer platforms
/tmp/treport_cavect.t	Contributing Analyses
/tmp/treport_convcr.t	Circuit convergence criteria
/tmp/treport_csca.t	executive control parameter
/tmp/treport_ctrlstat.t	executive control parameter
/tmp/treport_convchk.t	previous, current iteration variables
/tmp/treport_ctrlstat.t	executive control parameter
Flags:	
/tmp/treport_platfav.flg	available computer platforms extracted
/tmp/treport_maxcirc.flg	max. circuits number extracted
/tmp/treport_cavect.flg	CAs extracted
/tmp/treport_convcr.flg	Circuit convergence criteria extracted
/tmp/treport_csca.flg	executive control parameter extracted
/tmp/treport_convchk.flg	executive control parameter extracted
/tmp/treport_convchk.flg	previous, current iteration variables extracted

/tmp/treport_iter.flg	nsquare updated, executive control parameter extracted

Other:

/tmp/t_ccheck.t	scratch file: convergence flag

• SENSITIVITY Block

Scripts:

/tmp/tscript_platf.t	extraction: available computer platforms
/tmp/tscript_groups.t	extraction: sequences, circuits, CA's
/tmp/tscript_gseextr.t	extraction: local sensitivities
/tmp/tscript_gsein.t	insertion: global sensitivities; status update
/tmp/tscript_gsein2.t	insertion: global sensitivities; completion query

Reports:

/tmp/treport_platfav.t	available computer platforms
/tmp/treport_groups.t	sequences, circuits, CA's
/tmp/treport_GSE.in	local sensitivities

Flags:

/tmp/treport_platfav.flg	available computer platforms extracted
/tmp/treport_groups.flg	sequences, circuits, CA's extracted
/tmp/treport_stopgse.flg	local sensitivities extracted
/tmp/treport_gsesp.flg	global sensitivities inserted

• General:

/tmp/tscript_stopdb.t	close data base and data base pipe

Files Generated by `monit`

(Numbers in square brackets refer to the associated process control menu option)

Scripts:

/tmp/tscript_startdbrmode.m	(1) open data base (rmode > 1 only) (2) extraction: executive control parameter, info parameter, optimization iteration step number (3) extraction: executive control parameter (change executive control parameter menu)

/tmp/tscript_abort	close data base, data base pipe on detected data base error
/tmp/tscript_ctrlreprmode.m	extraction: data [1]
/tmp/tscript_ctrlmupdrmode.m	update: executive control parameter [2]
/tmp/tscript_resetdb.m	update: data base reset [3]
/tmp/tscript_pausermode.m	update: executive control parameter -> -1 [4]
/tmp/tscript_rstupdrmode.m	(1) update: return to beginning of block (restart at last active block option) [5] (2) extraction: process pause location (restart at pause location option) [5]
Reports:	
/tmp/treport_openparrmode.m	(1) executive control parameter, info parameter, optimization iteration step number (initial) (2) executive conrol parameter [2]
/tmp/report_reprmode.m	data [1]
/tmp/treport_rstuprmode.m	process pause location (restart at pause location option) [5]

Flag Files:

/tmp/tscript_startdbrmode.flgm	data base opened (rmode > 1 only)
/tmp/tscript_openprmode.flgm	(1) executive control parameter, info parameter, optimization iteration step number extracted (initial) (2) executive control parameter extracted [2]
/tmp/report_reprmode.flgm	data extracted [1]
/tmp/treport_resetdb.flgm	data base reset [3]
/tmp/treport_rstrmode.flgm	process pause location extracted (restart at pause location option) [5]

Other:

control.list	restart location
dbpasswd	data base name and password

Files Generated by `run_ca`

Scripts:

/tmp/tscript_ cadbextr.a	extraction: CA input data* ; update: status

* only when called from ANALYSIS Block in `executive`

/tmp/tscript_ cadbins.a	insertion: CA input data*; update: status
Reports:	
/tmp/treport_ cadbout.a	CA input data*
Flags:	
/tmp/tscript_ cachk.a	CA input data extracted*

Files Generated by `sens_seq`

tfile_break.s	scheduled executive break flag file contents: finite differencing step number, CA index, executive control parameter
tfile_errorex.flg	flag file for immediate case termination (CA run time error detected); contents: executive control parameter
tfile_interrupt.flg	flag file for case pausing; contents: executive control parameter
/tmp/file_sseq_ nseq.s	scratch file
/tmp/tfile_seqnseq _tmp.s	scratch file
/tmp/tfile_seqnseq _tmp2.s	scratch file

/tmp/tfile_seqnseq _idp.s	unique list of independent variables for nseq columns: label, type, id, eps, reference value
/tmp/tfile_seqnseq _iot.s	list of Sequence nseq input / output data columns: label, type, id, old, eps, new, CA number, i/o index, reference value (i/o index: 1 = input; 2 = output; 3 = input and output - iteration variable)
/tmp/tfile_temp_ ca.s	scratch file
/tmp/tfile_ caib.s	CA input list
/tmp/tfile_ caob.s	CA output list; contains string "TERMINATE" if run time error message was detected in CA output file (initiating immediate shutdown of DOCC)

Scripts:

/tmp/tscript_ ca _dbextr.s	query script for ca i/o data extraction
/tmp/tscript_scr_seqnseqinit.s	iteration initialization
/tmp/tscript_scr_seqnseq _cixcixctrchk.s	status update
/tmp/tscript_seqnseq _ nidp.s	local sensitivity input into data base; status update

Reports:

/tmp/treport_ cscaib.s	input variables for ca
/tmp/treport_ caob.s	output variables for CA
/tmp/treport_ caochk.s	data base output completed

Flag Files:

/tmp/treport_scr_seqnseq _cixcixctrchk.s	status update; control variable check
/tmp/treport_rep_seqnseq _ ctrlchk .s	sensitivity spooling finished

F.6. Sample Case

A design problem for a Boeing 727 type aircraft from /Mistree et al 88/ was modified for validation of DOCC. All analyses were based on simple equations, which are documented in /Stettner et al. 95/. They were grouped into the four Contributing Analyses "D" (zero lift drag calculation in take-off/landing and cruise), "A" (lift to drag ratio), "W" (fuel weight ratios, useful load fraction), and "P" (achievable climb gradients and field length, one engine inoperative, take-off and landing), Fig. F.2(a). A fifth CA, "O," was added for calculation of the Productivity Index, PI, as the objective function, and proper constraint formulation for upper bounds on take-off and landing field length and wing aspect ratio, as well as lower bounds on achievable take-off and landing climb gradients, fuel balance, and useful load fraction. Wing span, b, fuselage length, l_f, wing area, S, installed thrust, T_i, and take-off gross weight, W_{TO}, were used as design variables.

Fig. F.2(a) indicates two closely coupled iteration loops; Drag, D, Aerodynamics, A, and Weights, W were accordingly combined into Circuit 1, Fig. 2(b). Three different Sequence groupings were used: First, only one Sequence including all CAs was formed (effectively a global finite differencing scheme; "fd" Fig. 2(c)). In a second scheme, Circuit 1 was "opened" by allocating D to Sequence 1, and A and W to Sequence 2 ("gseS," Fig. 2(d)). This grouping was particularly chosen to demonstrate Circuit iteration solution and sequential Circuit processing within a Sequence. Finally, in the scheme "gse," each CA represented a separate Sequence, Fig. 2(e).

For verification, the CA equations and analytical sensitivities were first hard-coded in a FORTRAN program which allows global sensitivity calculation by either global finite differencing ("fd") or solution of the GSE ("gse" Sequence grouping). Then the CAs were programmed as stand-alone resources, and coupled with DOCC.

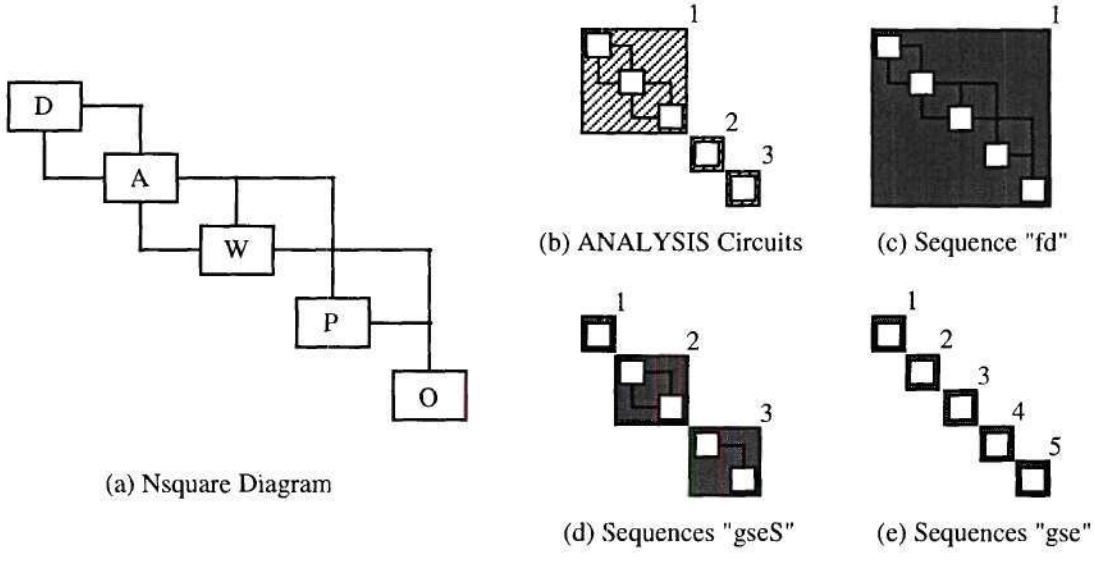

(a) Nsquare Diagram

(b) ANALYSIS Circuits

(c) Sequence "fd"

(d) Sequences "gseS"

(e) Sequences "gse"

Fig. F.2: Sample Case Circuits and Sequences

Objective function and fuel weight ratio constraint histories are shown in Figures F.3 and F.4, respectively. The initial design violates the fuel weight ratio constraint by approximately 5.5% (i.e. fuel weight required is 105.5% of fuel weight available). Results from the FORTRAN code are depicted as solid lines. The most significant deviations are detectable for the "fd" scheme as implemented in DOCC. Note that for this case, constraint violation is reduced slower than with the other methods, and a lower final PI is achieved. Judging by the histories of the other cases it appears that they converge to the same local optimum, in contrast to DOCC's "fd" case. This impression is furthermore supported by the history of the fuselage length, which shows the most irregular behavior of all traced Attributes, Fig. F.5. Clearly, the (fd, DOCC) case is locked at a particular value beginning with the first iteration. With the FORTRAN code, this is not the case; however, the response is strongly oscillatory. All cases using the GSE, however, show very smooth convergence.

Rounding errors are likely to occur in DOCC as a result of data filtering and conversion. Each global finite differencing step is equivalent to a complete analysis cycle, including iteration, which increases the potential for error accumulation. Based on the observations made, these global sensitivity errors are large enough to slow down convergence and initiate oscillations in the fuselage length with the FORTRAN code. With DOCC, they even cause the optimization to converge to a different (worse) local optimum. Breaking down iterations loops, as in the "gseS" case, already brings significant improvement. The "gse" approach, however, does not require iteration for sensitivity calculation, and is hence more robust with respect to accumulated errors. Breaking down iterations loops, as in the "gseS" case, already brings significant improvement.

Another interpretation based on linearity considerations is possible. Consider a system consisting of a series of linear Contributing Analyses. The local sensitivities can be obtained exactly due to linearity. Since the GSE solution is an exact operation, the global sensitivities thus obtained are also exact. The complete system, however, will be in general nonlinear. Global finite differencing can therefore only yield an approximation to the actual global sensitivities. In the present case, there is a weak, but highly nonlinear effect of the fuselage length on the objective function through the fuselage drag, which contains in its skin friction partition a logarithm. In order to drive this design variable in the "right" direction, this effect must be accurately measured in form of the sensitivity of PI with respect to it. This is clearly not the case when global finite differencing is used, where the small value is corrupted by iteration errors. If the nonlinearity is linearized "at the root" by local finite differencing, this sensitivity is propagated much more clearly through the GSE and allows more accurate control of this design variable.

In conclusion: The proper operation of DOCC was verified. Using global finite differencing, accumulation of errors from iteration loops is more pronounced in DOCC than in the hard-coded version. These errors have much less effect if local finite differencing and the GSE are used. Accuracy of the global sensitivities is primarily increased by opening iteration loops, not necessarily by finite differencing about the smallest unit possible.

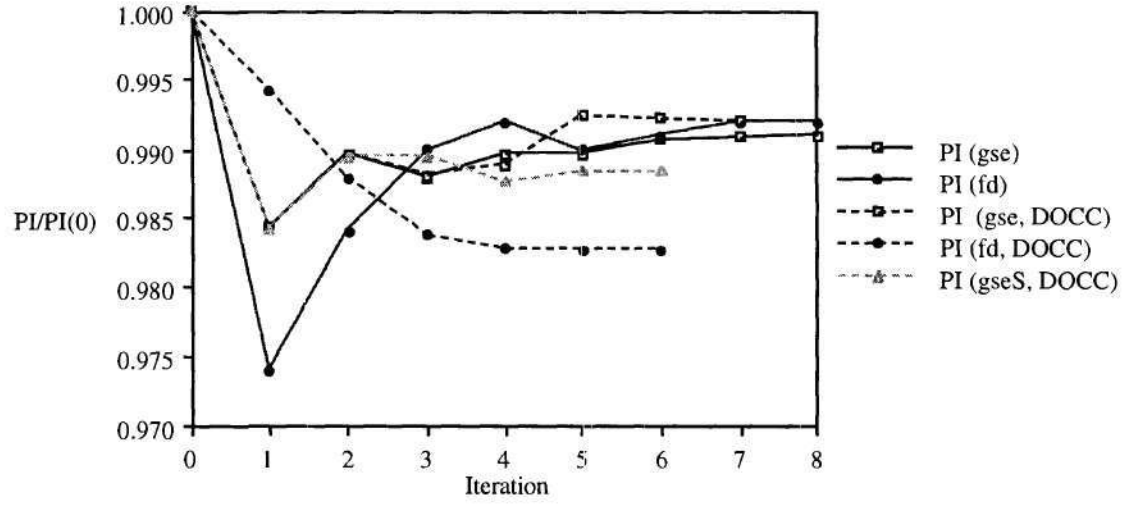

Fig. F.3: Objective Function History

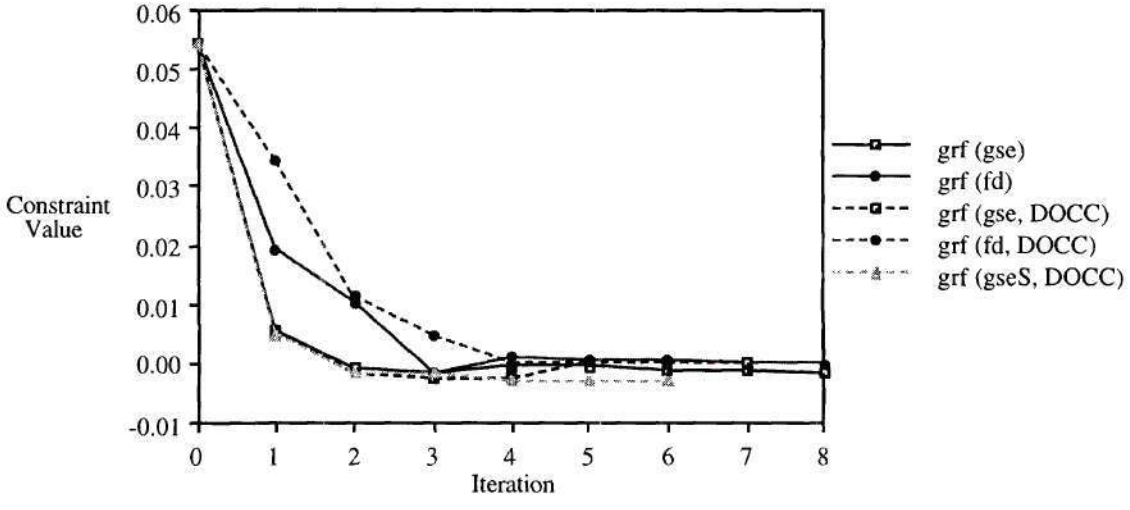

Fig. F.4: Fuel Weight Ratio Constraint History

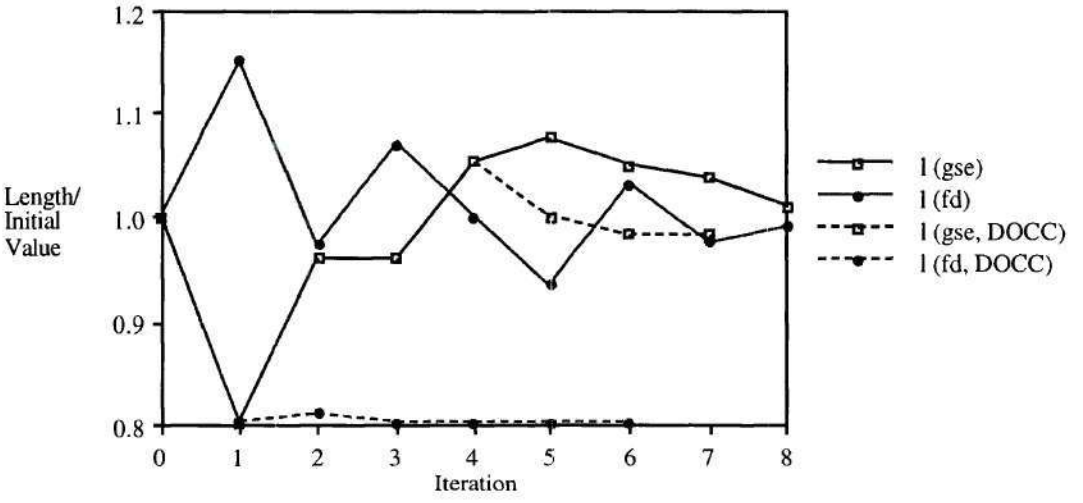

Fig. F.5: Fuselage Length History

APPENDIX G

INTEGRATION METHOD TERMINOLOGY

A_i - Analyzer, Discipline i (/Balling and Sobieski 94/)

ANALYSIS - the process by which the → Design Simulation Model generates zeroth order information about a point in the design space described by the → Problem Definition

Attribute - a single data item forming an element of a → Schema; defined in the context of → Level II Compatibility requirements /Hale and Craig 95/; Connective ~: origin (generation) within the → Design Simulation Model; Input ~: origin outside the → Design Simulation Model

[*wing area*]

Attribute Type - a classification of → Attributes based on → Contributing Analysis and → Design Simulation Model input/output; defined by → Level I and Level II Compatibility and → Problem Definition

[*Constant - 0, Design Variable - 1, → State - 2, → Behavior Variable - 3, Constraint - 4, Objective or Goal - 5*]

Basis Statement - a summary of the conditions which set the stage for the problem; part of a suggested structure for the → Problem Definition

[*constants, parts of a configuration to be varied, noise factors, design variables...*]

Behavior Variable - an → Attribute (Connective) entering the Global Sensitivity Equations

Circuit - a group of → Contributing Analyses which may be processed in parallel, for example in an iteration loop; → Level I Compatibility requires that Circuits are executed in sequence; the maximum number of Circuits is determined by → Level I Compatibility (origin: /Rogers 89/ - a minimum size feedback loop)

Constant - an → Attribute (input) which is not subject to modification in the design process; specified in the → Basis Statement

Contributing Analysis - a → Tool within the context of a → Design Simulation Model

Data Coupling Matrix (DCM) - a tabular representation of → Attribute input and output within the → Design Simulation Model; facilitates enforcement of → Level II Compatibility

Data Coupling Matrix, enhanced (DCM^+) - the → Data Coupling Matrix enhanced by information about → Contributing Analysis grouping into → Circuits and → SequencesDesign Simulation Model - a process transforming information contained in the → Problem Definition into knowledge about a point in the design space described by the → Basis Statement of the Problem Definition

Design Variable, also: Decision Variable - an → Attribute (input) which is subject to modification in the design process; a coordinate in the design space; specified in the → Basis Statement

Discipline - a branch of science associated with a → Model [*Aerodynamics*]

E_i - Evaluator, Discipline i (/Balling and Sobieski 94/)

Form - an element, physical or non-physical, that describes the design itself (/Hale and Craig 95/); physical: a geometrically describable element of an artifact (origin: /Pahl and Beitz 92/, /Stevens 93/)

[*wing*]

Function - a service to be provided by a → Form, a Form's functional purpose (origin: /Pahl and Beitz 92/, /Stevens 93/) [*create lift*]

Instance - the numerical value of an → Attribute

Intuitive Data Set - an intuitive, preliminary descriptor for information required or generated by a → Process [*configuration*]

Level I - → Process level, semi - intellectual level; pertaining to meta - design, Process scheduling; little or no dependency on fidelity

Level II - → Attribute level, physical level; pertaining to → Resource and fidelity

Level I Compatibility - connectivity between → Contributing Analyses during execution; proper execution order; validity (/Kroo and Takai 88/) of → Attributes used as inputs to Contributing Analysis; prerequisite: → Level II Compatibility; guaranteed by syntax of the → Problem Execution Code

Level II Compatibility - input / output connectivity of → Attributes within the → Design Simulation Model

Model - idealized representation of a → Process; approximate description of a Process in mathematical form using certain assumptions (origin: /Pahl and Beitz 92/)
[*Doublet Lattice Method*]

O_i - Optimizer, Discipline i (/Balling and Sobieski 94/)

Object - accuracy-independent partition of information required or generated by the → Design Simulation Model; Objects form disjoint sets in the set of Design Simulation Model → Attributes (/Hale and Craig 95/), may contain information pertaining to → Form or → Function (compare with → Schema)

Problem Execution Code - (a) the order in which → Contributing Analyses of the → Design Simulation Model are executed in order to address the problem specified in the → Problem Statement; (b) a short-hand notation for (a)

Process - a description of how Form achieves Function using (origin: /Pahl and Beitz 92/)
[*aerodynamic*]

Resource - an implementation of a → Model; an entity transforming information into knowledge (/Hale and Craig 95/)
[*computer program, engineer, team of engineers, experiment, response surface...*]

SA[ ] - System Analyzer (/Balling and Sobieski 94/)

SD[ ] - System Sensitivity Analyzer

SO[ ] - System Optimizer (/Balling and Sobieski 94/)

Schema - accuracy-dependent set of → Attributes which completely describe (not necessarily uniquely) an → Object; Schemas form disjoint sets in the set of → Design Simulation Model Attributes; Schema Evolution: the propagation of Schemas with differing accuracy (/Hale and Craig 95/)

[*Schema "trapezoidal wing planform":{wing area, taper ratio, sweep angle, aspect ratio}*]

SENSITIVITY - the process by which the → Design Simulation Model generates first order information about a point in the design space described by the → Problem Definition

Sequence - a group of → Contributing Analyses which are executed within a local sensitivity analysis, exchange → States between each other, exchange → Behavior Variables with other sequences; the maximum number of Sequences is equal to the number of Contributing Analyses

State - an → Attribute (Connective) which is generated and used within one → Sequence only, and hence does not enter the Global Sensitivity Equations

Tool - a → Resource or group of Resources processing → Objects which are received and sent in a standard format

[ ] - nested execution; coupled tasks (/Balling and Sobieski 94/)

⇒ - sequential execution (/Balling and Sobieski 94/)

|| - parallel execution (/Balling and Sobieski 94/)

REFERENCES

/Abbot et al. 60/ Abbot, F.T. jr., Kelly, H.N., and Hampton, K.D., "Investigation of 1/8 Size Dynamic-Aeroelastic Model of the Lockheed Electra Airplane in the Langley Transonic Dynamics Tunnel," NASA TM-SX 456, November 1960.

/Aho et al. 88/ Aho, A.V., Kernighan, B.W., and Weinberger, P.J., *The AWK Programming Language*, Addison-Wesley Publishing Company, Reading, MA, 1988.

/Albano and Rodden 69/ Albano, E., and Rodden, W.P., "A Doublet-Lattice Method for Calculating Lift Distributions on Oscillating Surfaces in Subsonic Flows," *AIAA Journal*, Vol. 7, No. 2, February 1969.

/Balling and Sobieski 94/ Balling, R.J., and Sobieszczanski-Sobieski, J., "Optimization of Coupled Systems: A Critical Overview of Approaches," Fifth AIAA / NASA / USAF / ISSMO Symposium on Multidisciplinary Analysis and Optimization, Panama City, FL, September 1994.

/Barthelemy et al. 91/ Barthelemy, J.-F. M., Coen, P.G., Wrenn, G.A., Riley, M.F., Dovi, A.R., and Hall, L.E., "Application of Multidisciplinary Optimization Methods to the Design of a Supersonic Transport," NASA-TM-104073, March 1991.

/Barthelemy and Hall 93/ Barthelemy, J-F. M., and Hall, L.E., "Application Report 1: Equivalent Laminated Plate Solution, ELAPS," Automatic Differentiation of FORTRAN (ADIFOR) User Workshop, NASA Langley Research Center, Hampton, Virginia, September 1993.

/Bennet and Bland 64/ Bennet, R.M., and Bland, S.R., "Experimental and Analytical Investigation of Propeller Whirl Flutter of a Power Plant on a Flexible Wing," NASA TN-D 2399, 1964.

/Bielawa 92/ Bielawa, R.L., *Rotary Wing Structural Dynamics and Aeroelasticity*, p. 347, AIAA Education Series, American Institute for Aeronautics and Astronautics, Washington, DC, 1992.

/Bischof et. al 91/ Bischof, C., Carle, A., Corliss, G., Griewank, A., and Hovland, P., "ADIFOR - Generating Derivative Codes for Fortran Programs," Argonne Preprint, MCS - P263 - 0991, 1991.

/Bloebaum 92/ Bloebaum, C.L., "An Intelligent Decomposition Approach for Coupled Engineering Systems," Fourth AIAA / USAF / NASA / OAI Symposium on Multidisciplinary Analysis and Optimization, Cleveland, OH, September 1992.

/Bloebaum et al. 90/ Bloebaum, C.L., Hajela, P., and Sobieszczanski-Sobieski, J., "Non-Hierarchic Decomposition in Structural Optimization," Third Air Force / NASA Symposium on Recent Advances in Multidisciplinary Analysis and Optimization, San Francisco, CA, September 1990.

/Boeing CTR 87/ Anonymous, "Civil Tiltrotor Missions and Applications: A Research Study," prepared by Boeing Commercial Airplane Co. et al., NASA CR 177451, November 1987.

/Bramwell 76/ Bramwell, A.R.S., *Helicopter Dynamics*, Edward Arnold (Publishers) Ltd., London, Great Britain, 1976.

/Bras and Mistree 91/ Bras, B.A., and Mistree, F., "Designing Design Processes in Decision - Based Concurrent Engineering," (SAE Publication SP-886) SAE Aerotech '91, Long Beach, CA, 1991.

/Caramaschi 91/ Caramaschi, V., "The EUROFAR Vehicle Overview," 47th Annual Forum of the American Helicopter Society, Phoenix, AZ, May 1991.

/Carlson and Walkley 84/ Carlson, H.W., and Walkley, K.B., "Numerical Methods and a Computer Program for Subsonic and Supersonic Design and Analysis of Wings with Attainable Thrust Considerations," NASA CR 3808, 1984.

/Chattopadhyay and Narayan 92/ Chattopadhyay, A., and Narayan, J. R., "Optimum Design of High Speed Prop-Rotors Using a Multidisciplinary Approach," 48th Annual Forum of the American Helicopter Society, Washington, DC, June 1992.

/Chattopadhyay et al. 93a/ Chattopadhyay, A., McCarthy, T.R., and Madden, J.F., "An Optimization Procedure for the Design of Prop Rotors in High Speed Cruise Including the Coupling of Performance, Aeroelastic Stability, and Structures," *Mathematical and Computer Modeling*, Special Issue on Rotorcraft, Part II, Vol. 17-B, 1993.

/Chattopadhyay et al. 93b/ Chattopadhyay, A., McCarthy, T.R., and Madden, J.F., "A Design Optimiation Procedure for Minimizing Drive System weight of High Speed Prop-Rotors," American Helicopter Society International Specialists Meeting on Rotorcraft Multidisciplinary Design and Optimization, Atlanta, GA, April 1993.

/Conway 91/ Conway, S., "Conclusions from High-Speed Rotorcraft Studies," NASA / Industry High - Speed Rotorcraft Meeting, Phoenix, AZ, May 1991.

/Davis et al. 95/ Davis, S.J., Moffitt, R., Quackenbush, T.R., and Wachspress, D.A., "Aerodynamic Design Optimization of a Variable Diameter Tilt Rotor," 51st Annual Forum of the American Helicopter Society, Fort Worth, TX, May 1995.

/Desmarais and Bennett 74/ Desmarais, R.N., and Bennett, R.M., "An Automated Procedure for Computing Flutter Eigenvalues," *J. Aircraft*, Vol. 11, No. 2, p. 75-80, February 1974.

/DeTore and Gaffey 70/ DeTore, J.A., and Gaffey, T.M., "The Stopped-Rotor Variant of the Proprotor VTOL Aircraft," *Journal of the American Helicopter Society*, Vol. 115, No. 3, July 1970.

/DOT 93/ Anonymous, "DOT User's Manual," VMA Engineering, Vanderplaats, Miura, and Associates, Inc., Goleta, CA, 1993.

/Dovi et al. 92/ Dovi, A.R., Wrenn, G.A., Barthelemy, J.-F. M., Coen, P.G., and Hall, L.E., "Multidisciplinary Design Integration System For a Supersonic Transport Aircraft," Fourth AIAA/USAF/NASA/OAI Symposium on Multidisciplinary Analysis and Optimization, Cleveland, OH, September 1992.

/Doyle 78/ Doyle, J.C., "Guaranteed Margins for LQG Regulators," *IEEE Transactions on Automatic Control*, AC-23, p. 756-757, 1978.

/Doyle and Stein 79/ Doyle, J.C., and Stein, G., "Robustness with Observers," *IEEE Transactions on Automatic Control*, AC-24, p. 607-611, 1979.

/Edwards 77/ Edwards, J.W., "Unsteady Aerodynamic Modeling and Active Aeroelastic Control," NASA CR-148019, 1977.

/Etkin 82/ Etkin, B., *Dynamics of Flight - Stability and Control*, 2nd Edition, John Wiley & Sons, Inc., New York 1982.

/Farrell 89/ Farrell, M.K., "Aerodynamic Design of the V-22 Osprey Proprotor," 45th Annual Forum of the American Helicopter Society, Boston, MA, May 1989.

/Fradenburgh 88/ Fradenburgh, E.A., "Improving Tilt Rotor Aircraft Performance with Variable - Diameter Rotors," 14th European Rotorcraft Forum, Milan, Italy, September 1988.

/Fradenburgh and Matuska 92/ Fradenburgh, E.A., and Matuska, D.G., "Advancing Tiltrotor State-of-the-Art with Variable Diameter Rotors," 48th Annual Forum of the American Helicopter Society, Washington, DC, June 1992.

/Frick and Johnson 74/ Frick, J.K., and Johnson, W., "Optimal Control Theory Investigation of Proprotor/Wing Response to Vertical Gust," NASA TM-X 62,384, September 1974.

/Friehmelt et al. 94/ Friehmelt, H., Reichert, G., Schrage, D.P., and Stettner, M., "Design of a Baseline Wing for a Tiltrotor Configuration," 19th Congress of the International Council of the Aeronautical Sciences, Anaheim, CA, September 1994.

/Gaffey 69/ Gaffey, T.M., "The Effect of Positive Pitch-Flap Coupling (Negative δ_3) on Rotor Blade Motion Stability and Flapping," *Journal of the American Helicopter Society*, Vol. 14, No. 2, p. 49-67, April 1969.

/Gage and Kroo 92/ Gage, P., and Kroo, I., "Development of the Quasi-Procedural Method for Use in Aircraft Configurational Optimization," Fourth AIAA/USAF/NASA/OAI Symposium on Multidisciplinary Analysis and Optimization, Cleveland, OH, September 1992.

/Ganguli and Chopra 92/ Ganguli, R., and Chopra, I., "Aeroelastic Optimization of a Composite Helicopter Rotor," Fourth AIAA/USAF/NASA/OAI Symposium on Multidisciplinary Analysis and Optimization, Cleveland, OH, September 1992.

/Gilbert 88/ Gilbert, M.G., "Result of an Integrated Structure / Control Law Design Sensitivity Analysis," NASA TM 101517, December 1988.

/Giles 89/ Giles, G.L., "Further Generalization of an Equivalent Plate Representation for Aircraft Structural Analysis," *Journal of Aircraft*, Vol. 26, No. 1, p. 67-74, January 1989.

/Haftka 84/ Haftka, R.T., "An Improved Computational Approach for Multilevel Optimum Design," *Journal of Structural Mechanics*, Vol. 12, No. 2, pp. 245-261, 1984.

/Haftka and Gürdal 92/ Haftka, R.T., and Gürdal, Z., *Elements of Structural Optimization - Third Revised and Expanded Edition*, Kluwer Academic Publishers, Dordrecht, The Netherlands, 1992.

/Hale and Craig 95/ Hale, M.A., and Craig, J.I., "On the Development of a Computing Infrastructure that Facilitates Integrated Product and Process Development from a Decision-Based Design Perspective," PFirst AIAA Aircraft Engineering, Technology, and Operations Congress, Anaheim, CA, September 1995, AIAA-95-3880.

/Hale and Craig 94/ Hale, M.A., and Craig, J.I., "Preliminary Development of Agent Technologies for a Design Integration Framework," Fifth AIAA/USAF/NASA/OAI Symposium on Multidisciplinary Analysis and Optimization, Panama City, FL, September 1994.

/Hall 66/ Hall, W.E., jr., "Prop-Rotor Stability at High Advance Ratios," *Journal of the American Helicopter Society*, June 1966.

/Ham and Whitaker 78/ Ham, N.D., and Whitaker, H.P., "A Wind-Tunnel Investigation of Tiltrotor Gust Allevation Systems," NASA CR 152264, January 1978.

/Harder and Desmarais 72/ Harder, R.L., and Desmarais, R.N., "Interpolation using Surface Splines," *J. Aircraft*, Vol. 9, No. 2, p. 189-191, 1972.

/Hassig 71/ Hassig, H.J., "An Approximate True Damping Solution of the Flutter Equation by Determinant Iteration," *J. Aircraft,* Vol. 8, No. 11, p. 885-889, November 1971.

/He 89/ He, C., "Development and Application of a Generalized Dynamic Wake Theory for Lifting Rotors," Ph.D. Dissertation, Georgia Institute of Technology, July 1989.

/He and Peters 88/ He, C., and Peters, D.A., "Numerical Computation of Associated Legendre Functions of the First Kind," Memorandum, School of Aerospace Engineering, Georgia Institute of Technology, March 1988.

/He and Peters 92/ He, C., and Peters, D.A., "Analytical Formulation of Optimum Rotor Interdisciplinary Design with a Three-Dimensional Wake," Fourth AIAA / USAF / NASA / OAI Symposium on Multidisciplinary Analysis and Optimization, Cleveland, OH, September 1992.

/Herendeen and Ludwig 88/ Herendeen, D.L., and Ludwig, M.R., "Interactive Computer Automated Design Database (CADDB) Environment User's Manual," Universal Analytics, Inc., Playa del Rey, CA, August 1988 (AFWAL-TR-88-3060).

/Hollowell and Bitten 92/ Hollowell, S., and Bitten, R., "Application of Multidisciplinary Optimization to Conceptual Aircraft Design at Rockwell International - A Status Report," AIAA Aerospace Design Conference, Irvine, CA, February 1992.

/Hoyle et al. 87/ Anonymous, "VTOL Intercity Feasibility Study Executive Summary," Hoyle, Tanner, & Associates, Inc., and J.A. Nammack Accociates, June 1987.

/Jones et al. 92/ Jones, K.H., Randall, D.P., and Cronin, C.K., "Information Management for a large Multidisciplinary Project," Fourth AIAA/USAF/NASA/ OAI Symposium on Multidisciplinary Analysis and Optimization, Cleveland, OH, September 1992.

/Johnson 74/ Johnson, W., "Analytical Model for Tilting Proprotor Aircraft Dynamics, Including Blade Torsion and Coupled Bending Modes, and Conversion Mode Operation," NASA TM-X 62369, August 1974.

/Johnson 75/ Johnson, W., "The Influence of Engine / Transmission / Governor on Tilting Proprotor Aircraft Dynamics," NASA-TM-X-62455, June 1975.

/Johnson 80a/ Johnson, W., *Helicopter Theory*, p. 471-484, Princeton University Press, Princeton, NJ, 1980.

/Johnson 80b/ Johnson, W., "A Comprehensive Analytical Model of Rotorcraft Aerodynamics and Dynamics," NASA TM 81182, 81183, and 81184, 1980.

/Johnson et al. 86/ Johnson, W., Lau, B., and Bowles, J., "Calculated Performance, Stability, and Maneuverability of High-Speed Tilting-Prop-Rotor Aicraft, 12th European Rotorcraft Forum, September 1986.

/Johnson 88/ Johnson, W., "CAMRAD/JA. A Comprehensive Analytical Model of Rotorcraft Aerodynamics and Dynamic. Johnson Aeronautics Version. Volume II: User's Manual," Johnson Aeronautics, Palo Alto, CA, 1988.

/Kinner 37/ Kinner, W., "Die Kreisförmige Tragfläche auf potentialtheoretischer Grundlage," *Ingenieur-Archiv*, Vol. VIII, p. 47-80, 1937.

/Kosmatka et al. 95/ Kosmatka, J.B., Idosor, F.R., and Lake, R.C., "Experimental / Analytical Investigation of the Free Vibration Behavior of Composite Spars with Initial Twist," 36th AIAA / ASME / ASCE / AHS / ASC Structures, Structural Dynamics, and Materials Conference, New Orleans, LA, April 1995.

/Kreisselmeir and Steinhauser 80/ Kreisselmeir, G., and Steinhauser, R., "Systematic Control Design by Optimizing a Vector Performance Index," *Computer Aided Design on Control Systems*, W.A. Cuenod, ed., Pergamon Press, p. 113-117, 1980.

/Kroo and Takai 88/ Kroo, I., and Takai, M., "A Quasi - Procedural, Knowledge - Based System for Aircraft Design," AIAA / AHS / ASEE Aircraft Design, Systems and Operations Meeting, Atlanta, GA, September 1988.

/Kvaternik 73/ Kvaternik, R.G., "Studies in Tiltrotor VTOL Aircraft Aeroelasticity," Doctoral Dissertation, Department of Solid Mechanics, Case Western Reserve, June 1973.

/Lacy and Wilkerson 95/ Lacy, R., and Wilkerson, J., "Evolution of the CTR2000 Civil Tiltrotor Configuration," American Helicopter Society Vertical Lift Aircraft Design Conference, San Francisco, CA, January 1995.

/Livne et al. 92/ Livne, E., Friedmann, P.P., and Schmidt, L.A., "Integrated Aeroservoelastic Wing Synthesis by Nonlinear Programming / Approximation Concepts," *Journal of Guidance, Control, and Dynamics*, Vol. 15, No. 4, p. 985-993, July-August 1992.

/Livne 93/ Livne, E., "Recent Developments in Equivalent Plate Modeling for Wing Shape Optimization," 34th AIAA/ASME/ASCE/AHS/ASC Structures, Structural Dynamics, and Materials Conference, La Jolla, CA, April 1993.

/Livne et. al. 93/ Livne, E., Sels, R.A., and Bhatia, K.G., "Lessons from Application of Equivalent Plate Structural Modeling to an HSCT Wing," 34th AIAA/ASME/ ASCE/AHS/ASC Structures, Structural Dynamics, and Materials Conference, La Jolla, CA, April 1993.

/McCullers 93/ McCullers, L.A., "FLight OPtimization System, User's Manual," Version 5.41, NASA Langley Research Center, December 1993.

/McVeigh et al. 83/ McVeigh, M.A., Rosenstein, H.J., and McHugh, F.J., "Aerodynamic Design of the XV-15 Advanced Composite Tilt Rotor Blade," 39th Annual Forum of the American Helicopter Society, St. Louis, MO, May 1983.

/McVeigh et al. 88/ McVeigh, M., Grauer, W.K., and Paisley, D.J., "Rotor/Airframe Interactions in Tiltrotor Aircraft," 44th Annual Forum of the American Helicopter Society, Washington, DC, June 1988.

/Miller and Ham 88/ Miller, D.G., and Ham, N.D., "Active Control of Tiltrotor Blade In-Plane Loads during Maneuvers," 14th European Rotorcraft Forum, Milan, Italy, September 1988.

/Matuska 93/ Matuska, D., Private Communication, June 1993.

/McCarthy et al. 94/ McCarthy, T., Chattopadhyay, A., Talbot, P.D., and Madden, J.F., "A Performance Based Optimization of High Speed Prop-Rotors," American Helicopter Society Aeromechanics Specialists Conference, San Francisco, CA, January 1994.

/McCarthy et al. 95/ McCarthy, T., Chattopadhyay, A., and Zhang, S., "A Coupled Rotor/Wing Procedure for High Speed Tilt Rotor Aircraft," 51st Annual Forum of the American Helicopter Society, Fort Worth, TX, May 1995.

/Mistree et al. 88/ Mistree, F., Marinopoulos, S., Jackson, D.M., and Shupe, J.A., "The Design of Aircraft Using the Decision Support Technique," NASA CR 4134, April 1988.

/Mistree et al. 93/ Mistree, F., Smith, W.F., and Bras, B.A., "Compromise Decision Support Problem and the Adaptive Linear Programming Algorithm," *Structural Optimization: Status and Promise*, p. 251-290, M.P. Kamat, Editor, AIAA, Washington, DC, 1993.

/Mistree et al 94/ Mistree, F., Patel, B., and Vadde, S., "On Modeling of Multiple Objectives and Multi-Level Decisions in Concurrent Design," ASME Design Automation Conference, Minneapolis, MN, September 1994.

/NASTRAN 83/ McCormick, C.W., Editor, "MSC/NASTRAN User's Manual," MacNeal-Schwendler Corporation, May 1983.

/NASTRAN 87/ Rodden, W.P., "MSC/NASTRAN Handbook for Aeroelastic Analysis, Volume 1," MacNeal-Schwendler Corporation, November 1987.

/Nasu 86/ Nasu, K.-I., "Tiltrotor Flutter Control in Cruise Flight," NASA TM 88315, December 1986.

/Newsom 79/ Newsom, J.R., "Control Law Synthesis for Active Flutter Suppression Using Optimal Control Theory," *J. Guidance and Control*, Vol. 2, No. 5, p. 388-394, Sept.-Oct. 1977.

/Nibbelink 92/ Nibbelink, B.D., and Peters, D.A., "Flutter Calculations for Fixed and Rotating Wings with State-Space Inflow Dynamics," 34th AIAA / ASME / ASCE / AHS / ASC Structures, Structural Dynamics, and Materials Conference, La Jolla, California, April 19-22, 1992.

/Nixon 92/ Nixon, M.W., "Parametric Studies for Tiltrotor Aeroelastic Stability in High-Speed Flight," 33rd AIAA/ASME/ASCE/AHS/ASC Structures, Structural Dynamics, and Materials Conference, Dallas, TX, April 1992.

/Notess 63/ Notess, B., "A Triangle, Flexible Airplanes, Gusts and Crew," Cornell Aero Laboratory, Inc., Memorandum No. 343, May 1963.

/Ormiston and Hodges 72/ Ormiston, R.A., and Hodges, D.H., "Linear Flap-Lag Dynamics of Hingeless Helicopter Blades in Hover," *Journal of the American Helicopter Society*, Vol. 17, No. 2, p. 49-67, April 1972.

/Padula and Polognone 90/ Padula, S.L., and Polignone, D.A., "New Evidence Favoring Multilevel Decomposition and Optimization," Third Air Force / NASA Symposium on Recent Advances in Multidisciplinary Analysis and Optimization, San Francisco, CA, September 1990.

/Padula et al. 91/ Padula, S.L., James, B.J., Graves, P.C., and Woodard, S.E., "Multidisciplinary Optimization of Controlled Space Structures with Global Sensitivity Equations," NASA TP 3130, November 1991.

/Pahl and Beitz 92/ Pahl. G., and Beitz, W., *Engineering Design: A Systematic Approach*, Springer - Verlag, Berlin, Germany, 1992.

/Parham and Chao 89/ Parham, T.C., and Chao, D., "Tiltrotor Aeroservoelastic Design Methodology at BHTI," 45th Annual Forum of the American Helicopter Society, Boston, MA, May 1989.

/Peters and He 87/ Peters. D.A., and He, C.J., "A Closed-Form Unsteady Aerodynamic Theory for Lifting Rotors in Hover and Forward Flight," 43rd Annual Forum of the American Helicopter Society, St. Louis, MO, May 1987.

/Peters et al. 87/ Peters, D.A., Boyd, D.B., and He, C.J., "Finite-State Induced-Flow Model Rotors in Hover and Forward Flight," 43rd Annual Forum of the American Helicopter Society, St. Louis, MO, May 1987.

/Peters and He 89/ Peters, D.A., and He, C.J., "Comparison of Measured Induced Velocities with Results from a Closed-Form Finite State Wake Model in Forward Flight," 45th Annual Forum of the American Helicopter Society, Boston, MA, May 1989.

/Peters and Su 91/ Peters, D.A., and Su., A., "An Integrated Airloads-Inflow Model for Use in Rotor Aeroelasticity and Control Analysis," 47th Annual Forum of the American Helicopter Society, Phoenix, AZ, May 1991.

/Peters and Johnson 94/ Peters, D.A., and Johnson, M.J., "Finite-State Airloads for Deformable Airfoils on Fixed and Rotating Wings," Symposium on Aeroelasticity and Fluid/Structure Interaction, ASME Winter Annual Meeting, Chicago, IL, November 1994.

/Peters and Karunamoorthy 94/ Peters, D.A., and Karunamoorthy, S., "State-Space Inflow Models for Rotor Aeroelasticity," 12th AIAA Applied Aerodynamics Conference, Colorado Springs, CO, June 1994.

/Peters et al. 94/ Peters, D.A., Barwey, D., and Su, A., "An Integrated Airloads-Inflow Model for Rotor Aeroelasticity and Control Analysis," *Mathematical and Computer Modeling*, Vol. 19, No. 3/4, p. 109-123, 1994.

/Popelka et al. 85/ Popelka, D., Sheffler, M., and Bilger, J., "Correlation of Stability Test Results and Analysis for the 1/5 Scale V-22 Aeroelastic Model," 41st Annual Forum of the American Helicopter Society, Fort Worth, TX, May 1985.

/Popelka et al. 95/ Popelka, D., Lindsay, D., Parham, T., Berry, V., and Baker, D.J., "Results of an Aeroelastic Tailoring Study for a Composite Tiltrotor Wing," 51st Annual Forum of the American Helicopter Society, Fort Worth, TX, May 1995.

/Reissner and Stevens 47/ Reissner, E., and Stevens, J.E., "Effect of Finite Span on the Airload Distributions for Oscillating Wings. II - Methods of Calculation and Examples of Application," NACA TN-1195, October 1947.

/Renaud and Gabriele 90/ Renaud, J.E., and Gabriele, G.A., "Direct Handling of Equality Constraints in Multilevel Optimization," Third Air Force / NASA Symposium on Recent Advances in Multidisciplinary Analysis and Optimization, San Francisco, CA, September 1990.

/Renaud and Gabriele 93/ Renaud, J.E., and Gabriele, G.A., "Improved Coordination in Non-Hierarchic System Optimization," *AIAA Journal*, Vol. 31, No. 12, December 1993.

/Renaud et al. 94/ Renaud, J.E., Sellar, R.S., Batill, S.M., and Kar, P., "Design Driven Coordination Procedure for Concurrent Subspace Optimization in MDO," 36th AIAA/ASME/ASCE/AHS/ASC Structures, Structural Dynamics, and Materials Conference, Hilton Head, SC, April 1994.

/Ribner 45/ Ribner, H.S., "Propeller in Yaw," NACA Rep. 820, 1945.

/Rogers 89/ Rogers, J.L., "DeMAID - A Design Manager's Aide for Intelligent Decomposition User's Guide," NASA TM 101575, March 1989.

/Roskam 89/ Roskam, J., *Airplane Design - Part III: Layout of Cockpit, Fuselage, Wing, and Empennage. Cutaways and Inboard Profiles*, Roskam Aviation and Engineering, Ottawa, Kansas, 1989.

/Safanov and Athans 77/ Safanov, M.G., and Athans, M., "Gain and Phase Margins of Multiloop LQG Regulators," IEEE Transactions on Automatic Control, AC-22, p. 173-179, 1977.

/Scanlan and Truman 50/ Scanlan, R.H., and Truman, J.C., "The Gyroscopic Effect of a Rigid Rotating Propeller on Engine and Wing Vibration Modes," Journal of the Aeronautical Sciences, Vol. 17, p. 653-659, October 1950.

/Schillings and Reinesch 87/ Schillings, J., and Reinesch, R., "Rotor/Airframe Aerodynamic Interference on the V-22 Tilt Rotor," AHS Specialists' Meeting on Aerodynamics and Aeroacoustics, Arlington, TX, February 1987.

/Schleicher 93/ Schleicher, D.R., "Advanced Civil Tiltrotor Design Optimization and Issues," 49th Annual Forum of the American Helicopter Society, St. Louis, MO, May 1993.

/Schmidt and Dyess 90/ Schmidt, A.H., and Dyess, S.B., "Tilt Rotor Wing Weight Estimation," SAWE Paper No. 1926, 1990.

/Schoen et al. 80/ Schoen, A. H., Rosenstein, H., Stanzione, K., and Wisniewski, J. S., "User's Manual for VASCOMP II, The V/STOL Aircraft Sizing and Performance Computer Program," Boeing Vertol Company Report D8-0375, Vol. VI, Third Revision, May 1980.

/Scott 91/ Scott, M.W., "Summary of Technology Needs for High Speed Rotorcraft Study," NASA / Industry High - Speed Rotorcraft Meeting, Phoenix, AZ, May 1991.

/Scott 95/ Scott, M.W., Private Communication, May 1995.

/Sewall 62/ Sewall, J.L., "An Analytical Trend Study of Propeller Whirl Instability," NASA TN-D 996, 1962.

/Sobieski 82/ Sobieszczanski-Sobieski, J., "A Linear Decomposition Method for Large Optimization Problems - Blueprint for Development," NASA TM 83248, February 1982.

/Sobieski 88a/ Sobieszczanski-Sobieski, J., "On the Sensitivity of Complex Internally Coupled Systems," NASA TM 100537, January 1988.

/Sobieski 88b/ Sobieszczanski-Sobieski, J., "Optimization by Decomposition: A Step from Hierarchic to Non-Hierarchic Systems," Second NASA / Air Force Symposium on Recent Advances in Multidisciplinary Optimization, Hampton, VA, September 1988.

/Sobieski et al. 88/ Sobieszczanski-Sobieski, J., Bloebaum, C.L., and Hajela, P., "Sensitivity of Control-Augmented Structure Obtained by a System Decomposition Method," 29th AIAA Structures, Structural Dynamics, and Materials Conference, Williamsburg, VA, April 1988.

/Sobieski 89/ Sobieszczanski-Sobieski, J., "Multidisciplinary Optimization for Engineering Systems: Achievements and Potential," NASA TM 101566, March 1989.

/Sprangers and Stevenson 86/ Sprangers, C.A., and Stevenson, M.K., "Results of the V-22 Preliminary Design Wing Test Program," 42nd Annual Forum of the American Helicopter Society, May 1986.

/SQL 86/ Anonymous, *ANSI Standard for Data Base Language*, SQL X3.135-1986.

/Stettner et al. 95/ Stettner, M., Mavris, D.N., and Schrage, D.P., "Aeroelastic Tailoring of a Civil Tiltrotor Configuration," American Helicopter Society Vertical Lift Aircraft Design Conference, San Francisco, CA, January 1995.

/Stevens 93/ Stevens, E. "LEGEND: Laboratory Environment for the Generation, Evaluation, and Navigation of Design," Ph.D. Dissertation, School of Aerospace Engineering, Georgia Institute of Technology, September 1993.

/Stevens et al. 94/ Stevens, D.C., Striz, A.G., and Yurkovich, R.N., "An Interactive Model Generator / Preprocessor for the Multidisciplinary Optimization of Aircraft," 5th AIAA/NASA/USAF/ISSMO Symposium on Multidisciplinary Analysis and Optimization, Panama City, FL, September 1994.

/Steward 81/ Steward, Donald, V., *Systems Analysis and Management: Structure, Strategy, and Design*, Petrocelli Books, New York, 1981.

/Studebaker and Matuska 93/ Studebaker, K., and Matuska, D., "Variable Diameter Tiltrotor Wind Tunnel Test Results," 49th Annual Forum of the American Helicopter Society, St. Louis, MO, May 1993.

/Suh 90/ Suh, N.P., *The Principles of Design*, Oxford University Press, New York, 1990.

/Taylor and Browne 38/ Taylor, E.S., and Browne, K.A., "Vibration Analysis of Aircraft Power Plants," *Journal of the Aeronautical Sciences*, Vol. 6, p. 43-49, December 1938.

/Theodorsen 35/ Theodorsen, T., "General Theory of Aerodynamic Instability and the Mechanism of Flutter," NACA Rep. 496, 1935.

/Torenbeek 82/ Torenbeek, E., *Synthesis of Subsonic Airplane Design*, Delft University Press, Martinus Nijhoff Publishers, Delft, Holland, 1982.

/Townsend et al. 93/ Townsend, J.C., Weston, R.P., and Eidson, T.M., "A Programming Environment for Distributed Complex Computing - An Overview of the Framework for Interdisciplinary Optimization (FIDO) Project," NASA-TM-109058, December 1993.

/Tsai and Massard 87/ Tsai, S.W., and Massard, T.M., Composites Design, 3rd Edition, Think Composites, Dayton, Ohio, 1987.

/van Aken 91/ van Aken, J.M., "Allevation of Whirl-Flutter on Tilt-Rotor Aircraft Using Active Controls," 47th Annual Forum of the American Helicopter Society, Phoenix, AZ, May 1991.

/Venkayya et al. 94/ Venkayya, V.B., Pitrof, S.M., Neill, D.J., and Tischler, V.A., "Automated Structural Optimization System (ASTROS) User Training Workshop," Wright Research and Development Center, Wright-Patterson Air Force Base, OH (notes of workhop held at the Georgia Institute of Technology, Atlanta, GA, May 16-20, 1994)

/Vepa 77/ Vepa, R., "Finite State Modeling of Aeroelastic Systems," NASA CR-2779, February 1977.

/Wagner 25/ Wagner, H., "Über die Entstehung des dynamischen Auftriebes von Tragflügeln," *Zeitschrift für angewandte Mathematik und Mechanik*, Vol. 5, No. 1, February 1925.

/Wang 92/ Wang, Y.-R., "The Effect of Wake Dynamics on Rotor Eigenvalues in Forward Flight," Ph.D. Dissertation, School of Aerospace Engineering, Georgia Institute of Technology, May 1992.

/Watkins et al. 59/ Watkins, C.E., Woolston, D.S., and Cunningham, H.J., "A Systematic Kernel Function Procedure for Determining Aerodynamic Forces on Oscillating or Steady Finite Wing at Subsonic Speeds," NASA TR R-48, 1959.

/Wernicke and Gaffey 67/ Wernicke, K.G., and Gaffey, T.M., "Review and Discussion of 'The Influence of Blade Flapping Restraint on the Dynamic Stability of Low Disk Loading Propeller-Rotors'," 23rd Annual Forum of the American Helicopter Society, Washington, DC, May 1967.

/Weston et al. 94/ Weston, R.P., Townsend, J.C., Eidson, T.M., and Gates, R.L., "A Distributed Computing Environment for Multidisciplinary Design," 5th AIAA / NASA / USAF / ISSMO Symposium on Multidisciplinary Analysis and Optimization, Panama City, FL, September 1994.

/Wilkerson and Schneider 91/ Wilkerson, J.B., and Schneider, J.J., "Technology Needs for High-Speed Rotorcraft - Conceptual Designs and Performance," 47th Annual Forum of the American Helicopter Society, Phoenix, AZ, May 1991.

/Wilkerson and Taylor 88/ Wilkerson, J.B., and Taylor, R.S., "Civil Tiltrotor Aircraft: A Comparison of Five Candidate Designs," 44th Annual Forum of the American Helicopter Society, Washington, DC, June 1988.

/Wrenn and Dovi 88/ Wrenn, G.A., and Dovi, A.R., "Multilevel Decomposition Approach to the Preliminary Sizing of a Transport Aircraft Wing," *Journal of Aircraft,* Vol. 25, No. 7, pp 632-638, July 1988.

/Yates 87/ Yates, E.C., "Aerodynamic Sensitivities from Subsonic, Sonic, and Supersonic Unsteady, Nonplanar Lifting-Surface Theory," NASA TM 100502, September 1987.

/Young and Lytwyn 67/ Young, M.I., and Lytwyn, R.T., "The Influence of Blade Flapping Restraint on the Dynamic Stability of Low Disk Loading Propeller-Rotors," 23rd Annual Forum of the American Helicopter Society, Washington, DC, May 1967.

VITA

Martin Stettner was born on February 5, 1965, in Neumünster, Germany. In 1985, he enrolled in the Mechanical Engineering program of the Technische Universität Braunschweig, where he received his Vordiplom in 1987. He then completed two more years of studies in Braunschweig, in which he specialized in Aerospace Engineering.

In September 1989, he joined the graduate program of the School of Aerospace Engineering at the Georgia Institute of Technology. After completion of his thesis research in aeroelasticity of servo flap-controlled rotors, he received the degree of Master of Science in March of 1991. He then joined the Ph.D. program at the same school and pursued research in aircraft preliminary design, tiltrotor aeroelasticity, unsteady aerodynamics, aeroservoelastic tailoring, and multidisciplinary optimization, which resulted in this thesis.